A Glimpse into the Polymorphic Landscape of Amyloids - Structural Investigation of Amyloid Fibrils by Cryo-Electron Microscopy

Inaugural-Dissertation

zur Erlangung des Doktorgrades
der Mathematisch-Naturwissenschaftlichen Fakultät
der Heinrich-Heine-Universität Düsseldorf

vorgelegt von
Christine Martina Röder
aus Recklinghausen

Düsseldorf, Februar 2021

Aus dem Institut für Physikalische Biologie
der Heinrich-Heine-Universität Düsseldorf
und dem Institut für Biologische Informationsprozesse, Strukturbiochemie (IBI-7)
des Forschungszentrums Jülich

Gedruckt mit der Genehmigung der

Mathematisch-Naturwissenschaftlichen Fakultät der

Heinrich-Heine-Universität Düsseldorf

Berichterstatter:

1. Prof. Dr. Gunnar Schröder
2. Prof. Dr. Georg Groth

Tag der mündlichen Prüfung: 07.05.2021

During the course of this work the following manuscripts have been published, submitted or are in preparation.

Röder, C., Vettore, N., Mangels, L.N. *et al.* Atomic structure of PI3-kinase SH3 amyloid fibrils by cryo-electron microscopy. *Nat Commun* **10,** 3754 (2019). https://doi.org/10.1038/s41467-019-11320-8

Received: 26 March 2019, Accepted: 09 July 2019, Published: 21 August 2019

Röder, C.*, Kupreichyk, T.*, Gremer, L. *et al.* Cryo-EM structure of islet amyloid polypeptide fibrils reveals similarities with amyloid-β fibrils. *Nat Struct Mol Biol* **27,** 660–667 (2020). https://doi.org/10.1038/s41594-020-0442-4

Received: 12 February 2020, Accepted: 30 April 2020, Published: 15 June 2020

Röder, C.*, Zielinski, M.*, Schröder, GF. Cryo-EM of amyloidogenic proteins. *J Biol Chem*

Manuscript submitted

Schenk, C., **Röder, C**. *et al.* Interface-Polymorphism and Secondary Nucleation in Aβ (1–42) Fibrils

In preparation

* authors contributed equally

The list of people to whom I owe my gratitude encompasses supervisors, colleagues, office and lab staff, and collaboration partners. Here, I would like to especially highlight the following collaborations and support without which this thesis could not have been successful:

Section IV: Atomic structure of an amyloid model system: src-homology domain 3
Thanks to Alexander Büll and his group for the fruitful collaboration. We teamed up with Nicola Vettore, who prepared a beautiful SH3 sample and together with Lena N. Mangels performed mutation experiments and measured aggregation kinetics.

Section IV, VI and IV: All measurements on cryo-electron microscopes
This work would not have been possible without the collaboration and great team work with the team from University Maastricht. Thanks to Raimond Ravelli for introducing us to the Tecnai Arctica and for (technical) support on multiple occasions. Many thanks to Hans Duimel who cared a lot about our samples and prepared all the cryo-grids on-site. Additional thanks go to Abril Gijsbers for preparation of the final pGlu-Aβ(3-42) sample.

Section V1: pGlu-Aβ(3-42)
I gratefully acknowledge support from the Alzheimer Forschung Initiative e.V. and Alzheimer Nederland (project no. 19082CB).
Thank you, Patrick Meckelburg, for introducing me to the lab at the IPB in Düsseldorf and making me familiar with pGlu-Aβ(3-42). And thanks to Lothar Gremer I learned a lot about the handling of amyloid fibrils and how to properly operate the HPLC system.

Section V1.3: Quality control of pGlu-Aβ(3-42)
I am thankful for the help of Sabine Metzger and Andreas Linden who performed mass spectrometric analyses on my samples without which I could not have shown the composition of the pGlu-Aβ(3-42) sample.

Section V1.5: Cryo-EM measurements on pGlu-Aβ(3-42)
I am glad to have worked with Carsten Sachse's lab at the Forschungszentrum Jülich. Thanks to Julio Ortiz who taught me the whole sample preparation workflow and together with Thomas Heidler supported microscope handling and data acquisition. And thanks to Sabrina Berkamp for helping out with sample preparation of pGlu-Aβ(3-42) for the measurement in 2019.

Section V2: Aβ36
Thank you, Martin Ingelsson, for trusting me with the precious Aβ36 samples and the great team work. Special thanks to Dieter Willbold and Lothar Gremer for initiating and partaking in this collaboration. Moreover, I would like to thank Mara Zielinski for moving on with this project and sharing your EM data with me.

Section V3: Aβ(1-42)-pS8

I would like to express further gratitude towards Jochen Walter and Sathish Kumar for confiding me with their Aβ(1-42)-pS8 samples. Many thanks to Lothar Gremer who initiated this collaboration and Benedikt Frieg who is taking this project to the next level.

Section V4 : Aβ(1-42) point mutants A21G, E22G, E22K, D23N

The number of mutants in this work would have been much smaller if not for the support of Elke Reinartz and Robin Backer. Thank you for assisting me and Lothar Gremer in establishing these mutants.

Section VI: **Structural similarities between IAPP and Aβ(1-42) fibrils**

Another fruitful collaboration, for which I have to thank Wolfgang Hoyer and Tatsiana Kupreichyk. Special thanks to Tatsiana Kupreichyk who put a lot of effort in creating the ideal environment for an IAPP sample well suited for cryo-EM. Also, thank you for carrying out AFM experiments.

Section X9.4 Circular dichroism spectroscopy

Many thanks to Rebecca Sternke-Hoffmann for introducing me to CD spectroscopy and carrying out the experiment with me.

Computational support and infrastructure

I gratefully acknowledge the computing time granted by the Jülich Aachen Research Alliance High-Performance Computing (JARA-HPC) Vergabegremium and VSR commission on the supercomputer JURECA at Forschungszentrum Jülich (1).

Computational support and infrastructure was provided by the "Centre for Information and Media Technology" (ZIM) at the University of Düsseldorf (Germany).

II Abstract – Zusammenfassung

Abstract

Amyloids are structurally characterized by a high β-sheet propensity. They form as aggregates from unfolded, mostly intrinsically disordered, peptides. The most prominent form of amyloid is the amyloid fibril, which is characterized by stacks of monomers resulting in a helical filament with a distinct cross-β structure. The repetitive, helical structure of amyloid fibrils makes them an ideal target for structural investigations via cryo-electron microscopy.
In recent years, it has been shown that amyloid fibrils usually exhibit different morphologies that might be linked to certain pathologies. This study aims at broadening our understanding of amyloid fibril structures and especially their polymorphism. The following amyloids have been investigated.

(i) As a model organism for protein folding, src-homology domain 3 from phosphatidyl-inositol-kinase 3 was examined under the cryo-electron microscope. Its atomic structure was modeled into a density map of 3.4 Å resolution. Subsequently, kinetic changes in fibril formation of point mutants could be explained with this model.

(ii) Amyloid-β, an amyloid infamous for its role in Alzheimer's disease, is known to occur in a variety of mutations and modifications. In this study, four point mutations were established for research. Additionally, a new familial mutation was shown to form either oligomers or fibrils depending on the buffer system, and prepared for structure elucidation via cryo-electron microscopy. Moreover, samples of post-translationally modified amyloid-β species were prepared and examined. Phosphorylated amyloid-β was prepared and optimized for cryo-electron microscopy experiments, and effects of sonication on the fibrils was tested. Cryo-electron microscopy measurements were performed on a truncated amyloid-β variant with a pyroglutamation at residue three. The study presents a density map of ~4 Å resolution together with a potential residue placement.

(iii) Islet amyloid polypeptide occurs in the pancreatic islands of β-cells of type II diabetes patients. In addition to its role in the disease, islet amyloid polypeptide has also been shown to be molecularly linked to Alzheimer's disease. In this work, the existence of this molecular link was demonstrated by elucidating the structure of islet amyloid polypeptide, which showed significant similarity with an amyloid-β fold.

Zusammenfassung

Amyloide zeichnen sich durch eine hohe Neigung zur Bildung von β-Faltblättern aus. Sie formen Aggregate aus entfalteten, meist intrinsisch ungeordneten, Peptiden. Diese Peptidmonomere stapeln sich in der prominentesten Erscheinungsform von Amyloiden, der Amyloidfibrille, zu einem helikalen Filament. Die dadurch entstehende, repetitive Struktur der Amyloidfibrillen macht sie zu einem idealen Objekt struktureller Untersuchungen mittels Kryo-Elektronenmikroskopie.

In den letzten Jahren wurde gezeigt, dass Amyloidfibrillen in der Regel unterschiedliche Morphologien aufweisen, die mit bestimmten Pathologien in Verbindung gebracht werden können. Die vorliegende Studie trägt dazu bei, den Aufbau von Amyloidfibrillen und insbesondere ihren Polymorphismus zu verstehen. Um dieses Ziel zu erreichen, wurden die folgenden amyloidogenen Proteine untersucht:

(i) Die src-Homologiedomäne 3 aus der Phosphatidyl-Inositol-Kinase 3, die als Modellorganismus für Proteinfaltung gilt, wurde unter dem Kryo-Elektronenmikroskop untersucht. Ihre atomare Struktur wurde in eine Dichtekarte mit 3,4 Å Auflösung modelliert. Anschließend konnte dieses Modell verwendet werden, um kinetische Veränderungen der Fibrillenbildung in Punktmutanten zu erklären.

(ii) Amyloid-β, ein Amyloid, das vor allem für seine Rolle in der Alzheimer-Krankheit bekannt ist, kommt in einer Vielzahl von Mutationen und Modifikationen vor. In dieser Studie wurden vier der bekannten, familiären Punktmutationen für spätere Forschungszwecke etabliert. Zusätzlich wurde für eine neuentdeckte familiäre Mutation, die ebenfalls für die Strukturaufklärung mittels Kryo-Elektronenmikroskopie präpariert wurde, gezeigt, dass sie in Abhängigkeit verschiedener Puffersysteme Oligomere oder Fibrillen bildet. Darüber hinaus wurden post-translational modifizierte Amyloid-β-Spezies untersucht. So wurde phosphoryliertes Amyloid-β für kryo-elektronenmikroskopische Experimente präpariert und optimiert. Zudem wurden kryo-elektronenmikroskopische Untersuchungen an einer verkürzten Amyloid-β-Variante, mit einem Pyroglutamat an Aminosäure drei, durchgeführt. Diese Untersuchungen führten zu einer Dichtekarte mit etwa 4 Å Auflösung, die hier zusammen mit einem potentiellen Modell diskutiert wird.

(iii) Insel-Amyloid-Polypeptid kommt in den Pankreasinseln der β-Zellen von Diabetes Typ II Patienten vor. Zusätzlich zu seiner Rolle in Diabetes Typ II wurde gezeigt, dass dieses Amyloid auf molekularer Ebene in Verbindung zur Alzheimer-Krankheit steht. Diese Verbindung konnte in der vorliegenden Arbeit dadurch bestätigt werden, dass die mittels Kryo-Elektronenmikroskopie aufgelöste Struktur signifikante Ähnlichkeit mit einem bekannten Amyloid-β-Polymorph aufwies.

III Introduction

1 Amyloids – A universal fold challenges the Anfinsen theorem

1.1 A short history of amyloid research[1]

The Anfinsen theorem (2) has gone unchallenged for a long time. Until the discovery of the amyloid fold it was thought that a protein's native fold is dictated exclusively by its primary sequence. Today, the amyloid fold is believed to be a generic fold, and that proteins can adopt this fold independent from their primary sequence (3, 4). The prominent amyloid fibril fold is characterized by the aggregation of proteins into homo-polymeric stacks of well-ordered β-sheets resulting in a so-called cross-β pattern (4–6) (see also section 2.2). Proteins that adopt this fold are summarized under the term amyloids. The definition has been extended to include disordered aggregates with high β-sheet-content, which are referred to as oligomers (see 1.2.2 and following).

The field of amyloid research has evolved rather slowly, although its beginning might date back to Nicolaus Fontanus' autopsy records, which are believed to describe amyloid deposits as early as 1639 (7–10). Research on amyloids progressed in the 19th century when Rudolf Virchow coined the term amyloid while dissecting human brains. At that time, he did so as reference to the Greek word for "starch" which was what he assumed amyloid consisted of because of its positive reaction to treatment with iodine and sulfuric acid (7, 11, 12). It was only a few years later that the first deposits were described as proteinaceous (7, 13). These proteinaceous aggregates showed enhanced birefringence with Congo red (7, 14) which together with the binding of Thioflavin T (ThT) (15) is considered a common indicator for amyloids.

Currently, more than 50 amyloids (5, 16, 17) are linked to protein misfolding diseases, or amyloidoses (18). Amongst them are common diseases such as Alzheimer's disease (AD) (19) Parkinson's disease (PD) (20, 21) and Type II diabetes (T2D) (22) as well as rare diseases such as hereditary transthyretin-related (23) and systemic light chain amyloidosis (24). Because most of the proteins involved in the aforementioned diseases happen to be intrinsically disordered proteins (IDPs) such as amyloid β (Aβ, found in AD) or amylin (found in T2D), it was commonly thought that only IDPs will aggregate into amyloid fibrils and oligomers. However, metabolites have been found to fold into disease-causing amyloid-like aggregates as well (25). Additionally, non-disease related amyloids such as src-homology domain 3 (SH3) can form amyloid fibril deposits *in vitro* when forced to unfold from their native state (26). Beyond that, functional amyloids, which are mostly found in fungi or bacteria where they often work as a defense mechanism against other species, have been described (27, 28).

[1] This section has been adopted from the manuscript for "Cryo-EM of amyloidogenic proteins" (39)

Some proteins only adopt the amyloid fold when being exposed to extreme conditions such as very low pH, high temperature and shaking (26, 29, 30). Another common driving force for aggregation is a coincidental increase in local concentration that boosts the misfolding reaction (31). Additionally, there are examples of proteins that have to undergo proteolytic truncations in order to aggregate (32).

Although amyloids share the common β-sheet architecture, the mechanism of their aggregation from an IDP or globular protein into amyloid is not yet understood. Given that such a wide variety of proteins and peptides are able to adopt one common fold, it is of great interest to understand why and how they do so. Elucidating why the fibrillar fold is functional in some organisms but becomes pathological in others can yield important insights into how such diseases might be prevented or treated.

1.2 What we know about amyloid formation

Disordered proteins – whether they are IDPs or unfolded proteins – can follow different pathways to form amyloid species (see Figure 1B). Disordered monomers are the starting point for amyloid formation although aggregation of monomeric species is considered thermodynamically unfavorable. Ten years ago, Schmit, Ghosh and Dill (33) proposed a phase diagram for amyloid formation that is similar to the crystallization process. Their theory posits that amyloid formation depends on monomer concentration: upon a certain threshold, termed the critical monomer concentration (CMC), a critical nucleus forms, which is described as the least stable structure that is necessary for oligomer or fibril formation. After overcoming the critical nucleus, aggregation is thermodynamically favorable and results in amyloid species such as oligomers or fibrils.

However, simulations showed that the nucleation process of amyloids cannot necessarily be directly compared to the crystallization process. Instead, fibril nucleation should be thought of as a two-step mechanism that depends on the local monomer concentration (Figure 1A). Specifically, the critical size of the oligomeric nucleus increases with the monomer concentration. Only at higher, usually unphysiological peptide concentrations, a nucleated polymerization process comparable to crystallization is observed. (34)

Amyloidogenic monomers can form toxic species by following two distinct pathways: In the off-pathway, or oligomer-pathway, (Figure 1A, dotted lines) monomers aggregate into disordered, globular structures – the so-called oligomers (35, 36) (Figure 1B, beige, see also (1.2.2)). These oligomers can then further aggregate into protofibrils (Figure 1B, petrol), a curvy-linear oligomer species. Contrary, in the classic pathway, or on-pathway, (Figure 1A, solid lines) monomers aggregate first into fibrillar oligomers (Figure 1B, green to brown) and from there into mature fibrils (Figure 1B, blue). The formation of a fibrillar oligomers has been shown to be comparably fast while the following progression into mature fibrils is considered the time-limiting step (37). The mature fibril state is considered the most stable protein state known (38).

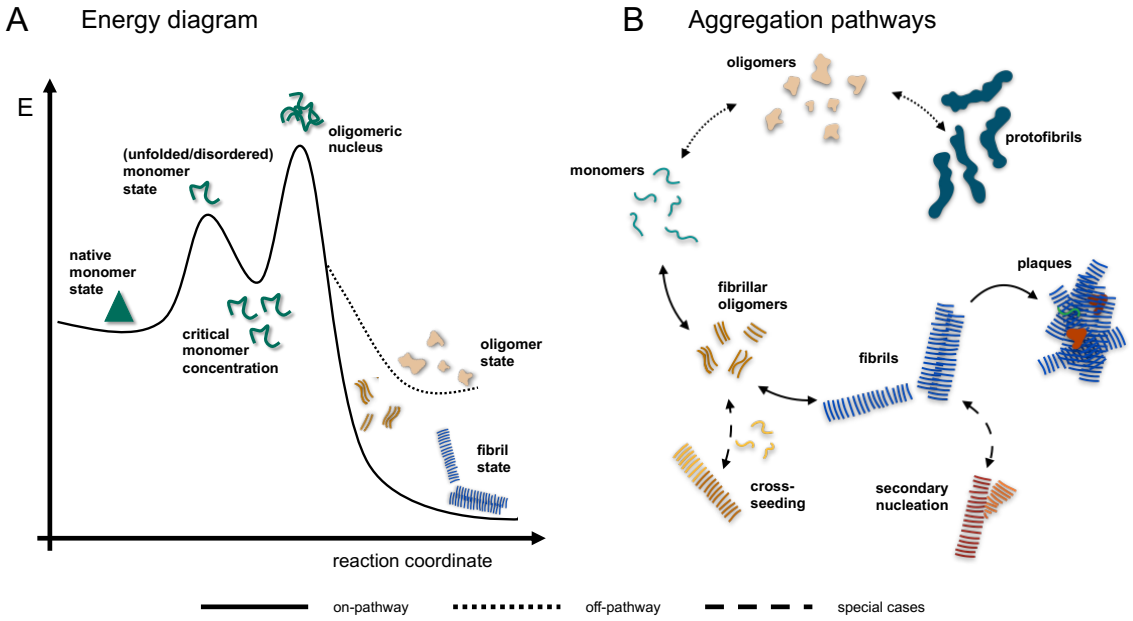

Figure 1: Amyloid formation schemes. (A) Schematic energy diagram of the amyloid formation reaction. Since amyloid formation is started from an unfolded protein state, potential native states first undergo unfolding. The disordered protein is accumulated up to the critical monomer concentration upon which the oligomeric nucleus is built. Once that state is reached, aggregation becomes thermodynamically favorable and oligomers (beige) (off-pathway, dotted line) respectively fibrils (blue) (on-pathway, solid line) are formed. (B) Aggregation pathways of amyloidogenic proteins. Considering (intrinsically) disordered monomers (green) as the starting point of aggregation, these monomers might aggregate into oligomers (beige) (off-pathway, dotted line) or fibrillar oligomers (brown) (on-pathway, solid line). Small oligomers might further aggregate into curvy-linear protofibrils (petrol). Fibrillar oligomers might mature into uni-proteinaceous fibrils (blue) or serve as seeds for cross-seeding with another protein species (yellow). Mature fibrils can deposit as plaques together with other species and/or serve as secondary nucleation site for further aggregation of monomers (red/orange). (Image modified according to Zielinski et al. (39) (submitted manuscript))

Mature fibrils may be considered the 'final state' of amyloid aggregation but they can still develop further into fibril plaques by coagulating in bulk together with other components. The resulting plaques are known as the hallmark of Alzheimer's disease (AD), for example (40–42). Moreover, mature fibrils can function as secondary nucleation sites (see "secondary nucleation" in 1.2.1). Secondary nucleation, which describes the possibility of new fibrils to grow on the surface of existing fibrils (Figure 1B, red/orange), is a well-known concept in crystallography (43) but a comparably new field of research in the amyloid context (44, 45).

In addition, several studies show that fibrillar oligomers or mature fibrils of one peptide might function as seeds for monomers of a different peptide to grow (Figure 1B, brown/yellow). This process is known as cross-seeding, which has been reported for example for Aβ (see 1.4.1) and IAPP (see 1.4.2) (46).

To date, the mechanisms of fibrillation are hardly understood. However, it has become obvious that fibrillation is affected by a number of factors, including but probably not limited to a protein's primary sequence, pH, temperature, local peptide concentration, metal concentration and salt concentrations (47, 48). While the primary sequence plays a critical role for native proteins, its importance for aggregation is most obvious when it comes to (point) mutations of certain amyloidogenic proteins (see 1.4.1.3). Although it has been

shown that generic hydrophobic stretches within the primary sequence of amyloidogenic proteins are sufficient to induce aggregation (34, 49), the primary sequence seems to play a role in amyloidoses since small specific sequence mutations still heavily influence disease progression (50–52).
A number of theories and models on the formation of amyloid has been proposed but, as described, there are many more factors to include until we will be able to fully understand the mechanism behind protein aggregation.

1.2.1 Primary and secondary nucleation

Primary nucleation can be described as polymerization of an initial fibril nucleus by monomer addition to the fibril ends (53). This mechanism is rate dependent on the concentration of available monomers (54). Secondary processes can lead to an increase in fibril concentration, namely fragmentation (fibril breakage) or secondary nucleation (55). These secondary processes are rate dependent on the concentration of already existing fibrils, meaning fragmentation solely depends on the concentration of existing fibrils while secondary nucleation is dependent on both monomer and fibril concentration (54). A visualization of the above-mentioned processes is displayed in Figure 2.

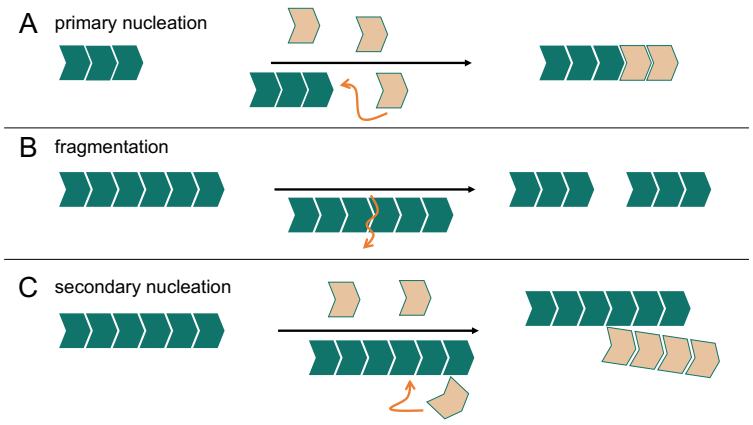

Figure 2: Primary and secondary nucleation pathways in amyloid formation. (A) Primary nucleation is dependent on monomer concentration (beige). The fibril nucleus (green) is growing into a fibril by monomer addition to the fibril ends. (B) Fragmentation is a secondary pathway, dependent on the fibril concentration. It increases the number of fibril ends by breakage of existing fibrils. (C) Secondary nucleation is dependent on both fibril and monomer concentration. Single monomers attach to the fibril along its axis and start nucleating there.

Primary nucleation (Figure 2A) is a straightforward nucleation process during which single monomers attach sequentially to an existing fibril end and thus aggregate into long fibrils. However, the longer a fibril becomes, the more likely it is to be fragmented (56)(Figure 2B). Fragmentation therefore increases the number of available fibril ends in the solution. It has been suggested that lengthy fibrils might enhance cytotoxicity by membrane disruption (57, 58) and indeed, cryo-ET (cryogenic electron tomography) and fluorescence microscopy images show distorted liposomes in direct contact with β2-microglobulin fibrils (59). Secondary nucleation (Figure 2C) is a different process in which monomers do not attach to

an existing fibril end. Instead, they attach alongside the fibril axis and begin to grow into a new fibril that will detach from the "mother fibril" in the course of its progression (54).

1.2.2 Oligomers

Oligomers and fibrils are amyloid species with distinct properties. Fibrils (see Figure 1B, blue) are known as stable and linear repetitive structures of monomeric proteins, whereas oligomers (see Figure 1B, beige) seem to be rather disordered, mostly globular aggregates from a small number of amyloidogenic proteins. They are considered micelle-like conglomerates of monomers held together by hydrophobic interactions (33), and are much smaller than fibrils with significantly lower molecular masses, which result in a higher mobility (60).

It is important to distinguish between two types of oligomers: on-pathway and off-pathway oligomers (see also 1.2). While the on-pathways oligomers are mainly an interim step between amyloidogenic monomer and amyloid fibrils, off-pathway oligomers are the ones believed to act as toxic species (61, 62). It was found recently that in contrast to on-pathway oligomer formation, off-pathway oligomer and resulting protofibril formation requires a much higher monomer concentration (63). On the other hand, similar to the notion that the propensity of proteins to form amyloid fibrils is ubiquitous, there are also studies that imply the ability to form toxic oligomeric aggregates might be a general phenomenon (36).

To date there is no high resolution structure of a toxic oligomer but first (cryo-)EM data show them in various shapes ranging from tubular assemblies to globular ones resembling erythrocytes (64–66). Considering the toxicity of amyloidogenic oligomer species, it is of interest to further understand their formation as well as their structures in order to target them for medical research.

1.2.3 Fibrils

Fibrillar structures are characterized as having a defined, regular arrangement of the respective building components. The same sort of building blocks are stacked upon each other and are for visualization purposes best thought of as Lego bricks (see Figure 3C).

A mature fibril usually consists of two protofilaments (Figure 3A,B). These two protofilaments wind around each other, resulting in a twisted fibril. This twist is one of the main characteristics of amyloid fibrils, which are usually described through their twist, rise, width, handedness and crossover distance or pitch, which is two times the crossover distance (see Figure 3A). While the rise is defined as the distance between two monomer layers in the fibril, the twist refers to the degree of rotation the fibril undergoes during one rise unit.

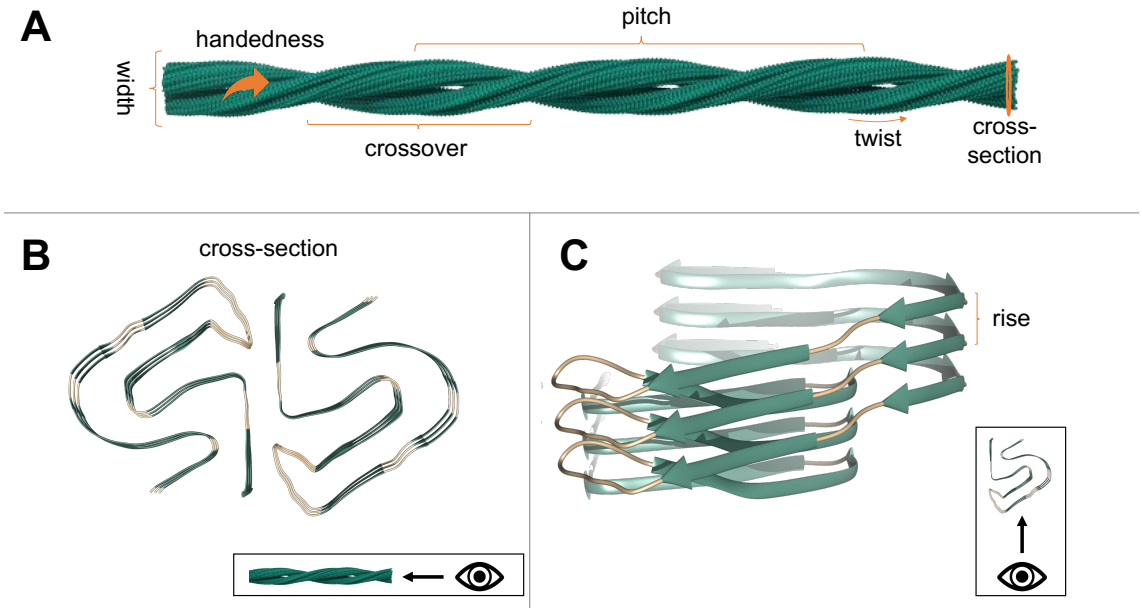

Figure 3: Parameters characterizing an amyloid fibril. (A) Macroscopic side view of a fibril displaying width, handedness, crossover, pitch, twist and cross-section. (B) Cross-section or "top view" of a fibril. (C) Close-up of a side view of one fibril protofilament displaying rise between β-sheets. Changes in perspective are indicated by the symbolic eye. (PDB: 6R4R)

These values can be derived from the measurements of the crossover distance. For the width, which can simply be measured, usually minimum and maximum values have to be given since the fibril becomes narrower at crossover points. The handedness of a fibril refers to its overall rotation being clockwise (left-handed) or anti-clockwise (right-handed). It is often determined by means of atomic force microscopy (AFM) (67–70) or platinum shadowing (71, 72). Besides these characteristics, the main attribute of amyloid fibrils is their distinct cross-β pattern (5, 6, 73) which occurs due to the repetitive stacking of amyloid monomers in a fibril. It can be observed by methods such as X-ray diffraction or cryo-EM and is displayed as a peak in the power spectrum at 4.7 Å and a minor peak at 10 Å (for more detailed information please refer to 2.2).

1.2.4 Polymorphism

Under the same conditions, a specific protein might aggregate into structurally very different fibrils, a phenomenon known as polymorphism (Figure 4). In order to describe polymorphism, it is important to understand the term (fibril) interface. The fibril interface (Figure 4, beige) is the contact point of two fibril filaments. Here, certain residues from one filament interact with residues from the opposing filament and thereby stabilize the formation of a twisted fibril. Polymorphism in amyloid fibrils might refer to

(i) packing polymorphism, in which the same interface can be observed in different overall topologies (Figure 4A) (74, 75) or

(ii) segmental polymorphism where different β-strand segments form different interfaces but the overall topology stays the same (Figure 4B) (74, 75), and

(iii) assembly polymorphism referring to the same fibril topology being connected to further fibrils through different interfaces (Figure 4C) (75, 76).

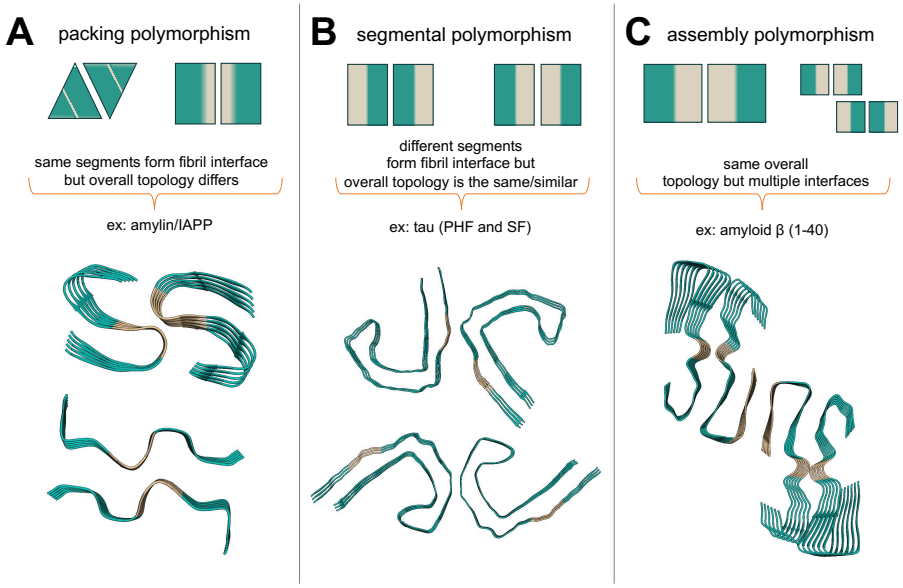

Figure 4: Polymorphism in amyloid fibrils. Fibrils are shown in green, core-forming segments (interfaces) are highlighted in beige (A-C). (A) Packing polymorphism refers to a fibril interface that consists of the same sequence segments within two polymorphs that show an overall different topology (PDB codes: 6Y1A, 6VW2). (B) In segmental polymorphism the overall topology of polymorphs is similar but the fibril interface is built by different sequence segments. (PDB codes: 6HRF, 6HRE) (C) Assembly polymorphism occurs if the same fibril topology can interact via different interfaces. (PDB codes: 6SHS).

When discussing polymorphism in amyloid fibrils, non-twisted fibrils should be mentioned as well. Due to their lack of repetitive features and thus difficulties in the reconstruction process, there are no structural data available yet, but untwisted fibrils or single protofilaments have been reported (77).

Although amyloid formation is very sensitive to factors such as pH and salt concentration (26, 29, 30), it remains unclear why fibrils exhibit such a wide range of polymorphism under the same conditions. Due to a limited number of *ex vivo* structures (72, 78–80), it is not yet known if polymorphism might be primarily an *in vitro* phenomenon. However, experiments with *in vitro* tau protein fibrils seeded from brain material indicate that polymorphs might be specific for certain disease manifestations (81–84). In order to better understand amyloid pathologies and fight them, moving forward, it is of great interest to further look into polymorph formation and distribution.

1.3 Model systems

Over the past decades it has been shown that amyloidogenic proteins play important roles in all kinds of organisms (85–88). But up to now we lack sufficient understanding of amyloid formation to explain for example which factors induce aggregation of IDPs into amyloid fibrils and which induce oligomer formation. Additionally, it is of interest to understand

what kinetics primary and secondary nucleation in amyloids follow and how a combination of these processes can be described mathematically.

For further understanding of underlying mechanisms and the ability to make assumptions about general principles that apply for amyloid fibril formation, model systems are of key importance. Model systems for amyloid formation include lysozyme (89), glucagon (90), and SH3 domains (26). As they are well-characterized biochemically and biophysically (89, 91–93), and more accessible for research due to commercial availability, these model systems have improved our understanding of the amyloid state as a protein state accessible for every protein. Among these model systems, SH3 is specifically interesting since there is a large family of evolutionary related proteins that share structural similarities paired with low sequence homology (94).

1.3.1 Src-homology domain 3 of Phosphatidylinositol 3-kinase

SH3 (src-homology domain 3) proteins are kinase subdomains of usually less than 100 amino acids length. They were first described three decades ago by Mayer *et al*. (95) and since have been found to be part of more than 350 proteins, ranging from kinases and GTPases to adaptor proteins and structural proteins, within all kind of organisms (96). SH3 domains are known to play a significant role in several signaling pathways, where they mediate protein-protein interactions by recognizing PxxP sequence motifs flanked by specific residues (97, 98).

Phosphatidylinositol 3-kinase (PI3K) belongs to the family of tyrosine kinases that phosphorylate tyrosine residues on substrate peptides in many signal transduction pathways (97). In cancer, kinases are frequently overexpressed, which makes them an important research subject for the development of targeted treatments (99).

The structure of natively folded PI3K-SH3, a domain consisting of 86 amino acids from bovine PI3K, has been well-characterized by X-ray crystallography and NMR spectroscopy (99–102). In contrast, atomic resolution structures of SH3 fibrils have been one of the great challenges in structural biology up to a few years ago. Complementary methods like NMR spectroscopy, ATR-FTIR, mass spectrometry and H/D exchange were applied to gain information on the molecular assembly of these fibrils (4, 103–107).

Former structural studies on SH3 fibrils suggest that they are likely to consist of two twisted protofilaments with each protofilament layer containing one or two SH3 monomers (108, 109). Characterization of SH3 fibrils on the structural level might reveal insights into the universal features of fibril formation.

1.4 Disease-related amyloids

There are over 50 amyloidogenic proteins that have been linked to a number of diseases (5, 17). These diseases range from commonly known ones such as Type II Diabetes (T2D) (110) to rare diseases such as systemic light chain amyloidosis (24). Infamous for its linkage to Alzheimer's disease is the amyloid β (Aβ) peptide, which had formerly been known as the amyloid A4 unit of a membrane-spanning protein called APP (amyloid precursor protein) (111).

1.4.1 Amyloid β – Alzheimer causing agent

Alzheimer's disease (AD) is known as memory-affecting neurological disease due to which patients and their relatives suffer from immense loss of quality of life. In 2018, there were over 1.5 million AD patients in Germany, of which two thirds were women and most had been older than 65 years. Worldwide, we count over 40 million patients today while expecting this number to grow to over 130 million by 2050 (112). With the number of people becoming sick rising and a concomitant increase in healthcare costs, the need for a treatment to cure or mitigate AD becomes even more pressing.

AD is coarsely divided into two main forms namely the familial AD (FAD) cases and sporadic AD (SAD) cases (113). The protein associated with AD is amyloid β (Aβ), an IDP which derives from cleavage of a precursor protein coded on the *app* gene (114, 115). While FAD cases are mainly believed to arise due to a number of known mutations in the *app* gene (116) or, since *app* is coded for on chromosome 21, as a side effect of down syndrome (116, 117), SAD cases appear spontaneously due to molecular alterations such as oxidative damage (118). Another classification of AD is based on differentiation between early onset AD (EOAD) before the age of 65 and late onset AD (LOAD) after the age of 65 (113).

In the 1980s, Glenner and Wong were the first to isolate and purify Aβ (119). They suspected it to be the causative agent in AD and a cleavage product of some precursor protein. APP, said precursor protein for Aβ, is a transmembrane protein with a large extracellular domain. The physiological function of APP in the human body remains unclear although studies report implications for brain development, neuronal plasticity and neuroprotection (120).

APP can be cleaved extracellularly by a number of enzymes such as the α-secretase ADAM10 (disintegrin and metalloproteinase domain-containing protein 10) (121), the β-secretase BACE1 (β-site of APP cleaving enzyme) (122) and γ-secretases. The proteolysis of APP by the α-secretase ADAM10 followed by γ-secretase does not result in Aβ as a cleavage product and therefore is referred to as the non-amyloidogenic pathway. Instead, Aβ is only produced if APP is cleaved by the β-secretase BACE1 (Figure 5) (115).

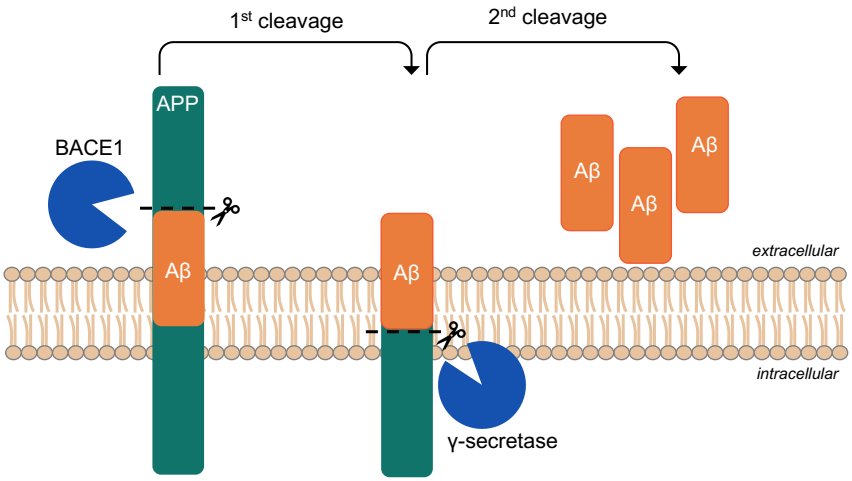

Figure 5: Cleavage of APP into Aβ. Schematic representation of the extracellular cleavage of the transmembrane protein APP (green) by BACE1 (blue, 1st cleavage) and the subsequent cleavage by the γ-secretase ADAM10 (blue, 2nd cleavage) resulting in free, monomeric Aβ (orange). Image modified according to (123).

However, multiple secretases have been identified to play a role in APP cleavage resulting in a variety of products (124).

The amyloidogenic pathway results in Aβ forms exhibiting lengths between 34 and 43 residues (125) with Aβ(1-40), Aβ(1-38) and Aβ(1-42) being the most abundant in AD (126). Interestingly, there are also indications for physiologically relevant roles of Aβ which range from neuro-protection (127) and regulation of synaptic signaling (128) to antimicrobial activity (129).

1.4.1.1 The amyloid cascade hypothesis

The most common reason for examination of Aβ remains the unsolved problem of AD. After having been discovered by Alois Alzheimer, Aβ was deemed the cause for AD. Established by research in the 1990s (130), the so-called amyloid cascade hypothesis proposes *„that deposition of amyloid β protein (AβP), the main component of the plaques, is the causative agent of Alzheimer's pathology and that the neurofibrillary tangles, cell loss, vascular damage, and dementia follow as a direct result of this deposition"* (131). Hence, severeness of the disease should increase with the number of fibril deposits (plaques) in the brain. However, in past years it has been shown that increased plaque levels do not lead to increased AD pathology (132, 133). Although the role of Aβ fibrils as toxic agent in AD is debated in the field, it is widely agreed that Aβ is indeed a good biomarker for AD (28) and therefore is a valid target for medical research. Accordingly, increasing the structural knowledge on Aβ in its different forms as well as its mutations and variants, will help advancing our understanding of the AD pathology as well as medical opportunities.

Moreover, a new, still debated hypothesis has emerged. It states that oligomers represent the toxic species (35, 134) and stable fibrils might actually resemble a harmless storage form of toxic oligomers (135). In recent literature, researchers now start to try and combine these two hypotheses while stressing the complexity of AD (136, 137).

1.4.1.2 Failed drug trials and the hope for new treatments

Although more than 200 candidates have been assessed, there has been no FDA (US Food and Drug Administration) approved treatment for AD after 2003 (138). Instead, there have been more than ten failed phase 3 trials within the last five years (123). Most of the candidates that made it into phase 3 clinical trials were targeting the amyloid deposit load and aimed at reducing it (138). Amongst these candidates, were inhibitors of γ-secretase (139, 140) and β-secretase (141, 142) as well a monoclonal antibodies (mAb) against Aβ (123, 143). However, none of these phase 3 trials showed sufficient improvement. Most of them failed due to a lack of efficacy while some of them actually failed due to toxicity (143). Drug candidates have been mostly tested on confirmed AD patients or pre-clinical candidates with detectable amyloid deposits (142) although AD is known to evolve long before first symptoms occur (144). Hence, a major criticism in the set-up of clinical trials has been the fact that treatments might simply come too late for patients with symptoms but could potentially still improve the lives of undiagnosed patients (145). Consequently, we are in need of early diagnostics that in the best case are minimally invasive such as blood tests (146–149).

Looking at the number of failed drug candidates and the years of discussion about the disease-causing agent in AD, we start to understand that most likely there is not one single enemy when fighting AD. Instead, we rather lack an adequate and thorough understanding of AD pathophysiology. Indeed, evidence indicates that AD is a multi-factorial disease. As an example, tau hyperphosphorylation is triggered by Aβ which makes the two proteins a dangerous pairing (41, 150). In their review Roberta Ricciarelli and Ernesto Fedele suggest that some of our very basic ideas about AD might be tragically wrong assumptions due to AD research relying on mouse models that cannot model human AD sufficiently. They argue: *„Indeed, the most critical issue, in our opinion, is that much of our knowledge on Aβ pathophysiology derives from transgenic AD mice, which are increasingly put into question as to whether or not they can represent adequate models of the human pathology. As these mice carry the mutations found in FAD, it is obvious that they are not representative of late onset SAD, which affects more than 95% of AD patients. Although the two forms of AD have similar anatomo-pathological features, it is well known that they manifest at different ages, and with distinctive cognitive symptoms and disease progression"* (136).

1.4.1.3 Amyloid β has a "hot spot" region for pathogenic mutations

As with almost every protein, for Aβ there is a number of known mutations, which have an influence on the course of AD. There are more than 15 characterized mutations in the Aβ sequence of which a summary and categorization can be seen in Figure 6.

Most AD cases appear to be sporadic with a late onset (151). However, 60 % of patients affected who develop EOAD display a family history with AD and one in seven of these patients inherited EOAD in an autosomal manner (151–153). Mutations in the *app* gene (Figure 6) are thought to be responsible for 10 – 15 % of FAD/EOAD cases (151, 154).

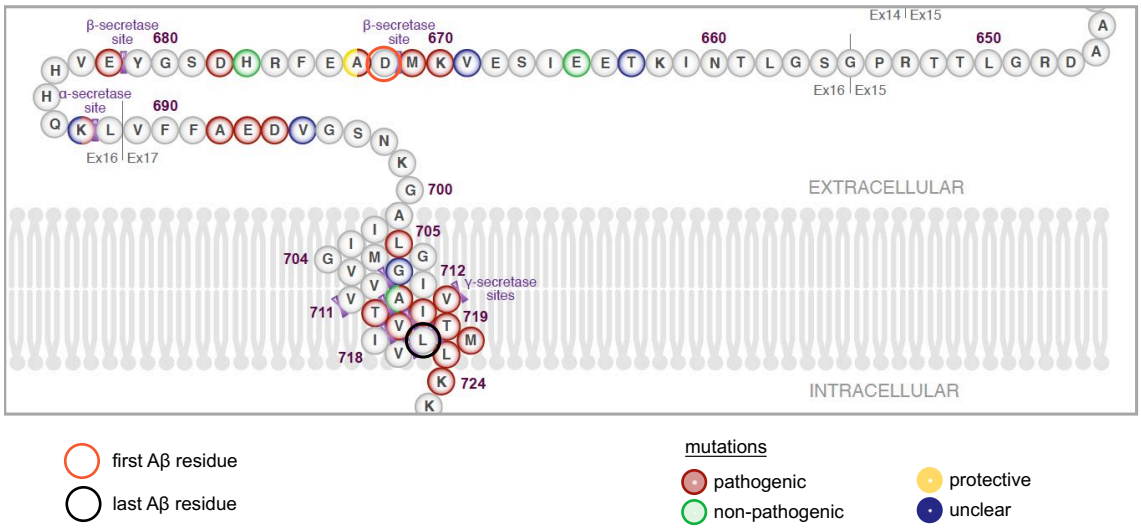

Figure 6: Mutations in the APP sequence. In the panel, a part of the APP sequence is shown as it is embedded in the membrane. In-between residues 650 and 724 the restriction sites of α-, β- and γ-secretases are indicated. The potential first (D672) and last (L720) residues of Aβ are highlighted by a red respectively black circle. Known mutations are accentuated in red (pathogenic), green (non-pathogenic), yellow (protective) or blue (unclear) according to their effect. Image taken from and modified according to (155).

As displayed in Figure 6, the region around residues 21 – 23 (AED, residues 692 – 694 in the figure) is one of the hotspots for pathogenic mutations in Aβ(1-42). Here, mutations at position 22 and 23 seem to increase aggregation propensity and toxicity while alterations at position A21G do not promote aggregation of Aβ (52). Mutations that increase Aβ's hydrophobicity have a distinct effect on its aggregation behavior, specifically on the size distribution of oligomers (156).

The A21G mutation, first reported in a Dutch family and hence referred to as the Flemish mutation (157), has been shown to increase both Aβ(1-40) and Aβ(1-42) levels in patients and is together with the Dutch mutation (E22Q) (158) associated with cerebral hemorrhages (159). Nevertheless, in vitro experiments with A21G have shown an if at all low aggregation propensity (52).

The Arctic mutation (E22G) is characterized by enhanced protofibril formation, up to twofold faster conversion from oligomers to fibrils compared to the wildtype (37), and increased proteotoxicity (160). Similarly, E22K, the Italian mutation, has been shown to aggregate faster compared to wildtype Aβ42 (52).

E22Δ, the Osaka variant, does hardy fibrillate. Still, the mutation, which forms soluble oligomers and then only very slowly converts into fibrils (161), shows an increased β-sheet propensity (162).

The D23N mutation has been identified in an Iowa-based family of German descent (163). Since then the mutation has been verified in further three European families as a driving force for EOAD (164–166). It exhibits two- to threefold higher cytotoxicity in cell assays compared to wildtype Aβ(1-42) (52).

In 2019, a new familial mutation has been identified in Uppsala, Sweden. A Swedish family who developed AD already in their 40s was found to show the novel mutation with

autosomal-dominant behavior. The Uppsala mutation is characterized by deletion of six amino acids in the central region of the peptide. Hence, this mutant is referred to as Aβ36 (mutated Aβ(1-42)) and Aβ34 (mutated Aβ(1-40)). Aβ36 seems to aggregate much faster than the wildtype. Deposits of the examined patients appeared unusually round and showed almost no wildtype aggregates. (167)

1.4.1.4 Post-translational modifications

In addition to the number of known familial mutations (see above, 1.4.1.3), multiple post-translational modifications (PTMs) have been discovered for Aβ (see Figure 7).
These include but are not limited to pyroglutamation, phosphorylation and glycosylation (125). Oxidation and nitration have been shown to be induced by the inflammatory milieu in AD brain (168).

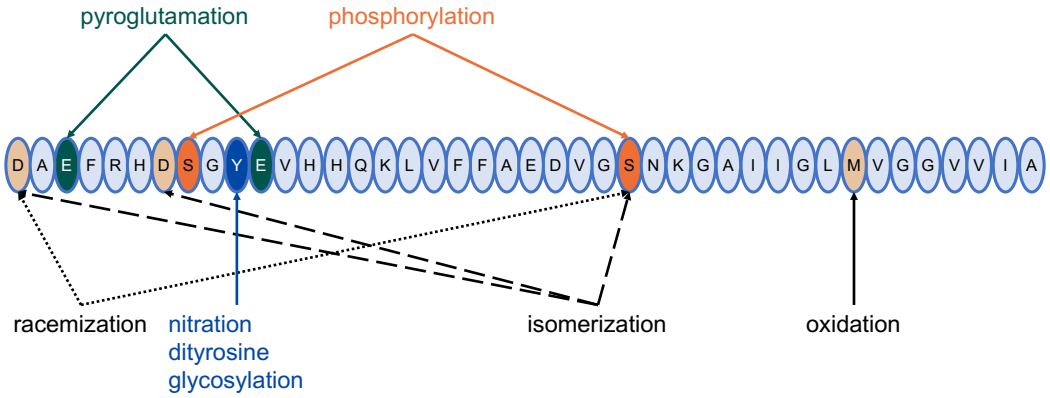

Figure 7: Post-translational modifications of Aβ. Post-translational modifications in the Aβ(1-42) sequence (light blue ovals) are indicated by color with pyroglutamation sites in green, phosphorylation sites in orange, modifications at Tyr10 in blue and further modifications highlighted with black arrows.

Amongst the better understood PTMs, pyroglutamation at residue three and phosphorylation are found. Pyroglutamated Aβ(3-42) (pGlu-Aβ(3-42)) is a highly amyloidogenic variant (169), which exhibits high β-sheet propensity and accelerated aggregation compared to Aβ(1-42) (170). Pyroglutamation at residue three is one of the major PTMs found in AD brain (171) where it exhibits low solubility and has been localized in plaques (172).
In vivo, conversion from Aβ(3-42) to pGlu-Aβ(3-42) is catalyzed by the glutaminyl cyclase (173) but it has been shown to occur *in vitro* under acidic conditions and elevated temperature (174) (Figure 8).

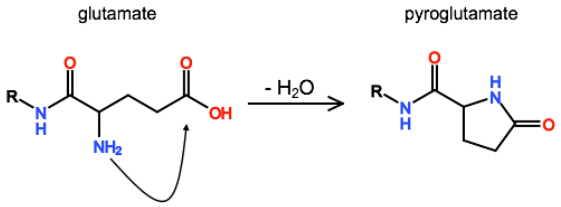

Figure 8: Formation of pyroglutamate from glutamate. In vivo, pyroglutamate formation is catalyzed by glutaminyl cyclase. (175)

Phosphorylation of Aβ(1-42) is known to occur on serine residues 8 and 26. While pS26-Aβ(1-42) (Aβ(1-42) phosphorylated at serine 26) does not form fibrils (176), pS8-Aβ(1-42) has been identified in fibrillar form in amyloid plaques (177) as well as in the intracellular space (178). In contrast, pS26-Aβ(1-42) aggregates into oligomers while simultaneously increasing neurotoxicity in mouse models and human neurons (176).
Similar to pGlu-Aβ(3-42), NMR studies with pS8-Aβ(1-42) showed that phosphorylation affects the fibril structure N-terminally which likely results in less compact fibril conformations compared to wildtype (179).

Due to their characteristics, PTMs have been proposed and examined as potential drug targets or biomarkers (125). Recently, Eli Lilly released a report stating that their monoclonal antibody (mAb) treatment donanemab slows clinical decline in a phase 2 clinical trial by 32 % (180). In contrast to most other mAbs against Aβ, donanemab specifically targets pGlu-Aβ(3-42) and is supposed to clear plaques in the brain. Donanemab is one of the few current drug candidates addressing AD. Therefore the positive outcomes of this study can be seen as a silver lining for AD patients although future trials will have to prove donanemab's ability to turn into a potent treatment.
While a lot of structural data on amyloid fibrils has been published in recent years (16, 69, 72, 181–186) including *ex vivo* structures (72, 187–189), structural information on PTMs have only been reported for tau protein (183, 190) and α-synuclein so far (191). Nevertheless, PTMs play an important physiological role in AD disease progression (125) and polymorphism of disease-related amyloids (192), which leaves them as an attractive subject for structural studies.

1.4.2 Type II diabetes and its linkage to Alzheimer's disease

The word diabetes originates from the Greek *diabanein* (to pass through) in reference to one of the major symptoms, excessive urine production in diabetes patients (193). Although it has been discovered that insulin injections mitigate the disease (194), diabetes joined the top 10 causes of death worldwide in 2019 (195). Accordingly, diabetes remains a pressing global health issue and continues to be a major field in biomedical research.
There are three subtypes of diabetes that are type I (T1D, affecting 10 – 15 % of diabetes patients (196)), type II (T2D), and gestational diabetes. The latter can be developed during

pregnancy and usually disappears after conclusion of the pregnancy (197). T1D patients do not produce insulin due to a loss of pancreatic β-cells and therefore have to supplement it (196). In contrast, T2D patients show impaired cell responses towards insulin and impaired insulin secretion due to which patients to not reach required levels of insulin. The T2D type most often occurs in older people and accounts for the majority of diabetes cases. (198)

Associated with T2D is a short polypeptide, namely amylin or IAPP (islet amyloid polypeptide) (199). Functionally, IAPP is involved in glucose homeostasis with indications that it may operate as a regulator of insulin and glucagon secretion (200, 201). However, IAPP is able to form amyloid deposits that occur in pancreatic islets of Langerhans cells (200, 202). Aggregated IAPP is believed to be involved in apoptosis (203), chronic inflammation (204) and membrane disruption (205) but ultimately it remains elusive how IAPP turns into toxic aggregates.

Although the role of IAPP in the disease is debated (206), IAPP remains an interesting target when studying the structural space of amyloid fibrils. Not only due to its relevance as a potential drug target against T2D but rather as a logical extension from AD and Aβ research. Notably, the risk for T2D patients to develop AD is double as high as for non-diseased groups (207). Additionally, several studies suggest a link between AD and T2D (207, 208). On the molecular level it has been reported that Aβ fibrils function as seeds for IAPP fibril formation (209, 210) and that both peptides colocalize in AD brain tissue (209).

Earlier structural studies on human IAPP fibrils reported that they exhibit a left-handed twist (211), that specifically the structure fragments NNFGAIL and SSTNVG partake in fibril formation (212) and that, while the majority of the 37 amino acid sequence contributes to the fibril core, the N-terminus is located peripherally (213–215). Therefore, shining more light on the structure of IAPP fibrils could support the search for drug targets against fibril formation in diabetic patients.

2 History and development of cryogenic electron microscopy[2]

Cryogenic electron microscopy (cryo-EM) is based on a technique called transmission electron microscopy (TEM), which has been developed by pioneers in the field such as Ernst Ruska and Max Knoll who published a description of the first electron microscope they had built in 1931 (216) (see Figure 9A).

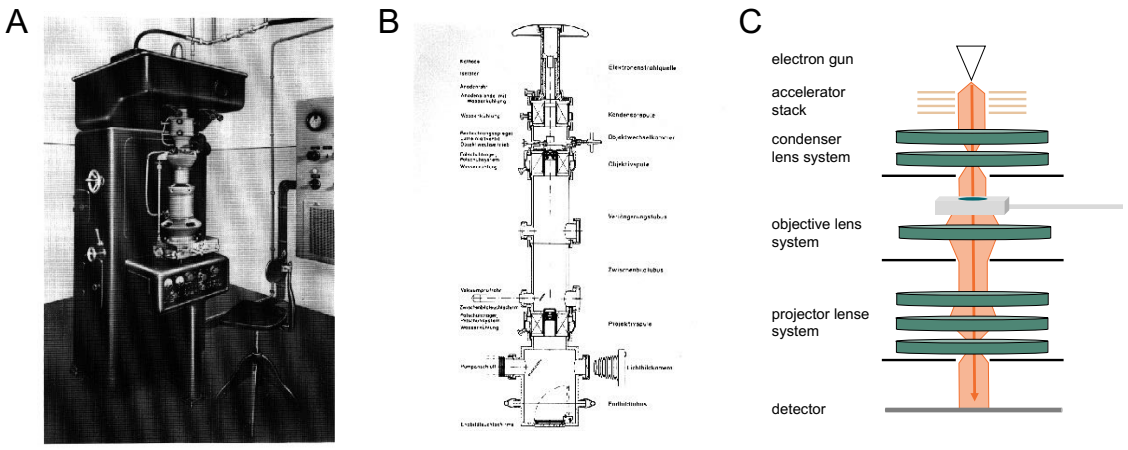

Figure 9: The first electron microscope and its setup. (A) The first serially produced electron microscope by Siemens (submitted 1939) (217). (B) Sketch by E. Ruska of the first (two-stage) electron microscope (218). (Images taken from (219)) (C) Schematic drawing of a TEM setup. The electron gun (white triangle) emits an electron beam (orange) which is intensified through the accelerator stack (beige) and focused through different lens (green) and aperture (black) systems. After passing through the sample (green circle) sitting in the sample holder (light grey) the electron beam finally hits the detector (dark grey line) and information is transmitted. Image modified according to (220).

While the resolution of the human eye is about 0.1 – 0.2 mm, a good light microscope reaches a few 100 nanometers. And through the utilization of electrons instead of light, it is possible to resolve up to the sub-atomic level (e.g., a 100 keV TEM reaches a theoretical resolution of 4 pm) due to an electron's wavelength being smaller than that of light. (221)
A major difference between TEM and the classic light microscope is the use of a different illumination source. Apart from that, the overall idea and construction of an electron microscope is similar to that of a light microscope (Figure 9C). Electrons are released from an electron source and accelerated through a Wehnelt cylinder. The resulting electron beam is then aligned and focused by several kinds of lenses that, in contrast to the light microscope, in TEM consist of magnetic coils . When the electron beam hits the sample the resulting pattern of unscattered and scattered electrons at the detector is translated into an interpretable image on the computer. (220)

[2] Parts of this section have been adopted from the manuscript for "Cryo-EM of amyloidogenic proteins" (39)

In 1986, Ruska together with Gerd Binnig and Heinrich Rohrer received the Nobel prize in physics for their contributions towards the development of TEM (216). By that time EM already was an established method in the fields of material science and biology.
Cryo-EM as an improvement or extension to TEM has been developed since the 1970s (see Figure 10). This was after the first biological samples had been analyzed by negative stain EM (222), which resulted in the first three-dimensional (3D) structure of the T4 bacteriophage (223, 224). Negative stain EM nowadays is often used as a fast and easy screening method (222, 225). The samples are stained with solutions of uranyl acetate, tungsten or ammonium molybdate which all exhibit a high electron density (226). Accordingly, the specimen that has been embedded in the staining solution, is visualized as a negative of the staining solution, a process that might be compared to the development of photographs.

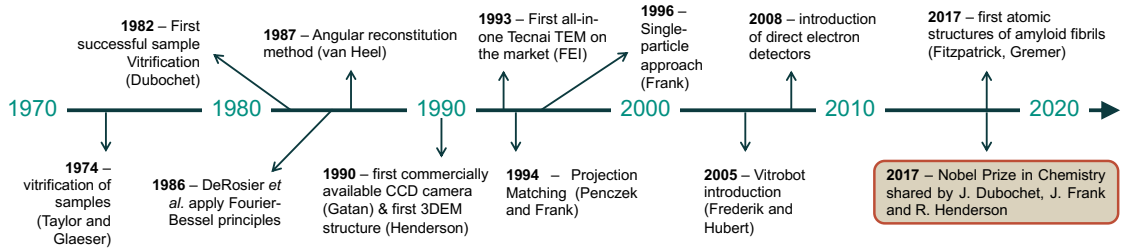

Figure 10: Timeline of the development of cryo-EM. Visual summary of the biggest milestones in cryo-EM between 1970 and 2020 with a special focus on helical reconstruction.

Cryo-EM facilitated the imaging of radiation-sensitive samples. The discovery of the advantages that come with vitrifying biological samples (see 2.1.2), was one of the biggest breakthroughs in the development of cryo-EM because cryogenic conditions preserve the sample in a native-like environment and reduce the radiation damage that result from the interaction of a sample with high-energy electrons (227–229).

In the years to come, cryo-EM would be often referred to as “blobology” within the structural biology community since the resolutions in early experiments had been rather low and the process of data acquisition and reconstruction slow and complex.
Major breakthroughs in the field were the development of CCD (charge-coupled device) cameras (230, 231) and most importantly direct electron detectors compared to photographic film (230, 232), which not only made the cryo-EM workflow much faster but also more accurate with an improved signal to noise ratio (SNR) than CCD cameras.
Another improvement that helped cryo-EM advance into a powerful and widely used technique within structural biology, is the progress that has been made in computation. Nowadays, we easily acquire, store and transfer data sets of several tera bytes (TB) and with the help of high performance and supercomputing systems are able to analyze data within hours or days compared to weeks and months (233). While computing time is still expensive, in the future cloud solutions could lower these costs (234).

In the early days of (cryo-)EM, highly symmetric and therefore often helical structures were among the first specimen to be described because of their inherent advantage of a 360° view on the sample (235–237) (see also 2.2). Later, a major leap for cryo-EM was enabled by the development of single particle reconstruction (SPR), which allows to combine the information of hundreds of particles to produce a three dimensional (3D) model. SPR is based on the groundwork of Joachim Frank and colleagues (238) and the "projection matching" approach he developed together with Pawel Penczek (239). Projection matching enabled the assignment of orientations for experimental images in 3D. Another pioneer in the field is Marin van Heel who made sample tilting redundant by the introduction of his "angular reconstitution" method in 1987 (240).

All of these techniques paved the way for today's software packages (241) of which according to EMDB statistics, RELION – developed by Sjors Scheres in 2012 (242) – is the most commonly used software with it being mentioned in 45 % of all released maps (243).

2.1 The Cryo-EM workflow

The overall workflow of a successful cryo-EM procedure (Figure 11) consists of five major steps that will be explained in more detail below: sample purification and preparation (A), vitrification (B), data acquisition (C) and data analysis including density reconstruction (D) and model refinement (E).

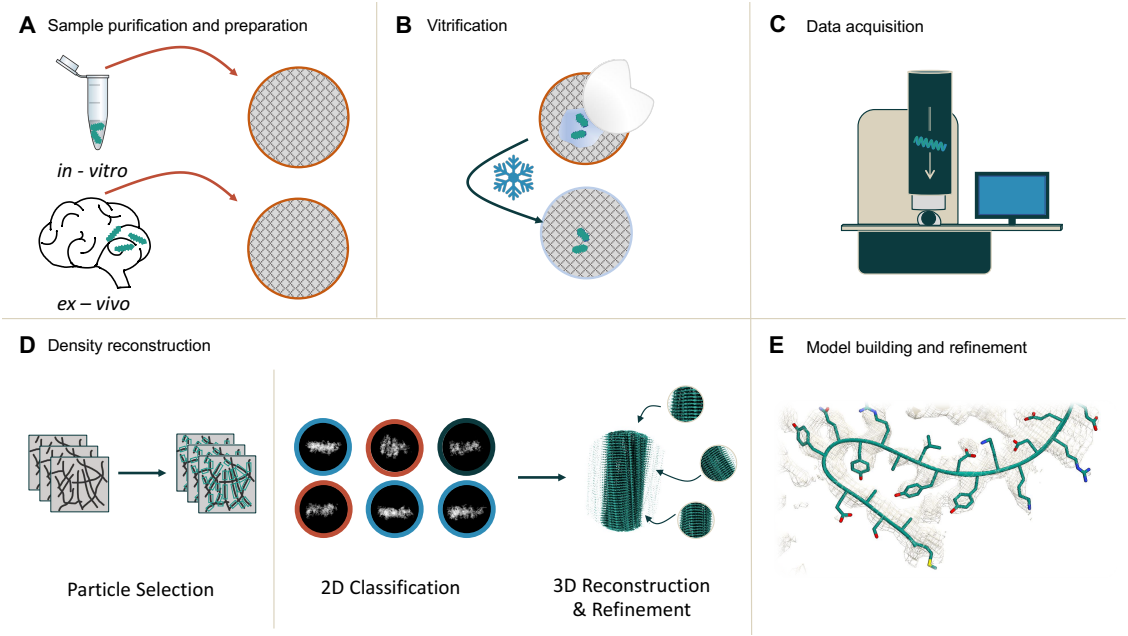

Figure 11: Cryo-EM workflow. A typical cryo-EM experiment starts with sample purification and preparation. The suitable sample is transferred onto the cryo-EM grid (A) and after excess solution has been blotted away, gets vitrified (B). The frozen grid is loaded into the microscope and data are acquired (C). Subsequently, the data set is analyzed by pre-processing, particle selection (D, left) followed by 2D and 3D classification including reconstruction and refinement (D, right). An atomic model can be built into the final density and eventually refined to match the density best (E). Image taken from Zielinski et al. (39)

2.1.1 Sample preparation

Although sample preparation in cryo-EM shows several advantages over other techniques, such as a tolerance for lower concentrations and the possibility to vitrify samples in the preferred buffer, which is specifically important for lipid-embedded proteins (244), sample preparation is one of the major time-consuming steps in cryo-EM. A well-suited sample (245) fulfills the following prerequisites; it is sufficiently concentrated, highly homogenous, and adequately pure.

A suitable sample can still contain some impurities that might later be eliminated during image analysis. This makes cryo-EM samples a bit easier to handle compared to protein crystallography and NMR. Nevertheless, impurities or the addition of detergents (246) might interfere with the image formation in EM and therefore can result in lower resolution. However, also for cryo-EM, the sample preparation needs to be optimized to find conditions leading to thin ice and a favorable particle distribution. Samples for cryo-EM might be derived from synthetic peptides (70, 186) in a suitable buffer or purified from eu- or prokaryotic cells (68, 247) or tissue (78, 81, 187, 248).

2.1.2 Vitrification

Vitrification is a process through which the sample at hand is rapidly frozen, usually in a liquid ethane or propane bath around -160 to -175 °C (249). In contrast to other freezing methods, during this very fast cooling process the sample is transferred into a glass-like state often also described as non-crystalline amorphous ice (227, 250). Embedded in amorphous ice, biological samples will keep their "natural" conformations because molecular motions are arrested (251). Compared to the crystallization process, one observes not only a single protein conformation but usually a broad conformational distribution of a protein (245, 252).

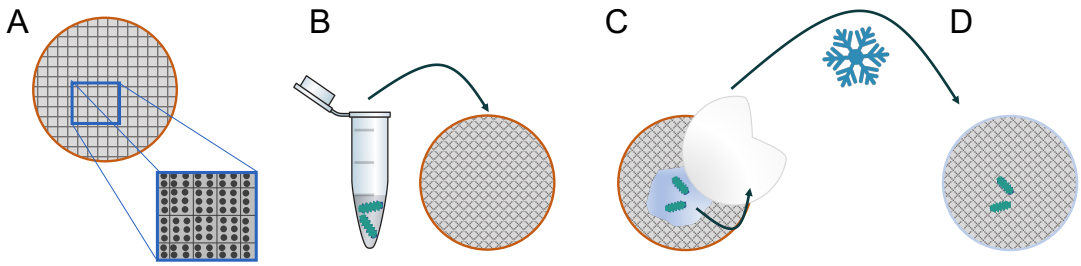

Figure 12: Schematic representation of the vitrification process. Representation of a cryo-EM grid (orange) with carbon support film (grey). The close up (blue box) shows the film holes within the metal squares. (B) The sample is transferred onto the cryo-EM grid (right). (C) Excess sample solution is blotted away and the grid is subsequently plunged into the vitrification solution (D).

Figure 12 displays the protein sample in solution entering the stage of vitrification and grid preparation. The cryo-EM grid, a sample carrier, is a metal grid usually covered with a holey carbon support film (253). The metal grid (Figure 12A) is divided into several squares (Figure 12A, big picture) which – when taking a closer look – are again subdivided into

several small holes (Figure 12A, blue box) in the carbon film. Ideally, the sample is located within these holes in sufficient amounts.
The sample is transferred onto the cryo-EM grid (Figure 12B) where prior to plunge-freezing excess solution is blotted away (Figure 12C). Frozen grids (Figure 12D) are then loaded into the cryo-EM where grids are first screened and then data acquisition is set up.

2.1.3 Data acquisition

When the frozen sample has been successfully loaded into the microscope, screening of the sample begins. First, the grid quality regarding ice quality and sample distribution has to be assessed (253). This is done by first acquiring an overview image of the whole grid (atlas). If the atlas passes the quality test, the grid is further examined in more detail and suitable regions on the grid, meaning holes with a sufficient amount of particles and a good ice thickness, will be selected for data acquisition. Of each selected area, multiple (image) frames are acquired which result in an image stack or 'movie'. Usually, data acquisition for a data set on a 200 kV Tecnai Arctica or 300 kV Krios microscope (both FEI/Thermo Fisher) will take 24 – 48 h for ~ 1,000 – 2,000 movies.

2.1.4 Density reconstruction

Following the data acquisition, the resulting data set will be further analyzed after so called pre-processing steps. First, the raw movies undergo motion correction (254) during which motions that occur during the acquisition due to movements of the specimen or microscope are balanced. Then, contrast transfer function (CTF) estimation (see 2.1.4.1) is performed (255, 256). Pre-processing of micrographs, which is what the resulting motion corrected movie averages are called, finalizes the data set preparation for the subsequent steps of particle picking (2.1.4.2), classification (2.1.4.3) and reconstruction (2.1.4.4).

2.1.4.1 CTF estimation

The CTF is a function of defocus, astigmatism, lens errors, electron wavelength and temporal and spatial coherence of the electron beam (255, 257). It describes how different electrons contribute to the resulting image contrast (258). Technically, the CTF could be directly deduced from the Thon rings, which emerge in the power spectrum of an image, but in order to so all information about the before-mentioned parameters would be needed (255). Programs such as CTFFIND (259) or Gctf (256) are therefore designed to determine the unknown CTF parameters from the defocus and astigmatism values and estimate an accurate CTF in order to guarantee accurate high-resolution information to be taken from micrographs. With these estimates, CTF corrections can be carried out during further steps of the reconstruction process.

2.1.4.2 Particle picking

A crucial step, especially in the field of amyloid research, is the particle picking. Here, micrograph areas depicting the sample are selected to separate the sample from background or impurities. Originally, the selection of sample particles from the micrographs had to be carried out manually. Nowadays, there are several tools available for automatic particle picking (260–263) although only few of them offer helical particle selection (264). Accordingly, many fibril projects still require manual selection in this step. After particle picking, filaments are extracted from the micrographs, meaning they are basically "cut out" of the images. The extracted filament images are then "boxed" into uniformly sized segments. (Figure 11D). From here on these boxed segments is what will be referred to as "particles".

2.1.4.3 2D classification

When all micrographs have been examined and particles have been picked and extracted, 2D (two dimensional) classification is performed (Figure 13 and Figure 11D).

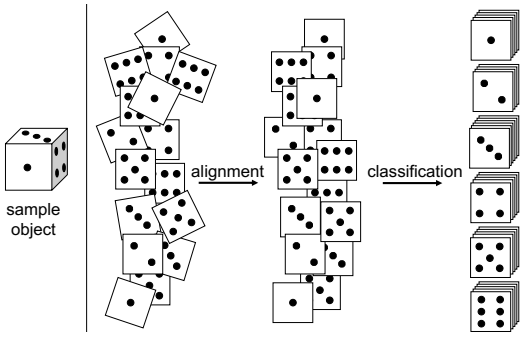

Figure 13: 2D classification scheme. After particles have been selected from the images containing different views of sample object (left) 2D classification is performed. Here, the unsorted particles (right) are first aligned and then sorted into classes which that contain a certain view of the object. These classes are then averaged to improve the SNR.

During 2D classification the extracted particles are first aligned such that all particles are in the same position. Then, these aligned particles are classified by their orientation.

2.1.4.4 3D classification

Following particle selection, alignment and 2D classification, 3D classification and reconstruction (Figure 11D) can be carried out. First, an initial model has to be generated, which might either be some sort of cylinder (265) or derived from projection images of 2D classes (266). The orientations of the particles that have undergone 2D classification are then estimated and the particles are assigned orientations within the model. 3D classification – a process similar to 2D classification – is then performed to determine the particles which are best suited for further reconstruction cycles. (267)

Figure 14 displays a schematic 3D classification in which three classes have been calculated of which the best class is selected and used for reconstruction of a 3D model.

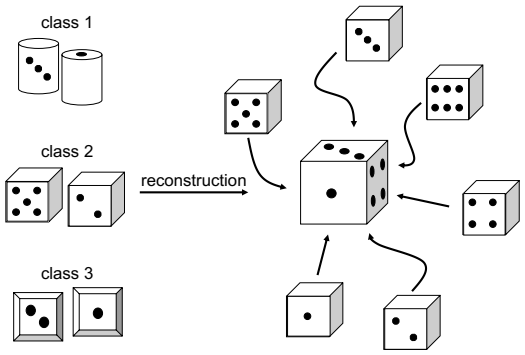

Figure 14: 3D classification and density reconstruction scheme. First, 3D classification is carried out. Particles are aligned and oriented in 3D space. Classification is carried out similar to 2D classification such that similar models are grouped into one class and averaged (left). Classification allows to reject mis-picked particles. Only the best class (class 2, left) is used for reconstruction of a 3D density (right) whereby particle orientations of the selected class are optimized to the highest possible resolution.

Through iteration of the before-mentioned steps of alignment, classification, orientation determination and reconstruction the resolution of the model density increases up to a final value (267).

2.1.5 Model building and refinement

If the final model shows a sufficiently high resolution which usually is < 3.5 Å, the identification of amino acids in the 3D density becomes possible and an atomic model can be built. Model building usually is carried out in the software coot (268, 269). In coot, the primary sequence of the protein can be fitted into the density and optimized by taking structural constraints into account. The finalization of the model, namely the refinement steps that give important information about the quality of the model, are performed by phenix (270).

2.2 Cryo-EM and amyloid

2.2.1 Structure elucidation of amyloid fibrils

Structural knowledge about amyloids is still rather limited. Especially cryo-EM has presented itself as a promising technique to tackle this problem. As shown in Figure 15, the number of protein structures solved by cryo-EM has risen immensely since 2000 (green bars).

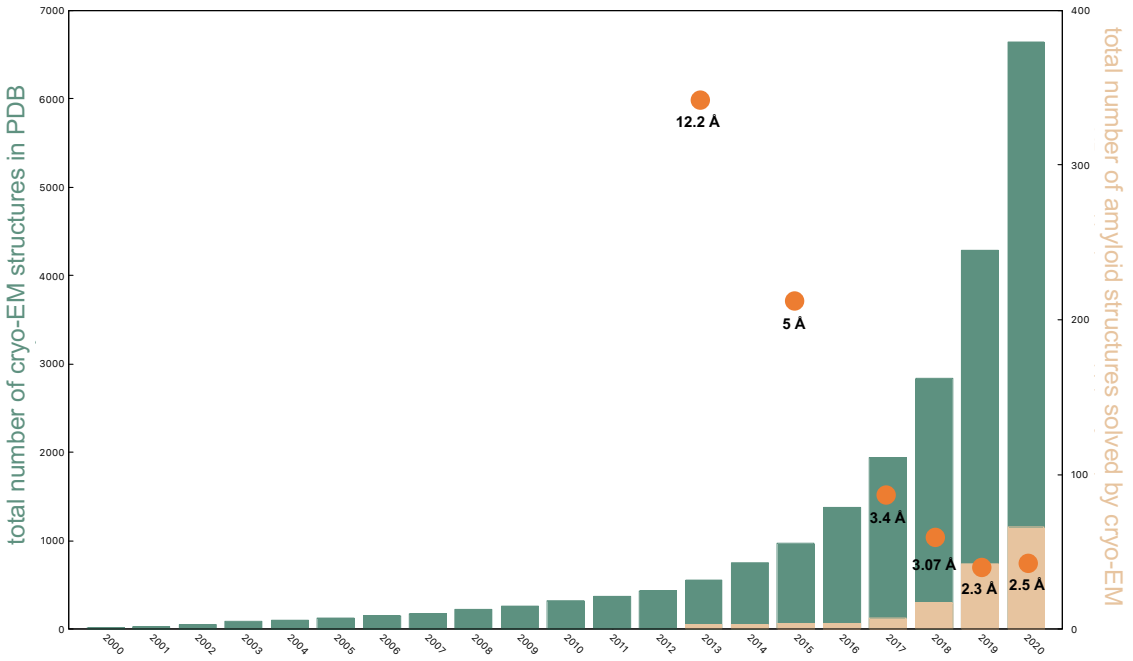

Figure 15: Development of cryo-EM structures in the Protein Data Bank (PDB) from 2000 to 2020. Displayed are the total numbers of cryo-EM structures in the PDB since 2000 (green, left y-axis) as well as the total number of amyloid structures deposited since 2000 (beige, right y-axis). Orange dots visualize the highest resolution reached by cryo-EM for an amyloid in the respective year. In 2014 and 2016 no new amyloid structures were deposited, therefore no resolution is depicted. (data status of December 27, 2020, figure modified according to Zielinski et al. (39))

A couple of years later, amyloid fibril structures are increasingly targeted by cryo-EM and structures have been solved successfully since 2017 (Figure 15, beige bars) with the highest resolution achieved to date being 2.3 Å for a tau filament from chronic traumatic encephalopathy (Figure 15 , orange dot, 2019) (271). Although especially amyloid fibril structures have proven themselves as suitable samples for cryo-EM studies (68, 69, 272, 273, 70, 77, 78, 83, 184, 187, 189, 271), atomic insights about oligomeric species (section 1.2.2) and secondary nucleation sites (section 1.2.1) are still lacking.

The first amyloid structures solved by cryo-EM have been tau filaments (81) and an Aβ fibril (181) in 2017. The wildtype Aβ(1-42) in pH 2, was shown to exhibit an LS-topology (Figure 16A) in which the N- and C-terminus of the respective monomers are in close contact and form the fibril interface (Figure 16B).

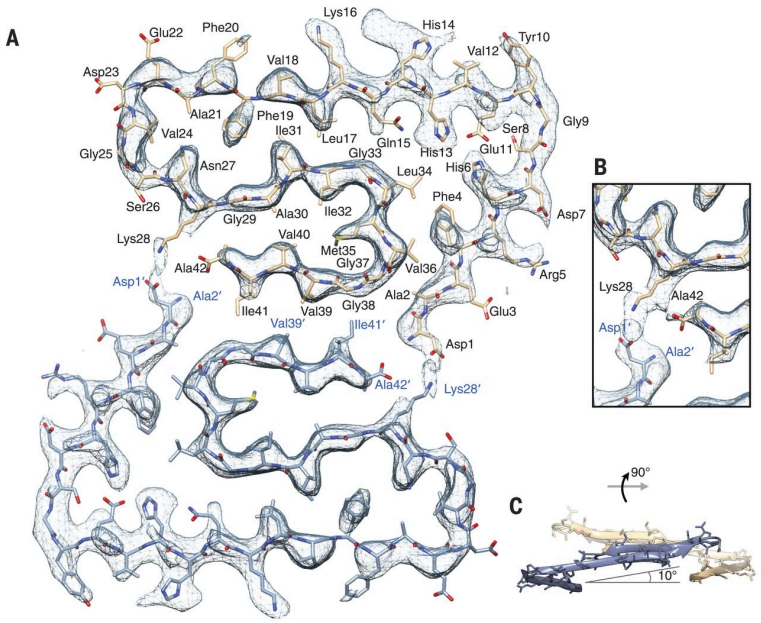

Figure 16: Amyloid fibril structure of Aβ(1-42). (A) The cross-section of the fibril exhibiting an LS-shape. (B) Close-up of the interaction between Asp1 and Lys28 of the opposing filament. (C) Display of the relative orientation of two subunits in a plane perpendicular to the axis. Image taken from (181).

Point group symmetry is an important concept in structural biology to describe the overall symmetry of a molecule. C_n symmetry for example refers to a rotary axis with *n* symmetry elements. In the case of C_2 this refers to a rotary axis with one mirror plane. C_1, which is a rotary axis without symmetry elements is an exception from this rule. (274)

Rather than a classic C_2-symmetry, the Aβ(1-42) fibril exhibited a 2_1-screw symmetry in which the monomer subunits display a staggered arrangement (Figure 16C). Therefore, the fibril rise is 2.335 Å while the twist is -179.275 ° indicating a left-handed fibril. (181) Due to the staggered arrangement the rise is only half the 4.7 Å signal and from one monomer to the next, one has to move roughly 180° instead 360° as in case of C_2-symmetry.

2.2.2 Why amyloid fibril reconstruction can be considered a special case of single particle reconstruction [3]

Reconstruction of helical filaments is carried out by adapting the SPR process to the characteristics of filaments. The overall workflow (2.1) stays the same but additional features have to be taken into consideration e.g., the difficulty of particle picking. Helical filaments are reconstructed more easily if all picked particles have been selected from straight filaments.

But helical samples also have intrinsic advantages over globular proteins. First, all information needed for reconstruction are sufficiently provided in one single image because of the helical symmetry. And second, the repeating asymmetrical units (= monomeric

[3] Parts of this section have been adopted from "Structure elucidation of amyloids with cryo-EM" (39)

subunits) in a helical filament have fixed relative orientations which can be derived from the helical parameters described above (twist, rise and pitch, Figure 3A) (275). Due to helical symmetry, the SNR can be significantly increased by averaging over many asymmetrical units (265, 276).

Also, for amyloid fibrils the determination of helical parameters is highly facilitated by the cross-β pattern or more specifically by the 4.7 Å (meridian) signal, which is observed in the diffraction pattern and power spectrum of an amyloid fibril (Figure 17). While the more prominent 4.7 Å peak arises due to the regular stacking distance of 4.7 Å between monomer layers, the 10 Å (equatorial) peak is associated with the distance between C_α-chains in the x-plane. (277)

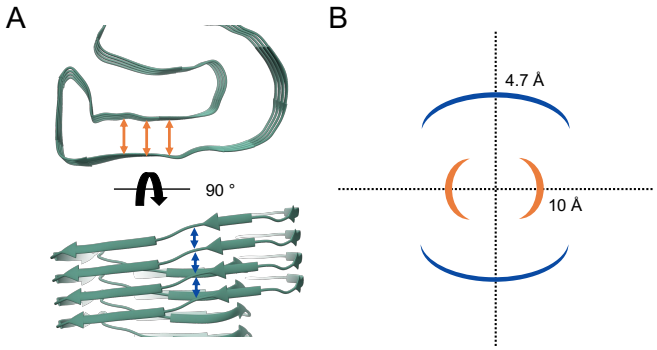

Figure 17: The cross-β pattern and the fibril diffraction pattern. The cross-β pattern, repetitive stacking of amyloid monomers along a fibril axis (A), evokes two distinct signals in the diffraction pattern (B). The most significant is the 4.7 Å signal (blue) which represents the separation of β-strands along the fibril axis (blue arrows). As a minor signal, usually the 10 Å signal (orange) is visible due to β-strands that run perpendicular to the axis and are separated by ~ 10 Å (orange arrows). Figure modified according to Morris and Serpell (277).

The only caveat of the 4.7 Å signal on the other hand, is its predominance which might dominate other structural features and therefore complicate high-resolution reconstruction (266). However, cryo-EM has proven itself to be a strong technique to elucidate the structures of helical assemblies and specifically amyloid fibrils. The technique has developed fast since its "resolution revolution" and has surpassed the number of yearly NMR structures in drug design by now. Hence, cryo-EM will play a key role in future drug design particularly in regard to large assemblies, such as amyloid fibrils and plaques, and membrane proteins. (278)

3 Objective

This work has been greatly motivated by the ongoing fight against Alzheimer's disease, which has been described 100 years ago and is a growing burden in modern society because it affects the increasing number of elderly and results in both high healthcare and personal costs. With the number of therapies being negligible and the understanding of the pathology limited, there is a lot to understand about Alzheimer's disease and its hallmark, the amyloid β. In comparison to Alzheimer's disease, the research on amyloidogenic proteins is rather young (~50 years). Accordingly, the knowledge we have so far is limited. Especially structural information on the atomic level were missing when this project started since commonly used techniques such as NMR and X-ray crystallography face intrinsic challenges with amyloid fibrils such as size and mass of these fibrils and their polymorphism.
With the resolution revolution in cryo-EM it became clear that it would also start a new era in the field of amyloid research. Since 2017 the number of atomic structures of amyloid fibrils has risen immensely.

The goal of this thesis is to shine some light on the structural space of amyloid fibrils and their inherent polymorphism. It hereby focuses on disease-associated amyloids. First and foremost mentioning amyloid-β, linked to Alzheimer's disease, of which several post-translational modifications and mutations are known and linked to varying severity and time-of-onset for the disease. During this work specifically, post-translational modifications such as phosphorylation at serine 8 and pyroglutamation at residue three were prepared for cryo-EM measurements, with the aim to elucidate their structures. Additionally, a newly discovered amyloid-β mutation as well as known point mutations from the region around residues 21 – 23 were prepared to different degrees for later cryo-EM experiments.
In order to cover a wide range of amyloids, a second disease-related protein – IAPP – and a non-disease related amyloid – SH3 domain of the phosphatidyl-inositol kinase 3 – were examined. The cryo-EM reconstructions of these peptides reached up to 3.4 Å resolution, which allowed for building of atomic models. With detailed structural information on src homology domain 3 fibrils, we would like to facilitate ongoing research on amyloid formation kinetics and thus support the search for underlying principles of the aggregation mechanism. By examining IAPP, which is related to type II diabetes, we aim at showing molecular similarities to the atomic detail and thereby enhance our knowledge about the link between Alzheimer's disease and type II diabetes.

Elucidating the structural composition of amyloids has a great importance for our understanding of diseases such as Alzheimer's disease or type II diabetes. These insights will facilitate the search for drug candidates and may result in a mitigation or cure for these diseases, eventually.

4 Outline

Section IV Atomic structure of an amyloid model system: src-homology domain 3
consists of a publication in Nature communications (2019) in which we describe the first atomic-detail structure of an amyloid fibril formed by PI3-kinase SH3. Additionally, we were able to explain the effect of point mutations onto elongation rates with the structure.

Section V1 pGlu-Aβ(3-42)
describes the recombinant growth and purification of the Aβ variant pGlu-Aβ(3-42). The successfully purified protein has been prepared for cryo-EM measurements of which three led to data acquisition. Reconstruction of a ~4 Å density was possible although an atomic model could not be generated up to now.

Section V2 Aβ36
explains the preliminary work on synthetic samples of the novel Uppsala mutant Aβ36, which results in alarmingly early-onset of Alzheimer's disease. Aβ36 was shown to form oligomers or fibrils dependent on buffer conditions.

Section V3 Aβ(1-42)-pS8
describes the preparation of synthetic samples of Aβ(1-42)-pS8, which contains a post-translational phosphorylation at serine 8, for cryo-EM experiments. In order to improve sample preparation, sonication experiments have been carried out with this variant.

Section V4 Aβ(1-42) point mutants A21G, E22G, E22K, D23N
displays the initial work for further understanding of the polymorphic landscape of Aβ with regard to familial Aβ mutations.

Section VI Structural similarities between IAPP and Aβ(1-42) fibrils
consists of a publication in Nature Structural & Molecular Biology (2020) in which we describe the amyloid fibril structure of IAPP at physiological pH and discuss striking similarities with one Aβ fold.

Section IX Conclusion and outlook
sums up the outcomes of this work and discusses perspectives for the project and open questions in the field.

IV Atomic structure of an amyloid model system: src-homology domain 3

1 Publication I: Atomic structure of PI3-kinase SH3 amyloid fibrils by cryo-electron microscopy

In a collaboration with the group of Alexander K. Büll, we examined the fibrillated form of the src-homology 3 domain (SH3) of phosphatidyl-inositol kinase (PI3K) via cryo-electron microscopy, solved its structure to atomic detail and combined structural information with biophysical and biochemical data of the collaborators. The resulting article has been published in *Nature Communications* in 2019 (68). I summarized the article below and both the article and its supplemental information can be found in the appendix Publication I: Atomic structure of PI3-kinase SH3 amyloid fibrils by cryo-electron microscopy.

1.1 Summary

The SH3 domain of the PI3K is a model system for amyloid formation since it has been discovered to form amyloids *in vitro*. As a model system it plays a crucial role in helping to understand the mechanisms of protein misfolding and aggregation. In order to describe the kinetics of amyloid aggregation mathematically, our collaboration partner Nicola Vettore investigated the amyloid formation of SH3 (279).

With the help of our cryo-EM density, which could be resolved to 3.4 Å, a sufficient atomic model was built which consists of residues 1 – 77 out of 86. This way, we could present the first atomic model of a non-disease related amyloid fibril. Interestingly, although the reconstructed polymorph showed a rather large interface that is mainly based on hydrophobic interactions, AFM measurements showed a second polymorph with only half the width. Hence, we proposed that protofilaments of the reconstructed polymorph might also be stable as single fibrils.

Moreover, together with data from co-author Lena N. Mangels, we could show why point mutations in the sequence influence the aggregation of SH3 the way they did in the experiments. While mutations located at the C-terminus, which in the density appeared to be highly flexible, had close to no effect on the aggregation behavior, mutations in the core of the fibril showed decreasing aggregation propensity. Additionally, formerly described sequence alterations from literature could be explained with our model.

1.2 Contribution

For this study, I performed image processing and most of the reconstruction, model building and model refinement steps. Additionally, I contributed with writing the manuscript, creating most of the figures and discussing the results with my co-authors. I am first author of this article.

V Results and discussion on amyloid-β variants

1 pGlu-Aβ(3-42)

Linked to EOAD, pGlu-Aβ(3-42) is an interesting target for cryo-EM experiments. Due to the promising first study of wildtype Aβ(1-42) (181), this project has been approached similarly. After recombinant expression and purification of E3Q-Aβ(3-42) that was kindly supported by Isoloid GmbH (section 1.1), ring closure of pyroglutamate was performed according to Dammers et al. (174) (section 1.2). The fibrillated sample was then examined under the AFM (section 1.4).
During the course of this project, several cryo-EM data sets were acquired with the results of the latest being presented in section 1.5. Since this project was pursued for a long time, quality of the sample was tested by mass spectrometry, which was performed by Sabine Metzger from Universität zu Köln and Andreas Linden from MPI für biophysikalische Chemie in Göttingen (section 1.3).

1.1 Expression and purification of E3Q-Aβ(3-42)

Expression and purification of labelled [U-13C,15N]-E3Q-Aβ(3-42) had been established by Patrick Meckelburg (280) and was carried out accordingly (sections 8.3, 8.4) for unlabeled E3Q-Aβ(3-42). A representative SDS-gel (Figure 18) displays the overexpression of the target protein E3Q-Aβ(3-42) with the fusion construct along the first purification steps. The fusion construct consists of a TEV-cleavage site, a His_6-tag and a (NANP)19 solubility tag. Together, the target protein and the fusion construct result in an overall molecular weight of ~19 kDa.

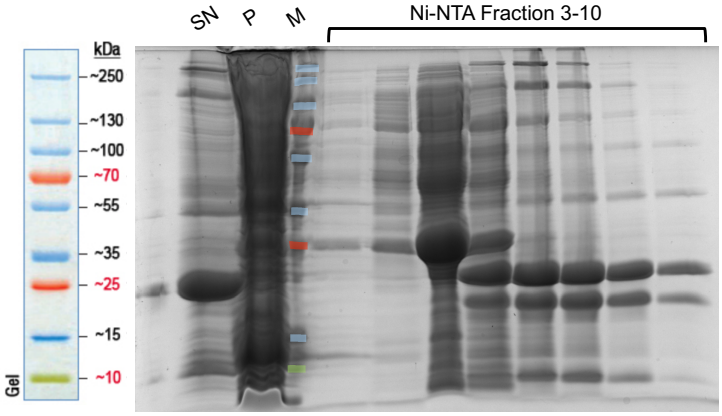

Figure 18: SDS-gel of E3Q-Aβ(3-42) harvest and purification. Left: Legend for PageRuler Plus Prestained (Thermo Fisher) with respective bands highlighted in lane "M". Right: SDS-gel showing samples of supernatant (SN) and pellet (P) after cell harvest and centrifugation and Fraction 3-10 after affinity chromatography (Ni-NTA Fraction 3-10). The expected size of the target protein is 19 kDa.

The successful overexpression of the target protein is already well visible in the supernatant (Figure 18, SN) around 19 kDa. The pellet does not show a significant band at this height. Due to overloading of the pellet lane, residual target protein in the pellet cannot be fully excluded. According to the SDS gel, fractions 7 and following, which contained the target

protein of 19 kDa, were pooled and concentrated to a final volume of 1.5 mL and a concentration of 7.44 mg/mL (appendix, Figure 78).

After pooling of the fractions, E3Q-Aβ(3-42) was separated from the fusion construct by TEV digestion, which was verified by semi-preparative HPLC. Figure 19 displays a semi-preparative RP-HPLC test run of E3Q-Aβ(3-42) after TEV cleavage. The elution profile is in good agreement with former protocols (280). The first peak at 5 min retention time shows TEV protease followed by the E3Q-Aβ(3-42) peak at 14 min. A minor peak at 17 min could possibly show some already converted pGlu-Aβ(3-42) while remaining fusion construct and other residuals show a retention time of more than 25 min and only elute from the column shortly before the gradient from 30 % to 80 % AcN reached a plateau.

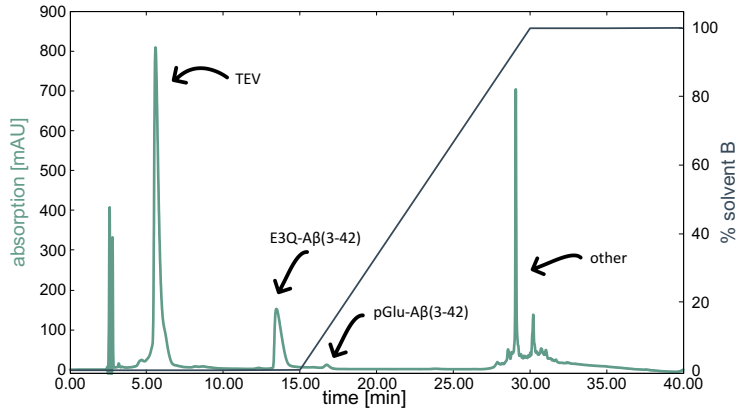

Figure 19: Chromatogram of E3Q-Aβ(3-42) after TEV-cleavage. The chromatogram of an RP-HPLC run of E3Q-Aβ(3-42) after TEAV-cleavage reveals two major peaks at 5 min (TEV-protease) and 14 min (E3Q-Aβ(3-42)), another minor one well below 100 mAU around 17 min (pGlu-Aβ(3-42)) and one peak at consisting of fusion construct and other residuals after 25 min when the gradient of solvent B (HPLC buffer) had reached 80 %.

The E3Q-Aβ(3-42) peak is well separated from all other peaks and thus could be collected after elution in a single fraction. Purity of the resulting sample is displayed in Figure 20.

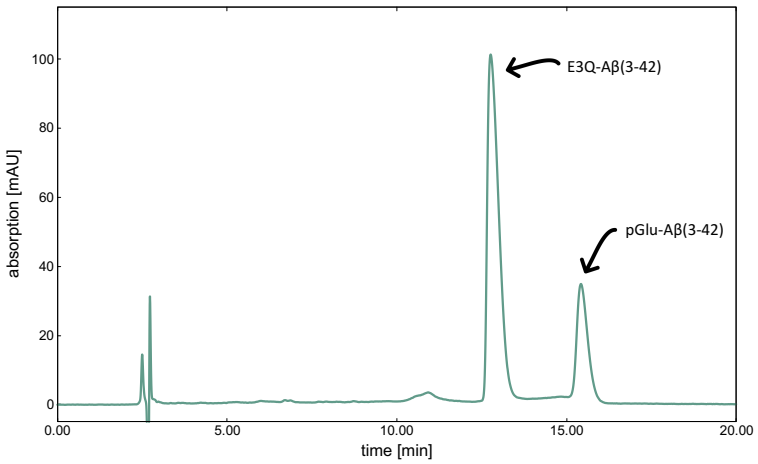

Figure 20: Chromatogram of E3Q-Aβ(3-42) after separation from TEV-protease and fusion construct. An isocratic gradient after lyophilization and re-hydration of the purified sample shows two major peaks at 14 (E3Q-Aβ(3-42)) and 16 min (pGlu-Aβ(3-42)).

After separation of Aβ(3-42) from TEV and other impurities, two peaks are left, which display mainly E3Q-Aβ(3-42) but additionally some already cyclized pGlu-Aβ(3-42). Conversion of the remaining E3Q-Aβ(3-42) into pGlu-Aβ(3-42) had to be catalyzed and is discussed in the next section.

1.2 Conversion from E3Q-Aβ(3-42) to pGlu-Aβ(3-42)

The conversion of the remaining E3Q-Aβ(3-42) to pGlu-Aβ(3-42) was started four weeks after the semi-preparative RP-HPLC (see sections 1.1, X9.1.1.1). During this time the sample had been incubated at room temperature under quiescent conditions. According to a protocol by Dammers *et al.* (174), E3Q-Aβ(3-42) should be incubated for 24 h at 45 °C in NaAc buffer at pH 3.5 while gently shaking. Following this protocol, E3Q-Aβ(3-42) was incubated in HPLC buffer for 48 h at 45 °C. The conversion was then verified by RP-HPLC. Figure 21 shows analytical RP-HPLC data of an E3Q-Aβ(3-42)/pGlu-Aβ(3-42) sample after 0, 1, 24 and 48 h of incubation at 45 °C in HPLC buffer. In order to balance slight differences in concentration or injection volume, the data were min/max normalized.

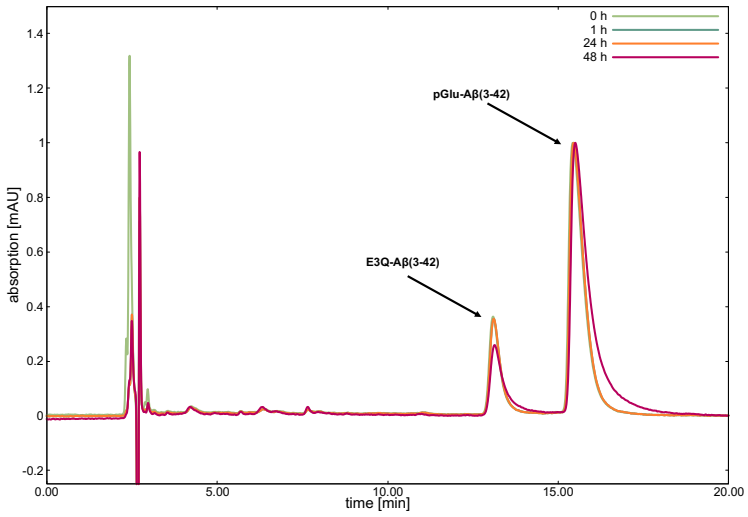

Figure 21: Elution behavior of mixtures of E3Q-Aβ(3-42) and pGlu-Aβ(3-42). Two main peaks emerge at 13 and 16 min which can be assigned to E3Q-Aβ(3-42) and pGlu-Aβ(3-42), respectively. Absorption measured at 214 nm.

When the experiment was started (Figure 21, 0 h), conversion to pGlu-Aβ(3-42) in HPLC buffer (pH 2) had already progressed (compare to Figure 20). Apparently, conversion does not have to be catalyzed by high temperature but will self-initiate over time under highly acidic conditions. Hence, roughly 80 % of E3Q-Aβ(3-42) had already undergone the pyroglutamic ring closure. Nevertheless, conversion from E3Q-Aβ(3-42) to pGlu-Aβ(3-42) was substantially increased by application of 45 °C and gentle shaking after 48 h (Figure 21, 48 h), which is displayed by the decrease of the E3Q-Aβ(3-42) peak at 13 min and a broadening of the pGlu-Aβ(3-42) peak at 16 min retention time.

The remaining E3Q-Aβ(3-42) was separated from pGlu-Aβ(3-42) via semi-preparative RP-HPLC (X9.1.1.2) after lyophilization (sectin X9.3) and monomerization (section X9.1.1.3). Subsequently, the eluate containing pGlu-Aβ(3-42) was lyophilized and monomerized again in order to prepare a final semi-preparative RP-HPLC run with the sample to transfer it into the fibrillization conditions (section X9.1.1.5). The RP-HPLC profile of the resulting pGlu-Aβ(3-42) sample is displayed in Figure 22.

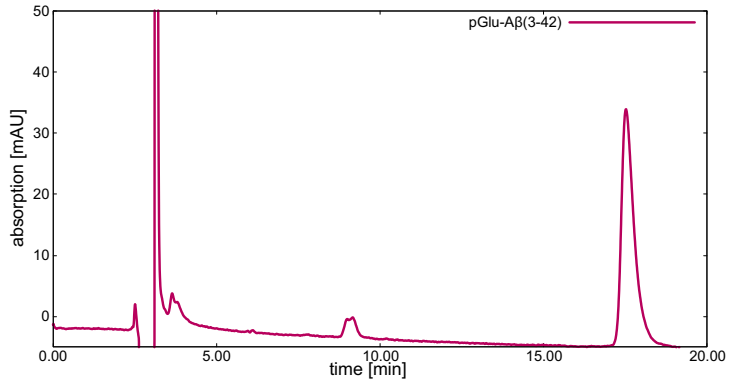

Figure 22: Final purity of pGlu-Aβ(3-42). Chromatogram of the final RP-HPLC run with pGlu-Aβ(3-42) after lyophilization and monomerization. A major product peak is visible at 17 min retention time and a minor double-peak after 9 min. Absorption measured at 214 nm.

In the chromatogram, at ~17 min a clear pGlu-Aβ(3-42) peak is visible and only a minor impurity peak with a double-tip at ~9 min. The minor peak had already been observed in other pGlu-Aβ(3-42) and further Aβ variant purifications in our institute. It had been shown to not interfere with solid state NMR measurements and hence was considered negligible (280). The eluate of the final RP-HPLC run was collected in three 50 mL reaction tubes that were stored at room temperature under quiescent conditions for fibrillation.

1.3 Quality control of pGlu-Aβ(3-42)

To assure persisting quality of the sample after nearly one year, pGlu-Aβ(3-42) samples were analyzed via analytical RP-HPLC (X9.1.2.3). The chromatograms show two distinct peaks at 7.6 min and 15.6 min with the latter being the higher one in Figure 23.

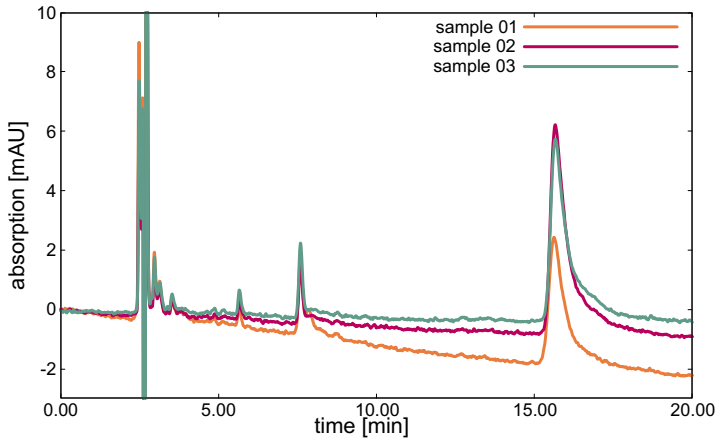

Figure 23: RP-HPLC chromatograms of all pGlu-Aβ(3-42) samples to check quality. For all samples, three peaks are visible with them appearing at 7.6 min (minor) and 15.6 min (main) retention time. Samples 02 (pink) and 03 (green) show similar peak heights while sample 01 (orange) displays a slightly lower peak height.

Retention times for pGlu-Aβ(3-42) from former experiments (see Figure 22) identify the peak at 15.6 min to contain pGlu-Aβ(3-42) while the other peak, which has also been observed before but considered negligible, had increased over time. The respective peak areas and the resulting amount of impurities are listed in Table 1.

Table 1: Degradation product in pGlu-Aβ(3-42)

Sample	**Peak area 7.6 min [mAU*s]**	**Peak area 15.6 min [mAU*s]**	**Impurity [%]**
1	35.6	150.6	14
2	15.1	283.1	5
3	21.3	242.5	8

According to Table 1, sample fraction 1 contains the most impurities with a total of 14 % while the other two sample fractions remain below 10 %. Because the emerging peak at 7.6 min had already been observed during the sample purification (Figure 22), its increase could hint towards time-dependent degradation of pGlu-Aβ(3-42). Considering the harsh incubation conditions, namely pH 2 in an organic solvent, which were applied over a long time period, degradation seems likely. Moreover, oxidation of the methionine in position 35 could be responsible for the increase of that peak as well. For verification of this hypothesis, mass spectrometric analyses were performed on the supposed “degradation” peak and sample 1 (sections 1.3.1 and 1.3.2). Sample 1, which showed the highest amount of impurity, was lyophilized and prepared for re-fibrillation experiments by separation of pGlu-Aβ(3-42) from the supposed “degradation” product via semi-preparative RP-HPLC (see section X9.1.1.3). Samples 2 and 3 were considered to still show sufficient purity for cryo-EM experiments.

1.3.1 ESI-MS with pGlu-Aβ(3-42) in May 2019

A lyophilized sample of the supposed "degradation" peak at 7.6 min as well as a sample of the freshly recycled pGlu-Aβ(3-42), which had been separated from the "degradation" peak, were sent for mass spectrometric analysis (section X9.5.1). First ESI-MS analyses were performed and evaluated by Sabine Metzger, who provided an overview of the results. Figure 24A shows that both fractions contain full-length pGlu-Aβ(3-42). As expected, the 7.6 min peak contains oxidized methionine. Another main species in this peak has been identified as pGlu-Aβ(8-42), again with oxidized methionine.
The peak at 15.6 min does not show any oxidized pGlu-Aβ species. Instead, as expected it mainly consists of pGlu-Aβ(3-42), as mentioned before, and a rather large fraction of Aβ(8-42). Moreover, minor shares of pGlu-Aβ(3-23), pGlu-Aβ(3-25) and pGlu-Aβ(3-37) have been identified. All identified pGlu-Aβ species are displayed in Figure 24B.

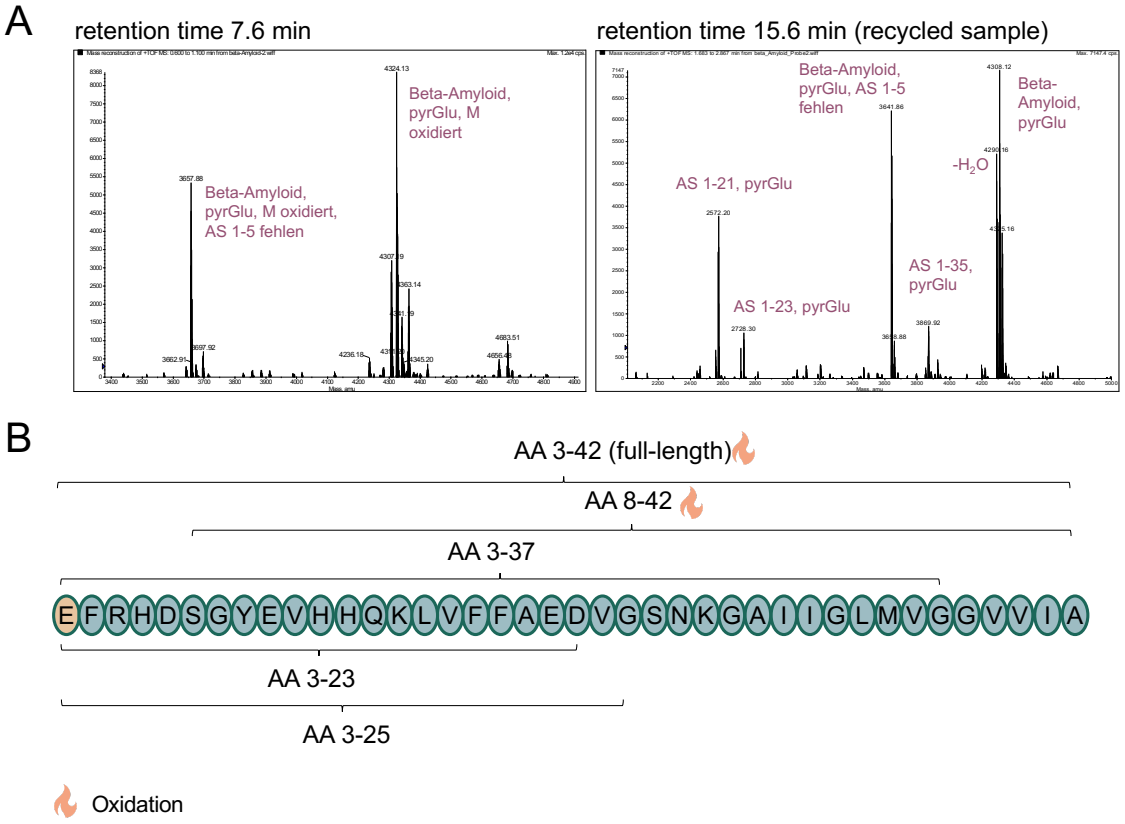

Figure 24: Mass spectrometric analysis of pGlu-Aβ(3-42) quality control. (A) Original annotations for the samples of 7.6 min ("degradation peak") and 15.6 min ("sample peak" of the recycled pGlu-Aβ(3-42)) retention time by Sabine Metzger. (B) Visualization of pGlu-Aβ(3-42) species found by MS. Pyroglutamate at position 3 is highlighted in beige. Possible oxidations at methionine 35 are indicated by symbols and have been found exclusively in the "degradation" peak.

The results for the "degradation" peak at 7.6 min were within the expectations since methionine is known to be easily oxidized (281, 282). N-terminal fractions (AA 3-23, 3-25 and 3-37) are observed without matching C-terminal fragments, which could be an indication for C-terminal degradation of the sample.

However, N-terminal loss of five amino acids seems to occur in high quantities as indicated in Figure 24A. Differences of this dimension should have already been observable in RP-HPLC runs, especially since former RP-HPLC experiments prove to be able to differentiate between pGlu-Aβ(3-42) and E3Q-Aβ(3-42) (see Figure 21), which is less than one amino acid difference.

1.3.2 Orbitrap-MS with pGlu-Aβ(3-42) in December 2020

Stability of the pGlu-Aβ(3-42) sample of May 2019 (re-fribillated sample 1) was tested again after 1.5 years. The sample and a control that consisted of freshly dissolved synthetic pGlu-Aβ(3-42), were run over an analytical RP-HPLC column. Figure 25 shows the results of the test run with pGlu-Aβ(3-42) from May 2019, and synthetic pGlu-Aβ(3-42) that was freshly dissolved in HPLC buffer. The control sample shows a clear product peak after 14 min retention time plus the ("degradation") peak at 7 min. Both these peaks are found as well in the pGlu-Aβ(3-42) sample of May 2019. Additionally, the pGlu-Aβ(3-42) sample of May 2019 shows a rather large peak at 12 min and a minor peak in the tailing of the 14-min-peak after 16 min.

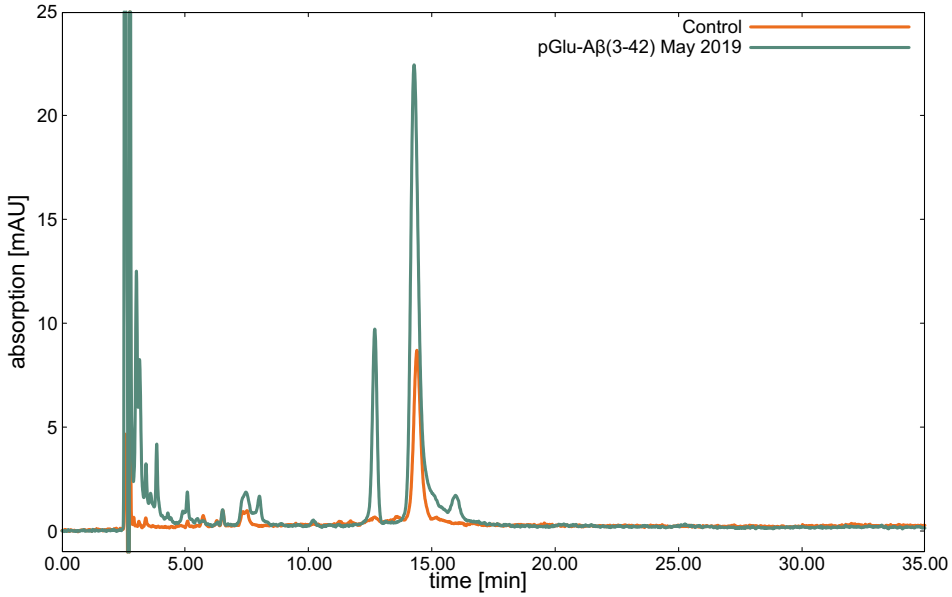

Figure 25: Chromatogram of pGlu-Aβ(3-42) of May 2019 and control sample. Absorption measured at 214 nm displays one distinct peak at 14 min for the control (pink, synthetic pGlu-Aβ(3-42)) as well as a minor double peak around 7 min. Both peaks are also visible in the pGlu-Aβ(3-42) May 2019 sample with additional peaks around 12 and 16 min.

It can thereby be directly deduced from the RP-HPLC data that still after 1.5 years the majority of the sample consists of pGlu-Aβ(3-42). Nevertheless, a non-neglectable part of the samples seems to have undergone some changes, which were further analyzed by mass spectrometry.

Orbitrap-MS analyses were carried out and evaluated by Andreas Linden on a lyophilized sample of recycled sample 1 (pGlu-Aβ(3-42) of May 2019) after 1.5 years, and a control sample of synthetic pGlu-Aβ(3-42) from BACHEM kindly provided by Lothar Gremer and Soumav Nath.

Results of the experiments are summed up in Figure 26. The MS profiles (Figure 26A) clearly show that both sample and control mainly consist of full-length pGlu-Aβ(3-42) (blue peak). Nevertheless, they both also contain a variety of other pGlu-Aβ(3-42) species (Figure 26B) namely fragments of residues 8-42, 3-25 and 26-42. Additional fragments that were exclusively found in the sample, were of residues 3-37, 3-23 and 24-42 (pink). A lot of these fragments show indications for modifications such as H_2O loss (contoured waterdrop) or hydroxylation (waterdrop).

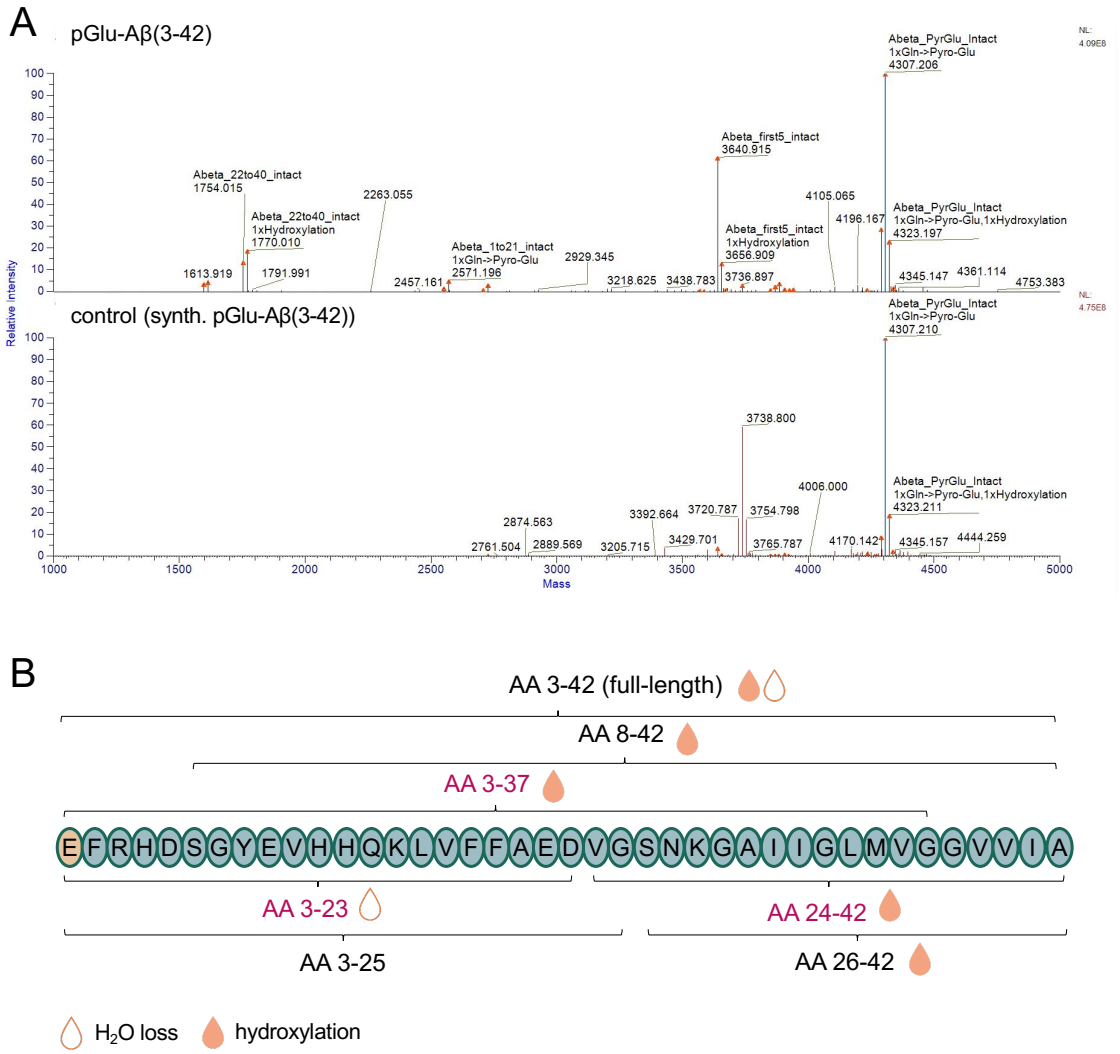

Figure 26: Mass spectrometry results on pGlu-Aβ(3-42). (A) MS profiles of complete samples of pGlu-Aβ(3-42) (top) and the synthetic pGlu-Aβ(3-42) control (bottom). (B) Visualization of pGlu-Aβ(3-42) species found by MS. Pyroglutamate at position 3 is highlighted in beige. All species that have been found in the pGlu-Aβ(3-42) exclusively are highlighted in pink. Possible H_2O loss and/or hydroxylation are indicated by symbols. All species were also detected without any of these modifications.

Residues prone to H_2O loss comprise asparagine, glutamate, serine and threonine (283) of which all but threonine are part of the pGlu-Aβ(3-42) sequence. Especially N-terminal glutamates are likely to lose NH_4 or H_2O (284). However, minor modifications like these are not the main concern in this study since they will likely not have such a big influence on the overall amyloid structure, particularly, because the predominant variant still is the non-modified pGlu-Aβ(3-42). The two large fragmentations (AA 3-23/24-42 and AA 3-25/2624) only occur to a minor proportion. Moreover, they should result in a clearly different fibril or, even more likely should be fragmented single monomers.
Striking on the other hand is the notion, that again, also in the second analysis, pGlu-Aβ(8-42) acts as the major contaminant. Interestingly, in this analysis the sample also contained a C-terminally truncated version missing the last five residues (AA 3-37). Potentially, the N- and C-terminus are rather flexible within the fibril and therefore exposed to the solvent and more likely to be affected over time.

1.4 Pitch and twist: Helical symmetry of pGlu-Aβ(3-42)

For helical reconstruction, the knowledge or at least a reasonable guess for the helical parameters of a fibril is imperative. Hence, characterization of fibrillated pGlu-Aβ(3-42) was carried out via AFM prior to EM studies.

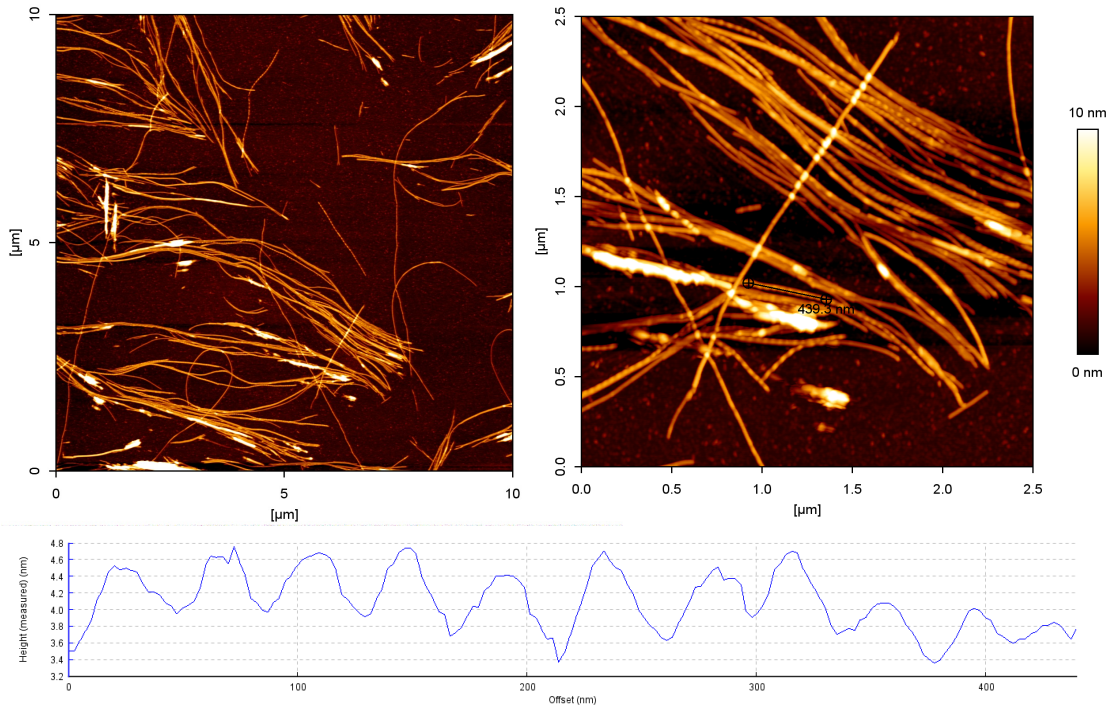

Figure 27: AFM measurements of pGlu-Aβ(3-42). Exemplary AFM images of pGlu-Aβ(3-42), 5 µL undiluted taknen from sample fraction II (21.06.2018) and dried on mica. Height profile (bottom) is shown exemplary across one fibril (top right) to measure pitch and crossover distance.

Analysis of the fibril pitch was performed by averaging peak distances of cross-sections along multiple fibrils for pGlu-Aβ(3-42) and wildtype Aβ(1-42). Figure 27 displays two

exemplary AFM images which have been used for analysis of fibril morphology details. Both images show clearly fibrillated pGlu-Aβ(3-42) with filaments lengths around 5 µm and longer. A large portion of these fibrils shows a distinct twist in the sample. Twisted fibrils were further analyzed with JPKSPM Data Processing software in order to evaluate their pitch. In each case, cross-sections of three fibrils were measured across eight or nine crossovers (see Figure 3 in section III1.2.3) resulting in average values shown in Table 2.

Table 2: Crossover distances of pGlu-Aβ(3-42) and Aβ(1-42)

	average crossover	**standard deviation**	**standard error**
pGlu-Aβ(3-42)	41.1 nm	6.827	± 1.4 nm
Aβ(1-42)	47.8 nm	7.556	± 1.3 nm

Accordingly, the pGlu-Aβ(3-42) variant shows a pitch of ~80 nm, which is significantly smaller than the pitch of ~90 nm for the wildtype. Comparing this to cryo-EM data from Gremer et al. (181) according to which Aβ(1-42) has a pitch of ~115 nm, a pitch of ~100 nm can be expected for pGlu-Aβ(3-42) in cryo-EM measurements.
This increase of roughly 25 % from AFM measurements to cryo-EM data might be explained with the drying of proteins during the sample preparation for AFM (section X9.2.1.2). Similar differences have been reported for IAPP measured in liquid or dried state under AFM (285).
In addition to information about length and crossover distances, AFM images also provide insights about the handedness of fibrils. Analysis on handedness was performed on AFM images in which clearly twisted fibrils were visible. The analysis revealed a second polymorph (Figure 28B, iii), which exhibits a larger crossover distance than the first polymorph (B, ii).

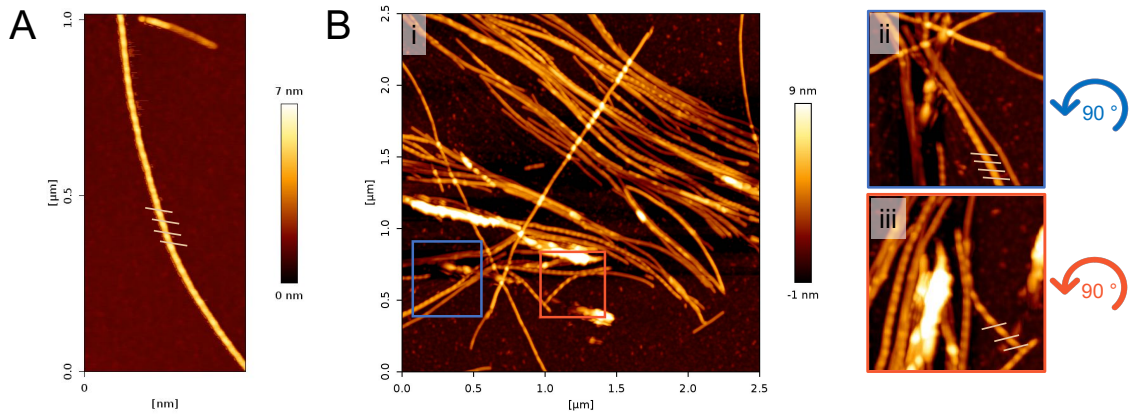

Figure 28: Analysis of AFM images regarding helical twist of pGlu-Aβ(3-42). (A) Single fibril exhibiting a left-handed twist indicated by beige lines. (B) (i) Overview image displaying different pGlu-Aβ(3-42) polymorphs. (ii) Close-up of a polymorph with small crossover and left-handed twist (indicated by lines) that is also seen in (A). (iii) Close-up of a second polymorph with larger crossover but also left-handed twist (indicated by lines).

Although their handedness is hardly visible, Figure 28 indicates that pGlu-Aβ(3-42) fibrils are slightly left-handed. Left-handedness is very common for amyloid fibrils, which is in good agreement with the fact that β-sheets are most commonly left-handed (286). Nevertheless, few examples of right-handed fibrils have been reported (70, 187).

1.5 Cryo-EM measurements on pGlu-Aβ(3-42)

Cryo-EM measurements on pGlu-Aβ(3-42) were performed multiple times under different conditions (see Table 30: Sample preparation of fibril samples for cryo-EM). In three cases this led to the acquisition of data sets (section X9.6.3.1). Representative micrographs from these data acquisitions on either Tecnai Arctica or Titan Krios microscopes are shown in Figure 29.

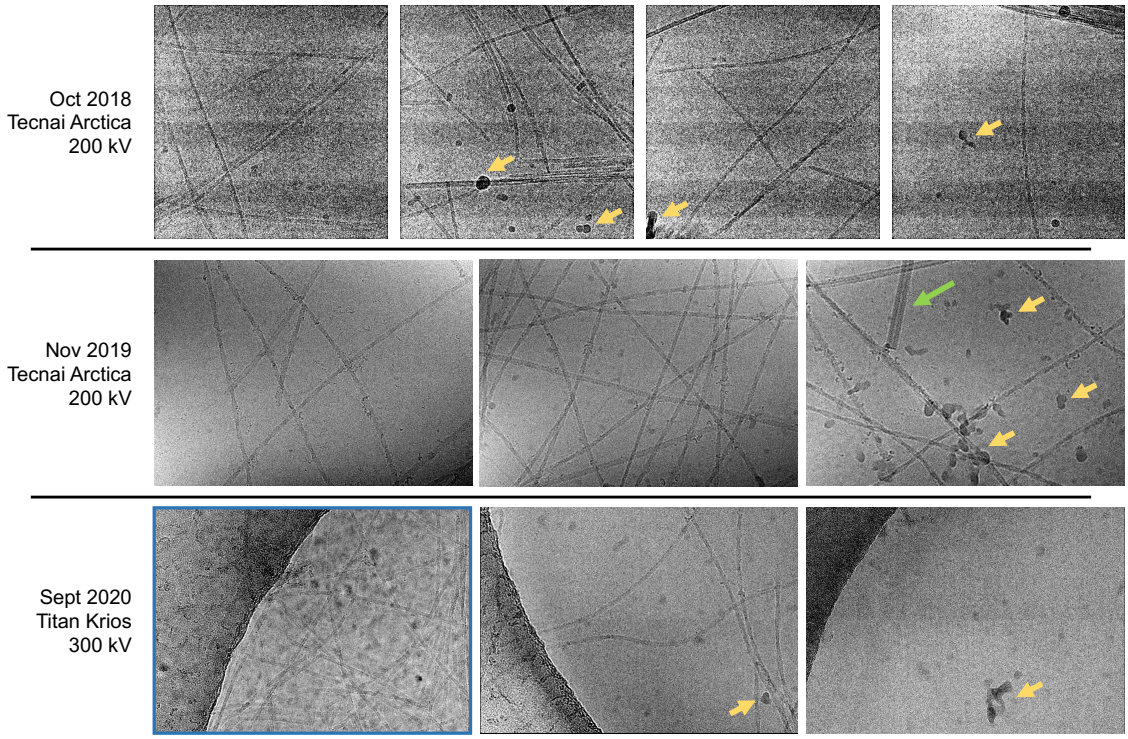

Figure 29: Exemplary micrographs from cryo-EM measurements on pGlu-Aβ(3-42). All data sets were acquired on undiluted sample either at a Tecnai Arcitca (200 kV) or Titan Krios (300 kV) microscope. Impurities are highlighted by yellow arrows. The data set from October 2018 (Oct 2018) shows a good image contrast and sufficient fibril density but also impurities. The November 2019 (Nov 2019) data set had really high fibril concentrations and good contrast. Here, the sample had been contaminated with tobacco mosaic virus (green arrow) particles. The final data set of September 2020 (Sept 2020) showed mixed fibril concentrations in the holes but high fibril density (blue frame) dominated in this case.

As can be seen, fibrils have been present in every measurement. While the "Oct 2018" dataset shows multiple fibrils which are evenly distributed, it also shows a rather dark background. With a thin amorphous ice layer, which is fairly transparent, sample proteins should be clearly seen against the background. However, thick ice results in less contrast and therefore dark background (Figure 29, top row). In comparison to this, the other two datasets present a much better, lighter background. While the "Nov 2019" dataset often

shows higher fibril concentrations in the holes (Figure 29, middle row, central image), the fibril concentration in the "Sept 2020" dataset is comparably low. In the latter, approximately 25 % of the micrographs do not show any fibrils (Figure 29, bottom row, right image). Regarding impurities (yellow arrows), the earliest dataset was the most promising neglecting the dark background that likely was the reason the reconstructions would only reach a resolution of ~6 Å. For the "Nov 2019" dataset, the micrographs sometimes show quite a lot of impurities including a tobacco mosaic virus contamination from former Vitrobot™ users (Figure 29, green arrow). For this dataset, an unsolved issue led to problems with the CTF fitting of the micrographs due to which no reconstructions were performed.

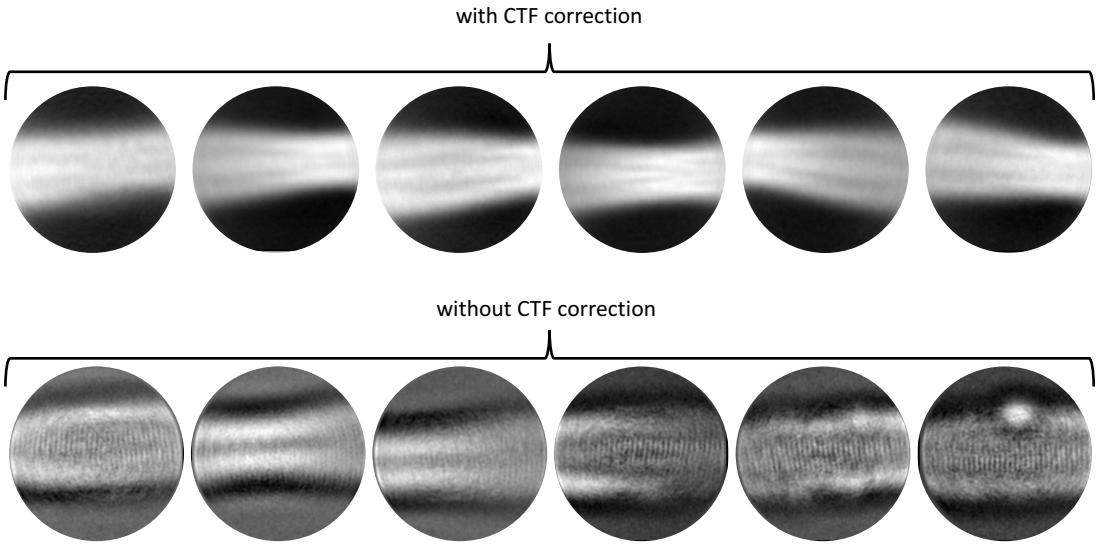

Figure 30: Examplary 2D classes of pGlu-Aβ(3-42) dataset "Nov 2019". Six of the highest populated 2D classes of pGlu-Aβ(3-42) with (top) and without (bottom) CTF correction and parameter T = 8.

Without CTF correction the β-sheet pattern for dataset of "Nov 2019" is much more visible compared to 2D classification with CTF correction (Figure 30). Normally, CTF correction should lead to better particle alignment due to an improved signal and this in turn should have resulted in clear separation of β-sheets in 2D classification.

1.5.1 Reconstruction of the September 2020 dataset

The latest data set on pGlu-Aβ(3-42) was acquired in September 2020 on a Krios 300 kV at the NeCen facility in Leiden, Netherlands with support of Abril Gijsbers and Raimond Ravelli. A total of 1,861 raw movies was collected at -1.5, -1.8, -2.1, -2.4, -2.7 and -3.0 µm defocus with three exposures per hole and a total dose of 40 electrons/Å^2 (for more information see Table 33 in XVI3.1).

1.5.1.1 Preprocessing

The raw movies were imported to RELION-3.1.0 (266) and averaged using its internal motion correction with a B-factor of 150 and a binning factor of 2. Subsequently, CTF estimation was carried out on the motion corrected micrographs via CTFFIND-4.1 (259) .
The power spectra, an example of which is shown in Figure 31, of the corrected micrographs exhibit the 4.7 Å signal, which is characteristic for the β-sheet stacks in amyloid fibrils.

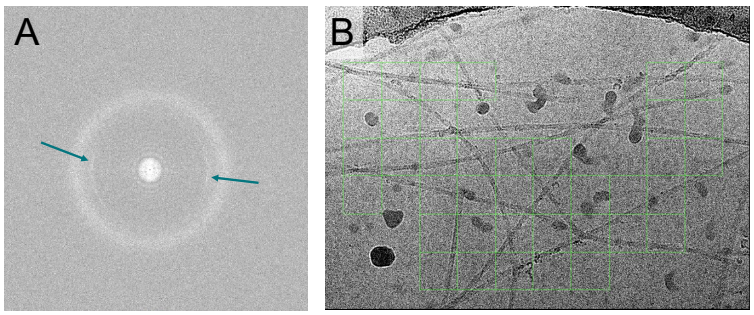

Figure 31: Exemplary power spectrum from the pGlu-Aβ(3-42) dataset September 2020. (A) Power spectrum of the micrograph in (B) with the 4.7 Å signal indicated by arrows. (B) Micrographs displaying the areas (green boxes) for which the averaged power spectrum has been calculated with EMAN2.

Thinner ice would likely result in more Thon rings and an increased 4.7 Å signal. However, according to CTF estimations, good resolution of 4 Å or better is expected for most of the micrographs.
Following the preprocessing steps of motion correction and CTF estimation, the fibrils had to be selected from the motion-corrected micrographs. Although there are tools that support automatic picking of filaments (262, 264, 287), the differentiation between multiple polymorphs is still difficult. Hence, micrographs were examined manually to determine the number of polymorphs in the sample. The observed polymorph species are displayed in Figure 32 that displays six representative micrographs with three distinguishable polymorphs (highlighted in blue, red and yellow) of pGlu-Aβ(3-42).

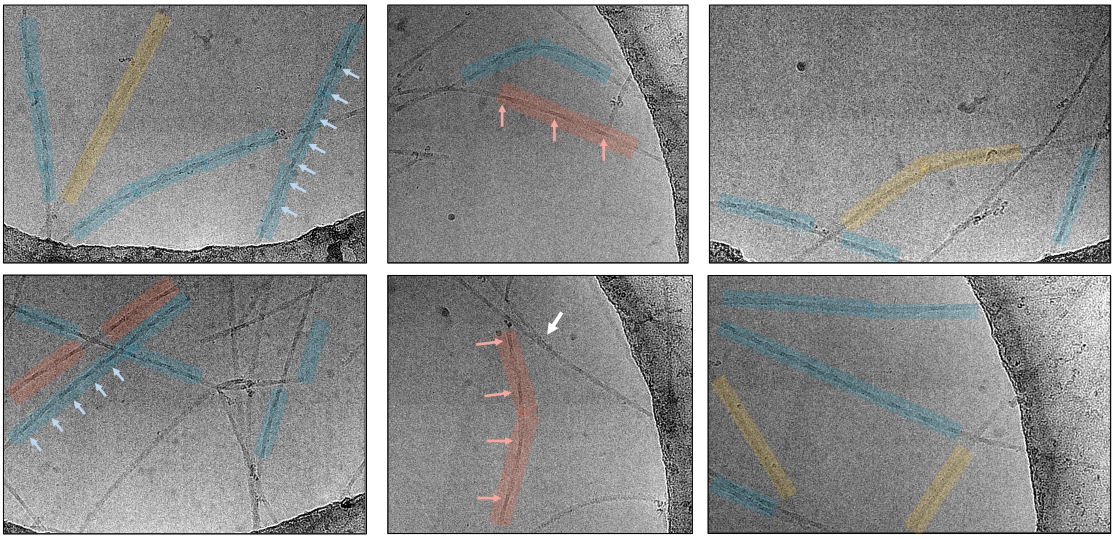

Figure 32: Representative micrographs from the pGlu-Aβ(3-42) September 2020 dataset. Six micrographs (carbon parts have been cropped) displaying at least three different polymorphs of pGlu-Aβ(3-42). The main polymorph, PM1 (blue) is once observed as a double-fibril or a fibril with a split end (white arrow). A second polymorph (red) exhibits a larger twist compared to PM1 and a third polymorph does not show any twist (yellow). Fibrils that are not highlighted, could not be unambiguously identified as one of the beforementioned polymorphs.

All species show lengths spanning the grid hole (1.2 µm) and roughly the same width of around 80 Å. For the two twisted polymorphs, crossover distances could be measured. Polymorph I (PM1, blue) has a crossover distance of 400 Å and the second twisted polymorph (PM2, red) a crossover distance of ~750 Å. The third polymorph (PM3, yellow) did not exhibit any twist.

Due to its high abundance, PM1 was picked manually resulting in a total of 3,500 picked segments from 1,841 micrographs. From these micrographs, 45,199 particles were extracted with a box size of 300 pix, a tube diameter of 140 Å, 5 asymmetrical units, an inter-box distance of 9.4 % and an expected helical rise of 4.7 Å according to the cross-β signal.

1.5.1.2 2D classification and initial model building

After preprocessing and picking, the resulting particles were used for 2D classification. 2D classification was carried out with 50 classes, a tau parameter of 1, a tube diameter of 140 Å and a helical rise of 4.7 Å. The 12 highest populated classes from 2D classification are displayed in Figure 33 with a close-up of the first class, which clearly displays β-sheet stacks (orange circle).

From these classes, all particles with an estimated resolution of 5 Å or better were selected and another 2D classification was performed. The resulting 2D classes were used as input for a first 3D reconstruction run, for which the initial model was based on a featureless cylinder.

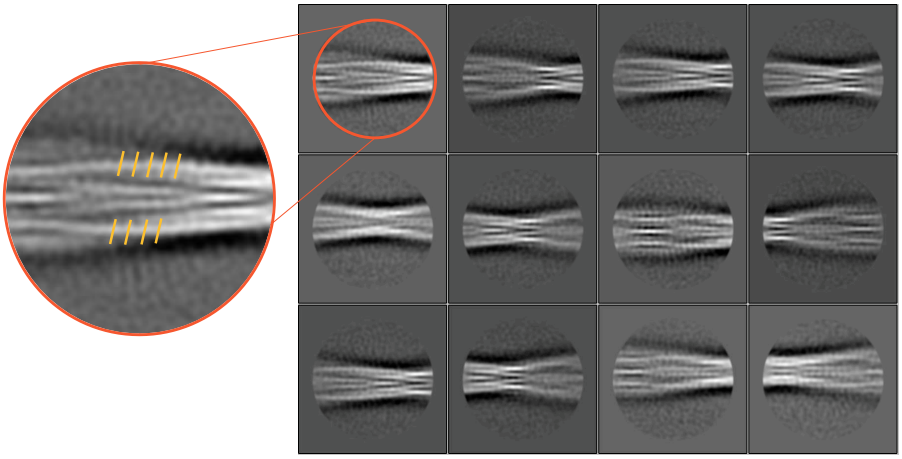

Figure 33: 2D classification of pGlu-Aβ(3-42) PM1. Displayed are the 12 out of 50 highest populated classes with a close-up (orange circle) of the first class. Stacking of β-sheets is indicated by yellow lines.

Initial models (mesh) and resulting reconstructions (blue) are displayed in Figure 34A. For the first reconstruction (i) a box size of 300 pix and a cylinder diameter of 100 Å were used. In the second trial (ii), the same cylinder was used, but the mask diameter was reduced from 220 Å to 180 Å. For the third run (iii), the box size was increased to 400 pix. The output of the second trial (ii) was used for further 3D reconstruction and resulted in the density shown in Figure 34B, which was calculated with a mask of 220 Å, a resolution limit of 8 Å, a tau parameter of 2 and an outer helix diameter of 120 Å.

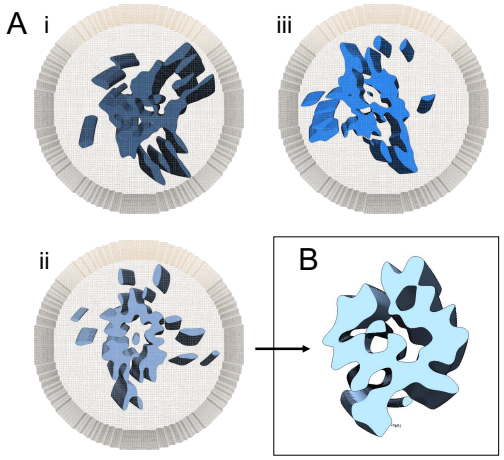

Figure 34: Initial model of pGlu-Aβ(3-42) PM1. (A) Initial models (mesh) with resulting first 3D reconstructions (blue). Reconstructions with featureless cylinders as initial models were run with (i) box size of 300, cylinder diameter 100 Å, mask of 220 Å (ii) box size of 300, cylinder diameter 100 Å, mask of 180 Å and (iii) box size of 400, cylinder diameter of 100 Å, mask of 180 Å. (B) Subsequent reconstruction of (A, ii) with a mask of 220 Å, resolution limit of 8 Å and a helix diameter of 120 Å.

As shown in Figure 34B, first trials to calculate useful initial reconstructions were unsuccessful. Accordingly, 2D classification was repeated to exclude interfering particles from the dataset. The number of classes was increased to 100 to facilitate the sorting of poorly occupied classes. However, a large fraction of these 100 classes was left empty eventually. The three highest populated classes of this 2D classification run are displayed in

Figure 35A together with less populated classes that show some sort of circular shadows or budding at the side of the fibril (Figure 35B, indicated by green arrows).

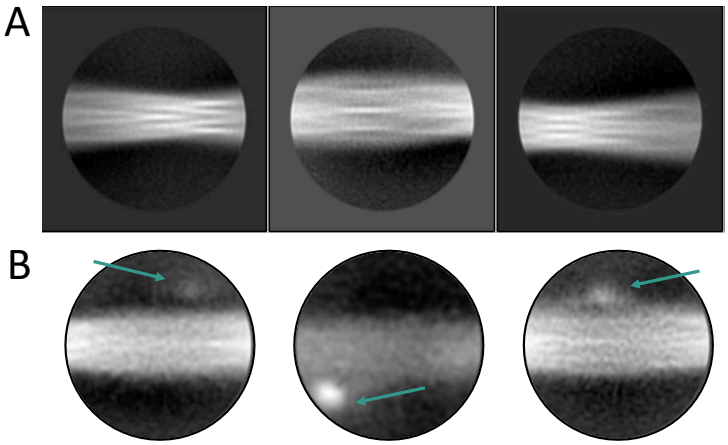

Figure 35: Second 2D classification of pGlu-Aβ(3-42) PM1. (A) The three highest populated classes out of 100. Representative classes with budding or shadows indicated by green arrows.

It remains unclear what these globular densities along the fibril axis represent. Potentially, they emerge due to irregularities within the fibril. If those kind of irregularities are averaged, they might result in a signal as seen in Figure 35B. This hypothesis is supported by the fact that in the mentioned classes no β-sheet separation is visible anymore and therefore β-sheets might not contribute most of the signal in these classes.

On the other hand, the additional densities might arise due to secondary nucleation processes, which take place alongside the fibril axis. Although secondary nucleation has been examined via EM (288), there are no detailed structural insights, yet. For atomic detail, secondary nucleation sites would have to occur in sufficient amounts within the data set and always involve the same residues.

2D classes displaying budding or circular shadows next to the fibril (Figure 35B) (Class2D/job166) were discarded from the data set resulting in a total of 42,176 particles afterwards (Select/job171). Based on this selection, an initial model was calculated with the new RELION-3.1.0 implementation relion_helix_inimodel2d (266). As a preparatory step for calculation of the initial model, 2D classification (Class2D/job180) was performed (Figure 36A) with a box size of 500 pix in order to span a whole crossover, which was expected to be 400 Å. Then, the smallest 2D class, which contained 3,896 particles displaying a whole fibril crossover and exhibiting clearly separated β-sheets, was selected (Select/job184) and used as an input for relion_helix_inimodel2d. The program was run by using the following command:

relion_helix_inimodel2d --i bigclass.star --iter 1 --sym 1 --crossover_distance 400 --angpix 0.836 --o inimodel_bigclass_sym1_box300.mrc --mask_diameter 180

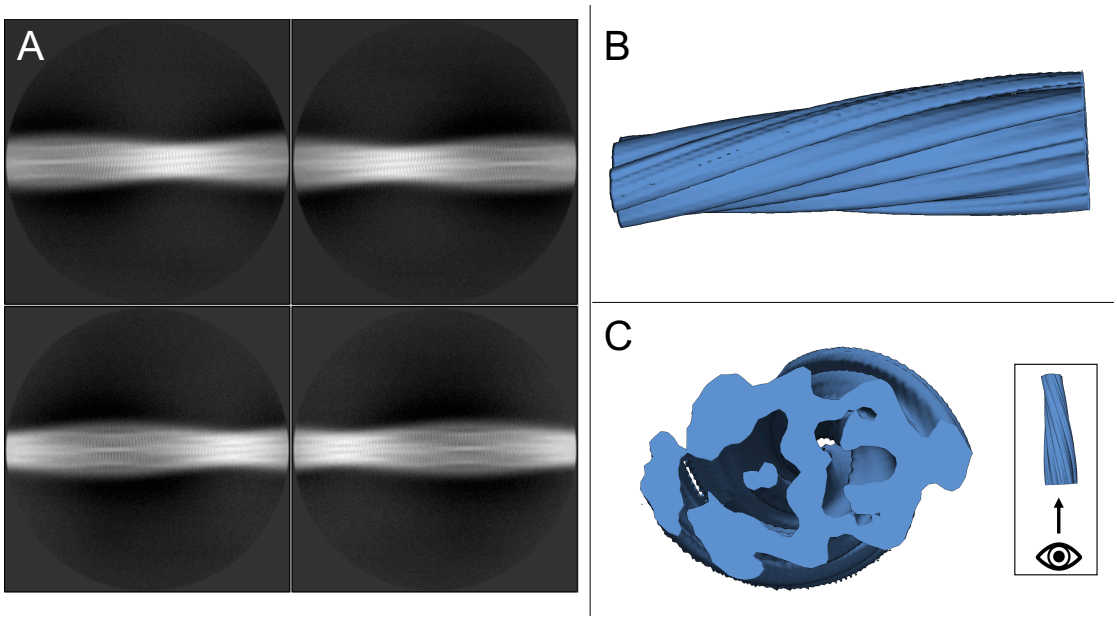

Figure 36: Crossover 2D classes and initial model. (A) Representative 2D classes spanning a whole crossover distance of pGlu-Aβ(3-42) PM1. (B) Side view of the initial model from relion_helix_inimodel2d from crossover-spanning 2D classes. (C) Cross-section of the initial model.

Although the 2D classes displayed in Figure 36A seem to exhibit a C_2 symmetry, the symmetry could not be unambiguously defined. Accordingly, the resulting initial model is displayed in Figure 36B and C, is based on a C_1 symmetry. The initial model was used to calculate an initial reconstruction out of all 42,176 particles ((Select/job171), for details see section XVI3.1.1.1).

1.5.1.3 3D classification

Early 3D classifications were performed with a C_1 symmetry and only one class in order to determine the correct helical parameters. After several rounds of 3D classification, which did not seem to improve the resolution significantly, a C_2 symmetry was applied. By application of C_2 symmetry, symmetric parts of the fibril should evolve first. After determination of the helical parameters, the reconstruction should then be examined again for C_1 or C_2 symmetry (see Figure 44). In addition to C_2 symmetry, also a 2_1 screw symmetry (see III2.2.1) was tested. However, 2_1 screw symmetry worsened the resolution.
The evolution of the density map after the latest particle selection is displayed in Figure 37 and will be described in the following. For a more detailed view on the course of reconstruction see appendix Figure 68.

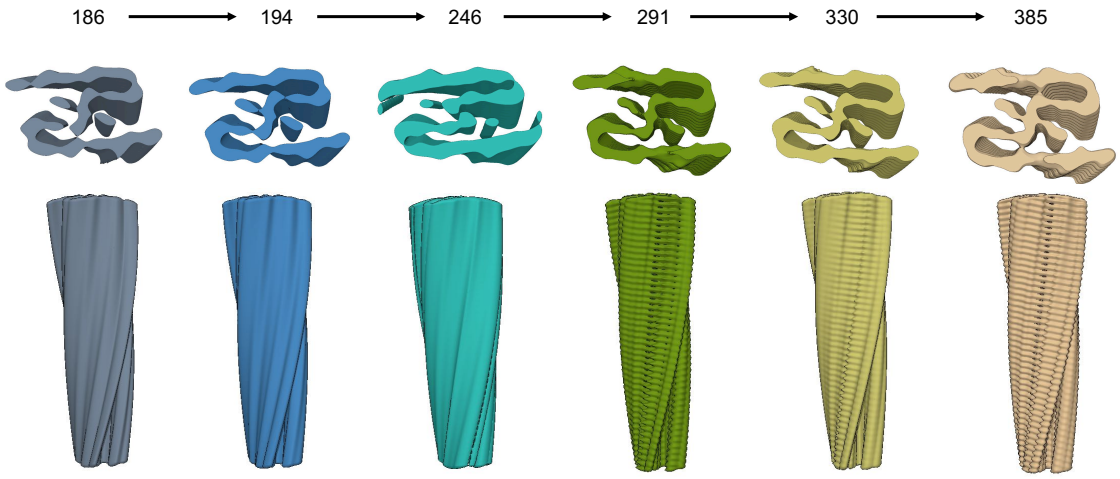

Figure 37: Evolution of pGlu-Aβ(3-42) PM1 3D models. Displayed are the unsharpened cross-section (top pictures) and the side view (bottom pictures) of 3D classification jobs 186, 194, 246, 291, 330 and 385. Job186 was the first 3D classification performed with the initial model from 2D classification. The tilt parameters were corrected to 90 ° for job194. For job246, classes with large central density were excluded from the dataset. For job291 the tau parameter was increased to 20. Job330 closed the hole, which was introduced by masking and job385 is the result of the final 3D classification run.

The first 3D reconstruction from the initial model (Figure 36B, C) yielded already a good resolution and a lot of detail in the cross-section (Figure 37, job186). The cross-section indicated a fibril consisting of two protofilaments. However, one consistent problem during reconstruction was the interface or central part of the fibril, which did not separate. Because simultaneously, there were no β-sheets emerging, the tilt prior and angles were manually corrected to 90 °C (for Class3D/job194, Figure 37). This problem has already been described in another project (68), in which the tilt angles of the reconstructions did not show a bi-modal distribution around 90 ° but instead fluctuated across a larger range. Hence, in the following 19 classification runs the tilt priors were mostly kept fixed in order to foster a bi-modal distribution.

A classification run with four classes and without image alignment, yielded one distinct class that showed high density in the middle of the fibril. Due to the problem stated above, the lack of separation in the central fibril part, this class, which contained 26 % of all particles, was discarded. 31,408 particles were left (Select/job245), which were used for further reconstructions (Figure 37, job246).

At this point, the helical symmetry parameters were not determined in detail but had turned out to be ~2.2 ° in twist and ~4.7 Å in rise. In the following rounds of 3D classification, these parameters were optimized by search for helical symmetry in RELION. Additionally, the tau parameter was raised to 20 in order to increase the weight on experimental data and reveal more details. Although increasing the tau parameter did help with the resolution of β-sheets (Figure 37, job291), the interface of the pGlu-Aβ(3-42) PM1 remained unclear.

In order to facilitate the separation of the supposedly two monomers in the fibril, a cylindric mask was applied in the subsequent 3D classification runs. This mask had a hole of 5 Å in the center in order to cut off signal from the interface. By cutting off signal from the central

part of the fibril, more weight was forced on the exterior when calculating particle orientations. By assigning the correct particle orientations of the exterior, in later runs the interface would potentially be easier to separate.
The resulting 3D density is displayed in Figure 38 (light yellow). It reveals more detail compared to former 3D classification runs and additionally shows an improvement in separation of the β-sheets.

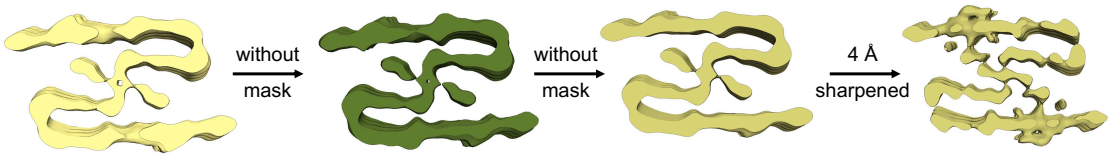

Figure 38: 3D reconstructions after application of a holey mask. Cross-sections of jobs 302 (yellow), 310 (green) and 330 (khaki). For reconstruction of job302 a mask with a central 5 Å hole was applied. Following 3D reconstructions were performed without mask to close the introduced hole in the density map. Job330 resulted in a density map without central hole. A sharpened version of this reconstruction reveals a more detailed view on the cross-section. Sharpening was performed with visdem.

However, Figure 38 also shows that due to the masking a hole was introduced to the density. Subsequent 3D classification runs were performed without the mask and therefore exploited all available orientations. Although again, no interface separation is observable, a gain in cross-section detail could be achieved (Figure 38). As soon as more details in the density map were revealed, more parameters were refined. Hence, in subsequent 3D classification runs the angular sampling steps were decreased to 1.8 ° and the helical outer diameter was lowered to 120 Å.
In a next step (Class3D/job364), helical symmetry parameters were further refined by performance of local searches, helical symmetry search and increase of the tau parameter to a value of 50. After having decreased the helical outer diameter to 110 Å (Figure 37, job385) the resolution again improved. The resulting 3D reconstruction was sharpened to 3.5 Å with visdem and later on flipped to match the supposed left-handedness from the AFM analysis. After sharpening, which revealed significantly more detail compared to the unsharpened map, the characteristic zig-zag of a protein backbone became visible although the interface did not separate (Figure 39). However, densities of electron dense residues started to form and β-sheet separation improved.

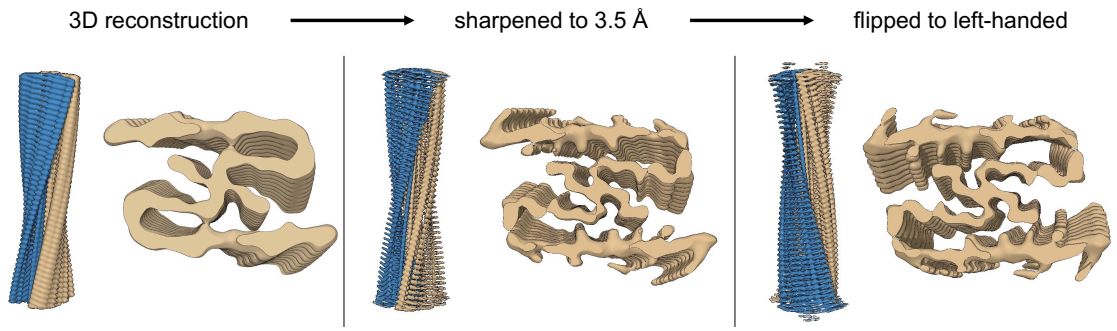

Figure 39: Sharpened density map of the final 3D classification run. The initial density map (left) was first sharpened to 3.5 Å (center) and then flipped to exhibit a left-handed twist (right). All steps are displayed through a two-colored side view indicating the two protofilaments and a cross-section top-view of the fibril.

1.5.1.4 Polymorph 1 of pGlu-Aβ(3-42) could exhibit a hairpin- or S-fold

The resulting 3D density map with the helical parameters being 2.21 ° (twist) and 4.7 Å (rise) reveals an amyloid fibril consisting of two protofilaments with a 385 Å crossover distance and clearly separated β-sheets (Figure 40A, B, E). The cross-section section of the fibril exhibits the characteristic zig-zag of a protein backbone but the interface remains unresolved (Figure 40C, D). The angular distribution of the 3D reconstruction (Figure 40F) is fairly even with a focus area in the central part of the z-axis, which indicates that the angular distribution has not reached its optimum.

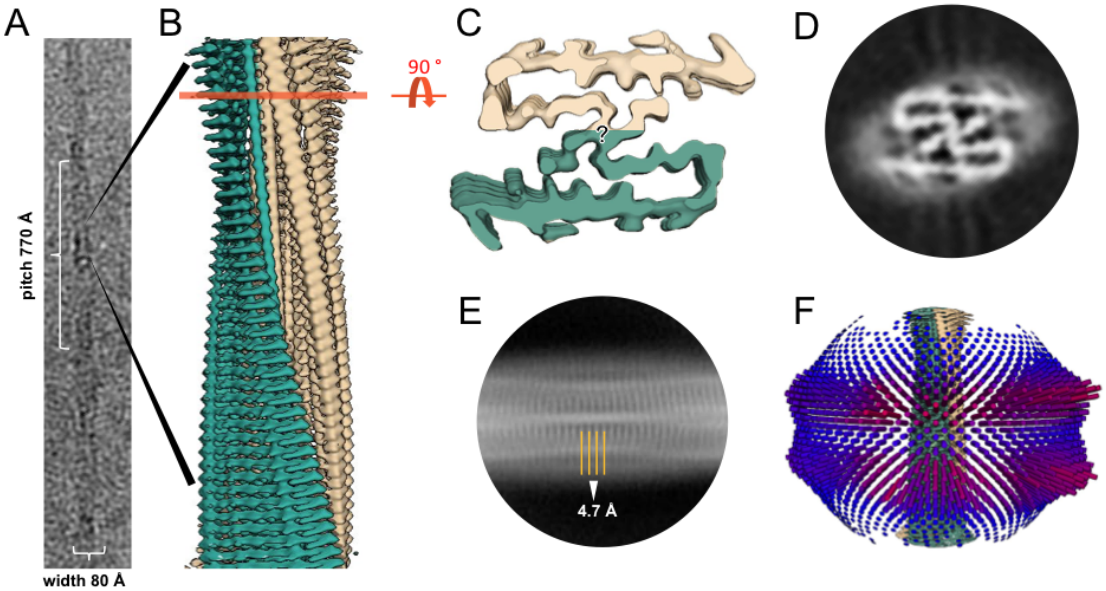

Figure 40: Polymorph 1 of pGlu-Aβ(3-42). (A) Image section from one micrograph displaying PM1 and indicating pitch and width. (B) Side view of the reconstructed, left-handed density map of PM1. Two protofilaments are indicated by different colors. (C) Cross-section of PM1 with indicated two monomers in one layer. Since the interface has not clearly separated, coloring is preliminary. (D) 2D projection of the final 3D classification run displaying the cross-section. (E) Close-up of a 2D class highlighting the 4.7 Å rise (yellow lines). (F) Angular distribution histogram of the reconstructed density map.

Since cryo-EM data do not allow for interpretation of the handedness of a fibril, the reconstruction was performed with a twist resulting in a right-handed fibril. AFM images,

which do provide information about handedness, indicated a left-handed twist to be more likely. Accordingly, the fibril in Figure 40 is presented as left-handed. Nevertheless, more data coming from e.g., platinum-shadowing will have to be conducted in order to make a claim about the handedness.

The cross-section shows that the fibril likely consists of two monomers facing each other. With a final resolution of ~4.0 Å the reconstructed density could be sufficient to build an atomic model *de novo,* since it is already close to the threshold for building atomic models *de novo*, which usually is around 3.5 Å. However, local resolution might deviate from that value and since the fibril interface and the rest of the density is not sufficiently resolved, no unambiguous model building was possible.
Nevertheless, putative C_α-traces for pGlu-Aβ(3-42) PM1 are shown in Figure 41. Conceivably, each monomer exhibits either a hairpin fold (A) or an S-fold (B). In regard of a recent cryo-EM study on a fibril from immunoglobin light chain amyloidosis (188), maybe both folds can be found in the fibril. In the beforementioned study, the authors report two different folds within one fibril. If signals from two folds overlay, they might result in an unresolvable density as seen for pGlu-Aβ(3-42) PM1.

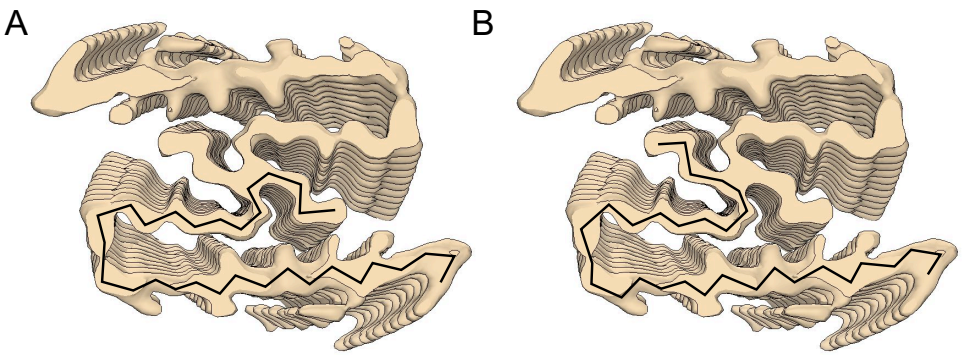

Figure 41: Possible C_α-trace and interface of pGlu-Aβ(3-42) PM1. There are two possible C_α-traces for pGlu-Aβ(3-42) PM1. Based on the sharpened density, and the interface not being resolved sufficiently, the protein backbone could form a hairpin (A) or S-like fold (B).

In any case, it is apparent that the gap between the two monomers is very small and the peptide chain is rather curvy in this part of the fibril. Accordingly, small and highly flexible residues will likely be located at the interface. C-terminally, pGlu-Aβ(3-42) contains two consecutive glycine residues , which would fit perfectly well into the interface. Accordingly, a potential interface is displayed in Figure 42 (A and B).

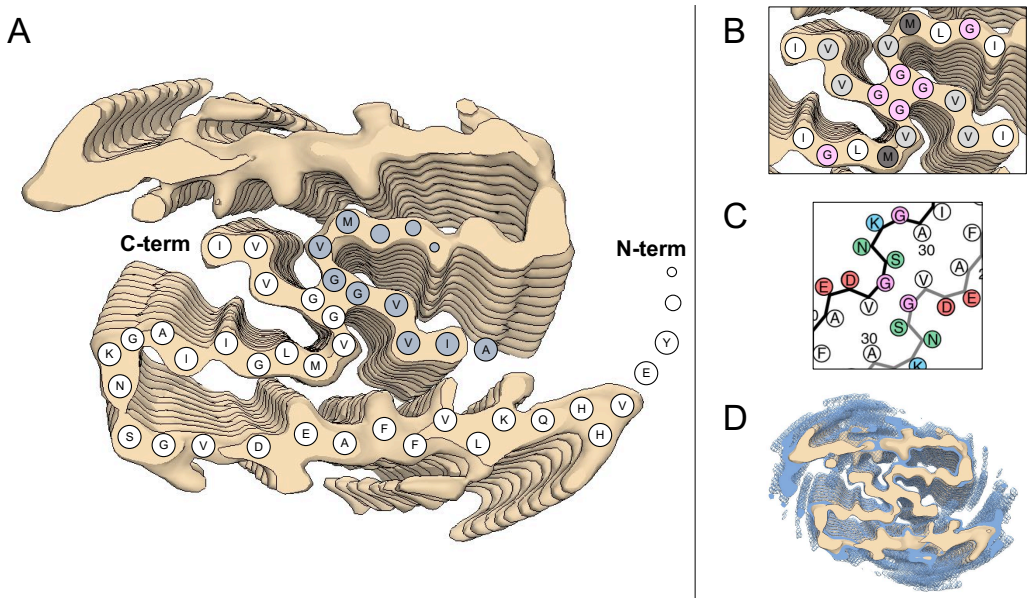

Figure 42: Putative residue placement and interface of pGlu-Aβ(3-42) PM1. (A) Putative residue arrangement based on the GG-interface and S-fold. (B) The GG-interface. (C) Glycine residues were also shown to take part in interface formation of Aβ(1-40) fibrils (taken from (187)). (D) Model density (beige) overlaid with the same density map with higher density threshold (blue) to display the continuation of density.

Assuming this would be the true interface, Figure 42B clearly shows that the exact course of the C_α-trace would hardly matter. Instead, the interface and two putative C_α-traces represent something best described as a structural palindrome. The residues following the unresolved interface would be the same whether the fold turns out to be a hairpin or S-fold. For the S-fold a potential sequence arrangement is displayed in Figure 42A. An initial backbone, which encompassed 31-33 residues depending on the S- or hairpin fold was built with coot (268, 269) (see Figure 67, appendix). Accordingly, more than 30 residues out of 40 would fit into the density that displays most of the C-terminus and a flexible N-terminus. However, at this point the backbone trace remains a sketch since the density is not resolved to sufficient resolution and hence, register shifts are possible in addition to other sequence arrangements.

One detail pointing towards the hairpin fold might be the fold resemblance of an Aβ(1-40) polymorph from human brain (187) that is displayed in Figure 42D and also contains a glycine at the center of the fibril. Additionally, the interface of the Aβ(1-40) polymorph shows a similar bending compared to the potential hairpin fold in pGlu-Aβ(3-42) PM1.

On the other hand, the Aβ(1-42) wildtype polymorph that has been prepared under the same conditions as pGlu-Aβ(3-42), exhibits a C-terminal S-fold, too. An overlay of the wildtype structure with the pGlu-Aβ(3-42) density map is displayed in Figure 43A. Another amyloid, which exhibits this kind of S-fold, is the human IAPP that has been molecularly linked to Aβ(1-42) (Figure 43B).

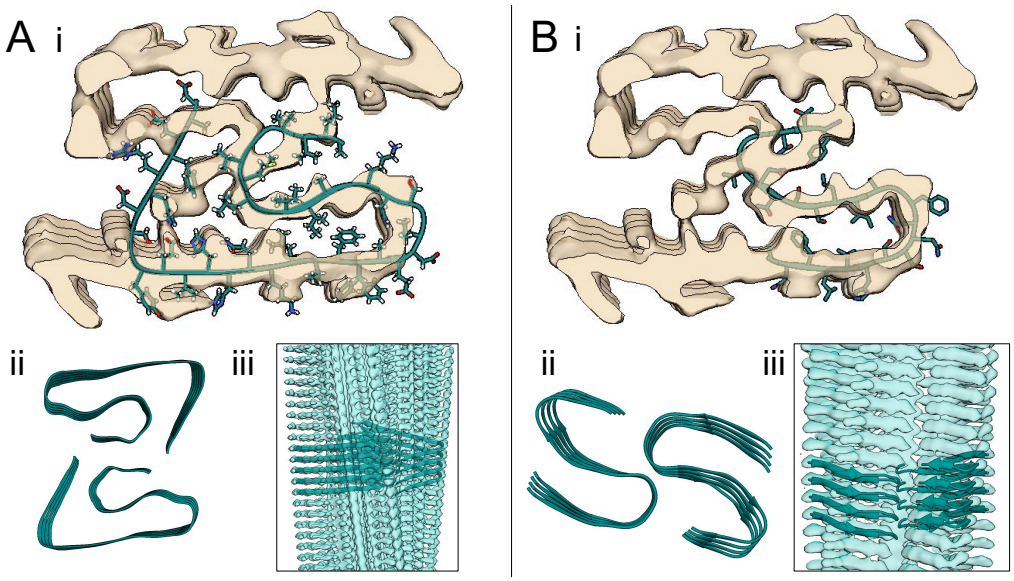

Figure 43: Comparison of the pGlu-Aβ(3-42) PM1 density map with other fibril models. Comparison of pGlu-Aβ(3-42) with Aβ(1-42) (181). (i) The S-part of the LS-fold of Aβ(1-42) (green) fits well into the pGlu-Aβ(3-42) PM1 density. (ii) LS-fold of Aβ(1-42) (PDB: 5oqv). (iii) Atomic model (green) and density map (blue) of Aβ(1-42). (B) Comparison of pGlu-Aβ(3-42) with IAPP (70). (i) The IAPP S-fold (green) fits well into the pGlu-Aβ(3-42) PM1 density. (ii) S-fold of IAPP (PDB: 6y1a). (iii) Atomic model (green) and density map (blue) of IAPP.

Before moving on with this model, C_1 symmetry was tested again based on Class3D/job385. The resulting reconstruction is displayed in Figure 44A. The reconstruction was sharpened to 4 Å (B) and compared to the C_2-symmetrical reconstruction (C).

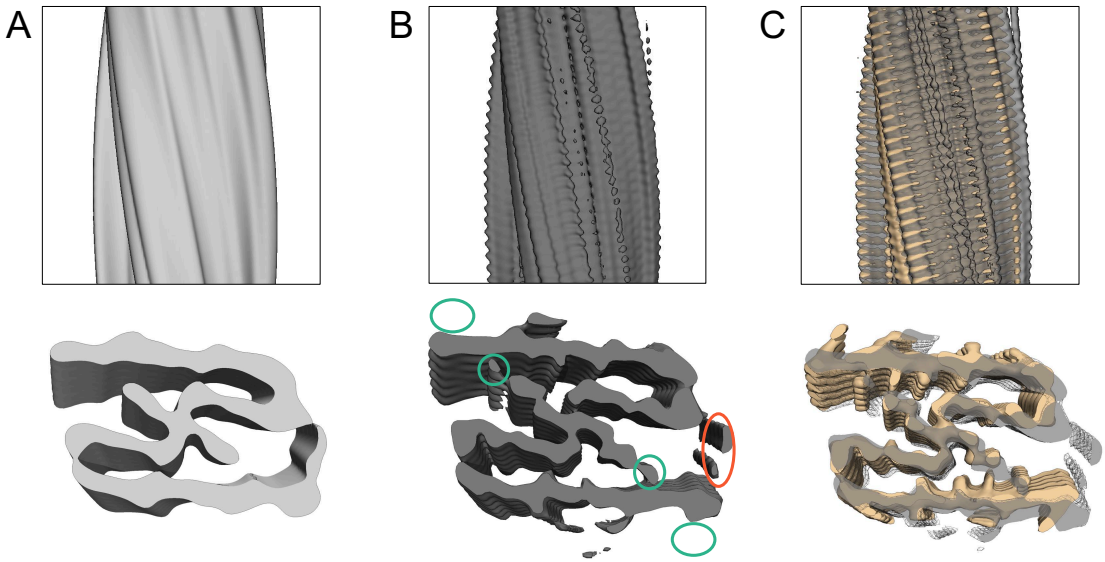

Figure 44: Repetition of the final reconstruction with C_1 symmetry. Based on the reconstruction from Class3D/job385 with C_2 symmetry, another reconstruction with a C_1 symmetry was calculated. All images display a view along the fibril axis (top) and the cross-section (bottom). (A) Result of the reconstruction with C_1 symmetry. (B) Density map of the same job sharpened to 4 Å. Symmetric differences to C_2 symmetry are highlighted in green, asymmetric differences are highlighted in red. (C) Overlay of the reconstruction with C_1 (dark grey) and C_2 (beige) symmetry.

The unsharpened density map (Figure 44A) does not exhibit any β-sheets along the z-axis but the cross-section is very similar to the one with C_2 symmetry, except for an additional

density that extends the supposed N-terminus in one of the monomers. The sharpened density map reveals more details in the cross-section as well as emerging β-sheets, which are still less pronounced than for the C_2 symmetry (B). Differences to the C_2-based reconstruction are highlighted. The overlay of the two symmetry variants shows that the C_2-based reconstruction overall exhibits more detail compared to C_1 symmetry (C).

1.5.1.5 Refinement and post-processing of the most promising model

Eventually, two refinement jobs were performed with Class3D/job385 and a tau parameter of 8 or 4 respectively. Final post processing runs resulted in two densities with 3.8 Å resolution (Figure 45A and B).

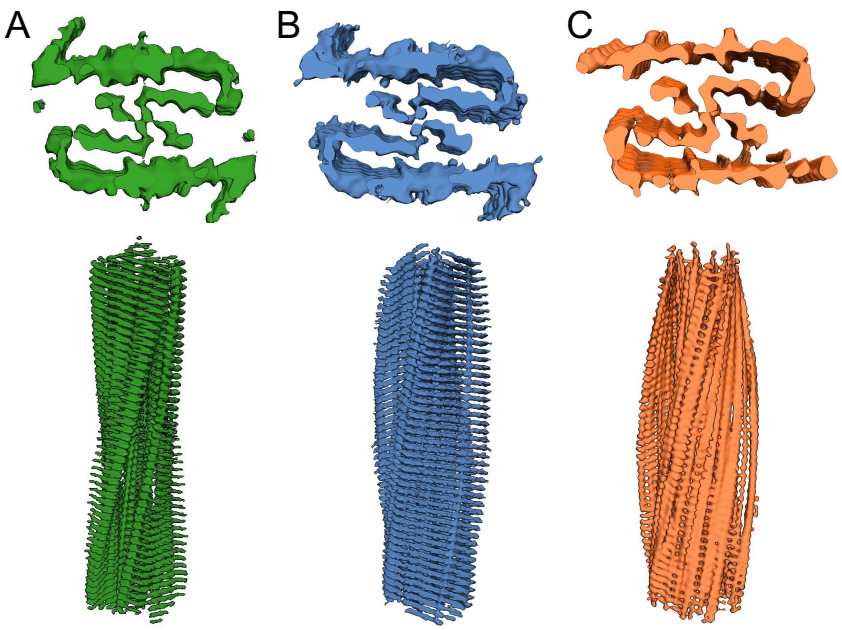

Figure 45: Post-processing results from 3D refinements. (A) Result from PostProcess/job394. Final resolution yielded 3.8 Å. Displayed are the fibril density along the Z-axis (top) and the cross-section (bottom). The resolution along the Z-axis shows clearly separated β-sheets. The cross-section is detailed in the center but less at the periphery. No interface separation. (B) Result from PostProcess/job398. Final resolution yielded 3.8 Å. Displayed are the fibril density along the Z-axis (left) and the cross-section (middle). The resolution along the Z-axis shows clearly separated β-sheets. The cross-section reveals the hairpin fold in the center but shows less detail in the periphery. (C) Result from PostProcess/job407. Final resolution yielded 4.4 Å. Displayed are the fibril density along the Z-axis (bottom) and the cross-section (top). While the resolution along the Z-axis is worse compared to (A) and (C), and β-sheets are not separated, the overall resolution of the cross-section, especially at the periphery, is better.

Both 3.8 Å density maps display good β-sheet resolution. Interestingly, the one with a forced tau value of 8 in the refinement (Figure 45A) appears a bit smoother and less overfitted in the cross-section compared to the density map calculated with a tau value of 4 (B). Although the overall backbone in PostProcess/job398 is blurred, here for the first time a separation of the interface can be observed, which indicates the hairpin fold. However, forcing the usage of the tau parameter during the refinement runs did lead to overfitting in both density maps, which is obvious in the periphery of the densities that are not well defined and show increasing noise. Hence, the revelation of the hairpin fold could be an overfitting artifact.

The hairpin fold cannot be observed in Figure 45A, which is based on a refinement job with a tau of 8 and therefore should have put more weight on the experimental data. However, the true interface fold is not revealed by 3D refinement and post-processing. Additionally, due to overfitting, the resolution of 3.8 Å cannot be recognized as the true resolution, which is expected to be slightly worse and around ~4.0 Å.
Figure 45C displays the result from PostProcess/job407, which is based on a refinement with a tau value of 4 and a C_1 symmetry. Although the periphery of the cross-section here is better resolved compared to C_2 symmetry, again the resolution along the z-axis deteriorated and resulted in a lack of β-sheet separation and a final resolution of 4.4 Å.
An overview of the complete reconstruction process at the example of PostProcess/job398 is displayed in the appendix section XVI3.1.3, Figure 68.

1.6 Conclusion

After expression in *E. coli* cells, the Aβ variant E3Q-Aβ(3-42) was successfully purified and converted to pGlu-Aβ(3-42). Following purification, fibrils were grown under acidic, quiescent conditions. Morphology and quality of these fibrils were examined with means of AFM and MS respectively. After several attempts, one cryo-EM dataset with good quality was acquired eventually. Although the reconstruction of pGlu-Aβ(3-42) PM1 did not yield sufficient resolution for atomic model building, many information can be drawn from this work. The pGlu-Aβ(3-42) amyloid fibril sample assembled at pH 2 consists of at least three polymorphs with ~80 Å width, of which two show a twist and therefore were suitable for reconstruction. PM1 consists of two protofilaments with a rise of 4.7 Å and a twist of 2.21 °, which results in a crossover distance of 385 Å and a total pitch of 770 Å, which is in good agreement with data from AFM measurements. Additionally, AFM data indicate the fibril to be left-handed. Looking at the cross-section of the fibril, each monomer either exhibits a hairpin or S-fold. The fibril center likely comprises four glycine residues surrounded by hydrophobic residues valine, isoleucine and alanine. The N-terminus of PM1 seems to be rather flexible. Accordingly, the N-terminus is not visible but up to 33 residues are expected to fit into the visible part of the density map.
Future experiments will have to validate the overall fold, the handedness of the fibril and the C_2 symmetry.

2 Aβ36

A novel Aβ mutation has been described by our collaboration partners at Uppsala University in Sweden (*not published*). This variant lacks six residues in the central region of Aβ. With a total amount of 36 residues left, it was termed Aβ36. (167)
The goal of this project was to prepare samples for cryo-EM experiments and subsequent reconstruction of this variant. The synthetic sample was provided by Martin Ingelsson and used for several fibrillation approaches (sections 2.1.1 and 2.2) Since Aβ36 did not fibrillate easily, a CD measurement was performed with the support of Rebecca Sternke-Hoffmann to prove the aggregation of Aβ36 (section 2.1.1.2). On-going (cryo-)EM measurements are carried out by Mara Zielinski.

2.1 Purification of synthesized samples and fibril growth

Quality and purity of synthesized samples of the new Uppsala mutant were assessed via RP-HPLC (section X9.1.1.4) while transferring the desired peptide into fibrillation conditions. Figure 46A displays the chromatograms of the provided Aβ species, Aβ34 and Aβ36, which correspond to wildtype Aβ(1-40) and Aβ(1-42) with a deletion of six residues.

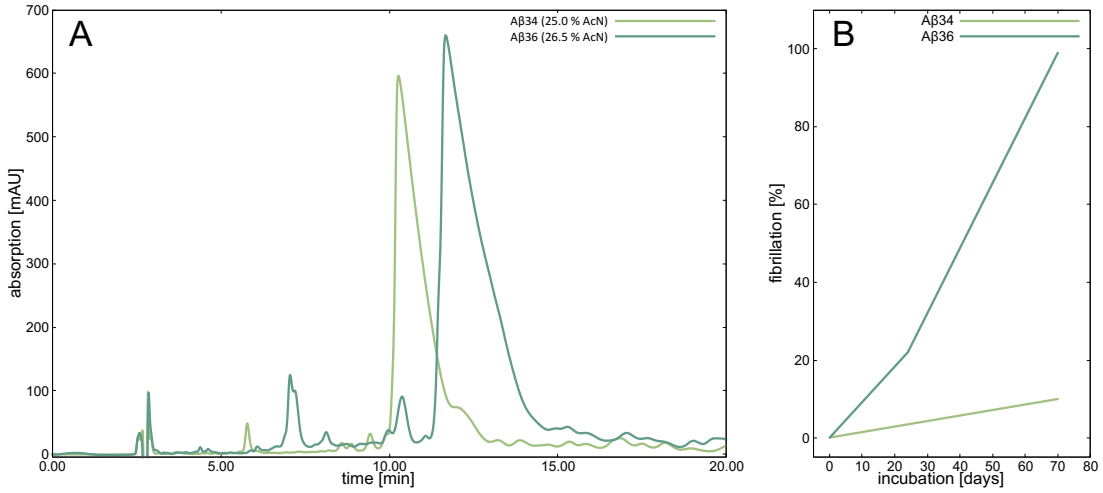

Figure 46: RP-HPLC chromatograms of Aβ34 and Aβ36 species measured at 214 nm and fibrillation curve. (A) Both samples were run isocratic with Aβ34 at 25 % AcN, 0.1 % TFA and Aβ36 at 26.5 % AcN 0.1 % TFA. Aβ34 (light green) shows a main peak at 11 min retention time and minor peaks at 6 and 9 min. Aβ36 (dark green) shows a main peak at 13 min and minor peaks at 8 and 10 min. (B) Concentration of monomeric Aβ was measured after 0, 24 and 70 days (Aβ36) and 0 and 70 days (Aβ34). Percentage of fibrillated material was plotted against incubation duration.

Both peptides show distinct peaks for the main product at 11 (Aβ34) and 13 min (Aβ36) respectively. Nevertheless, minor impurity peaks are visible for both species but could be separated from the product peaks.
Immediately after the RP-HPLC runs, the samples were stored in the elution buffer under dark and quiescent conditions for several days. The fibrillation progress was measured according to section 9.1.2.2 and is displayed for both proteins in Figure 46B. The Aβ36

mutant (dark green) fibrillated much faster compared to the Aβ34 variant. After 70 days the fibrillation was completed for Aβ36 but had only reached 10 % for Aβ34. This result is in agreement with former studies, which show that Aβ(1-40) usually aggregates slower than Aβ(1-42) (19, 289). Accordingly, the six missing residues likely do not alter the overall kinetics of Aβ aggregation.

2.1.1 Aggregation behavior of Aβ36 changes at low temperatures

According to our collaboration partners from the Uppsala University, Aβ36 showed significantly faster aggregation compared to wildtype Aβ(1-42). In order to try and slow down the aggregation process, the idea was to decrease Brownian motion by keeping the sample cold: Aβ36 samples (Table 24, samples 8 and 9) were dissolved in NaP_i buffer on ice and subsequently stored at 6 °C for 24 h. The aggregation of Aβ36 at low temperatures was then assessed via AFM (section 2.1.1.1) and CD spectroscopy (section 2.1.1.2).

2.1.1.1 Pre-cooled Aβ36 adapts to mica surface structure

The samples incubated at 6 °C were prepared for AFM (section X9.2.1.4) and examined under the microscope. Resulting AFM images (B, C) and reference images of the mica surface (A) are displayed in Figure 47.

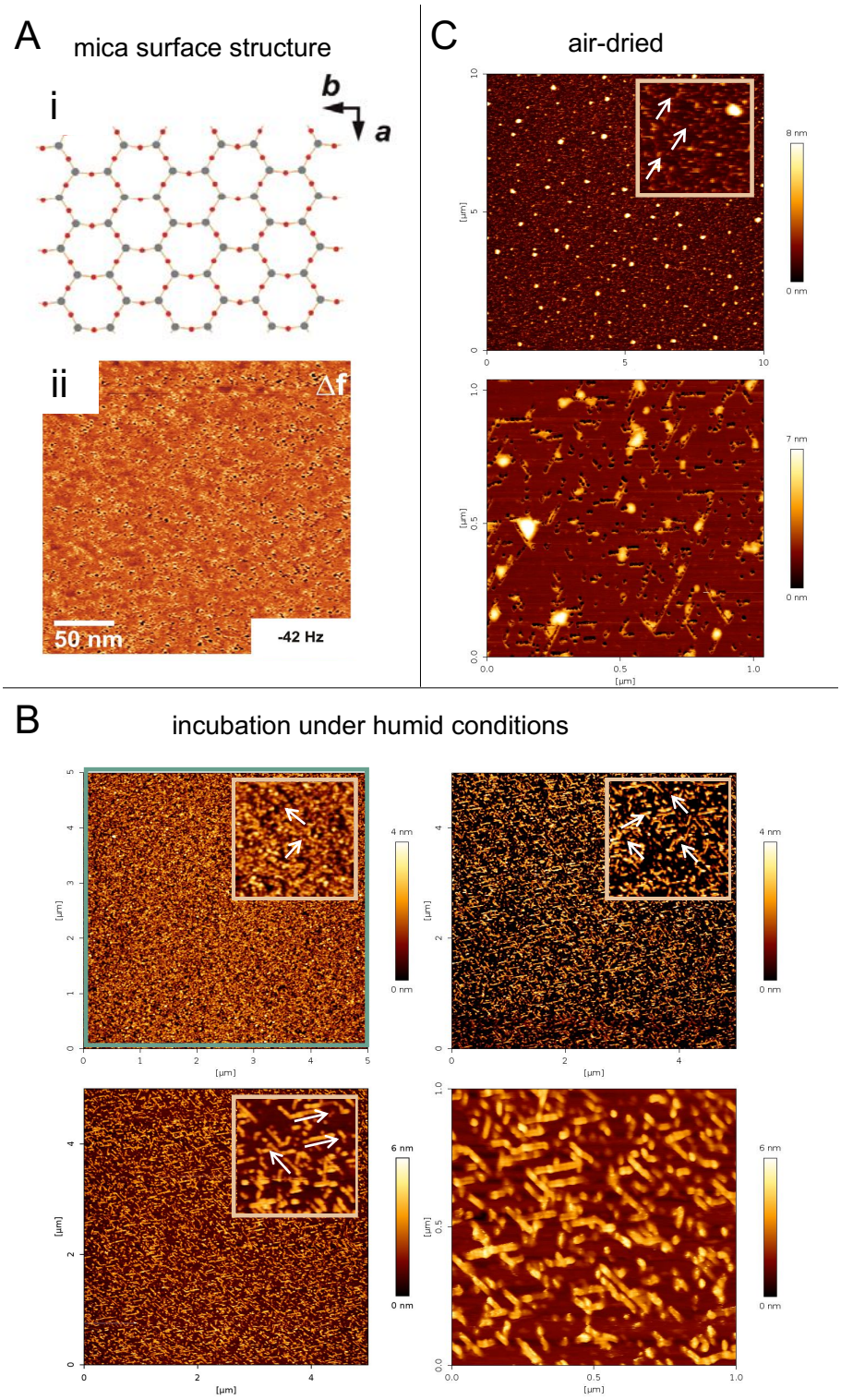

Figure 47: AFM images on pre-cooled Aβ36 after incubation on the mica surface under different conditions. (A) The mica surface structure as sketch (i) and an AFM image of a clean mica surface (ii), taken from Ostendorf et al. (290). (B) Pre-cooled Aβ36 after incubation under humid conditions for 10 – 15 min (green box: 20 µM Aβ36 monomer equivalent (sample 9), rest: 8 µM Aβ36 monomer equivalent (sample 8)). (C) 8 µM Aβ36 monomer equivalent air-dried on the mica surface. Beige boxes are close-ups from the respective image with white arrows highlighting the adjustment of fibrils to the surface.

As displayed, short fibrils in the AFM images exhibit distinct orientations on the surface, independent from their preparation under humid conditions or air-dried (Figure 47B and

C). Since this behavior has also been observed for α-synuclein (291), it is highly likely that aggregation of Aβ36 is suppressed at temperatures around 6 °C and only starts after the sample has been transferred onto the mica surface at room temperature. Under these conditions, fibril growth appears to be highly influenced by the underlying mica structure (see Figure 47A).
To support the hypothesis that aggregation behavior is suppressed at low temperatures, CD spectroscopy was carried out in a following step.

2.1.1.2 Circular dichroism spectroscopy shows aggregation propensity at lower temperatures for Aβ36

CD spectroscopy was performed to verify that Aβ36 does not aggregate at low (< 10 °C) temperatures. The sample that has been examined, was stored in the fridge at 6 °C for several weeks after having been dissolved in 50 mM NaP_i buffer, pH 7.3, to a monomer concentration of 20 mM (see Table 24, sample 9). Since the CD spectrometer could only reach a minimum temperature of 10 °C, the sample has been kept on ice until shortly before the experiment. Results of the CD measurements for a monomer control (orange) and the sample incubated at 6 °C (pink) are displayed in Figure 48.

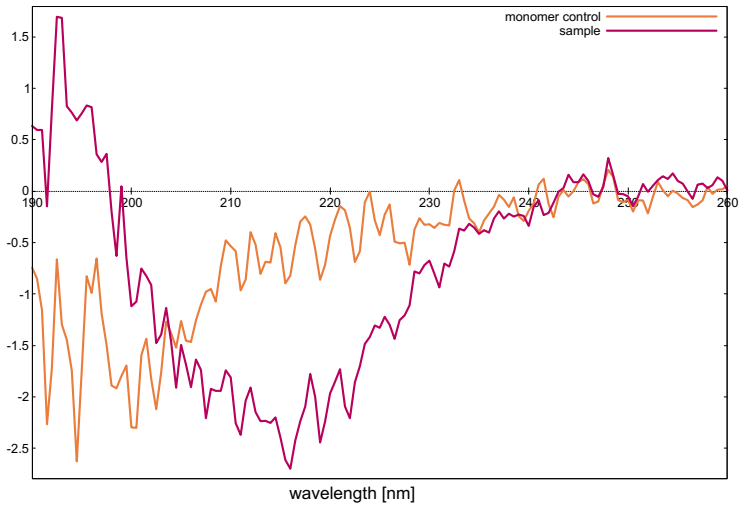

Figure 48: Circular dichroism spectra of Aβ36. The CD spectrum of an incubated Aβ36 sample (pink) and a fresh monomer control (orange) at 10 °C. While the monomer control shows the typical 200 nm minimum for a random coil formation, the sample displays a minimum at 215 nm, typical for β-sheet secondary structures.

The reference-controlled CD spectra show that the freshly dissolved monomer control is in random coil formation (minimum at 200 nm). The Aβ36 sample, which had been incubated at 6 °C for 7 weeks, on the other hand exhibits a β-sheet signal at 215 nm (292). This indicates that Aβ36 does indeed aggregate at low temperatures. However, it does not exclude the conclusion drawn from AFM experiments (2.1.1.1) that aggregation is heavily decreased by temperatures below 10 °C. In order to quantify the extent of aggregation at low (< 10 °C) temperatures compared to higher temperatures (> 20 °C), aggregation experiments should be carried out with Aβ36 at different temperatures. Although ThT

assays are a sophisticated method for monitoring fibrillation (15), the devices lacked the possibility for cooling below 10 °C. And trials to monitor ThT kinetics with a stopped flow device, which can be cooled down to 4 °C, failed (data not shown). However, looking further into this observation will be of interest for our understanding of Aβ aggregation kinetics.

2.2 Aβ36 oligomers form in citrate buffer at different pH values

Knowing that the fibrillation behavior of amyloids is highly dependent on their environment, aggregation across a wide pH range was tested. Lyophilized protein was dissolved in citrate buffer at pH 3 – 7 (section X8.7.2.1). After incubation of the samples for 21 days at room temperature under quiescent conditions, they were examined at the AFM. While pH values 3 – 6 showed globular aggregates or no aggregates at all (appendix XVI3.3, Figure 75), a few fibrils could be observed for pH 7 (Figure 49).

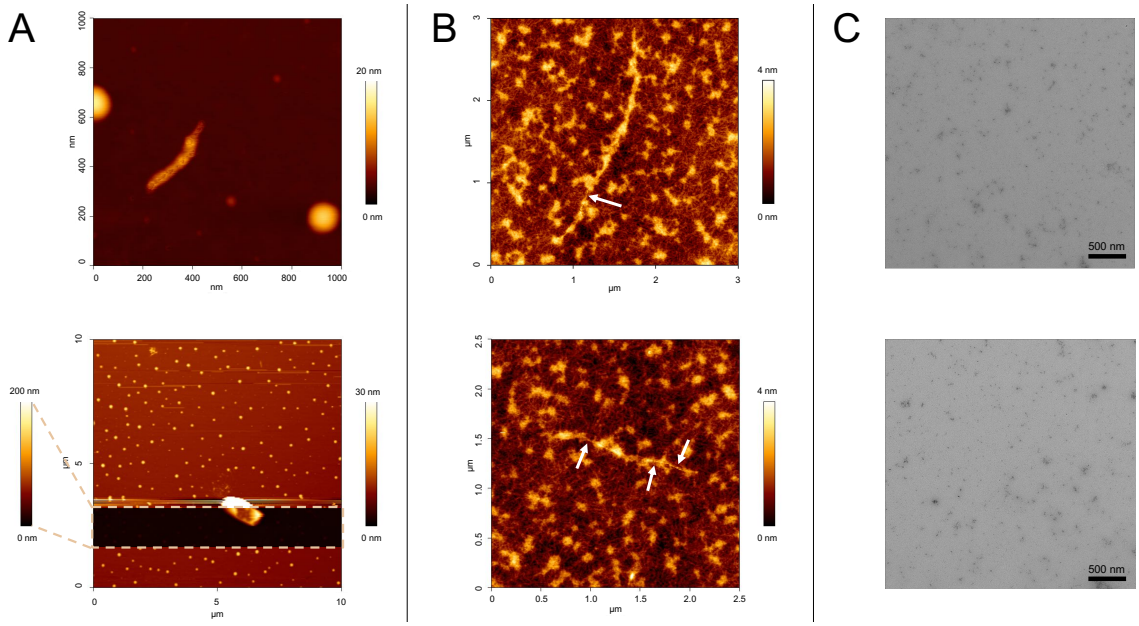

Figure 49: Microscopy images of Aβ36 in citrate buffer at pH 7. (A) AFM images of the sample after 21 days of incubation. The bottom picture shows a partial overlay of one section with two different height profiles. (B) AFM images of the sample after 28 days of incubation. Fibrils are indicated by white arrows. (C) Negative stain EM images after 50 days of incubation.

AFM images of Aβ36 at pH 7 after 21 days showed mainly globular aggregates of up to 30 nm height and up to several nanometers radius (Figure 49A). After 28 days, the same sample began to show fibrillar structures (B, indicated by white arrows). Since it was not clear whether the background in these pictures showed very thin fibrillar aggregates, probably protofibrils, or buffer artifacts, the probe was washed with ddH_2O and dried again. If the background consisted of protofibrils, they would be expected to stick, while buffer artifacts should have been washed away leaving only fibrils. The following measurements showed empty mica surfaces without any (proto-)fibrillar aggregates (data not shown).

Hence, fibrillar aggregates have likely been removed from the surface, including the network which they were part of.

Negative stain EM images (Figure 49B) display only very small globular particles, which could represent oligomeric species. However, no fibrils could be observed with negative stain EM and only few via AFM, leading to the conclusion that fibrillation of Aβ36 under these conditions is not preferred.

This conclusion was verified a year later, when the Aβ36 samples were examined again (Figure 50) and mostly showed oligomeric species.

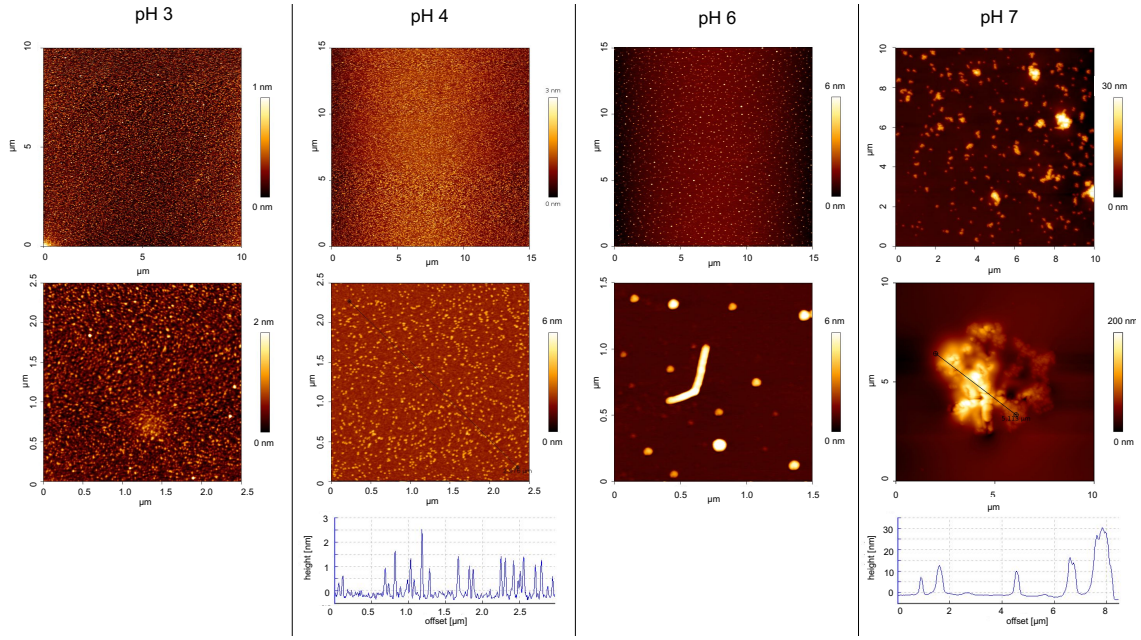

Figure 50: AFM images of Aβ36 in citrate buffer at different pH values. All images were acquired after one year of incubation. The samples show oligomeric species of different sizes. The oligomers at pH 4 are the most homogeneous with an average diameter of 1.5 nm (see height profile). Only the sample at pH 6 displayed one fibrillar species. At pH 7, Aβ36 also showed large globular aggregates with heights of up to 200 nm. Height profiles and their respective cross-sections are indicated by a black line in the respective image.

At pH 3, the sample displayed a lot of small but inhomogeneous oligomers. Contrary, Aβ36 at pH 4 displayed homogeneous oligomers with an average diameter of 1.5 nm. The sample at pH 6 was the only one in which a fibrillar species could be observed. Nevertheless, the majority of this sample was composed of oligomers. At pH 7, Aβ36 grew into larger oligomeric aggregates with up to 200 nm height. After one year, no more fibrillar aggregates could be observed in the sample. Hence, citrate buffer of different pH values results in Aβ36 following the off-pathway and aggregate into oligomers that do not evolve further into fibrils, the number of which would be expected to have increased significantly after one year incubation.

2.3 Aβ36 fibrils are promising candidates for structural investigations

Aβ36 fibrils from ~300 µM monomer equivalent in pH 2 (sample 1, Table 24) incubated for nine months in HPLC buffer were first examined by AFM (Figure 51) followed by negative stain EM (Figure 52A) and cryo-EM (Figure 52B).

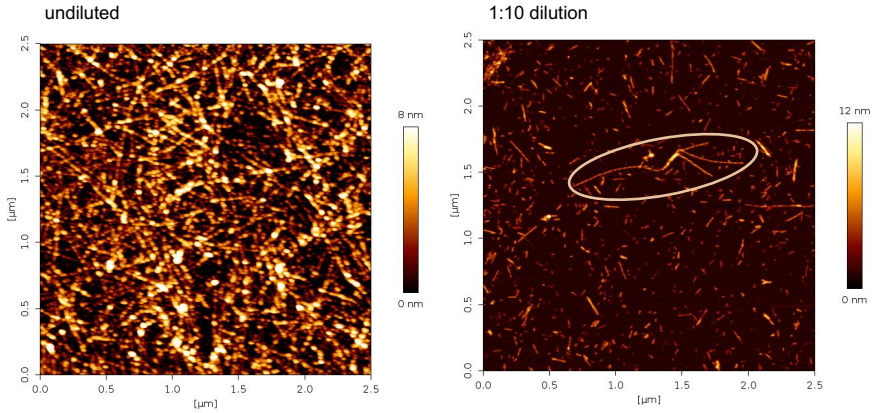

Figure 51: AFM images of Aβ36 in 30 % AcN, 0.1 % TFA. Undiluted (left) and diluted (1:10, right) samples were imaged at the AFM and revealed high fibril concentration. The fibrils show a regular twist (encircled).

AFM images of an undiluted Aβ36 sample and a 1:10 dilution were taken. The undiluted sample (Figure 51, left) showed a high fibril density. Although the fibril load is so high that single fibrils can hardly be distinguished from the network, it can still be observed that these fibrils are twisted.

The diluted sample (Figure 51, right) revealed mostly short fibrils of a few 100 nm. Since hole sizes of a cryo-EM grid are usually around 1.2 µm, fibrils of this length are suitable for cryo-EM experiments. Again, fibrils exhibit regular twists (encircled).

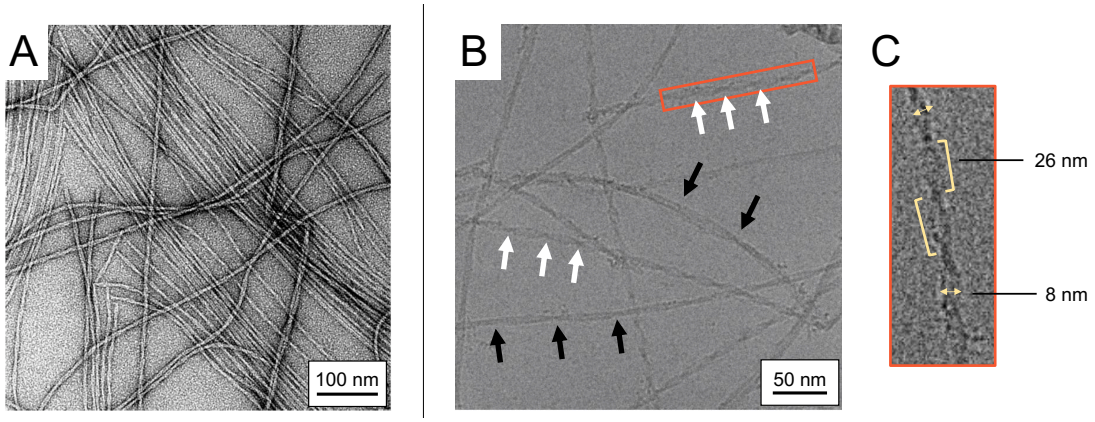

Figure 52: Negative stain and cryo-EM micrographs of Aβ36. (A) Representative negative stain micrograph displaying high fibril density. (B) Representative cryo-EM micrograph with different polymorphs highlighted (short twist: white arrows, wider twist: black arrows). (C) Close-up of a fibril from image (B) showing crossover distance and width of the short twisted polymorph. (Data acquired and provided by Mara Zielinski)

Figure 52 displays representative micrographs from negative stain EM and cryo-EM experiments. As for AFM, negative stain data (Figure 52A) also show a high fibril

concentration. Although fibril twist is easier to observe in AFM images, there are some fibrils exhibiting a clear, regular pitch also in negative stain EM. Due to the high quality of the sample proven by AFM and negative stain EM, a data set on an Arctica microscope (200 kV) was acquired. A representative micrograph of this data set is displayed in Figure 52B. Fibrils in this image show different twists (black and white arrows). Hence, at least two different polymorphs are present in this data set. The dominant polymorph (close-up in red frame) exhibits a rather small twist (white arrows) with a fibril width of 8 nm and a crossover distance of 26 nm. The resulting pitch of 52 nm is therefore significantly smaller compared to wildtype Aβ(1-42) with a pitch around 115 nm (181) and what is the expected pitch of pGlu-Aβ(3-42) with 100 nm (section 1.4).

3 Aβ(1-42)-pS8

In collaboration with Jochen Walter and Sathish Kumar (AG Molekulare Neurologie, Uniklinikum Bonn), fibrillation and EM experiments on phosphorylated Aβ species were performed. The collaborators provided vials containing 1 mg of the Aβ species listed in Table 3.

Table 3: List of Aβ species provided by Uniklinikum Bonn.

	modification	**mass**
Aβ(1-40)	/	2x 1 mg
Aβ(1-42)	/	2x 1mg
Aβ(1-40)-pS8	Phosphorylation at serine 8	2x 1mg
Aβ(1-40)-pS26	Phosphorylation at serine 26	2x 1mg
Aβ(1-42)-pS8	Phosphorylation at serine 8	2x 1mg

3.1 Purification of synthesized samples

Quality and purity of synthesized samples (see Table 3) were assessed via RP-HPLC (section X9.1.1.4) while transferring the desired peptide into fibrillation conditions. Figure 53 displays the chromatograms of all Aβ species provided. For Aβ(1-40) and phosphorylated variants (Figure 53a), all chromatograms show a peak at 10 min, which according to the profile of Aβ(1-40), represents the wildtype protein. Hence, it can be concluded that the phosphorylation of Aβ(1-40)-pS26 and Aβ(1-40)-pS8 has only been successful to a certain degree and unphosphorylated or fragmented species, as seen for pGluAβ(3-42) (section 1.3) are present in the sample.

Aβ(1-40)-pS8 does not show one distinct main peak but rather a double peak at 10 min (Aβ(1-40)) and 10.5 min. The latter peak is more likely to represent Aβ(1-40)-pS8 due to its height, since the main product is expected to yield the highest amount of peptide. In the case of Aβ(1-40)-pS26 there is a second peak at 7.5 min in addition to the Aβ(1-40) peak around 10 min. Additionally, all chromatograms show minor peaks around 5 min which in accordance with former experiments are expected to contain insignificant amounts of methylated or fragmented Aβ species (see section 1.3).

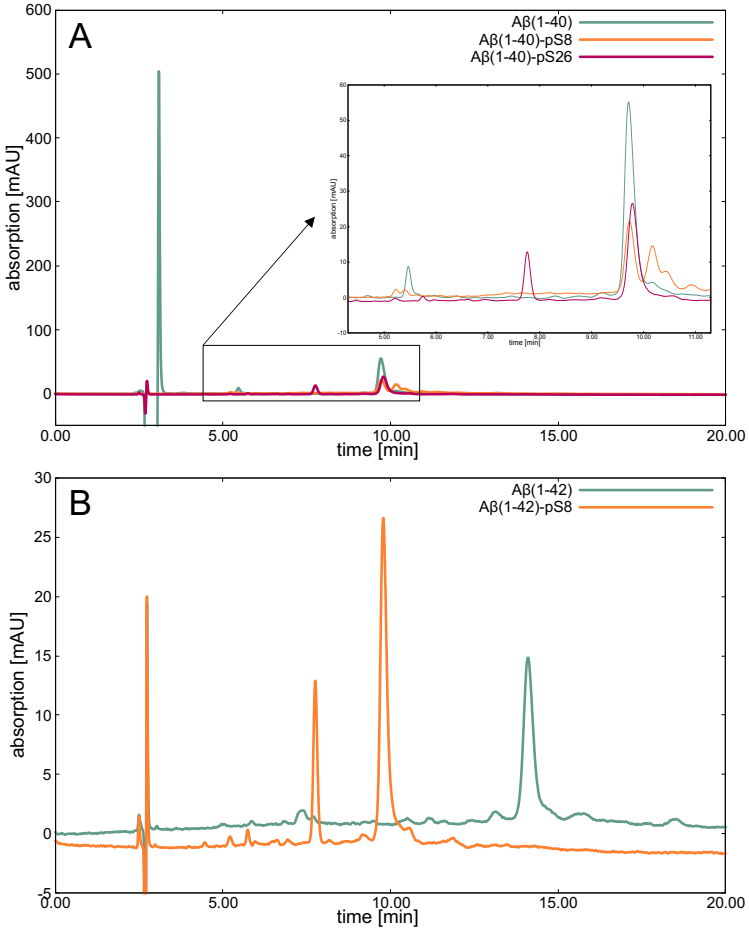

Figure 53: RP-HPLC chromatograms of phosphorylated Aβ(1-40) and Aβ(1-42) and wildtype species at 214 nm. Of each sample 10 µL of peptide in solution was loaded onto the column. (A) Profiles of Aβ(1-40) (green), Aβ(1-40)-pS8 (orange) and Aβ(1-40)-pS26 (red). (a, inlet) Close-up of the product peaks between 5 and 12 min. (B) Profiles of Aβ(1-42) (green) and Aβ(1-42)-pS8 (orange).

In the case of Aβ(1-42), the wildtype appears in the chromatogram in a distinct main peak around 14 min (Figure 53b). The profile of Aβ(1-42)-pS8 on the other hand shows two main peaks at 7 and 10 min. In addition to the height of the second peak, impurities for Aβ are expected to arise around 7 min and also the Aβ(1-42) chromatogram shows a minor peak at this point. Hence, it is likely that Aβ(1-42)-pS8 elutes after a retention time of 10 min. Taken together, after separation of phosphorylated Aβ species from the samples at hand, a significant loss of material due to impurities and incomplete phosphorylation had to be accepted.

3.2 Aβ species form fibrils when phosphorylated at serine 8 but not serine 26

Synthetic samples of Aβ(1-40) and Aβ(1-42) wildtype as well as phosphorylated species Aβ(1-40)-pS8, Aβ(1-40)-pS26 and Aβ(1-42)-pS8 were kindly provided by Jochen Walter and Sathish Kumar. All samples were prepared by purification via RP-HPLC and subsequent fibrillation under quiescent conditions at pH 2 (see sections X9.1.1.4 and X9.1.1.5).

Fibrillation was verified by AFM (section X9.2.1.2) and is displayed in Figure 54. Fibrils have evolved in all samples with the exception of Aβ(1-40)-pS26 (Figure 54, middle left). Regarding the wildtype fibrils, Aβ(1-40) (bottom left) shows a higher fibril density compared to Aβ(1-42) (top left) with the former also displaying clearly twisted fibrils. Aβ(1-40)-pS8 fibrils were evenly distributed across the sample and show a clear twist, too. Slight blurring of the images is caused by the stickiness of the respective sample. Aβ(1-42)-pS8 samples were observed as thick fibril bundles (top, middle) as well as evenly distributed fibrils (top right) mostly without any visible twist. All Aβ(1-42) and the Aβ(1-40) wildtype fibrils were rather long with lengths of up to 10 µm.

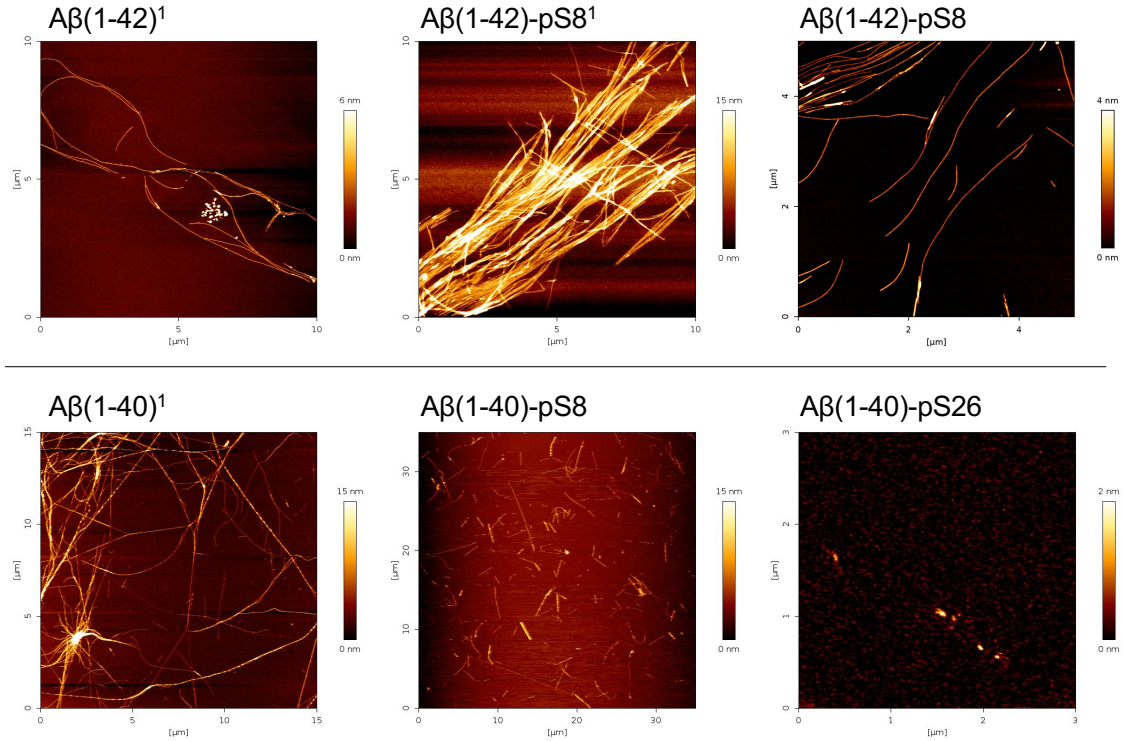

Figure 54: AFM images of synthetic Aβ(1-40) and Aβ(1-42) wildtypes and phosphorylated variants. AFM measurements were performed after one or three[1] months of fibrillation. Samples were prepared by drying of 10 µL undiluted sample on a mica slide. Images scale from 3 – 35 µm with normalized height bars between 4 – 15 nm.

With the exception of Aβ(1-40)-pS26, samples of phosphorylated Aβ(1-40) and Aβ(1-42) were suitable for cryo-EM experiments according to AFM images. Aβ(1-40)-pS26 was identified in a mouse model to form off-pathway oligomers (176, 293), hence the lack of fibrils in this sample was expected. Nevertheless, these experiments considered brain material and *in vitro* material at pH 7.4. Accordingly, aggregation behavior at pH 2 could have been different.

The sample, which was of highest interest for the collaborators, was Aβ(1-42)-pS8. Accordingly, it has been examined extensively via cryo-EM. However, measurements on this sample turned out to be rather difficult. Especially the concentration on the grid often was too low. Possibly, a lot of material was lost during the blotting step of grid preparation due

to the average length of an Aβ(1-42)-pS8 fibril. More precisely, one fibril sticking to the blotting paper might be attached to a whole network of fibrils and therefore will remove a lot of material from the grid. Contrary, shorter fibrils should not form networks of this size and therefore more fibril material should stick to the grid after blotting.
In order to verify this bottle neck and avoid it in future measurements, increasing the local fibril concentration by decreasing fibril length was attempted as described in section 3.3.

3.3 Increasing the fibril load of Aβ(1-42)-pS8

Cryo-EM measurements have shown that equal distribution of fibrils and high sample volume is a regularly occurring problem on proper data set acquisition. In order to enhance the distribution of sample across the grid while at the same time increasing sample concentration locally, centrifugation and sonication experiments were performed with Aβ(1-42)-pS8.

3.3.1 Centrifugation of Aβ(1-42)-pS8

A centrifuged sample of Aβ(1-42)-pS8 was examined regarding the question whether centrifugation would lead to a local increase in fibril concentration within the reaction tube. For this, negative-stain-EM grids were prepared from droplets taken from either the top or bottom liquid layer of the centrifuged sample. Figure 55 shows the resulting negative-stain-EM micrographs from this experiment.

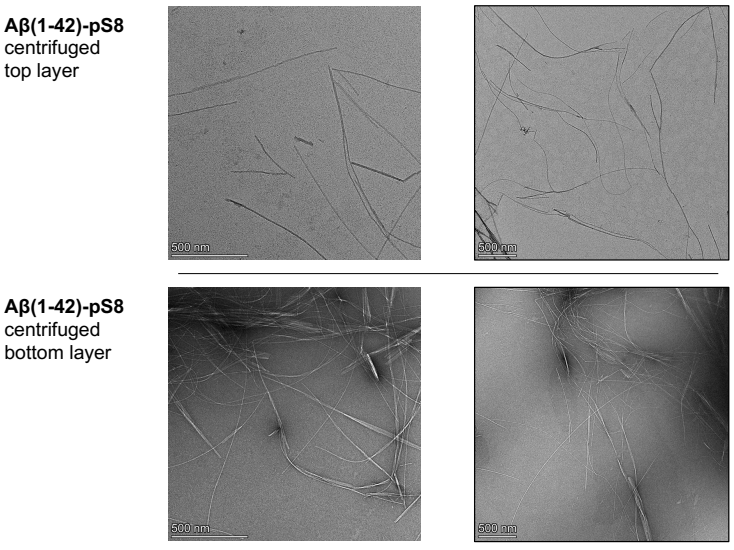

Figure 55: Negative stain electron microscopy on Aβ(1-42)-pS8 after centrifugation. Representative negative stain micrographs acquired on a Talos 120. Samples were either centrifuged for 10 min at 16,000 *g* and taken either from the top or bottom liquid layer. Magnification: right: 17,300x, left: 35,500x.

There is no major difference between the top and bottom layer of a centrifuged Aβ(1-42)-pS8 sample in regard to fibril concentration. The top layer contains slightly less fibrils which are evenly distributed. The fibrils in the bottom layer, which are slightly higher

concentrated than the top layer fibrils, seem to be stuck together. Either fibrils that stick together already existed in the sample, or the fibrils started clumping due to the centrifugation step. In the former case, the fibrils would have ended up in the bottom layer after centrifugation due to their higher density.
Nevertheless, centrifugation for 10 min and 16,000 *g* does not seem to increase the sample concentration significantly. Similarly, centrifugation for 30 and 60 min did not result in sufficient fibril density (see appendix XVI3.4, Figure 76). Since the possibility of inducing formation of fibril bundles cannot be excluded, intensifying centrifugation of fibrils prior to EM experiments has not been pursued any further.

3.3.2 Sonication of Aβ(1-42)-pS8

Aβ(1-42)-pS8 samples were sonicated at amplitudes of 40, 50, 60, 70, 80 and 90 % (X9.6.4), and examined under the electron microscope. Representative micrographs of samples at 40, 60 and 80 % are displayed in Figure 56.

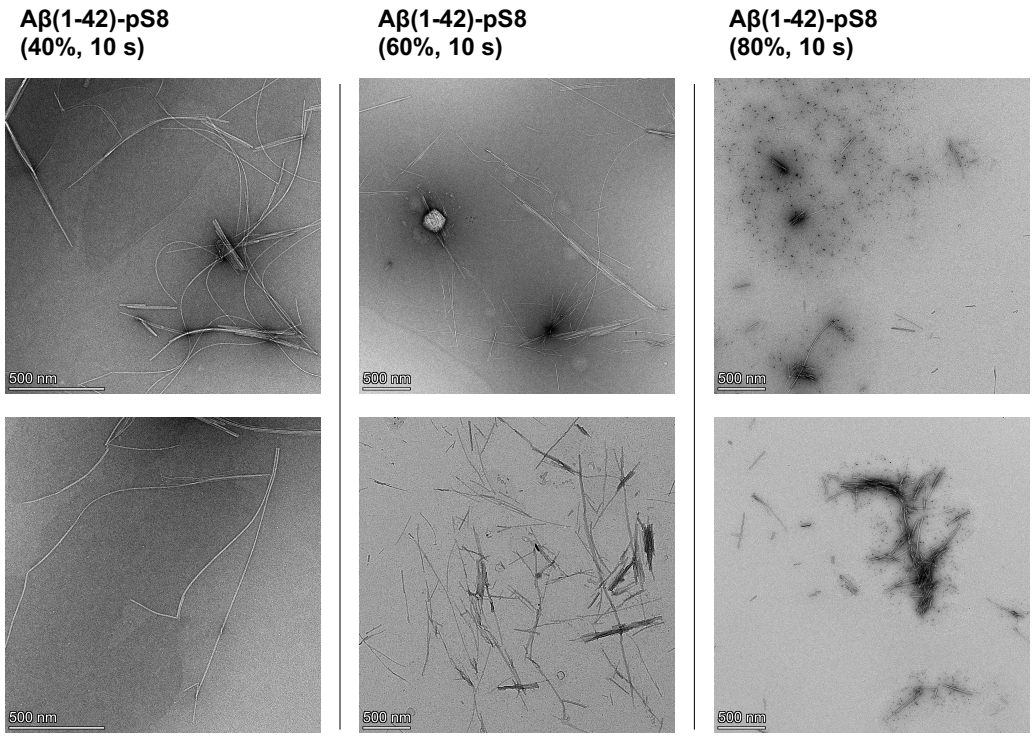

Figure 56: Negative stain electron microscopy on Aβ(1-42)-pS8 after sonication. Representative negative stain micrographs acquired on a Talos 120. Samples were sonicated for 10 s and 40 – 90 % amplitude in a VialTweeter. Exemplary images have been taken from sonication at 40, 60 and 80 % amplitude. Images were acquired at 17,300x (60 %, 80 %) or 35,500x (40 %) magnification.

When being sonicated at 80 % amplitude or higher (Figure 56, right), Aβ(1-42)-pS8 seems to start degrading. Micrographs acquired under this condition show a high amount of impurity consisting of a dark background with small, black dots that likely represent small fibril parts. These fibril parts could either be detached oligomers or heterogenous fibril

fragments. Since single Aβ(1-42)-pS8 monomers would not be observable at this magnification, it can be excluded that the dots represent monomers.

On the contrary, sonication at only 40 % does not seem to have any impact on the fibril sample. Here, the sample still consists of relatively long (>2 µm) fibrils with uneven distribution. However, one of the micrographs (Figure 56, top left) shows fibrils that occur in bundles. In-between bundles, the staining solution can accumulate, which results in bundle centers appearing darker.

The most promising results were gained at an amplitude of 60 % (Figure 56, middle) where an even distribution of smaller fibrils (0.5 – 1 µm) could be observed. Again, these fibrils showed the tendency to bundle. Moreover, shorter fragments that might not be well suitable for reconstruction, can be observed as well. Additionally, the fragments of 60 % amplitude exhibit very straight fibrils (Figure 56, middle bottom) in comparison to the curved fibrils at 40 % amplitude. Nevertheless, sonication at 60 % amplitude has been repeated and combined with the centrifugation approach described above, which resulted again in a non-suitable distribution of fibril fragments (see appendix XVI3.4, Figure 77). Taken together, sonication easily disrupts and degrades amyloid fibrils of Aβ(1-42)-pS8 or shows only limited effects on total fibril concentration on the grid. Accordingly, none of these samples were further analyzed by cryo-EM.

4 Aβ(1-42) point mutants A21G, E22G, E22K, D23N

A protocol for cloning of Aβ(1-42) with fusion construct in *E. coli* cells has been established and shared with us by the Isoloid GmbH (Düsseldorf, Germany). According to this protocol, Aβ(1-42) point mutants A21G, E22G, EE2K and D23N that are located in a mutation "hot spot" region of Aβ(1-42) were cloned (X7.2). The respective plasmids were generously provided by Isoloid.

Agarose gels of isolated plasmid DNA after PCR are displayed in Figure 57.

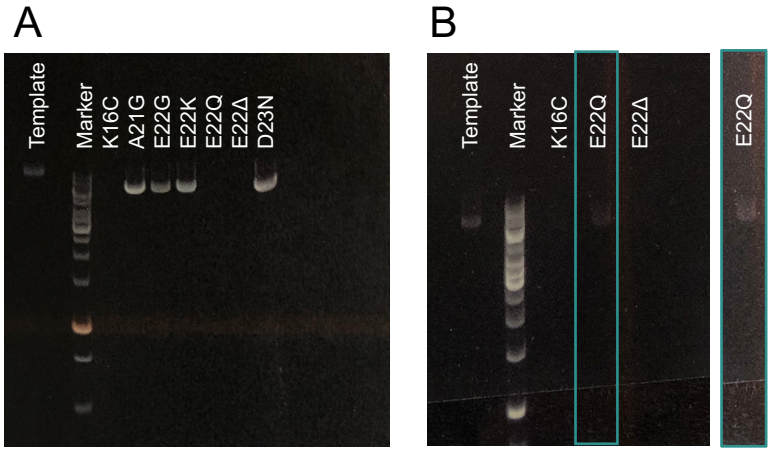

Figure 57: Agarose gels of Aβ(1-42) point mutants after PCR. (A) After the first cloning attempt, mutants A21G, E22G, E22K and D23N showed DNA bands on the agarose gel. K16C (sample of Elke Reinartz), E22Q and E22Δ did not show a DNA band. (B) After a second attempt to clone Aβ(1-42) mutants, a slight DNA band is visible for E22Q (green box, E22Q lane with changed contrast to increase visibility of the band).

Except for E22Δ, all point mutants were successfully cloned. Due to a primer error, E22Δ did not show the desired deletion. It was later successfully cloned by Robin Backer (data not shown). Following the cloning, heterologous expression of the point mutants A21G, E22G, E22K and D23N was tested and verified in *E. Coli Bl21 (DE3)* cells in LB-medium (section X8.3.1) as shown in Figure 58.

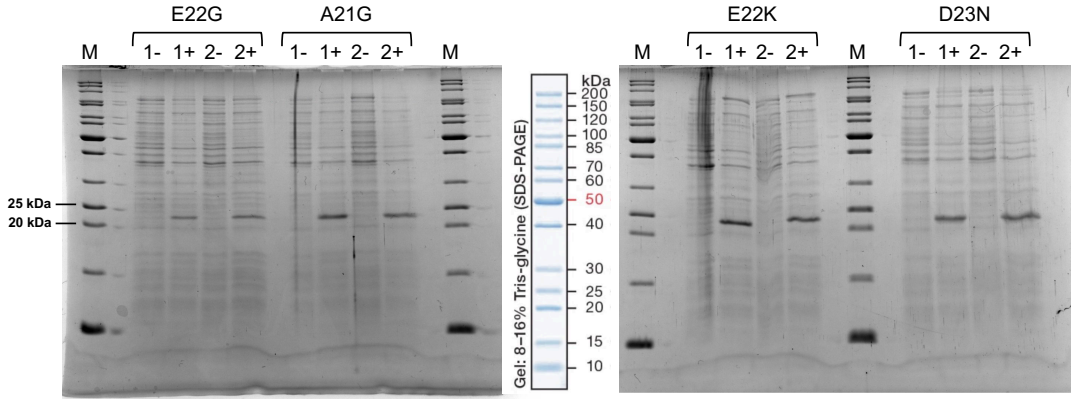

Figure 58: Glycine gel of point mutant test expression. Test expression results of point mutants Aβ(1-42)-E22G, -A21G (left) and Aβ(1-42)-E22K, -D23N (right) visualized on an SDS-gel. Of each mutant, two clones exist ("1" and "2") of which two test cultures were prepared each. For every mutant one test culture was induced with IPTG ("+") and one negative control was not induced ("-"). Samples of all test cultures were loaded onto the gel. All induced cultures ("+") show protein band between 20 and 25 kDa with the expected site of the target proteins being 19 kDa. In the middle, the marker (M in the SDS-gels) PageRuler unstained protein ladder is shown (294).

The figure displays two SDS-gels with samples from test expressions of all mutants “without induction” (-) and “with induction” (+). In induced samples (+) the gels clearly show a protein band between 20 and 25 kDa which fits the expected size of Aβ(1-42) with the fusion construct. Cloning and test expressions of mutant Aβ(1-42)-E22G, -A21G, -E22K and -D23N therefore was successful. Going forward, the expression and purification of these mutants will be an important step towards the better understanding of FAD cases. Recombinant Aβ might be used for studies of aggregation kinetics, cell toxicity assays and structural studies, which will give further insights into the characteristics of FAD.

VI Structural similarities between IAPP and Aβ(1-42) fibrils

1 Publication II: Cryo-EM structure of islet amyloid polypeptide fibrils reveals similarities with amyloid-β fibrils

In collaboration with the group of Wolfgang Hoyer, we examined the amyloid fibril form of islet amyloid polypeptide (IAPP) via AFM and cryo-EM, and were able to solve the structure of the main polymorph at pH 6.0. Moreover, we were able to reconstruct density maps of two further polymorphs. On one of these model fitting with DireX (295) was performed to propose an atomic model.
The resulting article has been published in *Nature Structural & Molecular Biology* in 2020 (70). I summarized the article below and both the article and its supplemental information can be found in the appendix Publication II: Cryo-EM structure of islet amyloid polypeptide fibrils reveals similarities with amyloid-β fibrils.

1.1 Summary

IAPP is a short peptide linked to type II diabetes (T2D). It is found aggregated in the pancreatic islets and associated with β-cell loss. Several studies suggest a molecular link between IAPP from T2D and Aβ from AD. In this paper, the atomic structure of one IAPP polymorph, which has been solved by cryo-EM, is presented. The cryo-EM density of the main polymorph reached a resolution of 4.2 Å, which was sufficient to fit 25 out of 37 residues into the map. The first 12 residues could not be resolved due to high flexibility in the N-terminus. Nevertheless, the amidated C-terminus is clearly visible and involved in stabilizing the fibril's interface. Interestingly, the fold of this polymorph at physiological pH shows similarities with the "S-fold" that has been observed in Aβ fibrils. This common feature is in support of studies describing a cross-seeding ability of IAPP and Aβ. Moreover, the "S-fold" could be linked structurally to known mutations in IAPP (S20G) and Aβ (E22G). In addition to the main polymorph, densities of two further polymorphs are described qualitatively.

1.2 Contribution

For this work, I performed image processing and reconstruction as well as model building and refinement for polymorph I. Additionally, I participated in writing the manuscript, preparing figures and discussing the results with my co-authors. I am a shared first author of this paper.

IX Conclusion and outlook

Amyloids are ubiquitously found proteins that often result in pathogenicity. Although the number of studies and knowledge about these proteins are continuously growing, there is still a lack of understanding regarding the pathways amyloids undergo, the kinetics of their formation and the reasons for their (dys-)functionality. By determining the structures of various amyloidogenic proteins, especially disease-related amyloids that are a pressing issue for today's society, we support the understanding of the beforementioned aspects, the development of drug candidates and finding of interaction partners. Although amyloid fibrils, which exhibit the distinct cross-β signal, are macroscopically similar with several nanometers in width and micrometers in length, studies in recent years confirm that on the microscopical level they open up into a variety of different folds. This realization increased the number of questions in regard to amyloid formation in general and in the medical field specifically. It is yet to understand whether the pluralistic forms of polymorphism occur due to environmental conditions exclusively or if certain amyloid folds are pathology-specific or even individual. Accordingly, this work is supposed to offer new insights into the wide landscape of amyloid fibril polymorphism and the various factors favoring it.

IDPs, which are strongly connected to amyloid formation, are suspected to have played an important role in the evolution of life (296). Accordingly, understanding why IDPs aggregate into functional or pathologic assemblies, might also shed some light on the origin of live. By solving the structure of the SH3 amyloid fibril model system, we could increase the understanding of its folding kinetics and thereby expanded the knowledge of fibril formation mechanisms. This fundamental work will support the full comprehension of amyloid folding dynamics and thus will influence the field of amyloid research.

IAPP with its implication in T2D and its molecular link to Aβ is an important research target for researchers from both fields. Hence, by solving the structure of human IAPP at physiological pH, we presented the first IAPP fibril structure alongside with two other groups (69, 186), and therefore took a step closer to the understanding of T2D. Additionally, the findings support the structural link of IAPP to Aβ by displaying similarities in the S-fold. Moreover, the description of the third IAPP polymorph, which likely consists of two IAPP polymorph I fibrils, opens the door to look further into secondary nucleation since the existence of a second interface facing outward of a fibril might be the basis for this mechanism.

The successful cloning of four familial mutants of AD in this study, will allow the recombinant expression of these peptides. By moving forward with this project, new fibrillation conditions should be examined that are closer to *in vivo* conditions, which have been shown to have an immense effect on the aggregation behavior of amyloidogenic proteins (297). A first step towards this goal would be to shift the fibril growth to physiological pH. From there, other co-factors could be added and their effects analyzed by means of kinetic assays or imaging.

The work on Aβ36 revealed that fibril growth could be decelerated by incubation at low temperatures. Experiments with Aβ36 at pH values 3 – 7 showed that it is prone to

oligomerization in citrate buffer. Hence, for examination of Aβ36 fibrils at physiological pH, different buffer systems will have to be tested. Additionally, it was shown that fibril assembly of the monomeric mutant can be influenced by the underlying material, as seen for mica, which so far had only been observed for α-synuclein.

During this work, Aβ36 fibrils have been prepared at pH 2 for cryo-EM experiments. With this promising start into the collaborative project, we would like to look into the possibility of extracting Aβ36 directly from patient brain and examining the *ex vivo* material by cryo-EM. Recent publications have shown that *ex vivo* structures tend to differ from *in vitro* material (190, 298). Hence, future projects will focus on *ex vivo* material on the one hand, and a better of understanding of how solution conditions impact fibrillation on the other hand.

Although it is agreed upon that PTMs affect the fibrillation of amyloids, there is a lack of structural insights in regard to modified Aβ variants. Hence, the successful growth, purification and preparation of pGlu-Aβ(3-42) for cryo-EM experiments support the efforts to close this knowledge gap. Examination of pGlu-Aβ(3-42) data revealed at least three distinct polymorphs of which one did not exhibit any twist. The main polymorph was reconstructed to a resolution of ~4 Å. When reaching higher resolution, the cross-section is expected to reveal similarities with the LS-fold of Aβ(1-42) and the S-fold of IAPP. In the future, this project can reveal structural information on the remaining polymorphs. Eventually, we will be able to solve structures of untwisted fibrils as described here for SH3 and pGlu-Aβ(3-42), which in turn will enhance our knowledge about an amyloid species that has lacked attention so far.

For phosphorylated Aβ(1-40) and Aβ(1-42) species it was shown that they form into fibrils at pH 2 when phosphorylated at serine 8 but not with a phosphorylation at serine 26. The resulting fibrils are suitable for cryo-EM experiments, as verified via AFM. However, they turned out to be challenging when attempting to reach high concentrations on the cryo-EM grid. In an attempt to overcome this problem, sonication of Aβ fibrils was shown to lead to shorter fragments, which are not necessarily well-suited for cryo-EM. In the future, finding ways to grow shorter fibrils from the beginning or improving the sonication conditions may lead to better suited samples. Additionally, the possibility of aligning long fibrils on a grid such that they would not build fibril networks would facilitate the picking and reconstruction process of these samples.

Taken together, this work reveals structural insights into three amyloidogenic systems, SH3, IAPP and pGlu-Aβ(3-42) and sets the basis for future projects on structural investigations on Aβ mutants and variants via cryo-EM. Accordingly, this work contributes to the field of amyloid research as it broadens the knowledge about fibril formation on the atomic level.

In the future, the question whether certain amyloid folds are pathology-specific and therefore are powerful biomarkers in the diagnosis of diseases, will have to be answered. As recent studies have mostly examined amyloid fibrils from a limited number of patients,

broader studies are needed that specifically look into pathology-specificity and have access to a high number of patient material to map the number of polymorphs. Simultaneously, the structure determination of amyloid fibrils will have to be accelerated. Automation of cryo-EM and -ET is expected to be the next big leap in the technical development and will allow for higher throughput in measurements. Nevertheless, sample preparation, especially when talking about *ex vivo* material, will remain a potential bottleneck, which has to be overcome by establishing suitable protocols for extraction of amyloid fibrils from patient material. Establishment of these protocols could help to understand the influence of post-translational modifications and co-factors on amyloid fibrils. While post-translational modifications are important for our perception of disease-related amyloids, the understanding how co-factors influence the formation of amyloid might allow us to control their formation. This in turn would open up the opportunity to influence their functionality and potentially use amyloidogenic proteins as biomaterials.

Cryo-ET will become more important when trying to gain further insights into amyloids in their cellular environment. Examination of cells with cryo-ET might reveal interaction partners of amyloid fibrils and co-aggregating factors in amyloid plaques. On a more mechanistic level, cryo-ET might be better suitable to investigate secondary nucleation in amyloids as it allows for examination of irregular and heterogenous aggregates, which also encompasses oligomers. Additionally, cryo-ET might show advantages over classical cryo-EM for solving structures of untwisted fibrils since reconstruction in cryo-EM is based on helical attributes.

The last five years have demonstrated the power of cryo-EM as a technique in supporting the understanding of amyloid structures on the atomic level. Moreover, we start to realize the diversity of the folding landscape of amyloids, which going forward will be assessed and understood in more detail. It is to be expected that in the following years the recent findings and ideas will be utilized to advance both cryo-EM as a technique and the field of amyloid research.

X Material and methods for amyloid-β and its variants

1 List of devices

The devices that have been used for this work are listed in Table 4. Microscope details are listed separately in Table 5.

Table 4: Devices

Device	Model	Manufacturer
Autoclave	VX-150	Systec
CD spectrometer	J-815	JASCO
Centrifuge (JLA-10.500 rotor)	Avanti J-26 XP	Beckman Coulter
Chromatography system	Prime plus	Äkta
Clean bench	HERA safe, KS 15	Thermo Electron LED GmbH
Drying cabinet (for glassware)	HeraTherm (50 °C)	Thermo Scientific
Gel chamber	Mini-Protean System incl. Tetra vertical system and power supply	Bio-Rad, CA
Gel documentation	ChemiDoc MP	Bio-Rad, CA
Glow discharge cleaning system	easiGlow	Pelco
Heating block	Ori-Block OB3	Techne
Heating cabinet (for glassware)	T5050 (60 °C)	Heraeus
High performance liquid chromatography system	1260 / 1290 Infinity Series	Agilent Technologies, CA
Incubation shaker	Multitron Standard	Infors HT
Incubator	INB200	Memmert
Lyophilizer	LT-105	Christ, GER
Microfluidics system	Flow Mk-1 (prototype)	Cambridge Analytica
Minifuge	ROTILAB	Roth
PCR Thermocycler	Mastercycler-ep	Eppendorf
pH meter	Basic Meter PB-11	Sartorius
Photometer	OD600 DiluPhotometer	Implen
Plasma cleaner	Zepto	diener electronic
Plunge freezing device	Vitrobot	Thermo Fisher Scientific
Scales	Extend, BP 4100 S	Sartorius
Shaker	N/A	GFL
Sonicator	Sonopuls incl. UW3200 holder	Bandelin
Spectrophotometer	Nanodrop 2000	Thermo Fisher Scientific
Vacuum Concentrator	SpeedVac RVC 2-18	Christ, GER
Table top centrifuges	5415R, 5804R	Eppendorf
Thermomixer	comfort, compact	Eppendorf
Ultra-centrifuge (Ti70, 55.2 rotor)	Optimax XPN-80	Beckman Coulter
Ultrapure water system	Q-Pod, Elix, 60 L tank	Merck Millipore
Ultrasound bath	Sonorex RK100H	Bandelin
VialTweeter	Vialtweeter incl. UP200St	Hielscher
Vibration isolator table	halcyonics_i4	Accurion
Vortex mixer	N/A	VWR

1.1 List of microscopes

Table 5: Microscopes

Application	Microscope	Manufacturer	Camera	Manufacturer
Atomic force microscopy	NanoWizard 3	JPK instruments		Navitar
Cryo-electron microscopy	Tecnai Arctica	FEI	Falcon 3	FEI
Cryo-electron microscopy	Titan Krios	FEI	K3	FEI
Electron microscopy	Talos 120	Thermo Fisher Scientific	Ceta CMOS	Thermo Fisher Scientific

1.2 List of computer programs

Program	Version	Source
Agilent ChemStation Method and Run Control	N/A	Agilent Technology
Agilent ChemStation Data Analysis	N/A	Agilent Technology
CHEP	N/A	Schroderlab.org (299)
Chimera	N/A	UCSF (300)
ChimeraX-Daily	N/A	UCSF (301)
coot	0.8.9.1	MRC-LMB (268, 269)
EMAN2	N/A	BCM (302)
EPU	1,2	Thermo Fisher Scientific
Gnuplot	5.4	gnuplot.info
JPKSPM Data Processing	N/A	JPK Instruments AG
Microsoft Office	2016	Microsoft
phenix	1.13	phenix-online.org (270)
RELION	2.0, 3.0, 3.1	MRC-LMB (242, 265)
Visdem	N/A	Schroderlab.org

2 Mutants and microorganisms

Table 6: List of utilized Aβ mutants and variants.

Plasmid	**Provider**
E3Q-Aβ(3-42)	Isoloid GmbH, Düsseldorf
Template	**Provider**
Aβ(1-42)A21G	Isoloid GmbH, Düsseldorf
Aβ(1-42)E22G	Isoloid GmbH, Düsseldorf
Aβ(1-42)E22K	Isoloid GmbH, Düsseldorf
Aβ(1-42)E22Q	Isoloid GmbH, Düsseldorf
Aβ(1-42)E22Δ	Isoloid GmbH, Düsseldorf
Aβ(1-42)D23N	Isoloid GmbH, Düsseldorf
Peptide	**Provider**
Aβ(1-40)	Jochen Walter, Uniklinikum Bonn
Aβ(1-42)	Jochen Walter, Uniklinikum Bonn
Aβ(1-40)-pS8	Jochen Walter, Uniklinikum Bonn
Aβ(1-40)-pS26	Jochen Walter, Uniklinikum Bonn
Aβ(1-42)-pS8	Jochen Walter, Uniklinikum Bonn
Aβ34	Martin Ingelsson, Uppsala University, Sweden
Aβ36	Martin Ingelsson, Uppsala University, Sweden
pGlu-Aβ(3-42)	Bachem, Switzerland

Table 7: List of utilized E. Coli strains.

Strain	**Genotype/description**
BL21(DE3)	F– ompT hsdSB(rB– mB–) gal dcm (DE3)
XL1-Blue	endA1 gyrA96(nal^R) thi-1 recA1 relA1 lac glnV44 F'[::Tn10 $proAB^+$ $lacI^q$ Δ(lacZ)M15] hsdR17(r_{K^-} m_{K^+})

3 Buffers and solutions

Table 8: Buffers and solutions for bacterial growth, harvest and purification.

Name	Ingredients per liter	Comment
Growth		
5x M9 Salt	37.5 g Na_2HPO_4	
	15 g KH_2PO_4	
	2.5 g NaCl	
		ad 1 L H_2O
100x trace elements	100 mg $ZnSO_4$ x 7 H_2O	
	30 mg $MnCl_2$ x 4 H_2O	
	300 mg H_3BO_3	
	200 mg $COCl_2$ x 6 H_2O	
	10 mg $CuCl_2$ x 2 H_2O	
	20 mg $NiCl_2$ x 6 H_2O	
	30 mg Na_2MoO_4 x 2 H_2O	
		ad 1 L H_2O
Harvest		
Lysis buffer	50 mM $Na_xH_yPO_4$	
	200 mM NaCl	
	0.4 mM PMSF	
	1 mg/ml lysozyme	
	5 µg/mL DNAse I	
Purification		
Loading buffer A	870 mL NaP_i stock I	
	130 mL NaP_i stock II	
		incl. 200 mM NaCl
Elution buffer B	870 mL NaP_i stock I	
	130 mL NaP_i stock II	
	500 mM imidazole	
		incl. 200 mM NaCl

Table 9: Buffers and solutions for gel elctrophoresis.

Name	Ingredients per liter	Comment
LiOAc		kindly provided by Elke Reinartz
Laemmli (5x)		kindly provided by Elke Reinartz
Gel buffer (10x, BioRad)	25 mM Tris-HCl	
	192 mM Glycine	
	0.1 % (m/V) SDS	pH 8,3
Coomassie	2 g Coomassie-Brilliant-Blue	
	75 mL acetic acid	
	500 mL EtOH	
		ad 1 L H_2O
Destaining solution	100 mL acetic acid	
	200 mL EtOH	
		ad 1 L H_2O

Table 10: Stock solutions.

Name	Ingredients per litre
NaP_i stock I	8.9 g Na_2HPO_4
	11.69 g NaCl
NaP_i stock II	6.9 g NaH_2PO_4
	11.69 g NaCl

4 Enzymes and commercially available kits

Table 11: Enzymes

Name	Application	Manufactuer
DpnI	Digestion of methylated DNA	New England BioLabs Inc.
Phusion High-Fidelity DNA Polymerase	PCR polymerase	New England BioLabs Inc.
TEV protease	Restriction enzyme for cleaving His_6-tags	Bernd Ersters, IPB Düsseldorf

Table 12: Commercially available kits

Application	Name	Manufactuer
Purification of plasmid DNA	NucleoSpin Plasmid / Plasmid (NoLid)	Macherey-Nagel
Purification of PCR products	NucleoSpin Gel and PCR Clean-up	Macherey-Nagel

5 Primers

All primers in Table 13 have been purchased at Sigma-Aldrich in October 2018.

Table 13: List of primers for point mutants.

Name	Sequence (5'-3')
Abeta_1-42_A21G_rev	CTGCCCACATCTTCTCAAAAAACACCAGTTTCTGAT
Abeta_1-42_A21G_for	ATCAGAAACTGGTGTTTTTTGGAGAAGATGTGGGCAG
Abeta_1-42_E22G_rev	CTTTATTGCTGCCCACATCTCCTTGCAAAAAACACCAGTTTC
Abeta_1-42_E22G_for	GAAACTGGTGTTTTTTGCAGGAGATGTGGGCAGCAATAAAG
Abeta_1-42_E22K_rev	CTTTATTGCTGCCCACATCTTTTGCAAAAAACACCAGTTTCTG
Abeta_1-42_E22K_for	CAGAAACTGGTGTTTTTTGCAAAAGATGTGGGCAGCAATAAAG
Abeta_1-42_E22Q_rev	CTTTATTGCTGCCCACATCCTGTGCAAAAAACACCAGTTTCTGA
Abeta_1-42_E22Q_for	TCAGAAACTGGTGTTTTTTGCACAGGATGTGGGCAGCAATAAAG
Abeta_1-42_E22del_rev	TCAGAAACTGGTGTTTTTTGCACAGGATGTGGGCAGCAATAAAG
Abeta_1-42_E22del_for	CAGAAACTGGTGTTTTTTGCAGATGTGGGCAGCAATAAA
Abeta_1-42_D23N_rev	TTGCTGCCCACATTTTCTGCAAAAAACACCAGTTTCTG
Abeta_1-42_D23N_for	CAGAAACTGGTGTTTTTTGCAGAAAATGTGGGCAGCAA

6 Consumables and microscopy material

Table 14: List of general consumables.

Consumable	Type	Manufacturer
Reaction tube		
1.5 mL	Reagiergefäß 1.5 mL	Sarstedt
1.5 mL protein LoBind	Protein LoBind 1.5 mL	Eppendorf
50 mL centrifuge tube		
yellow	Centrifuge tube 50 (91050)	TPP
red (with stand)	115 x 28 mm, PP (62.559.001)	Sarstedt
red	114 x 28 mm, PP (62.547.254)	Sarstedt
Pasteur glass pipettes	230 mm	VWR
Parafilm	Parafilm M, 10 cm width	Pechiney Plastic Packaging
HPLC column		
analytical	ZORBAX 300 SB-C8, StableBond Analytical, 4.6 x 250 mm	Agilent
semi-preparative	ZORBAX 300 SB-C8, StableBond Semi-Preparative, 9.4 x 250 mm	Agilent
Glycine gel marker (prestained)	PageRuler Plus Prestained	ThermoFisher
Glycine gel marker (unstained)	PageRuler Unstained Protein Ladder	ThermoFisher
Tricine gel marker	Spectra Multicolor Low Range Protein Ladder	ThermoFisher
Agarose gel stain	GelRed Nucleic Acid Stain	Biotium
Concentrator	10 kDa, Vivaspin 2	Sartorius

Table 15: List of consumables and material for AFM.

Consumable	Type	Manufacturer
Cantilever	OMCL-AC160TS, silicone tip with 7 +/- 2 nm radius	Olympus
Cantilever holder	Fixed-spring cantilever holder	JPK
Mica	Glimmer, “V1”, 10 mm	Plano
Glue	Plus sofortfest, 2 component glue	UHU
Microscope slide	“ground edges frosted”, 631-1553	VWR
Razor blade	N.A.	Herkenrath Solingen

Table 16: List of consumables and material for (cryo-)EM.

Consumable	Type	Manufacturer
Grids		
UltrAuFoil®	R1.2/1.3	Quantifoil
Quantifoil®	R1.2/1.3	Quantifoil
Neg. Stain.	CF-300-Cu-50, carbon film 300 mesh copper	Electron Microscopy Sciences, PA
Tweezers		
N5	N5 - Inox -B	Dumont, CH
N5-AC	N5 AC-PO	Dumont, CH
N1	N1 - Dumoxel - H	Dumont, CH

7 Molecular biological methods

7.1 Gel electrophoresis

Electrophoretic separation methods are commonly used in molecular biology to separate proteins, RNA or DNA. By applying voltage to a gel that functions as a molecular sieve, molecules are separated according to their net charge and their size. While agarose gels (section 7.1.1) have relatively large pores that make them suitable for separation of nuclear acids, the preferred use for polyacrylamide gels (section 7.1.2) is the separation of proteins.

7.1.1 Agarose gel electrophoresis

Classic agarose gel electrophoresis is a well-established method to separate RNA or DNA molecules according to their size. Here, agarose gel electrophoresis was performed to verify the success of a PCR experiment (section 7.2.1). For one 0.8 % agarose gel, 0.4 g agarose were dissolved in 50 mL of 5 mM LiOAc and gently heated in the microwave until the agarose had been fully dissolved. While stirring, the solution was cooled until lukewarm. As a next step, 3 µL of GelRed® were added and the solution was poured into a gel mold. After the gel had set, samples were prepared by adding 5 µL of sample or marker to 5 µL ddH_2O and 2 µL 6x dye, and loaded onto the gel. Gels were then run for ~1 h at 150 V in LiOAc buffer.

7.1.2 SDS-PAGE

SDS-PAGE (SDS-polyacrylamide gel electrophoresis) is one of the most common electrophoretic separation methods. After denaturation of the protein samples by addition of SDS, samples are loaded onto a polyacrylamide gel and separated according to their charge an size. (303)

7.1.2.1 Glycine gels

Glycine gels were prepared according to Table 17 and utilized to show protein growth and isolation. Stacking and separating gel solution were freshly prepared in 50 mL reaction tubes and polymerization was induced by adding APS and TEMED at last.
Molecule separation was achieved by combination of a stacking gel followed by a 15 % separating glycine gel. To 32 µL of sample, 8 µL of 5x Laemmli buffer including β-ME, kindly provided by Elke Reinartz. The samples were denaturated for 10 min at 90 °C in a heating block and subsequently, shortly and gently centrifuged in a minifuge. 12 µL of each sample mix were loaded onto the gel together with 3 µL of PageRuler Plus Prestained Marker. Gels were run in 1x TGS buffer (Bio-Rad) for 50 min at 25 mA per gel. Subsequently, gels were stained for 30 min in a Coomassie blue solution, provided by Patrick Meckelburg, and destained for 16 h in ddH_2O while shaking.

Table 17: Solutions for preparation of 15 % glycine gels.

Stacking gel	**2 gels**
ddH_2O	2.98 mL
0.5 M Tris, pH 6.8	1.25 mL
Acrylamide solution	670 µL
10 % SDS	50 µL
10 % APS	50 µL
TEMED	5 µL
Separating gel	2 gels
ddH_2O	2.2 mL
1.5 M Tris ,pH 8.8	2.6 mL
Acrylamide solution	5 mL
10 % SDS	100 µL
10 % APS	100 µL
TEMED	10 µL
Acrylamide solution	
Acrylamide	30 % (w/v)
Bis-acrylamide	0.8 % (w/v)

7.1.2.2 Tricine gels

In comparison to the classic glycine gels (section 7.1.2.1) which cover a great range of molecular weight, tricine gels have been proven to be more suitable for very small proteins up to 30 kDa (304). Tricine gels were prepared according to Table 18. Stacking and separating gel solution were freshly prepared in 50 mL reaction tubes and polymerization was induced by adding APS and TEMED at last.

Table 18: Solutions for preparation of 20 % tricine gels.

Stacking gel (5.6 %)	**2 gels**
ddH_2O	3.1 mL
Acrylamide solution	1 mL
Gel buffer	2.08 mL
10 % APS	50 µL
TEMED	15 µL
Separating gel (20 %)	2 gels
Acrylamide solution	8.5 mL
Gel buffer	5 mL
Glycerol	1.6 mL
10 % APS	50 µL
TEMED	25 µL

Acrylamide solution	
Acrylamide	34.3 % (w/v)
Bis-acrylamide	1.1 % (w/v)
Gel buffer	
3 M Tris Base	181.71 g
0.3 % SDS	15 mL (10 % stock)
	pH 8.45
Anode buffer	per litre
Tris Base	0.2 M
	pH 8.9
Cathode buffer	per litre
Tris Base	0.1 M
Tricine	0.1 M
SDS	0.1 %
	pH 8.25
Loading buffer	
SDS	4 %
Glycerol	12 %
Tris Base	50 mM, pH 7.4
β-ME	2 %
ddH_2O	ad 5 mL

For sample preparation 20 µL of the respective sample were mixed with 20 mL loading buffer and incubated for 10 min at 95 °C on a heating block. Of each sample, 15 µL were loaded onto the gel except for the Spectra Multicolor Low Range Protein Ladder of which 4 µL were sufficient according to manufacturer's information. The cathode buffer was filled into the gel chamber and the anode buffer covered the surroundings. Gels were run at 40 mA per gel until the marker had separated. Subsequently, gels were stained in Coomassie Blue solution by Patrick Meckelburg for 30 min and destained in ddH_2O overnight. Both steps were carried out with the gel placed on a shaker to ensure uniform (de-)staining.

7.2 Cloning of Aβ(1-42) variants

For cloning of Aβ(1-42) mutants K16C, A21G, E22G, E22K, E22Q, E22Δ and D23N, primers were ordered at Sigma-Aldrich (see section 5). They were dissolved in fresh ddH_2O in 1.5 mL reaction tubes and diluted to a final concentration of 100 µM based on the manufacturer data. After a quick vortexing step, the primers were incubated for 1 h at room temperature to guarantee equal distribution in the solution through diffusion. Subsequently the primers were further diluted to 10 µM in ddH_2O and stored at -20 °C.

7.2.1 Polymerase chain reaction (PCR)

For creation of several Aβ(1-42) mutants, site-directed mutagenesis (quickchange) PCR was performed (305). Here, specific mutations can be introduced into a plasmid by selection of the appropriate primer. The primers are designed such that the region, which should be mutated, is surrounded by 20 – 30 bases in both directions. The composition of each 50 µL PCR solution is shown in Table 19.

Table 19: Composition of PCR mixture.

PCR	Volume
5x NEB Phusion Buffer	10 µL
Template (10 ng/µl)	10 µL
10 mM dNTP mix	1 µL
DMSO	1.5 µL
Primer reverse	125 ng in solution
Primer forward	125 ng in solution
Phusion Polymerase	0.5 µL (1 unit)
ddH_2O	ad 50 µL

Amplification of the respective mutant DNA was carried out with the temperature program shown in Table 20.

Table 20: PCR program.

	Time [min]	Temperature [°C]
1x	02:00	95
	00:20	95
	00:10	72
	03:20	72
1x	10:00	72
	Total:	18 cycles
	∞	8 °C (storage)

The original templates were digested by a restriction enzyme by addition of 20 U of DpnI (20.000 U/ml), which digests methylated DNA exclusively, each PCR product and incubation at 36 °C for 1 h. Subsequently, the PCR product was purified by use of the NucleoSpin Gel and PCR Clean-up kit from Macherey-Nagel.

7.2.2 Transformation of *E. coli* cells

For transformation of E. coli cells a heat shock protocol was followed. First, a thermomixer was pre-heated to 42 °C and an aliquot of E. coli XL1 Blue cells was thawn on ice before 2 µL of the respective PCR product (section 7.2.1) were added to 50 µL of chemical competent E. coli XL1 Blue cells, which were provided by Elke Reinartz. The mixture was incubated on

ice for 30 min. Subsequently, the heat shock through which cells are enabled to take up DNA was carried out by transferring the reaction tube to the 42 °C shaker for 30 s. Immediately, the mixture was again incubated on ice for 5 min before 500 µL of 2xYT medium were added. The bacteria were then incubated at 37 °C and 400 rpm for 60 or 90 min and 750 rpm before 100 µL of cells were distributed onto an ampicillin agar plate by shaking of the plate with three glass beads. The agar plate was incubated overnight at 36 °C or at room temperature for at least three days. The reaction tube was kept at 6 °C until growth of colonies on the agar plate had been verified.

7.2.3 Plasmid preparation

Isolation of plasmid DNA was carried out, after baking of two glass test tubes per clone for 1 h at 50 °C. Each test tube was then filled with 5 mL of 2xYT medium incl. 100 µg/ml ampicillin. Off the agar plate (section 7.2.2), one colony per clone and test tube was picked. The resulting pre-culture was incubated overnight at 37 °C while rotating. Plasmid isolation was then carried out using the NucleoSpin Plasmid / Plasmid (NoLid) kit from Macherey-Nagel. Simultaneously, a 'quick and dirty' glycerol stock was prepared from each pre-culture by mixing 500 µL SOB medium incl. glycerol (provided by Elke Reinartz) with 500 µL of the respective pre-culture. Success of the cloning process was verified by sequencing of the final plasmid preparations at SeqLab/MicroSynth by sending in 12 µL of DNA (45 – 60 ng/µl) and 3 µL of sequencing primer (T7 promotor). If cloning was proved to be successful, the glycerol stocks and the plasmid preparations were stored at -80 °C until further use. A list of successful plasmid preparations can be found in Table 21.

Table 21: Successful mutations and their plasmid concentrations.

Mutant	Concentration [ng/µl]
Aβ(1-42)A21G-1	57
Aβ(1-42)A21G-2	49
Aβ(1-42)E22G-1	58
Aβ(1-42)E22K-1	54
Aβ(1-42)E22K-2	51
Aβ(1-42)D23N-1	56
Aβ(1-42)D23N-2	57
Aβ(1-42)E22Q-1	113
Aβ(1-42)E22Q-2	54

Due to an error in primer design, Aβ(1-42)E22Δ was unsuccessful and resulted in amplification of the wildtype template.

8 Protein biochemical methods

8.1 Protein concentration measurements

Protein concentration was either measured by RP-HPLC (section 9.1.2.1) or a prototype microfluidics system Mk1 from Cambridge Analytica. The Mk1, or Fluidity One, is a microfluidic diffusional sizing platform. The device measures two-dimensional diffusion profiles in a single step without any need for *a priori* knowledge about the tested solution. It determines the hydrodynamic radius by measurement of the diffusion rate of the protein in a steady state laminar flow. (306) Additionally, the device determines the protein concentration by measurement of the fluorescence intensity with ortho-phthalaldehyde, which reacts with primary amines (307).
For analysis, 6 µL of sample were transferred onto a microchip, which displays a sample inlet and the channels the sample solution will flow through. The microchip was inserted into the device and measurement and analysis were carried out automatically.

8.2 DNA concentration measurements

DNA concentration measurements were performed at the NanoDrop microvolume sample retention system by ThermoFisher Scientific. In comparison to classical spectrophotometers, this device only needs very small sample volumes to perform concentration measurement. The measurements were carried out according to the protocol by Desjardins and Conklin (308). In short, first 1 µL sample solution were transferred onto the device. Following the closure of the lever arm, the concentration measurement was started and analysis was carried out automatically.

8.3 Cell growth and heterologous expression

8.3.1 Test expressions for mutants

For text expression of the mutants Aβ(1-42) E22G, E22K, A21G and D23N in E. coli BL12(DE3) cells, a pre-culture in LB medium had been prepared by Elke Reinartz. For the main culture, 30 µL of pre-culture and 3 µL ampicillin (100 µg/mL) were added to 3 mL 2xYT medium in glass test tubes of 10 mL volume. Two cultures for each mutant were prepared in order to induce one of them later on with IPTG and leave the remaining one as a control without induction. The test tubes were incubated at 37 °C and 200 rpm for 1 h before their OD_{600} was checked. If the optical density at 600 nm (OD_{600}) reached values between 0.2 and 0.5, every second culture was induced with a final concentration of 0.2 mM IPTG followed by another incubation of all cultures at 37 °C and 140 rpm for 5 h. After incubation, 100 µL of each culture were diluted with 900 µL 2xYT medium and their OD_{600} was measured. Then, again 100 µL of each culture were taken and centrifuged for 10 min at

11,000 *g*. The supernatant was discarded and the pellet resuspended in 50 µL 5x Laemmli buffer provided by Elke Reinartz. The samples were analyzed by SDS-PAGE (see 7.1.2.1).

8.3.2 Cell growth and heterologous expression of E3Q Aβ(1-42)

For cell growth, an agar plate with colonies of E. coli BL21(DE3) cells with E3Q Aβ(1-42) has been friendly provided by Elke Reinartz and Stefan Klinker. A pre-culture of 100 mL LB-medium, which had been inoculated with one of the colonies, was shaken at 37 °C, 160 rpm for 23 h.

4 mL pre-culture were diluted into 800 mL M9 medium after addition of 800 µL ampicillin (50 mg/ml). While shaking at 37 °C, 160 rpm, the optical density of the solution was followed over a time course of 7 h until the OD_{600} reached 0.3. Subsequently, the cell medium was induced with a final concentration of 0.2 mM IPTG (320 µL of a 0.5 M IPTG stock solution) before left for growth at 25 °C, 160 rpm for 15 h, at which point the D_{600} had risen to 0.95. In order to harvest the cells, the culture was distributed onto four centrifuge tubes. Cells were centrifuged at 5000 *g* and 4 °C in a JLA-10.500 rotor for 15 min . The supernatant was discarded and pellets were transferred into a 50 mL reaction tube with the help of a disposable blade. Any leftovers were diluted in NaP_i buffer which was provided by Patrick Meckelburg and transferred to the 50 mL reaction tube as well. The pellets were then centrifuged in a table top centrifuge for 10 min at 3000 *g* and 4 °C and subsequently stored at -20 °C for later use.

8.4 Protein extraction and purification

Frozen cell pellets (see section 8.3) were thawed and resuspended in 20 mL lysis buffer (for 1.6 g cell pellet). Cell disruption was achieved by ultra-sonication: the sample was placed on ice such that the liquid in the 50 mL reaction tube was covered by it and then sonicated with a VS 70 T sonotrode (pulse: 10 s, pause: 60 s, time: 2x 17,5 min). To separate cell debris from soluble proteins, the lysate was centrifuged at 4 °C and 3000 *g* for 15 min. A spade point of sample of the resulting pellet was taken, resuspended in 32 µL NaP_i buffer A, and the remains were discarded. The supernatant was transferred into tubes for ultra-centrifugation at 4 °C, 42,000 rpm for 40 min in a Ti 70 rotor. After ultra-centrifugation, another sample from the supernatant was taken for later analysis and the remaining supernatant, containing the desired protein, was loaded onto an Äkta system to carry out affinity chromatography.

8.4.1 Affinity chromatography

In order to isolate the target protein from lysate, an affinity chromatography, more precisely immobilized metal affinity chromatography (IMAC) was carried out. The target protein carries a fusion construct consisting of a (NANP)19 solubility-tag, a TEV cleavage site and a His_6-tag to facilitate purification by IMAC. The His_6-tag has a strong affinity to the nickel-

chelate complex on the column, which is only interrupted by addition of higher concentrations of imidazole. In the process, a gradient is rum from 0 – 500 mM imidazole that gradually releases unspecifically bound protein until a concentration high enough to interrupt the His_6-tag binding, is reached and the target protein is released.
The bacterial lysate was loaded onto a 5 mL Protino® Ni-NTA column with a flowrate of 2 mL/min and run with loading buffer A and elution buffer B. Throughout the elution and fractionation, samples were taken regularly for later analysis. According to results from SDS-PAGE (section V1.1) fractions were pooled from the IMAC run, resulting in a total sample volume of 18 mL. The sample was then concentrated in NaP_i buffer in a concentrator with a MW_{cutoff} of 10 kDa in a table top centrifuge at 4 °C and 3000 *g* for 10 min. This step was repeated until the final volume was 1 mL. Subsequently, the sample was washed three times with 1 mL NaP_i buffer an concentrated to a final volume of 1.5 mL. Concentration measurement with a 1:100 dilution of the sample in a FlowMatic device (see section 8.1) resulted in a total protein concentration of 74.4 µg/ml translating to a total of 12 mg protein in 1.5 mL.

8.4.2 TEV-protease digestion

The total concentration of 12 mg protein refers to the target protein (4 kDa) still carrying its His_6-tag. In order to digest the rather large tag and to prevent it from interfering with further experiments, a TEV-protease digestion was performed. TEV-protease and protein were mixed in a ratio of 1:100. The 1.2 mg TEV-protease (6.8 mg/ml, stored at -80 °C) were kindly provided by Bernd Esters. The protein solution was incubated with TEV-protease for 18.5 h, at 6 °C, and subsequently frozen and stored at -80 °C until further usage. Completeness of TEV-protease digestion was verified by SDS-PAGE with 15 % glycine gels (section 7.1.2.1) or tricine gels (section 7.1.2.2). If the digestion was incomplete, the protein solution was incubated again with double the amount TEV-protease for another 5 – 6 h. This step was repeated until TEV-protease digestion was completed. Afterwards, samples were loaded onto a RP-HPLC column (section 9.1).

8.5 Ring-closure of E3Q- Aβ(3-42)

The lyophilized protein (section 9.1.1) was resuspended in 30 mL HPLC buffer with the help of a Pasteur glass pipette (230 mm) in order to reduce protein loss, since Aβ is known to stick easily to plastic surfaces and less to glass surfaces. Subsequently, the protein solution was transferred into a 50 mL reaction tube (yellow).
Ring-closure transforming E3Q-Aβ(3-42) into pGlu-Aβ(3-42) (see Figure 59) was carried out by incubation at 45 °C for 48 h based on a protocol of Dammers *et al*. (174).

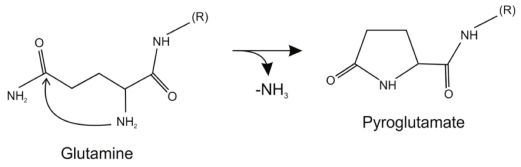

Figure 59: Chemical conversion of glutamine to pyroglutamate. An N-terminal glutamine can be converted to pyroglutamate by intramolecular formation of a lactam ring induced by a nucleophilic attack and resulting in the release of NH3. (Figure taken from (309))

The 50 mL reaction tube containing ~30 mL of E3Q-Aβ(3-42) was sealed with parafilm and incubated at 45 °C for 48 h. Temperature was controlled by placing an adjacent water-filled 50 mL reaction tube with a thermometer next to the protein solution. Samples of 60 µL taken after 0, 1, 24, and 48 h were frozen in liquid N_2 and stored at -80 °C. After 48 h the protein solution was stored at 6 °C until the completeness of the reaction was verified by analytical RP-HPLC (section 9.1.2.2). Residual E3Q-Aβ(3-42) was separated from pGlu-Aβ(3-42) by semi-preparative RP-HPLC (section 9.1.1.2).

8.6 Recycling of Aβ samples

To prevent protein samples from being wasted due to overproduction (e.g., in cases of very high volume of a certain preparation) or to the buffer system for different experiments, Aβ samples were recycled when possible. The fibrillated or at least dissolved Aβ samples were first lyophilized (section 9.3) and then dissolved in HFIP. Incubation in HFIP lasted from hours to days in order to guarantee monomerization of fibrillated protein (310, 311). Subsequently, the samples were freeze-dried again and afterwards dissolved in the respective buffer to the desired concentration.

8.7 Sample preparation

8.7.1 Sample preparation of Aβ(1-42)-pS8

Synthesized phophorylated Aβ variants and wildtype controls (see Table 22) were delivered in glass vials containing 1 mg of peptide each.

Table 22: Variants of Aβ provided by collaboration partners from Uniklinikum Bonn

	modification	**mass**
Aβ(1-40)	/	2x 1 mg
Aβ(1-42)	/	2x 1mg
Aβ(1-40)-pS8	Phosphorylation at serine 8	2x 1mg
Aβ(1-40)-pS26	Phosphorylation at serine 26	2x 1mg
Aβ(1-42)-pS8	Phosphorylation at serine 8	2x 1mg

Of each sample, 1 mg peptide were dissolved in 1 mL light HPLC buffer and transferred into a 1.5 mL protein LoBind tube. The tubes were held on ice during the subsequent semi-preparative RP-HPLC (9.1.1.4). The retention times of the phosphorylated species Aβ(1-40)-pS8 and -pS26 and Aβ(1-42)-pS8 were assumed to be in close proximity to those already known from the wildtypes Aβ(1-42) and Aβ(1-40) under the same conditions. Accordingly, wildtype samples were applied onto the RP-HPLC column to use their elution behavior as reference. RP-HPLC analysis was started for each sample by application of 10 µL sample via the 1 mL loop to check the elution behavior of the respective variant before increasing the volume. Eluates were collected in yellow 50 mL reaction tubes resulting in collection of one tube of Aβ(1-40) and Aβ(1-40)-pS8, one tube of Aβ(1-42) and Aβ(1-42)-pS8 and two tubes of Aβ(1-40)-pS26 due to two main product peaks (see Table 23).

Table 23: RP-HPLC retention times of Aβ variants from Uniklinikum Bonn

sample	comment
Aβ(1-40)	/
Aβ(1-42)	Rather dirty sample, no clear main peak
Aβ(1-40)-pS8	No clear peak, the main "double peak" was collected
Aβ(1-40)-pS26	Two main peaks collected, unclear which one is the correct product
Aβ(1-42)-pS8	/

8.7.2 Sample preparation of Aβ36

Parts of the Aβ36 utilized in section V2.1 to fibrillate in HPLC buffer, was recovered by lyophilization of the residual 25 mL of sample overnight in the LT-105 lyophilizer (see section 9.3). The dried protein was dissolved in 3.5 mL HFIP and incubated for two days. The solution was transferred to six 1.5 mL protein LoBind reaction tubes in equal volumes (566 µL each). Those were left in the vacuum concentrator (section 9.3) overnight. Out of these six samples, samples 1 – 3 were dissolved according to Table 24, before being vortexed for 30 s. Sample 6 later was dissolved in 600 µL HFIP overnight, vortexed and centrifuged in a minifuge before distribution across eight 1.5 mL protein LoBind reaction tubes (sample 7-14). Subsequently, samples 6 – 14 were freeze-dried in the vacuum concentrator within 90 min.
Similary, sample 4 was dissolved in 500 µL HFIP and incubated for 3 h. 333 µl of the solution stayed in tube "4" while the remaining 167 µl were evenly distributed across ten 1.5 mL protein LoBind reaction tubes into sample 15 – 24.

Table 24: Overview on Aβ36 samples.

sample	total protein [µg]	buffer	volume [µL]	protein concentration [µM]
1	125	HPLC buffer	100	300
2	125	1x PBS*	100	300
3	125	NaP_i**, pH 7.4	100	300
4***	83			
5	125			
6***	15.6	50 mM NaP_i, pH 7.3	100	40
7	15.6	1x PBS*	100	
8	15.6	50 mM NaP_i, pH 7.3	500	8
9	15.6	50 mM NaP_i, pH 7.3	200	20
10	15.6			
11	15.6			
12	15.6	50 mM NaP_i, pH 7.3	200	20
13	15.6	50 mM NaP_i, pH 7.3	500	8
14	15.6			
15	3.75	Citrate buffer, pH 3	100	10
16	3.75	Citrate buffer, pH 4	100	10
17	3.75	Citrate buffer, pH 5	100	10
18	3.75	Citrate buffer, pH 6	100	10
19	3.75	Citrate buffer, pH 7	100	10
20	3.75			
21	3.75			
22	3.75			
23	3.75			
24	3.75			

* Filip Hasecke, ** Michael Wördehoff, *** original sample was dissolved in HFIP and split up in tinier portions

8.7.2.1 pH testing

For testing the fibril growth of Aβ36, samples 15 – 19 (see Table 25) were dissolved in 100 µL of citrate buffer with different pH values ranging from pH 3 – 7. For the respective pH value, 0.25 M citric acid and 0.5 M Na_2HPO_4 (both kindly provided by Lothar Gremer) were mixed to a total volume of 10 mL (Table 25).

Table 25: Composition of citrate buffers with different pH values.

pH	Citric acid [mL]	Na_2HPO_4 [mL]	Salt concentration [M]
3	7.945	2.055	0.3
4	6.145	3.855	0.35
5	4.85	5.15	0.38
6	3.685	6.315	0.4
7	1.765	8.235	0.45

In order to lower the salt concentration (Table 25) in the solution, the respective buffer was diluted for each sample according to Table 26.

Table 26: Dilution scheme of citrate buffers.

sample	pH	Citrate buffer [µL]	ddH_2O	Concentration
15	3	16.67	ad 100 µL	50 mM
16	4	14.2		
17	5	13.16		
18	6	12.5		
19	7	11.1		

1 min after dissolving the protein in citrate buffer, 15 µL of each sample were taken, frozen in liquid N_2 and stored at -80 °C. The remaining samples were incubated at room temperature and examined at the AFM after three weeks.

9 Biophysical methods

9.1 High performance liquid chromatography

HPLC allows for molecule separation on a very high level. While other methods such as size exclusion chromatography usually do not reach such high resolution, with reversed phase HPLC (RP-HPLC) even slight differences in a molecule's composition can be distinguished. While in classical HPLC the mobile phase is non-polar and the stationary phase consists of polar material, it is the opposite for RP-HPLC. Here, the non-polar stationary phase reduces the retardation time of polar samples, which is interesting for working with proteins. Hence, RP-HPLC is one of the most common HPLC techniques. During this work, RP-HPLC was performed to separate the target protein from impurities such as other proteins, to separate different states of the target protein from each other or to analyze the fibrillization state of the target protein. Depending on the research question either semi-preparative or analytic RP-HPLC was applied.

9.1.1 Semi-preparative HPLC

Semi-preparative RP-HPLC was performed to purify recombinant or synthesized protein before carrying out aggregation experiments. In order to run large sample amounts with protein concentrations of around 1 mg/mL, a ZORBAX 300SB-C8 Stable Bond (9.4 x 250 mm, 5 micron) column has been used on a 1260/1290 Infinity system from Agilent Technologies, California. If not stated differently, samples were loaded onto the column via a 1 mL loop.

9.1.1.1 Separation of E3Q-Aβ(3-42) from TEV-protease and impurities

For separation of the target protein, E3Q-Aβ(3-42), from its tag and remaining impurities the protein solution after TEV-digestion (section 8.4.2) was run over a ZORBAX 300SB-C8 column with a gradient following the scheme in Figure 60 at 80 °C.

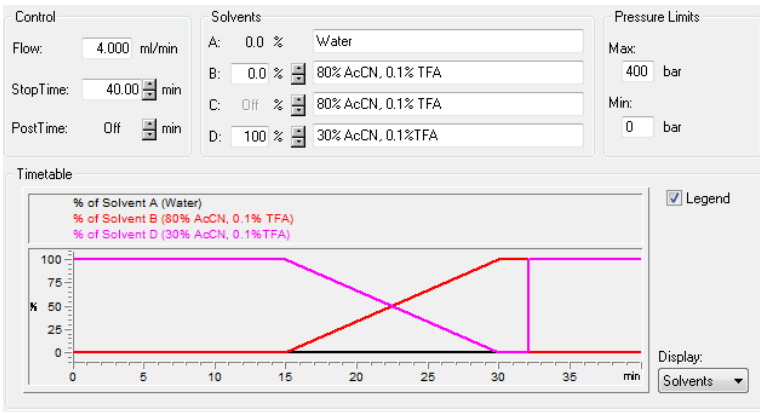

Figure 60: Gradient protocol for analytical RP-HPLC. The program runs for 40 min with at flow rate of 4 mL/min. From minute 15 to 30 a gradient increases the AcN concentration from 30 % to 80 %,

In total, 1.36 mL had to be run over the column, which had a 1 mL loop attached for loading of sample. First, 10 µL sample loaded onto the column to verify that the chosen program, specifically the AcN concentrations would lead to good peak separation in the sample. Subsequently, the remaining sample was loaded onto the column in volumes between 200 and 400 µL. The emptied reaction tube was washed with 400 µL NaP_i buffer and the wash was again loaded onto the column. All eluates of the main peak after 13 min were collected in one 1 L round-bottomed flask and stored at room temperature (eluate I). The eluates of a second peak at 19 min were collected in a 50 mL reaction tube (eluate II).
The eluates were later merged with eluate I of a second round of purification (analog to sections 8.3 and 8.4), which yielded 47.25 mg protein in a total of 2.1 mL solution.
The combined eluates were frozen in liquid N_2 and lyophilized in a 1 L round-bottomed flask until further use.

9.1.1.2 Separation of pGlu-Aβ(3-42) from E3Q-Aβ(3-42)

After four weeks of incubation at room temperature and 48 h at 45 °C, the conversion from E3Q-Aβ(3-42) to pGlu-Aβ(3-42) was completed to ~85 % (see section V1.2). To separate the remaining E3Q-Aβ(3-42) from pGlu-Aβ(3-42). the solution was first lyophilized, then resuspended in 5 mL HFIP in order to monomerize the protein (310, 311), and after incubation overnight at room temperature and then five more days at 6 °C, lyophilized again. Subsequently, the lyophilized product was resuspended in 2.5 mL Light HPLC buffer and ran over a ZORBAX 300SB-C8 column at a flowrate of 4 mL/min and 80 °C in volumes of 50 – 100 µL. The peak fractions of pGlu-Aβ(3-42) (~470 mL in total) were collected in a 1 L round-bottomed flask, while the peak fractions of E3Q-Aβ(3-42) (~125 mL in total) were collected in a 250 mL round-bottomed flask. A reference sample of each fraction was taken, frozen in liquid N_2 and stored at -80 °C. Both peak fractions were then lyophilized.

9.1.1.3 Recovery of pGlu-Aβ(3-42) samples

In case of any setbacks such as occurrence of degradation products in the case of pGlu-Aβ(3-42), monomeric Aβ peptides were recovered from aggregates in solution. First, the proteins in solution were lyophilized (section 9.3). The dried peptides were then dissolved in HFIP to guarantee monomerization and incubated for several hours up to days. Subsequently, the sample was either aliquoted into the desired number of aliquots or directly lyophilized again. After the final lyophilization, monomeric Aβ peptide was dissolved in light HPLC buffer and loaded onto a ZORBAX 300SB-C8 column in volumes of up to 750 µl with a 1 mL loop. The RP-HPLC protocol is displayed in Figure 61 (note: the flow rate for semi-preparative runs is 4 mL/min).

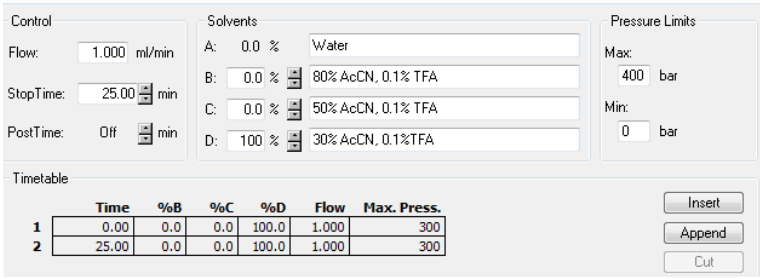

Figure 61: Isocratic protocol for recovery of pGlu-Aβ(3-42) samples. The program runs for 25 min with a flow rate of 4 mL/min instead of 1 mL/min at 30 % AcN, 0.1 % TFA.

The peak fraction of the desired protein was collected and used for further experiments.

9.1.1.4 Purification of synthesized Aβ variants

Synthetic Aβ variants were dissolved in 30 % AcN, 0.1 % TFA and run isocratically over the RP-HPLC column according to the protocol in Figure 61 with a flow of 4 mL/min. First, a test run was performed with 5-10 µL of the respective sample to assess its elution behavior. If the elution behavior showed a clear product peak, volumes of up to 500 µL were loaded onto the column at once and the eluate of the main peak was collected. If the elution profile did not show a clear product peak, further test runs were performed in which the AcN concentration was adjusted by dilution with water (Solvent D in Figure 61) until a clear separation of the main product from other impurities was possible. For example, for Aβ36 and Aβ34 this resulted in an AcN concentration of 26.5 % and 25 %, respectively.

9.1.1.5 Preparation of amyloid fibrillization

For fibrillization of amyloid at low pH, a condition which favors slow aggregation and results in high homogeneity of the sample (181), the protein sample was first run over a semi-preparative RP-HPLC column and afterwards directly collected in the mobile phase (HPLC buffer).
When starting with lyophilized protein, the protein in question was resuspended in a few milliliters of HFIP and incubated for 24 – 48 h before being lyophilized. Subsequently, the protein was resuspended in few milliliters of Light HPLC buffer, just enough for the protein to dissolve. Afterwards, the protein was loaded onto a ZORBAX 300SB-C8 column using 500 µL of protein solution per run. RP-HPLC runs were carried out at 80 °C with a flowrate of 4 mL/min. The peak fractions were collected in 50 mL reaction tubes (yellow).

9.1.2 Analytical HPLC

Analytical RP-HPLC runs on a ZORBAX 300 SB-C8 Analytical column were commonly performed to assess either protein concentration or fibrillization status. In both cases the runs were carried out at 80 °C, a flowrate of 1 mL/min and with HPLC buffer as mobile phase. See Figure 62 for further details on the program.

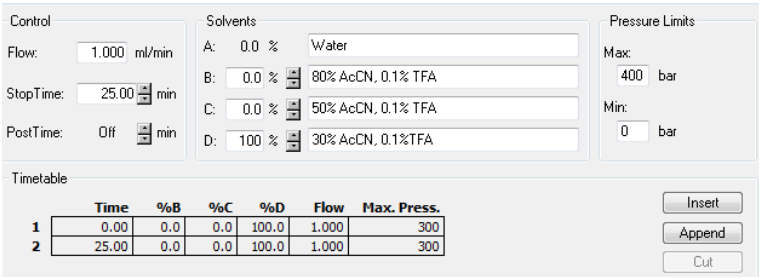

Figure 62: Isocratic protocol for analytical RP-HPLC. The program runs for 25 min with a flow rate of 1 mL/min at 30 % AcN, 0.1 % TFA.

9.1.2.1 Protein concentration measurement

With the help of a protein concentration gradient of Aβ(1-42) measured on a ZORBAX 300 SB-C8 Analytical column by Lothar Gremer, the concentration of other Aβ species was approximately calculated. The equation for the concentration of Aβ species is

$$c = \left(\frac{A}{m}\right) \cdot d$$

with c = concentration in µM
A = peak area in mAU · s
m = slope in mAU · s · µM^{-1}
d = dilution factor.

According to prior experiments by Lothar Gremer the slope value is m = 45 mAU · s · µM^{-1}. The dilution factor, if not stated differently, is d = 1.5.

9.1.2.2 Fibrillization status

To check the fibrillization status of a protein, first the protein stock solution was gently mixed by cautious inversion or shaking. Then, 100 µL of the solution were transferred into a 1.5 mL LoBind reaction tube and centrifuged at 16,000 *g* and 25 °C for 10 min in a table top centrifuge to separate monomeric protein from aggregated protein. After the centrifugation step, 60 µL of supernatant, containing monomeric protein, were taken without agitating the stock solution, and subsequently diluted with 30 µL ddH_2O. Of these 90 µL, 30 µL were injected into the 20 µL loop and subsequently loaded onto the column by which the run was initiated.
For calculation of the fibrillization status, the concentration (see 9.1.2.1) of the monomeric protein in the sample was subtracted from the total monomeric protein at timepoint 0 before fibrillization.

9.1.2.3 Quality control on pGlu-Aβ(3-42) I

All sample fractions (1 – 3) of 21.06.2018 were tested on quality and stability after 11 months by running a small sample batch over an analytical RP-HPLC column. In each,

case 20 µL were loaded onto the column and run according to the protocol in Figure 62 (section 9.1.2). Samples of peak fractions were collected in 1.5 mL LoBind protein reaction tubes and stored for further mass spectrometric analysis (section 9.5). From the resulting peak areas, the amount of impurities evolved over time was calculated in relation to the amount of total protein in the sample.

9.1.2.4 Quality control on pGlu-Aβ(3-42) II

For a second mass spectrometric analysis, test runs of the following samples were performed:

i) Control: synthetic, pGlu-Aβ(3-42)
ii) Sample: pGlu-Aβ(3-42), recycled sample 01 from May 2019 (sample taken at 7.5 mL out of a 50 mL reaction tube).

Since the sample had a rather low concentration of ~6 µM monomer equivalent, two times 750 µL from the stock solution were transferred with a glass pipette into a 1.5 mL LoBind reaction tube and lyophilized overnight in the speedvac. Following an incubation of the sample fractions in 500 µL HFIP for 4 h, they were lyophilized again in the speedvac for 1 h. For the control, dried synthetic pGlu-Aβ(3-42), provided by Lothar Gremer and Soumav Nath (amount of protein equals 80 µM monomer equivalent in 100 µL buffer), was dissolved in 100 µL HFIP and equally distributed across three 1.5 mL LoBind reaction tubes. Subsequently, the control fractions were lyophilized for 30 min in the speedvac.
Dried sample and control fractions were analyzed on the RP-HPLC and remaining fractions were sent to the collaboration partner (section X9.1.2.4).

9.2 Atomic force microscopy

AFM is a type of scanning probe microscopy with nanometer resolution, which has been identified as useful to monitor amyloidogenic proteins and especially fibrils. For this thesis, it was mainly used to verify fibril growth, screen fibril conditions and characterize fibril samples.

9.2.1.1 Preparation of an object slide

Preparations for AFM start with cleaning of object slides by treating them with ultrasound in an ultrasonic bath at room temperature. For this, up to five object slides were put into a water-filled plastic case and fitted into a floating device such that ¾ of the plastic case were surrounded by water. After sonication of 3-5 min, the object slides were dried under N_2 flow. In a next step a mica slice had to be fixated on the object slide. Mica slices were placed in the middle of the object slide (Figure 63A) and fixated with two-component glue.

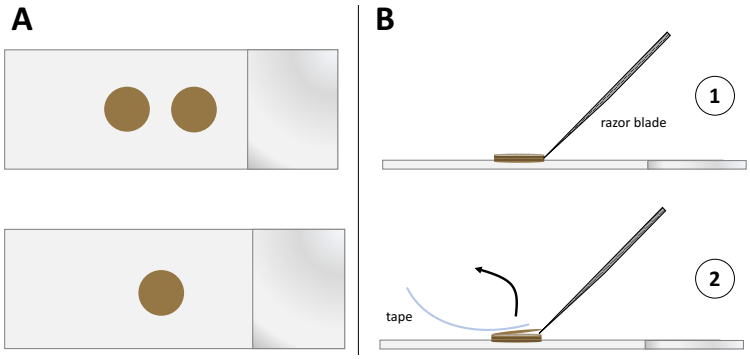

Figure 63: Schematic drawing of object slides with mica slices. (A) Optimal placement of mica slices (brown) on the object slide. (B1) Schematic of a razor blade (dark grey) to slice off a layer of mica (brown) and (B2) the subsequent step of removing the top layer of mica by attaching tape to it.

Following the drying of the glue, a top layer of mica was removed to generate an untouched new surface by first separating part of the top layer with a razor blade and second, removing the top layer using tape (Figure 63B).

9.2.1.2 Sample preparation and measurement

All sample measurements were carried out in tapping mode on dried samples. Buffer additives such as salts or high viscosity ingredients might influence the drying procedure, the orientation of the sample on the mica surface or lead to impurities. All of these can in turn limit the resolution of the AFM images to be obtained.

All steps of sample preparation were carried out under a clean bench. Amyloid fibril samples, which were held in HPLC buffer, were either prepared by simple drying of a 1 – 10 µL volume of the sample on the mica surface for 30 – 60 min, or incubation of the sample on the mica in a humid environment such that the fibrils could attach to the surface for 10 min before the sample was washed with fresh ddH_2O (see section 9.2.1.4). In the latter case, drying was performed by N_2 flow if not stated differently.

In case the sample was known to have a high concentration it was diluted accordingly with the respective buffer solution.

In case the sample showed some sort of impurities under the AFM, washing steps were performed. Until the sample reached sufficient purity, the dried sample was washed with 100 µL of fresh ddH_2O. Washing was done by pipetting the 100 µL drop onto the mica, letting it sit for 5 – 10 s and pipetting the solution several times up and down while trying to not hit the sample center with the tip. Extent liquid was then removed by pipetting and subsequent N_2 flow.

9.2.1.3 Quality check pGlu-Aβ(3-42)

After RP-HPLC profiles showed a change in the sample of pGlu-Aβ(3-42) , ~100 µL of each sample were transferred from a liquid level of 5 – 7 mL (ou of a 50 mL yellow reaction tube) into a 1.5 mL protein LoBind reaction tube. Of these samples 5 µL were transferred

undiluted onto a fresh mica surface. After the sample had dried, AFM measurements were carried out.

9.2.1.4 Aβ36 at low temperatures

Lyophilized samples 8 and 9 of Aβ36 were held on ice and dissolved in pre-cooled (6 °C) 50 mM NaP_i buffer, pH 7.3. Sample 8 was dissolved in 500 µL buffer while sample 9 was only dissolved in 200 µL of the same buffer. Both samples were incubated on ice for 24 h at 6 °C. Following the incubation, of each sample, 10 µL were transferred onto a mica slide in a humid environment: the object slide carrying the mica was placed in a petri dish that was padded with a wet Kimtech tissue. Remaining samples were stored in the fridge at 6 °C.
After sample application, the petri dish was closed and the samples incubated for 15 min. Subsequently, the samples were washed two times with ddH_2O and dried under N_2 flow.
The experiment was repeated with sample 8, and a control experiment in which the sample was not incubated in a humid environment but simply air-dried. In each case, 10 µL sample were applied onto a mica surface. The differences in protocol are displayed in Table 27.

Table 27: Protocols for AFM measurements on Aβ36

protocol	**air-dried**	**humid**
Incubation	On air, as long as needed until dry	Incubation in humid environment for 12 min
Washing	2x with 100 µL ddH_2O	
Drying	with N_2 flow	

9.3 Lyophilization of protein samples

Lyophilization, or freeze-drying is a convenient method for long-term storage of proteins (312). In the process, a frozen protein solution undergoes sublimation under vacuum. Depending on the sample volume, samples were either lyophilized at the LT-105 lyophilizer (for volumes > 2 mL) or in a vacuum concentrator (for volumes ≤ 2 mL).
If not stated differently, protein were dissolved in either HPLC buffer or HFIP, in which case the protein solution was incubated for several hours, before lyophilization. For lyophilization, the solutions were frozen in liquid N_2 in 1.5 mL reaction tubes, 50 mL reaction tubes or round-bottomed glass ware. Small reaction tubes of 1.5 mL or 2 mL volume were placed with open lids in the vacuum concentrator. Larger containers such as 50 mL reaction tubes were closed with a holey plastic lid, sealed with parafilm (Figure 64, left) and collected in a glass cup, which can be mounted onto the lyophilizer directly.

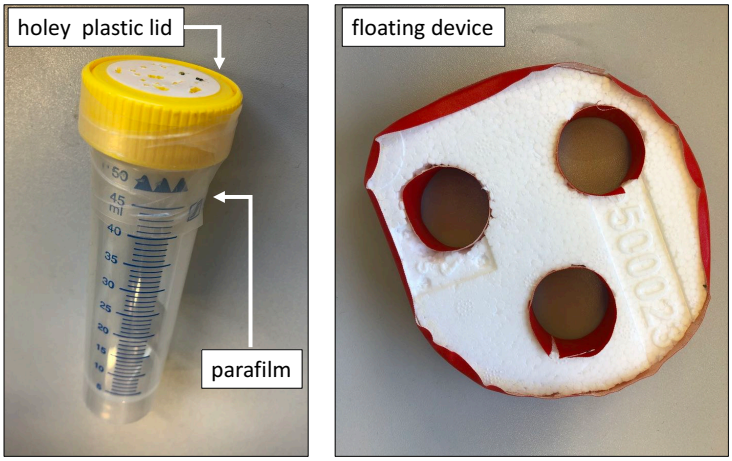

Figure 64: Utensils for lyophilization. Left: 50 mL reaction tube with a holey plastic lid to ensure evacuation and sealed with parafilm. Right: Floating device made from styrofoam with holes fitted to hold a 50 mL reaction tube in liquid nitrogen.

Likewise, round-bottomed glass ware was directly attached to the LT-105 lyophilizer. Depending on solvent and volume, lyophilization was performed in-between times of 30 min up to several days until the respective sample was completely de-hydrated, recognizable by a remaining white, fluffy powder.

9.4 Circular dichroism spectroscopy

Circular dichroism (CD) spectroscopy is a well-established method for the characterization of secondary structure in a protein sample. CD spectra form according to the unequal absorption of left-handed and right-handed circularly polarized light. Asymmetric molecules show different refraction patterns and extents of absorption to these phase-shifted light beams from which information about the secondary structures can be gained. (313) Secondary structures lead to distinct CD spectra that are characterized by certain minima and maxima. Helices show two minima at 210 and 220 nm and a maximum at 193 nm. Random coil structures show one minimum at 200 nm, and β-sheets a minimum at 217 nm and maximum at 195 nm. (292, 313) The experiment was prepared and conducted with the help of Rebecca Sternke-Hoffmann.

Prior to the experiment, a quartz cuvette with 1 mm window (Type: 110-QS) was cleaned by repeating washing steps with ddH_2O, SDS, ddH_2O and ethanol before drying under N_2 flow. The CD spectrometer was prepared by switching the device on and pre-cooling it to 8 °C. To prevent O_3 formation, the N_2 flow was started roughly 15 min before the first measurement.

Measurements were carried out at 10 °C, a spectrum of 260 – 190 nm, an interval of 0.5 nm, a bandwidth of 2 nm and a scanning rate of 50 nm/min. Samples measured were the following: 150 µL buffer control (50 mM NaP_i, cooled to 6 °C), 150 µL monomer control (of Aβ36 sample 12, see Table 24, held on ice and freshly dissolved in 200 µL 50 mM NaP_i buffer) and 150 µL Aβ36 sample 9 (see Table 24, stored at 6 °C for 7 weeks).

9.5 Mass spectrometry

Mass spectrometry (MS) is an established method for the identification of proteins, peptide fragments and other chemical components. By analysis of the mass-to-charge (*m/z*) ratio of ionized fragments, it is not only possible to determine which components are in a sample but also the relative abundance of those. In vacuum, these ionized particles pass the analyzer of the spectrometer before finding their way to the detector according to their *m/z* ratio. (314)

Purity and quality of pGlu-Aβ(3-42) have been examined via MS, specifically by an electron spray ionization (ESI) connected to a time-of-flight module (TOF, section 9.5.1) or an Orbitrap (section 9.5.2) Information about the applied protocols have been provided by the respective collaboration partners.

9.5.1 ESI-TOF mass spectrometry

ESI-TOF MS analyses were carried out by Sabine Metzger from the University of Cologne and the *Leibniz-Institut für Umweltforschung*.

For verification of purity and quality of pGlu-Aβ(3-42) after eleven months, a sample from each pGlu-Aβ(3-42) fraction was analyzed via RP-HPLC (section 9.1.2.3) and peak fractions were collected in 1.5 mL protein LoBind reaction tubes. The samples containing the supposed "degradation" peak with a retention time of 7.6 min and the pGlu-Aβ(3-42) peak at 15.6 min retention time were dried in the vacuum concentrator and sent to Sabine Metzger for analysis via ESI-MS. According to information by Sabine Metzger, prior to ESI-MS measurements, the lyophilized samples were dissolved in 60 % MeOH (v/v) and 40 % H_2O (v/v) with the latter including 5 % formic acid (FA). Ionized samples were then detected and analyzed via MS. Results were evaluated and provided by Sabine Metzger.

9.5.2 ESI mass spectrometry with an Orbitrap

For verification of purity and quality of pGlu-Aβ(3-42) after incubation of 1.5 years, pGlu-Aβ(3-42) of May 2019 was analyzed via RP-HPLC together with a synthethic control sample kindly provided by Lothar Gremer and Soumav Nath.

According to information by Andreas Linden from the *Max-Planck-Institut* in Göttingen, the lyophilized samples were dissolved in 50 µL 20% AcN and 0.1 % FA resulting in a concentration of roughly 1 pmol/µL. After analysing these samples by direct infusion into a Q Exactive HF-X mass spectrometer (Thermo Fisher Scientific), the samples were vacuum-dried again and subsequently dissolved in 8 µL of 20 % AcN, 0.1 % FA before separation via a monolithic HPLC column (PepSwift, Thermo Fisher Scientific), which is coupled online to the mass spectrometer. The HPLC run was done with a gradient from 20 – 50 % AcN and 0.08 % FA within 33 min. The complete endurance of the run was 48 min. Following the elution from the HPLC, the samples were directly measured in an orbitrap system as intact masses. Results were evaluated and provided by Andreas Linden.

9.6 Electron Microscopy

9.6.1 Sample preparation and transport conditions

For EM measurements the sample often had to be taken and sent or transferred to another location. Since usually only small amounts of sample (up to 3 µL per grid) are needed, 20-100 µL of the respective sample were transferred from the stock solution to a 1.5 mL protein LoBind reaction tube. When transfer was performed from 1.5 mL tube to another, the sample was taken with a Gilson 200 µL pipette, for sample transfer from 50 mL tubes or bigger containers, samples were taken with a glass pipette to reduce protein loss due to the tendency of Aβ to stick to plastic.
In order to transport the samples safely and without significant protein loss to the destined microscope, sample tubes were placed in a suitable rack which was stored in a plastic box to reduce possible influence from light. The box was then transported taking care that it was moved as less as possible so that the protein was prevented from attaching to the inner walls of the plastic sample tube.

9.6.2 Negative Stain-EM

For preparation of negative stain grids, the selected number of grids (CF-300-Cu-50, carbon film 300 mesh copper) were placed with tweezers on a metal carrier while taking care that they were touched gently only at the side of the grid, and glow discharged for 25 s (glow: 25 s, hold: 10 s) at 15 mA. Glow discharging, together with plasma cleaning, is the most common way to make the rather hydrophobic surface of a grid more hydrophilic (315). Since biological samples will almost exclusively sit in aqueous solutions, the sample application onto and distribution across the grid would be significantly harder without former glow discharging.
For transport of the grids from the glow discharger to the work bench, they were stored in a grid box. Grids were then stained according to one of the protocols shown in Table 28 and stored again in a grid box until further use.

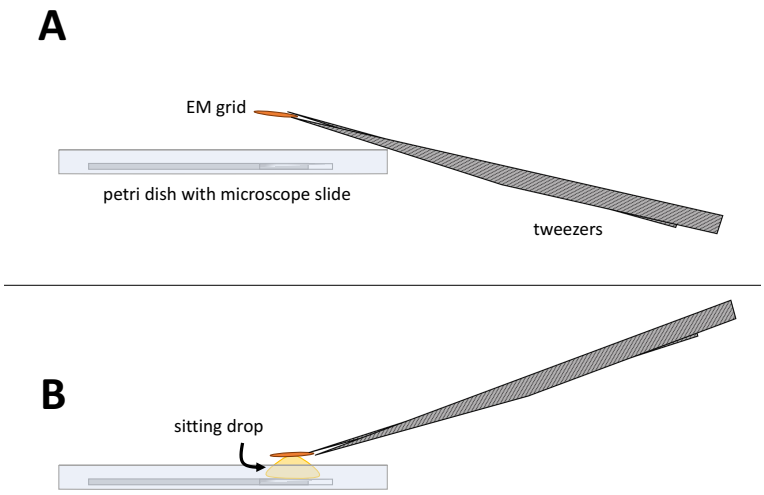

Figure 65: Set-up for negative stain sample preparation. (A) Tweezers holding an EM grid lean against a petri dish such that the grid is placed over a microscope slide wrapped in parafilm. (B) A sitting drop of ddH_2O or uranyl acetate is placed on top of the microscope slide and the grid can easily be washed in the drop.

For both protocols, a piece of parafilm was wrapped around a microscope slide which in turn was placed in a clean petri dish (see Figure 65). The parafilmed microscope slide serves two purposes. First, the grid, held by tweezers, will be placed over the microscope slide (Figure 65A) such that in case it slips, the grid will land on the clean parafilm and may not be completely destroyed and second, the parafilm is perfectly suited to place sitting drops of water or uranyl acetate on top of it so that the grid can easily be washed within them (Figure 65B).

Table 28: Negative stain protocols with uranyl acetate. Each step is followed by blotting of excess liquid after the respective waiting time.

protocol	**sitting drop**		**no wash**	
steps	sample application	2 min	sample application	1 min
	wash: ddH_2O	0 min		
	wash: uranyl acetate (1%)	0 min	2.5 µL uranyl acetate (1%)	0 min
	2.5 µL uranyl acetate (1%)	2 min	2.5 µL uranyl acetate (1%)	2 min
	drying	0.5 – 1 min	drying	0.5 – 1 min

For the *sitting drop* protocol, the sample was applied onto the glow discharged grid and blotted away after 2 min. This step was followed by two washing steps with ddH_2O and uranyl acetate during which the grid was dipped into a sitting drop of the respective solution (Figure 65 B) and excess solution was blotted away immediately. A final incubation with uranyl acetate was followed by a drying period before the grid was placed into the storage box.

The *no wash* protocol differs in design mainly in the skipping of the washing steps. Instead, uranyl acetate was applied two times onto the grid and blotted away after 0 respectively 2 min application time (Table 28).

9.6.3 Cryo-EM

9.6.3.1 Grid preparation and vitrification

Preparing a sophisticated grid lays the basis for a promising data collection. In order for this to happen, one has to choose the right combination of grid and sample. A list of grid types used in this work is shown in Table 29.

Table 29: List of grid types for cryo-EM

Grid	Type	Mesh	Coating	Foil	samples
Quantifoil®	R 1.2/1.3	300	Co	C	pGlu-Aβ(3-42) / Aβ(1-42)-pS8 *(April 2019)* / IAPP
UltrAuFoil®	R 1.2/1.3	300	Au	Au	Aβ(1-42)-pS8 *(Dec 2019)*

Quantifoil® grids consist of a copper coated holey grid with a carbon support film layer. While the grid material is selected due to its properties regarding radiation damage, the support film adds stability to the grid structure but also often results in physical and chemical changes upon electron irradiation (316) and beam-induced movement leading to an increased background signal (317). The latter is especially important for carbon films. In contrast, UltrAuFoil® grids are covered with a gold film which improves compatibility with most buffer solutions, increases radiation-resistance and decreases beam-induced movement resulting in a better signal-to-noise ratio (315, 318).
Before sample application, the respective grids have to be glow discharged, which was done at 15 mA, for 25 s (glow: 25 s, hold: 10 s) if not stated differently. Subsequently, glow discharged grids were transferred to the Vitrobot™ for sample application and plunge-freezing. Grid preparation and vitrification were performed by Hans Duimel (Division for Nanoscopy, Maastricht University), Julio Ortiz (ERC-3, FZ Jülich) or Sabrina Berkamp (ERC-3, FZ Jülich) according to the protocols in Table 30.

Table 30: Sample preparation of fibril samples for cryo-EM data collection

sample	Humidity [%]	Temp. [°C]	Vol. [µL]	Time [min]	Blot force	Blot time [s]	comments
SH3 (May 2018)	95	25	2.5	/	7,10,12	3.5	50 mM monomer equivalent, dilutions: 4x, 10x, 20x
pGlu-Aβ(3-42) ***(Oct 2018)***	95	25	2.5	1	5	4	Fraction 2, 100 µL sample 10 min at 16,000 g, 20 °C; 60 µL supernatant discarded, 7 s glow discharge
Aβ(1-42)-pS8 ***(April 2019)***	95	25	2.5	/	5	5	Sample of March 2018, sonicated at 40 % amplitude, 10 s, 1:2 dilution
IAPP (May 2019)	95	25	2.5	1	5	5	110 µM monomer equivalent
pGlu-Aβ(3-42) ***(Nov 2019)***	off	25	2.5	/	-10	1.5	Fraction 2, undiluted
Aβ(1-42)-pS8 ***(Dec 2019)***	95	25	2.0	/	5	5	Sample of 15.05.2018
pGlu-Aβ(3-42) ***(Sept 2020)***	off	25	2.5	/	-10	2	Sample of 21.05.2019 (re-lyophilized and re-fibrillated), undiluted

9.6.4 Sonication of Aβ fibrils

Over the course of time, most Aβ fibrils became very long, sometimes up to tens of µm. Since this seemed to correlate with a lack of fibril density in cryo-EM measurements, the hypothesis evolved that if parts of very long fibrils attach to a blotting paper, more fibril mass gets lost compared to shorter fibrils sticking to the blotting paper. Hence, sonication experiments on Aβ fibrils were performed to break them down to suitable length for cryo-EM.

For first trials, ~500 µl of fibrils were transferred with a Pasteur glass pipette from a 50 mL reaction tube (see Figure 66A) into a 2 mL protein LoBind reaction tube because 2 mL were shown to have better contact to the VialTweeter than the 1.5 mL reaction tubes (Figure 66B).

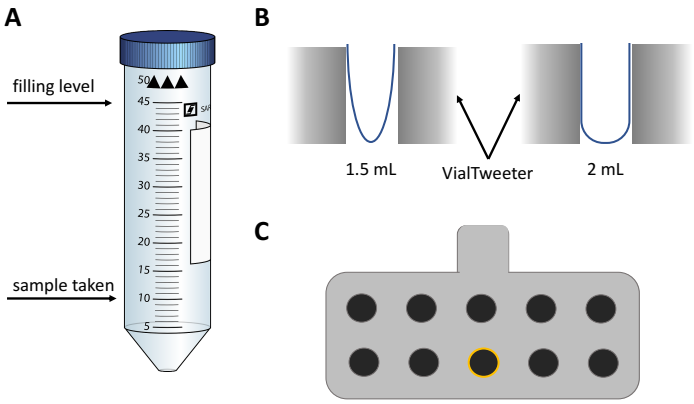

Figure 66 : Sonication of Aβ fibrils in the VialTweeter. A total sample level in a 50 mL tube. Level at which the sample was taken indicated by an arrow. B Comparison of contact areas of 1.5 mL and 2 mL tubes with the VialTweeter. C Top view of the VialTweeter with position of the sample highlighted in yellow.

The respective 2 mL tube was inserted into the VialTweeter as seen in Figure 66C and sonicated according to Table 31 for 0, 10, 20 or 30 s at 70 % amplitude or 10 s at 0, 30, 40, 50 or 70 % amplitude.

Table 31: Sonication protocols for Aβ(1-42) and Aβ(1-42)-pS8.

Protein	Time [s]	Amplitude [%]
Aβ(1-42)	10	0
	10	30
	10	50
	10	70
Aβ(1-42)	10	70
	20	70
	30	70
Aβ(1-42)-pS8	10	30
	10	40
	10	50

When the reaction tube is placed correctly into the VialTweeter, sonication will evoke bubbling and/or foam formation during the process. If foam is generated, sonication likely was too intense. Samples from sonication experiments were examined by AFM (section 9.2) and negative stain EM (section 9.6.2).

XI List of abbreviations

Table 32: Abbreviations

Abbreviation	Full text
Aβ	Amyloid β
AD	Alzheimer's disease
AFM	atomic force microscopy
APS	ammonium persulfate
ATR-FTIR	attenuated total reflexion – fourier transform infrared spectroscopy
CCD	charge-coupled device
CD	circular dichroism
CTF	contrast transfer function
ddH_2O	double distilled H_2O
DMSO	di-methyl-sulfoxide
EOAD	early onset Alzheimer's disease
EM	electron microscope / microscopy
ESI	electron spray ionization
FAD	familial Alzheimer's disease
FDA	Food and Drug Administration
HFIP	hexa-fluoro-isopropanol
HPLC	high performance liquid chromatography
IAPP	islet amyloid polypeptide
IDP	intrinsically disordered peptide
IMAC	immobilized metal ion affinity chromatography
IPTG	isopropyl-β-D-thio-galactoside
kDa	kilo Dalton
kV	kilo Volt
LC	liquid chromatography
LiAc	lithium acetate
LOAD	late onset Alzheimer's disease
MS	mass spectrometry
MW	molecular weight
NaCl	sodium chloride
NMR	nuclear magnetic resonance
OD	optical density
PAGE	polyacrylamide-gel-electrophoresis
PCR	polymerase chain reaction
pGlu	pyro-glutamate
PMSF	phenyl-methyl-sulfonyl-fluoride
PTM	post-translational modification

Abbreviation	Full text
SAD	sporadic Alzheimer's disease
SDS	sodium-dodecyl-sulfate
SH3	src homology domain 3
SNR	signal to noise ratio
SPR	single particle reconstruction
T1D	type I diabetes
T2D	type II diabetes
TEM	transmission electron microscope / microscopy
TEMED	tetra-methyl-ethylen-diamine
TEV	tobacco etch virus
TFA	trifluoroacetic acid
TGS	tris-glycine-SDS
TOF	time-of-flight
U	unit
β-ME	β-mercapto-ethanol
2D	two dimensional
3D	three dimensional
°C	celsius

XII List of references

1. Jülich Supercomputing Centre (2018) JURECA: Modular supercomputer at Jülich Supercomputing Centre. doi:http://dx.doi.org/10.17815/jlsrf-4-121-1.
2. Anfinsen CB (1973) Principles that govern the folding of protein chains. *Science*. doi:10.1126/science.181.4096.223.
3. Dobson CM (1999) Protein misfolding, evolution and disease. *Trends Biochem Sci*. doi:10.1016/S0968-0004(99)01445-0.
4. Sunde M, et al. (1997) Common core structure of amyloid fibrils by synchrotron X-ray diffraction. *J Mol Biol* 273:729–739.
5. Chiti F, Dobson CM (2006) Protein Misfolding, Functional Amyloid, and Human Disease. *Annu Rev Biochem* 75(1):333–366.
6. Petkova AT, et al. (2002) A structural model for Alzheimer's β-amyloid fibrils based on experimental constraints from solid state NMR. *PNAS* 99:16742–16747.
7. Cohen AS (1986) General introduction and a brief history of the amyloid fibril. *Amyloidosis*, eds Marrink J, Van Rijswijk M (Nijhoff, Dordrecht), pp 3–19.
8. Schwartz P (1970) *Amyloidosis Cause and Manifestation of Senile Deterioration* (Charles C Thomas Publisher, Springfield, IL).
9. Sipe JD, Cohen AS (2000) Review: History of the amyloid fibril. *J Struct Biol*. doi:10.1006/jsbi.2000.4221.
10. Makovitzky J, Appel TR (2007) Altersdegeneration: Amyloid und Amyloidkrankheiten. *BioSpektrum* (11):724–726.
11. Virchow R (1854) Weitere Mittheilungen über das Vorkommen der pflanzlichen Cellulose beim Menschen. *Arch für Pathol Anat und Physiol und für Klin Med*. doi:10.1007/BF01881064.
12. Virchow R (1854) Ueber eine im Gehirn und Rückenmark des Menschen aufgefundene Substanz mit der chemischen Reaction der Cellulose. *Arch für Pathol Anat und Physiol und für Klin Med*. doi:10.1007/BF01930815.
13. Friedreich N, Kekulé A (1859) Zur Amyloidfrage. *Arch für Pathol Anat und Physiol und für Klin Med* (16):50–65.
14. Missmahl HP, Hartwig M (1953) Polarisationsoptische untersuchungen an der amyloid substance. *Virchows Arch Pathol Anat* 324:489–508.
15. Xue C, Lin TY, Chang D, Guo Z (2017) Thioflavin T as an amyloid dye: Fibril quantification, optimal concentration and effect on aggregation. *R Soc Open Sci* 4(1). doi:10.1098/rsos.160696.
16. Iadanza MG, Jackson MP, Hewitt EW, Ranson NA, Radford SE (2018) A new era for understanding amyloid structures and disease. *Nat Rev Mol Cell Biol* 19(12):755–773.
17. Sipe JD, et al. (2016) Amyloid fibril proteins and amyloidosis: chemical identification and clinical classification International Society of Amyloidosis 2016 Nomenclature Guidelines. *Amyloid*. doi:10.1080/13506129.2016.1257986.
18. Baker KR, Rice L (2012) The Amyloidoses: Clinical Features, Diagnosis And Treatment. *Methodist Debakey Cardiovasc J* 8(3):3–7.
19. Murphy MP, Levine H (2010) Alzheimer's disease and the amyloid-β peptide. *J Alzheimer's Dis*. doi:10.3233/JAD-2010-1221.
20. Polymeropoulos MH, et al. (1997) Mutation in the α-synuclein gene identified in families with Parkinson's disease. *Science*. doi:10.1126/science.276.5321.2045.
21. Stefanis L (2012) α-Synuclein in Parkinson's disease. *Cold Spring Harb Perspect Med*. doi:10.1101/cshperspect.a009399.

22. Johnson KH, O'Brien TD, Betsholtz C, Westermark P (1989) Islet amyloid, islet-amyloid polypeptide, and diabetes mellitus. *N Engl J Med* 321(8):513–518.
23. Finsterer J, et al. (2019) Hereditary transthyretin-related amyloidosis. *Acta Neurol Scand*. doi:10.1111/ane.13035.
24. Dittrich T, Kommich C, Hegenbart U, Schönland SO (2020) Prognosis and Staging of AL Amyloidosis. *Acta Haematol* 143(4):388–400.
25. Adler-Abramovich L, et al. (2012) Phenylalanine assembly into toxic fibrils suggests amyloid etiology in phenylketonuria. *Nat Chem Biol*. doi:10.1038/nchembio.1002.
26. Guijarro JI, Sunde M, Jones JA, Campbell ID, Dobson CM (1998) Amyloid fibril formation by an SH3 domain. *PNAS* 95(8):4224–4228.
27. Loquet A, Saupe SJ, Romero D (2018) Functional Amyloids in Health and Disease. *J Mol Biol*. doi:10.1016/j.jmb.2018.07.024.
28. Hammond TC, et al. (2020) β-amyloid and tau drive early Alzheimer's disease decline while glucose hypometabolism drives late decline. *Commun Biol* 3(1). doi:10.1038/s42003-020-1079-x.
29. Guijarro JI, Morton CJ, Plaxco KW, Campbell ID, Dobson CM (1998) Folding kinetics of the SH3 domain of PI3 kinase by real-time NMR combined with optical spectroscopy. *J Mol Biol* 276(3):657–667.
30. Zurdo J, Guijarro JI, Jiménez JL, Saibil HR, Dobson CM (2001) Dependence on solution conditions of aggregation and amyloid formation by an SH3 domain. *J Mol Biol* 311(2):325–340.
31. Lomakin a, Chung DS, Benedek GB, Kirschner D a, Teplow DB (1996) On the nucleation and growth of amyloid beta-protein fibrils: detection of nuclei and quantitation of rate constants. *PNAS* 93(3):1125–1129.
32. Annamalai K, et al. (2017) Common Fibril Structures Imply Systemically Conserved Protein Misfolding Pathways In Vivo. *Angew Chemie Int Ed*. doi:10.1002/anie.201701761.
33. Schmit JD, Ghosh K, Dill K (2011) What Drives Amyloid Molecules To Assemble into Oligomers and Fibrils? *Biophys J* 100(2):450–458.
34. Šarić A, Chebaro YC, Knowles TPJ, Frenkel D (2014) Crucial role of nonspecific interactions in amyloid nucleation. *PNAS*. doi:10.1073/pnas.1410159111.
35. Ono K, Condron MM, Teplow DB (2009) Structure-neurotoxicity relationships of amyloid β-protein oligomers. *PNAS*. doi:10.1073/pnas.0905127106.
36. Bucciantini M, et al. (2002) Inherent toxicity of aggregates implies a common mechanism for protein misfolding diseases. *Nature* 416(6880):507–511.
37. Lee J, Culyba EK, Powers ET, Kelly JW (2011) Amyloid-β forms fibrils by nucleated conformational conversion of oligomers. *Nat Chem Biol*. doi:10.1038/nchembio.624.
38. Baldwin AJ, et al. (2011) Metastability of native proteins and the phenomenon of amyloid formation. *J Am Chem Soc* 133(36):14160–14163.
39. Zielinski M, Röder C, Schröder GF Cryo-EM of amyloidogenic proteins [submitted].
40. Strassnig M, Ganguli M (2005) About a peculiar disease of the cerebral cortex. By Alois Alzheimer, 1907. *Psychiatry* (412):30–33.
41. Bloom GS (2014) Amyloid-β and tau: The trigger and bullet in Alzheimer disease pathogenesis. *JAMA Neurol*. doi:10.1001/jamaneurol.2013.5847.

42. Alzheimer A (1907) Uber eine eigenartige Erkrankung der Hirnrinde. *Allg Zeitschrift für Psychiatr und Psych-Gerichtl Med Psych-Gerichtl Med*.
43. Denk EG, Botsaris GD (1972) Fundamental studies in secondary nucleation from solution. *J Cryst Growth* 13–14(C). doi:10.1016/0022-0248(72)90287-4.
44. Ferrone FA, Hofrichter J, Eaton WA (1985) Kinetics of sickle hemoglobin polymerization. II. A double nucleation mechanism. *J Mol Biol*. doi:10.1016/0022-2836(85)90175-5.
45. Ruschak AM, Miranker AD (2007) Fiber-dependent amyloid formation as catalysis of an existing reaction pathway. *PNAS*. doi:10.1073/pnas.0703306104.
46. Hu R, Zhang M, Chen H, Jiang B, Zheng J (2015) Cross-Seeding Interaction between β-Amyloid and Human Islet Amyloid Polypeptide. *ACS Chem Neurosci* 6(10):1759–1768.
47. Bhowmik D, et al. (2014) PH changes the aggregation propensity of amyloid-β without altering the monomer conformation. *Phys Chem Chem Phys*. doi:10.1039/c3cp54151g.
48. Gorman PM, Yip CM, Fraser PE, Chakrabartty A (2003) Alternate aggregation pathways of the Alzheimer β-amyloid peptide: Aβ association kinetics at endosomal pH. *J Mol Biol*. doi:10.1016/S0022-2836(02)01279-2.
49. Kim W, Hecht MH (2006) Generic hydrophobic residues are sufficient to promote aggregation of the Alzheimer's Aβ42 peptide. *PNAS*. doi:10.1073/pnas.0605629103.
50. Miravalle L, et al. (2000) Substitutions at codon 22 of Alzheimer's Aβ peptide induce diverse conformational changes and apoptotic effects human cerebral endothelial cells. *J Biol Chem*. doi:10.1074/jbc.M003154200.
51. Krone MG, et al. (2008) Effects of Familial Alzheimer's Disease Mutations on the Folding Nucleation of the Amyloid β-Protein. *J Mol Biol*. doi:10.1016/j.jmb.2008.05.069.
52. Murakami K, et al. (2002) Synthesis, aggregation, neurotoxicity, and secondary structure of various Aβ1-42 mutants of familial Alzheimer's disease at positions 21-23. *Biochem Biophys Res Commun*. doi:10.1016/S0006-291X(02)00430-8.
53. Johnson P (1976) Thermodynamics of the Polymerization of Protein. *Biochem Soc Trans*. doi:10.1042/bst0041168.
54. Cohen SIA, et al. (2013) Proliferation of amyloid- 42 aggregates occurs through a secondary nucleation mechanism. *PNAS* 110(24):9758–9763.
55. Gaspar R, et al. (2017) Secondary nucleation of monomers on fibril surface dominates α-synuclein aggregation and provides autocatalytic amyloid amplification. *Q Rev Biophys*. doi:10.1017/S0033583516000172.
56. Xue WF, Radford SE (2013) An imaging and systems modeling approach to fibril breakage enables prediction of amyloid behavior. *Biophys J*. doi:10.1016/j.bpj.2013.10.034.
57. Glabe CG (2006) Common mechanisms of amyloid oligomer pathogenesis in degenerative disease. *Neurobiol Aging*. doi:10.1016/j.neurobiolaging.2005.04.017.
58. Brender JR, et al. (2008) Amyloid fiber formation and membrane disruption are separate processes localized in two distinct regions of IAPP, the type-2-diabetes-related peptide. *J Am Chem Soc*. doi:10.1021/ja710484d.
59. Milanesi L, et al. (2012) Direct three-dimensional visualization of membrane disruption by amyloid fibrils. *PNAS*. doi:10.1073/pnas.1206325109.

60. Nagel-Steger L, Owen MC, Strodel B (2016) An Account of Amyloid Oligomers: Facts and Figures Obtained from Experiments and Simulations. *ChemBioChem*. doi:10.1002/cbic.201500623.
61. Cline EN, Bicca MA, Viola KL, Klein WL (2018) The Amyloid-β Oligomer Hypothesis: Beginning of the Third Decade. *J Alzheimer's Dis*. doi:10.3233/JAD-179941.
62. Kenjiro O, Tsuji M (2020) Protofibrils of Amyloid-β are Important Targets of a Disease-Modifying Approach for Alzheimer's Disease. *Int J Mol Sci* 21(3):952.
63. Hasecke F, et al. (2018) Origin of metastable oligomers and their effects on amyloid fibril self-assembly. *Chem Sci*. doi:10.1039/c8sc01479e.
64. Nicoll AJ, et al. (2013) Amyloid-β nanotubes are associated with prion protein-dependent synaptotoxicity. *Nat Commun*. doi:10.1038/ncomms3416.
65. Schützmann MP, et al. (2020) Endo-lysosomal Aβ concentration and pH enable formation of Aβ oligomers that potently induce Tau missorting. *bioRxiv*. doi:10.1101/2020.06.28.175885.
66. Tattum MH, et al. (2006) Elongated oligomers assemble into mammalian PrP amyloid fibrils. *J Mol Biol*. doi:10.1016/j.jmb.2006.01.052.
67. Chamberlain AK, et al. (2000) Ultrastructural organization of amyloid fibrils by atomic force microscopy. *Biophys J*. doi:10.1016/S0006-3495(00)76560-X.
68. Röder C, et al. (2019) Atomic structure of PI3-kinase SH3 amyloid fibrils by cryo-electron microscopy. *Nat Commun* 10(1):3754.
69. Gallardo R, et al. (2020) Fibril structures of diabetes-related amylin variants reveal a basis for surface-templated assembly. *Nat Struct Mol Biol*. doi:10.1038/s41594-020-0496-3.
70. Röder C, et al. (2020) Cryo-EM structure of islet amyloid polypeptide fibrils reveals similarities with amyloid-β fibrils. *Nat Struct Mol Biol* 27(7). doi:10.1038/s41594-020-0442-4.
71. Kensler RW, Levine RJC (1982) Determination of the handedness of the crossbridge helix of Limulus thick filaments. *J Muscle Res Cell Motil*. doi:10.1007/BF00713042.
72. Liberta F, et al. (2019) Cryo-EM fibril structures from systemic AA amyloidosis reveal the species complementarity of pathological amyloids. *Nat Commun* 10(1):1104.
73. Sunde M, Blake C (1997) The Structure of Amyloid Fibrils by Electron Microscopy and X-Ray Diffraction. *Advances in Protein Chemistry*, Protein Misassembly., eds Richards FM, Eisenberg DS, Kim PS (Academic Press), pp 123–159.
74. Wiltzius JJW, et al. (2009) Molecular mechanisms for protein-encoded inheritance. *Nat Struct Mol Biol*. doi:10.1038/nsmb.1643.
75. Riek R, Eisenberg DS (2016) The activities of amyloids from a structural perspective. *Nature* 539:227–235.
76. Paravastu AK, Leapman RD, Yau WM, Tycko R (2008) Molecular structural basis for polymorphism in Alzheimer's β-amyloid fibrils. *PNAS*. doi:10.1073/pnas.0806270105.
77. Schweighauser M, et al. (2020) Structures of α-synuclein filaments from multiple system atrophy. *Nature*. doi:10.1038/s41586-020-2317-6.
78. Schmidt M, et al. (2019) Cryo-EM structure of a transthyretin-derived amyloid fibril from a patient with hereditary ATTR amyloidosis. *Nat Commun*.

doi:10.1038/s41467-019-13038-z.
79. Liberta F, et al. (2019) Cryo-EM structure of an amyloid fibril from systemic amyloidosis. *Nat Commun* 10:1104.
80. Swuec P, et al. (2018) Cryo-EM structure of cardiac amyloid fibrils from an immunoglobulin light chain (AL) amyloidosis patient. *bioRxiv*:444901.
81. Fitzpatrick AWPP, et al. (2017) Cryo-EM structures of Tau filaments from Alzheimer's disease brain HHS Public Access. *Nature* 547(7662):185–190.
82. Falcon B, et al. (2018) Tau filaments from multiple cases of sporadic and inherited Alzheimer's disease adopt a common fold. *Acta Neuropathol* 136:699–708.
83. Falcon B, et al. (2018) Structures of filaments from Pick's disease reveal a novel tau protein fold. *Nature* 561(7721):137–140.
84. Lippens G, Gigant B (2019) Elucidating Tau function and dysfunction in the era of cryo-EM. *J Biol Chem*. doi:10.1074/jbc.REV119.008031.
85. Romero D, Kolter R (2014) Functional amyloids in bacteria. *Int Microbiol*. doi:10.2436/20.1501.01.208.
86. Ramsook CB, et al. (2010) Yeast cell adhesion molecules have functional amyloid-forming sequences. *Eukaryot Cell*. doi:10.1128/EC.00068-09.
87. Pham CLL, Kwan AH, Sunde M (2014) Functional amyloid: Widespread in Nature, diverse in purpose. *Essays Biochem*. doi:10.1042/BSE0560207.
88. Chiti F, Dobson CM (2017) *Protein misfolding, amyloid formation, and human disease: A summary of progress over the last decade* doi:10.1146/annurev-biochem-061516-045115.
89. Swaminathan R, Ravi VK, Kumar S, Kumar MVS, Chandra N (2011) Lysozyme: A model protein for amyloid research. *Advances in Protein Chemistry and Structural Biology* doi:10.1016/B978-0-12-386483-3.00003-3.
90. Maji SK, et al. (2009) Functional amyloids as natural storage of peptide hormones in pituitary secretory granules. *Science*. doi:10.1126/science.1173155.
91. Kurochkina N, Guha U (2013) SH3 domains: Modules of protein-protein interactions. *Biophys Rev*. doi:10.1007/s12551-012-0081-z.
92. Kaneko T, Li L, Li SSC (2008) The SH3 domain- A family of versatile peptide- and protein-recognition module. *Front Biosci*. doi:10.2741/3053.
93. Müller TD, Finan B, Clemmensen C, Di Marchi RD, Tschöp MH (2017) The new biology and pharmacology of glucagon. *Physiol Rev*. doi:10.1152/physrev.00025.2016.
94. Ventura S, Lacroix E, Serrano L (2002) Insights into the origin of the tendency of the PI3-SH3 domain to form amyloid fibrils. *J Mol Biol* 322:1147–1158.
95. Mayer BJ, Hamaguchi M, Hanafusa H (1988) A novel viral oncogene with structural similarity to phospholipase C. *Nature*. doi:10.1038/332272a0.
96. Larson SM, Davidson AR, Davidson AR (2000) The identification of conserved interactions within the SH3 domain by alignment of sequences and structures. *Protein Sci*. doi:10.1201/1086/43327.12.3.20030701/43625.6.
97. Koch CA, Anderson D, Moran MF, Ellis C, Pawson T (1991) SH2 and SH3 domains: Elements that control interactions of cytoplasmic signaling proteins. *Science* 252:668–674.
98. van der Geer P, et al. (1995) A conserved amino-terminal Shc domain binds to phosphotyrosine motifs in activated receptors and phosphopeptides. *Curr Biol*. doi:10.1016/S0960-9822(95)00081-9.

99. Batra-Safferling R, Granzin J, Mödder S, Hoffmann S, Willbold D (2010) Structural studies of the phosphatidylinositol 3-kinase (PI3K) SH3 domain in complex with a peptide ligand: Role of the anchor residue in ligand binding. *Biol Chem* 391:33–42.
100. Chen S, et al. (2011) X-ray structure of the SH3 domain of the phosphoinositide 3-kinase p85β subunit. *Acta Crystallogr Sect F Struct Biol Cryst Commun* 67(11):1328–1333.
101. Koyama S, et al. (1993) Structure of the PI3K SH3 domain and analysis of the SH3 family. *Cell* 72:945–952.
102. Liang J, Chen JK, Schreiber ST, Clardy J (1996) Crystal structure of PI3K Sh3 domain at 2.0 angstroms resolution. *J Mol Biol* 257:632–643.
103. Bayro MJ, et al. (2011) Intermolecular structure determination of amyloid fibrils with magic-angle spinning and dynamic nuclear polarization NMR. *J Am Chem Soc*. doi:10.1021/ja203756x.
104. Bayro MJ, Maly T, Birkett NR, Dobson CM, Griffin RG (2009) Structural Investigation of an SH3 Amyloid Protein Fibril. *Biophys J* 96(3):86a.
105. Sarroukh R, Goormaghtigh E, Ruysschaert JM, Raussens V (2013) ATR-FTIR: A "rejuvenated" tool to investigate amyloid proteins. *Biochim Biophys Acta - Biomembr*. doi:10.1016/j.bbamem.2013.04.012.
106. Carulla N, et al. (2009) Experimental characterization of disordered and ordered aggregates populated during the process of amyloid fibril formation. *PNAS*. doi:10.1073/pnas.0812227106.
107. Carulla N, et al. (2005) Molecular recycling within amyloid fibrils. *Nature* 436:554–558.
108. Jiménez JL, et al. (1999) Cryo-electron microscopy structure of an SH3 amyloid fibril and model of the molecular packing. *EMBO J* 18:815–821.
109. Bayro MJ, et al. (2010) High-resolution MAS NMR analysis of PI3-SH3 amyloid fibrils: Backbone conformation and implications for protofilament assembly and structure. *Biochemistry* 49:7474–7484.
110. Hull RL, et al. (2009) Amyloid formation in human IAPP transgenic mouse islets and pancreas, and human pancreas, is not associated with endoplasmic reticulum stress. *Diabetologia* 52(6):1102–11.
111. Kang J, et al. (1987) The precursor of Alzheimer's disease amyloid A4 protein resembles a cell-surface receptor. *Nature*. doi:10.1038/325733a0.
112. Radtke R Statistiken zum Thema Demenz weltweit. Available at: https://de.statista.com/themen/2032/demenzerkrankungen-weltweit/ [Accessed January 14, 2021].
113. Dorszewska J, Prendecki M, Oczkowska A, Dezor M, Kozubski W (2016) Molecular Basis of Familial and Sporadic Alzheimer's Disease. *Curr Alzheimer Res*. doi:10.2174/1567205013666160314150501.
114. Haass C, Selkoe DJ (1993) Cellular processing of β-amyloid precursor protein and the genesis of amyloid β-peptide. *Cell*. doi:10.1016/0092-8674(93)90312-E.
115. O'Brien RJ, Wong PC (2011) Amyloid precursor protein processing and alzheimer's disease. *Annu Rev Neurosci*. doi:10.1146/annurev-neuro-061010-113613.
116. Sorbi S, et al. (2001) Genetic risk factors in familial Alzheimer's disease. *Mechanisms of Ageing and Development* doi:10.1016/S0047-6374(01)00308-6.

117. Wiseman FK, et al. (2015) A genetic cause of Alzheimer disease: Mechanistic insights from Down syndrome. *Nat Rev Neurosci*. doi:10.1038/nrn3983.
118. Tönnies E, Trushina E (2017) Oxidative Stress, Synaptic Dysfunction, and Alzheimer's Disease. *J Alzheimer's Dis*. doi:10.3233/JAD-161088.
119. Glenner GG, Wong CW (1984) Alzheimer's disease: Initial report of the purification and characterization of a novel cerebrovascular amyloid protein. *Biochem Biophys Res Commun*. doi:10.1016/S0006-291X(84)80190-4.
120. Müller UC, Deller T, Korte M (2017) Not just amyloid: Physiological functions of the amyloid precursor protein family. *Nat Rev Neurosci*. doi:10.1038/nrn.2017.29.
121. Kuhn PH, et al. (2010) ADAM10 is the physiologically relevant, constitutive α-secretase of the amyloid precursor protein in primary neurons. *EMBO J*. doi:10.1038/emboj.2010.167.
122. Vassar R, et al. (1999) β-Secretase cleavage of Alzheimer's amyloid precursor protein by the transmembrane aspartic protease BACE. *Science*. doi:10.1126/science.286.5440.735.
123. Evin G (2016) Future Therapeutics in Alzheimer's Disease: Development Status of BACE Inhibitors. *BioDrugs*. doi:10.1007/s40259-016-0168-3.
124. Andrew RJ, Kellett KAB, Thinakaran G, Hooper NM (2016) A Greek tragedy: The growing complexity of Alzheimer amyloid precursor protein proteolysis. *J Biol Chem* 291(37). doi:10.1074/jbc.R116.746032.
125. Kummer MP, Heneka MT (2014) Truncated and modified amyloid-beta species. *Alzheimer's Res Ther* 6(3). doi:10.1186/alzrt258.
126. Bibl M, et al. (2012) Characterization of cerebrospinal fluid aminoterminally truncated and oxidized amyloid-β peptides. *Proteomics - Clin Appl* 6(3–4):163–169.
127. Soucek T, Cumming R, Dargusch R, Maher P, Schubert D (2003) The regulation of glucose metabolism by HIF-1 mediates a neuroprotective response to amyloid beta peptide. *Neuron*. doi:10.1016/S0896-6273(03)00367-2.
128. Kamenetz F, et al. (2003) APP Processing and Synaptic Function. *Neuron*. doi:10.1016/S0896-6273(03)00124-7.
129. Brothers HM, Gosztyla ML, Robinson SR (2018) The physiological roles of amyloid-β peptide hint at new ways to treat Alzheimer's disease. *Front Aging Neurosci*. doi:10.3389/fnagi.2018.00118.
130. Selkoe DJ, Hardy J (2016) The amyloid hypothesis of Alzheimer's disease at 25 years. *EMBO Mol Med*. doi:10.15252/emmm.201606210.
131. Hardy JA, Higgins GA (1992) Alzheimer's disease: The amyloid cascade hypothesis. *Science*. doi:10.1126/science.1566067.
132. Katzman R, et al. (1988) Clinical, pathological, and neurochemical changes in dementia: A subgroup with preserved mental status and numerous neocortical plaques. *Ann Neurol*. doi:10.1002/ana.410230206.
133. Aizenstein HJ, et al. (2008) Frequent amyloid deposition without significant cognitive impairment among the elderly. *Arch Neurol*. doi:10.1001/archneur.65.11.1509.
134. Teplow DB, Kirkitadze MD, Bitan G (2002) Paradigm shifts in Alzheimer's disease and other neurodegenerative disorders: The emerging role of oligomeric assemblies. *J Neurosci Res*.
135. Treusch S, Cyr DM, Lindquist S (2009) Amyloid deposits: Protection against toxic

protein species? *Cell Cycle* 8(11). doi:10.4161/cc.8.11.8503.
136. Ricciarelli R, Fedele E (2017) The Amyloid Cascade Hypothesis in Alzheimer's Disease: It's Time to Change Our Mind. *Curr Neuropharmacol*. doi:10.2174/1570159x15666170116143743.
137. Polanco JC, et al. (2018) Amyloid-β and tau complexity - Towards improved biomarkers and targeted therapies. *Nat Rev Neurol* 14(1). doi:10.1038/nrneurol.2017.162.
138. Yiannopoulou KG, Anastasiou AI, Zachariou V, Pelidou SH (2019) Reasons for failed trials of disease-modifying treatments for alzheimer disease and their contribution in recent research. *Biomedicines*. doi:10.3390/biomedicines7040097.
139. Doody RS, et al. (2013) A Phase 3 Trial of Semagacestat for Treatment of Alzheimer's Disease. *N Engl J Med*. doi:10.1056/nejmoa1210951.
140. Muntimadugu E, et al. (2016) Intranasal delivery of nanoparticle encapsulated tarenflurbil: A potential brain targeting strategy for Alzheimer's disease. *Eur J Pharm Sci*. doi:10.1016/j.ejps.2016.05.012.
141. Egan MF, et al. (2019) Randomized Trial of Verubecestat for Prodromal Alzheimer's Disease. *N Engl J Med*. doi:10.1056/nejmoa1812840.
142. Henley D, et al. (2019) Preliminary Results of a Trial of Atabecestat in Preclinical Alzheimer's Disease. *N Engl J Med*. doi:10.1056/nejmc1813435.
143. Mullard A (2019) Anti-amyloid failures stack up as Alzheimer antibody flops. *Nat Rev Drug Discov*. doi:10.1038/d41573-019-00064-1.
144. Jack CR, et al. (2010) Hypothetical model of dynamic biomarkers of the Alzheimer's pathological cascade. *Lancet Neurol*. doi:10.1016/S1474-4422(09)70299-6.
145. Volloch V, Olsen B, Rits S (2019) Alzheimer's Disease Prevention and Treatment: Case for Optimism. *Ann Integr Mol Med*. doi:10.33597/aimm.02-1008.
146. Kulawik A, Heise H, Zafiu C, Willbold D, Bannach O (2018) Advancements of the sFIDA method for oligomer-based diagnostics of neurodegenerative diseases. *FEBS Lett*. doi:10.1002/1873-3468.12983.
147. Herrmann Y, et al. (2017) sFIDA automation yields sub-femtomolar limit of detection for Aβ aggregates in body fluids. *Clin Biochem*. doi:10.1016/j.clinbiochem.2016.11.001.
148. Nabers A, et al. (2018) Amyloid blood biomarker detects Alzheimer's disease. *EMBO Mol Med*. doi:10.15252/emmm.201708763.
149. Nabers A, Hafermann H, Wiltfang J, Gerwert K (2019) Aβ and tau structure-based biomarkers for a blood- and CSF-based two-step recruitment strategy to identify patients with dementia due to Alzheimer's disease. *Alzheimer's Dement Diagnosis, Assess Dis Monit*. doi:10.1016/j.dadm.2019.01.008.
150. Ittner LM, Götz J (2011) Amyloid-β and tau - A toxic pas de deux in Alzheimer's disease. *Nat Rev Neurosci*. doi:10.1038/nrn2967.
151. Bekris LM, Yu CE, Bird TD, Tsuang DW (2010) Review article: Genetics of Alzheimer disease. *J Geriatr Psychiatry Neurol*. doi:10.1177/0891988710383571.
152. Campion D, et al. (1999) Early-onset autosomal dominant Alzheimer disease: Prevalence, genetic heterogeneity, and mutation spectrum. *Am J Hum Genet*. doi:10.1086/302553.
153. Brickell KL, et al. (2006) Early-onset Alzheimer disease in families with late-onset alzheimer disease: A potential important subtype of familial Alzheimer disease.

Arch Neurol. doi:10.1001/archneur.63.9.1307.
154. Janssen JC, et al. (2003) Early onset familial Alzheimer's disease: Mutation frequency in 31 families. *Neurology*. doi:10.1212/01.WNL.0000042088.22694.E3.
155. Alzforum MUTATIONS APP. Available at: https://www.alzforum.org/mutations/app [Accessed January 14, 2021].
156. Bernstein SL, et al. (2005) Amyloid β-protein: Monomer structure and early aggregation states of Aβ42 and its Pro19 alloform. *J Am Chem Soc*. doi:10.1021/ja044531p.
157. Hendriks L, et al. (1992) Presenile dementia and cerebral haemorrhage linked to a mutation at codon 692 of the β–amyloid precursor protein gene. *Nat Genet*. doi:10.1038/ng0692-218.
158. Levy E, et al. (1990) Mutation of the Alzheimer's disease amyloid gene in hereditary cerebral hemorrhage, Dutch type. *Science*. doi:10.1126/science.2111584.
159. De Jonghe C, et al. (1998) Flemish and Dutch mutations in amyloid β precursor protein have different effects on amyloid β secretion. *Neurobiol Dis*. doi:10.1006/nbdi.1998.0202.
160. Nilsberth C, et al. (2001) The "Arctic" APP mutation (E693G) causes Alzheimer's disease by enhanced Aβ protofibril formation. *Nat Neurosci*. doi:10.1038/nn0901-887.
161. Tomiyama T, et al. (2008) A new amyloid β variant favoring oligomerization in Alzheimer's-type dementia. *Ann Neurol*. doi:10.1002/ana.21321.
162. Inayathullah M, Teplow DB (2011) Structural dynamics of the ΔE22 (Osaka) familial Alzheimer's disease-linked amyloid β-protein. *Amyloid*. doi:10.3109/13506129.2011.580399.
163. Grabowski TJ, Cho HS, Vonsattel JPG, William Rebeck G, Greenberg SM (2001) Novel amyloid precursor protein mutation in an Iowa family with dementia and severe cerebral amyloid angiopathy. *Ann Neurol*. doi:10.1002/ana.1009.
164. Greenberg SM, et al. (2003) Hemorrhagic stroke associated with the Iowa amyloid precursor protein mutation. *Neurology*. doi:10.1212/01.WNL.0000050140.10044.A8.
165. Mok T, et al. (2014) Familial cerebral amyloid angiopathy due to the iowa mutation in an Irish family. *Can J Neurol Sci*. doi:10.1017/S031716710001859X.
166. Iwanowski P, Kozubski W, Losy J (2015) Familial cerebral amyloid angiopathy due to the iowa mutation in an irish family. *J Neurol Sci* 356(1–2):202–204.
167. Rogers Bowman M (2019) APP Upp: Mutation Nixes Six Amino Acids from Aβ, Spurs Aggregation. Available at: https://www.alzforum.org/news/conference-coverage/app-upp-mutation-nixes-six-amino-acids-av-spurs-aggregation [Accessed January 28, 2020].
168. Heneka MT, O'Banion MK, Terwel D, Kummer MP (2010) Neuroinflammatory processes in Alzheimer's disease. *J Neural Transm*. doi:10.1007/s00702-010-0438-z.
169. Nussbaum JM, et al. (2012) Prion-like behaviour and tau-dependent cytotoxicity of pyroglutamylated amyloid-β. *Nature*. doi:10.1038/nature11060.
170. Dammers C, et al. (2017) Pyroglutamate-Modified Amyloid-β(3–42) Shows α-Helical Intermediates before Amyloid Formation. *Biophys J*. doi:10.1016/j.bpj.2017.03.007.

171. Mori H, Takio K, Ogawara M, Selkoe DJ (1992) Mass spectrometry of purified amyloid β protein in Alzheimer's disease. *J Biol Chem*. doi:10.1016/s0021-9258(18)41896-0.
172. Saido TC, et al. (1995) Dominant and differential deposition of distinct β-amyloid peptide species, AβN3(pE), in senile plaques. *Neuron*. doi:10.1016/0896-6273(95)90301-1.
173. Schilling S, Hoffmann T, Manhart S, Hoffmann M, Demuth HU (2004) Glutaminyl cyclases unfold glutamyl cyclase activity under mild acid conditions. *FEBS Lett*. doi:10.1016/S0014-5793(04)00300-X.
174. Dammers C, et al. (2015) Purification and Characterization of Recombinant N-Terminally Pyroglutamate-Modified Amyloid-β Variants and Structural Analysis by Solution NMR Spectroscopy. *PLoS ONE* 10(10):e0139710.
175. Scilligence (2017) TouchMol. Available at: http://www.elncloud.com/touchmol/.
176. Kumar S, et al. (2016) Phosphorylation of the amyloid β-peptide at Ser26 stabilizes oligomeric assembly and increases neurotoxicity. *Acta Neuropathol*. doi:10.1007/s00401-016-1546-0.
177. Kumar S, et al. (2011) Extracellular phosphorylation of the amyloid β 2-peptide promotes formation of toxic aggregates during the pathogenesis of Alzheimer's disease. *EMBO J*. doi:10.1038/emboj.2011.138.
178. Kumar S, et al. (2013) Early intraneuronal accumulation and increased aggregation of phosphorylated Abeta in a mouse model of Alzheimer's disease. *Acta Neuropathol*. doi:10.1007/s00401-013-1107-8.
179. Rezaei-Ghaleh N, Kumar S, Walter J, Zweckstetter M (2016) Phosphorylation interferes with maturation of amyloid-β fibrillar structure in the N terminus. *J Biol Chem*. doi:10.1074/jbc.M116.728956.
180. Goodenough G, Hern K (2021) *Lilly's Donanemab Slows Clinical Decline of Alzheimer's Disease in Positive Phase 2 Trial* (Indianapolis) Available at: https://investor.lilly.com/news-releases/news-release-details/lillys-donanemab-slows-clinical-decline-alzheimers-disease.
181. Gremer L, et al. (2017) Fibril structure of amyloid-β(1–42) by cryo–electron microscopy. *Science* 358(6359):116–119.
182. Fitzpatrick AWP, et al. (2017) Cryo-EM structures of tau filaments from Alzheimer's disease. *Nature* 547(7662):185–190.
183. Arakhamia T, et al. (2020) Posttranslational Modifications Mediate the Structural Diversity of Tauopathy Strains. *Cell*. doi:10.1016/j.cell.2020.01.027.
184. Iadanza MG, et al. (2018) The structure of a β2-microglobulin fibril suggests a molecular basis for its amyloid polymorphism. *Nat Commun* 9(1):4517.
185. Guerrero-Ferreira R, et al. (2018) Cryo-EM structure of alpha-synuclein fibrils. *eLife* 7:e360402.
186. Cao Q, Boyer DR, Sawaya MR, Ge P, Eisenberg DS (2020) Cryo-EM structure and inhibitor design of human IAPP (amylin) fibrils. *Nat Struct Mol Biol*. doi:10.1038/s41594-020-0435-3.
187. Kollmer M, et al. (2019) Cryo-EM structure and polymorphism of Aβ amyloid fibrils purified from Alzheimer's brain tissue. *Nat Commun*. doi:10.1038/s41467-019-12683-8.
188. Radamaker L, et al. (2021) Cryo-EM reveals structural breaks in a patient-derived amyloid fibril from systemic AL amyloidosis. *Nat Commun* 12(1).

doi:10.1038/s41467-021-21126-2.
189. Radamaker L, et al. (2019) Cryo-EM structure of a light chain-derived amyloid fibril from a patient with systemic AL amyloidosis. *Nat Commun* 10(1):1103.
190. Zhang W, et al. (2020) Novel tau filament fold in corticobasal degeneration. *Nature*. doi:10.1038/s41586-020-2043-0.
191. Zhao K, et al. (2020) Parkinson's disease-related phosphorylation at Tyr39 rearranges α-synuclein amyloid fibril structure revealed by cryo-EM. *PNAS*. doi:10.1073/pnas.1922741117.
192. Li C, Li D (2021) Hierarchical chemical determination of amyloid polymorphs in neurodegenerative disease. *Nat Chem Biol*. doi:https://doi.org/10.1038/s41589-020-00708-z.
193. Shivashankar M, Mani D (2011) A brief overview of diabetes. *Int J Pharm Pharm Sci*.
194. Vecchio I, Tornali C, Bragazzi NL, Martini M (2018) The discovery of insulin: An important milestone in the history of medicine. *Front Endocrinol (Lausanne)*. doi:10.3389/fendo.2018.00613.
195. The top 10 causes of death (2020) Available at: https://www.who.int/news-room/fact-sheets/detail/the-top-10-causes-of-death.
196. Katsarou A, et al. (2017) Type 1 diabetes mellitus. *Nat Rev Dis Prim*. doi:10.1038/nrdp.2017.16.
197. Buchanan TA, Xiang AH (2005) Gestational diabetes mellitus. *J Clin Invest*. doi:10.1172/JCI200524531.
198. DeFronzo RA, et al. (2015) Type 2 diabetes mellitus. *Nat Rev Dis Prim*. doi:10.1038/nrdp.2015.19.
199. Jurgens CA, et al. (2011) β-Cell loss and β-cell apoptosis in human type 2 diabetes are related to islet amyloid deposition. *Am J Pathol* 178(6):2632–2640.
200. Westermark P, Andersson A, Westermark GT (2011) Islet amyloid polypeptide, islet amyloid, and diabetes mellitus. *Physiol Rev* 91(3):795–826.
201. Akter R, et al. (2016) Islet Amyloid Polypeptide: Structure, Function, and Pathophysiology. *J Diabetes Res*. doi:10.1155/2016/2798269.
202. Westermark P, Wernstedt C, Wilander E, Sletten K (1986) A novel peptide in the calcitonin gene related peptide family as an amyloid fibril protein in the endocrine pancreas. *Biochem Biophys Res Commun*. doi:10.1016/0006-291X(86)90708-4.
203. Zhang S, et al. (2014) The pathogenic mechanism of diabetes varies with the degree of overexpression and oligomerization of human amylin in the pancreatic islet β cells. *FASEB J* 28(12):5083–5096.
204. Masters SL, et al. (2010) Activation of the NLRP3 inflammasome by islet amyloid polypeptide provides a mechanism for enhanced IL-1β 2 in type 2 diabetes. *Nat Immunol* 11(10):897–904.
205. Janson J, Ashley RH, Harrison D, McIntyre S, Butler PC (1999) The mechanism of islet amyloid polypeptide toxicity is membrane disruption by intermediate-sized toxic amyloid particles. *Diabetes* 48(3):491–8.
206. Hull RL, Westermark GT, Westermark P, Kahn SE (2004) Islet amyloid: A critical entity in the pathogenesis of type 2 diabetes. *J Clin Endocrinol Metab*. doi:10.1210/jc.2004-0405.
207. Leibson CL, et al. (1997) Risk of Dementia among Persons with Diabetes Mellitus:

A Population-based Cohort Study. *Am J Epidemiol* 145(4):301–308.
208. Peila R, Rodriguez BL, Launer LJ (2002) Type 2 Diabetes, APOE Gene, and the Risk for Dementia and Related Pathologies. *Diabetes* 51(April):1256–1262.
209. Oskarsson ME, et al. (2015) In vivo seeding and cross-seeding of localized amyloidosis: A molecular link between type 2 diabetes and Alzheimer disease. *Am J Pathol* 185(3):834–846.
210. Moreno-Gonzalez I, et al. (2017) Molecular interaction between type 2 diabetes and Alzheimer's disease through cross-seeding of protein misfolding. *Mol Psychiatry* 9:1327–1334.
211. Bedrood S, et al. (2012) Fibril structure of human islet amyloid polypeptide. *J Biol Chem* 287(8):5235–41.
212. Wiltzius JJW, et al. (2008) Atomic structure of the cross-β spine of islet amyloid polypeptide (amylin). *Protein Sci* 17(9). doi:10.1110/ps.036509.108.
213. Kajava A V., Aebi U, Steven AC (2005) The parallel superpleated beta-structure as a model for amyloid fibrils of human amylin. *J Mol Biol* 348(2):247–52.
214. Luca S, Yau WM, Leapman R, Tycko R (2007) Peptide conformation and supramolecular organization in amylin fibrils: Constraints from solid-state NMR. *Biochemistry* 46(47):13505–22.
215. Weirich F, et al. (2016) Structural characterization of fibrils from recombinant human islet amyloid polypeptide by solid-state NMR: The central FGAILS segment is part of the β-sheet core. *PLoS ONE* 11(9):e0161243.
216. Robinson AL (1986) Electron microscope inventors share nobel physics prize. *Science*. doi:10.1126/science.234.4778.821.
217. Borries B, Ruska E (1939) Ein Uebermikroskop fuer Forschungsindustrie. *Naturwissenschaften* 27:577–582.
218. Ruska E (1934) über Fortschritte im Bau und in der Leistung des magnetischen Elektronenmikroskops. *Zeitschrift für Phys*. doi:10.1007/BF01333326.
219. Ruska E (1986) The development of the electron microscope and of early electron microscopy (Nobel lecture). Available at: http://ernst.ruska.de/daten_e/library/documents/999.nobellecture/lecture.html#E [Accessed January 15, 2021].
220. Jensen GJ, Caltech (2015) *Getting Started in Cryo-EM, Part 1: The Column* (Caltech, USA) Available at: https://www.youtube.com/watch?v=hc2s4uSbpyI&list=PL8_xPU5epJdctoHdQjpfHmd_z9WvGxK8-&index=8.
221. Williams DB, Carter CB (1996) *Transmission electron microscopy: A textbook for materials science* (Springer, Boston, MA, Boston) doi:10.1007/978-1-4757-2519-3_1.
222. Brenner S, Horne RW (1959) A negative staining method for high resolution electron microscopy of viruses. *BBA - Biochim Biophys Acta*. doi:10.1016/0006-3002(59)90237-9.
223. De Rosier DJ, Klug A (1968) Reconstruction of three dimensional structures from electron micrographs. *Nature*. doi:10.1038/217130a0.
224. DeRosier DJ, Moore PB (1970) Reconstruction of three-dimensional images from electron micrographs of structures with helical symmetry. *J Mol Biol*. doi:10.1016/0022-2836(70)90036-7.
225. De Carlo S, Harris JR (2011) Negative staining and cryo-negative staining of

macromolecules and viruses for TEM. *Micron*. doi:10.1016/j.micron.2010.06.003.
226. Scarff CA, Fuller MJG, Thompson RF, Iadaza MG (2018) Variations on negative stain electron microscopy methods: Tools for tackling challenging systems. *J Vis Exp*. doi:10.3791/57199.
227. Taylor KA, Glaeser RM (1976) Electron microscopy of frozen hydrated biological specimens. *J Ultrasructure Res*. doi:10.1016/S0022-5320(76)80099-8.
228. Taylor KA, Glaeser RM (1974) Electron diffraction of frozen, hydrated protein crystals. *Science*. doi:10.1126/science.186.4168.1036.
229. Adrian M, Dubochet J, Lepault J, McDowall AW (1984) Cryo-electron microscopy of viruses. *Nature*. doi:10.1038/308032a0.
230. McMullan G, Faruqi AR, Henderson R (2016) Direct Electron Detectors. *Methods in Enzymology* doi:10.1016/bs.mie.2016.05.056.
231. Krivanek OL, Mooney PE (1993) Applications of slow-scan CCD cameras in transmission electron microscopy. *Ultramicroscopy*. doi:10.1016/0304-3991(93)90216-K.
232. Xuong N-H, et al. (2004) First use of a high-sensitivity active pixel sensor array as a detector for electron microscopy. *Sensors and Camera Systems for Scientific, Industrial, and Digital Photography Applications V* doi:10.1117/12.526021.
233. Fernández JJ (2008) High performance computing in structural determination by electron cryomicroscopy. *J Struct Biol*. doi:10.1016/j.jsb.2008.07.005.
234. Cianfrocco MA, Leschziner AE (2015) Low cost, high performance processing of single particle cryo-electron microscopy data in the cloud. *eLife*. doi:10.7554/eLife.06664.
235. Yu X, Jin L, Zhou ZH (2008) 3.88 Å structure of cytoplasmic polyhedrosis virus by cryo-electron microscopy. *Nature*. doi:10.1038/nature06893.
236. Böttcher B, Wynne SA, Crowther RA (1997) Determination of the fold of the core protein of hepatitis B virus by electron cryomicroscopy. *Nature*. doi:10.1038/386088a0.
237. Zhang X, et al. (2008) Near-atomic resolution using electron cryomicroscopy and single-particle reconstruction. *PNAS*. doi:10.1073/pnas.0711623105.
238. Frank J (2010) *Three-Dimensional Electron Microscopy of Macromolecular Assemblies* doi:10.1093/acprof:oso/9780195182187.001.0001.
239. Penczek PA, Grassucci RA, Frank J (1994) The ribosome at improved resolution: New techniques for merging and orientation refinement in 3D cryo-electron microscopy of biological particles. *Ultramicroscopy*. doi:10.1016/0304-3991(94)90038-8.
240. Van Heel M (1987) Angular reconstitution: A posteriori assignment of projection directions for 3D reconstruction. *Ultramicroscopy*. doi:10.1016/0304-3991(87)90078-7.
241. EM Data Resource - EM Software Available at: https://www.emdataresource.org/emsoftware.html.
242. Scheres SHW (2012) RELION: Implementation of a Bayesian approach to cryo-EM structure determination. *J Struct Biol* 180:519–530.
243. Europe PDB in Trends and distribution of software package usage for released maps. Available at: https://www.ebi.ac.uk/pdbe/emdb/statistics_software.html/ [Accessed October 9, 2020].
244. Gewering T, Möller A (2020) Neue Möglichkeiten für die Strukturbestimmung

von Membranproteinen. *BioSpektrum*. doi:10.1007/s12268-020-1469-0.
245. Thompson RF, Walker M, Siebert CA, Muench SP, Ranson NA (2016) An introduction to sample preparation and imaging by cryo-electron microscopy for structural biology. *Methods*. doi:10.1016/j.ymeth.2016.02.017.
246. Gewering T, Januliene D, Ries AB, Moeller A (2018) Know your detergents: A case study on detergent background in negative stain electron microscopy. *J Struct Biol*. doi:10.1016/j.jsb.2018.05.008.
247. James ZM, et al. (2017) CryoEM structure of a prokaryotic cyclic nucleotide-gated ion channel. *PNAS*. doi:10.1073/pnas.1700248114.
248. Ghosh U, Thurber KR, Yau WM, Tycko R (2021) No Molecular structure of a prevalent amyloid-β fibril polymorph from Alzheimer's disease brain tissue. *PNAS* 118(4). doi:10.1073/pnas.2023089118.
249. Dobro MJ, Melanson LA, Jensen GJ, McDowall AW (2010) Plunge freezing for electron cryomicroscopy. *Methods in Enzymology* doi:10.1016/S0076-6879(10)81003-1.
250. Brüggeller P, Mayer E (1980) Complete vitrification in pure liquid water and dilute aqueous solutions. *Nature*. doi:10.1038/288569a0.
251. Fahy GM, MacFarlane DR, Angell CA, Meryman HT (1984) Vitrification as an approach to cryopreservation. *Cryobiology*. doi:10.1016/0011-2240(84)90079-8.
252. Nogales E, Scheres SHW (2015) Cryo-EM: A Unique Tool for the Visualization of Macromolecular Complexity. *Mol Cell*. doi:10.1016/j.molcel.2015.02.019.
253. Passmore LA, Russo CJ (2016) Specimen Preparation for High-Resolution Cryo-EM. *Methods in Enzymology* doi:10.1016/bs.mie.2016.04.011.
254. Zheng SQ, Palovcak E, Armache J-P, Cheng Y, Agard DA (2017) MotionCor2: Anisotropic correction of beam-induced motion for improved single-particle electron cryo-microscopy. *Nat Methods* 14:331–332.
255. Mindell JA, Grigorieff N (2003) Accurate determination of local defocus and specimen tilt in electron microscopy. *J Struct Biol*. doi:10.1016/S1047-8477(03)00069-8.
256. Zhang K (2016) Gctf: Real-time CTF determination and correction. *J Struct Biol* 193(1):1–12.
257. Zhu J, Penczek PA, Schröder R, Frank J (1997) Three-dimensional reconstruction with contrast transfer function correction from energy-filtered cryoelectron micrographs: Procedure and application to the 70S Escherichia coli ribosome. *J Struct Biol*. doi:10.1006/jsbi.1997.3845.
258. Jensen G, Caltech (2015) *Getting Started in Cryo-EM, Part 3: The Contrast Transfer Function* (Caltech, USA) Available at: https://www.youtube.com/watch?v=mPynoF2j6zc&list=PL8_xPU5epJdctoHdQjpfHmd_z9WvGxK8-&index=24.
259. Rohou A, Grigorieff N (2015) CTFFIND4: Fast and accurate defocus estimation from electron micrographs. *J Struct Biol* 192:216–221.
260. Punjani A, Rubinstein JL, Fleet DJ, Brubaker MA (2017) CryoSPARC: Algorithms for rapid unsupervised cryo-EM structure determination. *Nat Methods*. doi:10.1038/nmeth.4169.
261. Moriya T, et al. (2017) High-resolution single particle analysis from electron cryo-microscopy images using SPHIRE. *J Vis Exp*. doi:10.3791/55448.
262. Wagner T, et al. (2019) SPHIRE-crYOLO is a fast and accurate fully automated

particle picker for cryo-EM. *Commun Biol*. doi:10.1038/s42003-019-0437-z.
263. Zivanov J, et al. (2018) New tools for automated high-resolution cryo-EM structure determination in RELION-3. *eLife*. doi:10.7554/eLife.42166.
264. Wagner T, Raunser S (2020) The evolution of SPHIRE-crYOLO particle picking and its application in automated cryo-EM processing workflows. *Commun Biol*. doi:10.1038/s42003-020-0790-y.
265. He S, Scheres SHW (2017) Helical reconstruction in RELION. *J Struct Biol* 198:163–176.
266. Scheres SHW (2020) Amyloid structure determination in RELION-3.1. *Acta Crystallogr Sect D Struct Biol*. doi:10.1107/S2059798319016577.
267. Thuman-Commike PA (2001) Single particle macromolecular structure determination via electron microscopy. *FEBS Lett*. doi:10.1016/S0014-5793(01)02804-6.
268. Emsley P, Lohkamp B, Scott WG, Cowtan K (2010) Features and development of Coot. *Acta Crystallogr Sect D Biol Crystallogr* 66:486–501.
269. Emsley P, Cowtan K (2004) Coot: Model-building tools for molecular graphics. *Acta Crystallogr Sect D Biol Crystallogr* 60:2126–2132.
270. Adams PD, et al. (2010) PHENIX: A comprehensive Python-based system for macromolecular structure solution. *Acta Crystallogr Sect D Biol Crystallogr* 66:213–221.
271. Falcon B, et al. (2019) Novel tau filament fold in chronic traumatic encephalopathy encloses hydrophobic molecules. *Nature* 568(7752):420–423.
272. Li B, et al. (2018) Cryo-EM of full-length α-synuclein reveals fibril polymorphs with a common structural kernel. *Nat Commun* 9:3609.
273. Glynn C, et al. (2020) Cryo-EM structure of a human prion fibril with a hydrophobic, protease-resistant core. *Nat Struct Mol Biol* 27:417–423.
274. Reinhold J (2012) *Quantentheorie der Moleküle* (Springer Spektrum). 4th Ed. doi:10.1007/978-3-8351-9049-8.
275. Diaz R, Rice WJ, Stokes DL (2010) Fourier-bessel reconstruction of helical assemblies. *Methods in Enzymology* doi:10.1016/S0076-6879(10)82005-1.
276. He S (2018) Helical Reconstruction in RELION. Dissertation (University of Cambridge). doi:https://doi.org/10.17863/CAM.31456.
277. Morris KL, Serpell LC (2012) X-ray fibre diffraction studies of amyloid fibrils. *Methods Mol Biol*. doi:10.1007/978-1-61779-551-0_9.
278. Wigge C, Stefanovic A, Radjainia M (2021) The rapidly evolving role of cryo-EM in drug design. *Drug Discov Today Technol*. doi:10.1016/j.ddtec.2020.12.003.
279. Vettore N, Buell AK (2019) Thermodynamics of amyloid fibril formation from chemical depolymerization. *Phys Chem Chem Phys*. doi:10.1039/c9cp04524d.
280. Meckelburg P (2018) Festkörper-NMR-Spektroskopie von fibrillärem Amyloid-beta. Master Thesis (Heinrich-Heine-Universität Düsseldorf).
281. Kim G, Weiss SJ, Levine RL (2014) Methionine oxidation and reduction in proteins. *Biochim Biophys Acta - Gen Subj* 1840(2). doi:10.1016/j.bbagen.2013.04.038.
282. Liang X, et al. (2012) Characterization of methionine oxidation and methionine sulfoxide reduction using methionine-rich cysteine-free proteins. *BMC Biochem* 13(1). doi:10.1186/1471-2091-13-21.
283. Sun S, et al. (2008) Deriving the probabilities of water loss and ammonia loss for

amino acids from tandem mass spectra. *J Proteome Res*. doi:10.1021/pr070479v.
284. Neta P, Pu QL, Kilpatrick L, Yang X, Stein SE (2007) Dehydration Versus Deamination of N-Terminal Glutamine in Collision-Induced Dissociation of Protonated Peptides. *J Am Soc Mass Spectrom*. doi:10.1016/j.jasms.2006.08.016.
285. Maurstad G, Prass M, Serpell LC, Sikorski P (2009) Dehydration stability of amyloid fibrils studied by AFM. *Eur Biophys J*. doi:10.1007/s00249-009-0526-x.
286. Volpatti LR, Vendruscolo M, Dobson CM, Knowles TPJ (2013) A clear view of polymorphism, twist, and chirality in amyloid fibril formation. *ACS Nano*. doi:10.1021/nn406121w.
287. Huber ST, Kuhm T, Sachse C (2018) Automated tracing of helical assemblies from electron cryo-micrographs. *J Struct Biol* 202(1). doi:10.1016/j.jsb.2017.11.013.
288. Tornquist M, et al. (2020) Ultrastructural evidence for self-replication of alzheimer-associated Aβ42 amyloid along the sides of fibrils. *PNAS*. doi:10.1073/pnas.1918481117.
289. Nirmalraj PN, et al. (2020) Complete aggregation pathway of amyloid β (1-40) and (1-42) resolved on an atomically clean interface. *Sci Adv* 6(15). doi:10.1126/sciadv.aaz6014.
290. Ostendorf F, et al. (2008) How flat is an air-cleaved mica surface? *Nanotechnology*. doi:10.1088/0957-4484/19/30/305705.
291. Hoyer W, Cherny D, Subramaniam V, Jovin TM (2004) Rapid self-assembly of α-synuclein observed by in situ atomic force microscopy. *J Mol Biol* 340(1). doi:10.1016/j.jmb.2004.04.051.
292. Yang JT, Wu CSC, Martinez HM (1986) Calculation of Protein Conformation from Circular Dichroism. *Methods Enzymol* 130(C). doi:10.1016/0076-6879(86)30013-2.
293. Rezaei-Ghaleh N, et al. (2014) Turn plasticity distinguishes different modes of amyloid-β aggregation. *J Am Chem Soc* 136(13). doi:10.1021/ja411707y.
294. ThermoFisher Protein Standards and Ladders. Available at: https://www.thermofisher.com/de/de/home/life-science/protein-biology/protein-gel-electrophoresis/protein-standards-ladders.html [Accessed November 12, 2020].
295. Wang Z, Schröder GF (2012) Real-space refinement with DireX: From global fitting to side-chain improvements. *Biopolymers* 97(9):687–97.
296. Katsnelson A (2020) Did Disordered Proteins Help Launch Life on Earth? *ACS Cent Sci* 6(11). doi:10.1021/acscentsci.0c01499.
297. Owen MC, et al. (2019) Effects of in vivo conditions on amyloid aggregation. *Chem Soc Rev* 48(14):3946–3996.
298. Bansal A, et al. AA amyloid fibrils from diseased tissue are structurally different from in vitro formed SAA fibrils. *Nat Commun* (2021). doi:10.1038/s41467-021-21129-z.
299. Pothula KR, Smyrnova D, Schröder GF (2019) Clustering cryo-EM images of helical protein polymers for helical reconstructions. *Ultramicroscopy* 203. doi:10.1016/j.ultramic.2018.12.009.
300. Pettersen EF, et al. (2004) UCSF Chimera - A visualization system for exploratory research and analysis. *J Comput Chem* 25(13):1605–1612.
301. Goddard TD, et al. (2018) UCSF ChimeraX: Meeting modern challenges in visualization and analysis. *Protein Sci* 27(1):14–25.
302. Tang G, et al. (2007) EMAN2: An extensible image processing suite for electron

microscopy. *J Struct Biol*. doi:10.1016/j.jsb.2006.05.009.
303. Rehm H (2002) *Der Experimentator: Proteinbiochemie/Proteomics* (Spektrum Akademischer Verlag). 4th Ed. doi:10.1007/978-3-8274-2313-9.
304. Schägger H (2006) Tricine-SDS-PAGE. *Nat Protoc*. doi:10.1038/nprot.2006.4.
305. Ho SN, Hunt HD, Horton RM, Pullen JK, Pease LR (1989) Site-directed mutagenesis by overlap extension using the polymerase chain reaction. *Gene* 77(1). doi:10.1016/0378-1119(89)90358-2.
306. Arosio P, et al. (2016) Microfluidic diffusion analysis of the sizes and interactions of proteins under native solution conditions. *ACS Nano* 10(1). doi:10.1021/acsnano.5b04713.
307. Yates E V., et al. (2015) Latent analysis of unmodified biomolecules and their complexes in solution with attomole detection sensitivity. *Nat Chem* 7(10). doi:10.1038/nchem.2344.
308. Desjardins P, Conklin D (2010) NanoDrop microvolume quantitation of nucleic acids. *J Vis Exp* (45). doi:10.3791/2565.
309. Dammers C (2015) Structural analysis and aggregation of Alzheimer's disease related pyroglutamate-modified amyloid-β. Dissertation (Heinrich-Heine-Universität Düsseldorf).
310. Zhang-Haagen B, et al. (2016) Monomeric Amyloid beta peptide in hexafluoroisopropanol detected by small angle neutron scattering. *PLoS ONE*. doi:10.1371/journal.pone.0150267.
311. Broersen K, et al. (2011) A standardized and biocompatible preparation of aggregate-free amyloid beta peptide for biophysical and biological studies of Alzheimers disease. *Protein Eng Des Sel*. doi:10.1093/protein/gzr020.
312. O'Fágáin C (2004) Lyophilization of proteins. *Methods Mol Biol*. doi:10.1385/1-59259-655-x:309.
313. Greenfield NJ (2007) Using circular dichroism spectra to estimate protein secondary structure. *Nat Protoc* 1(6). doi:10.1038/nprot.2006.202.
314. Glish GL, Vachet RW (2003) The basics of mass spectrometry in the twenty-first century. *Nat Rev Drug Discov* 2(2). doi:10.1038/nrd1011.
315. Park J, Park J, Lee S, Roh S-H (2020) Grid selection strategy for high-resolution cryo-EM. *Korean Soc Struct Biol*. doi:10.34184/kssb.2020.8.2.41.
316. Russo CJ, Passmore LA (2016) Ultrastable gold substrates: Properties of a support for high-resolution electron cryomicroscopy of biological specimens. *J Struct Biol*. doi:10.1016/j.jsb.2015.11.006.
317. Russo CJ, Passmore LA (2016) Progress towards an optimal specimen support for electron cryomicroscopy. *Curr Opin Struct Biol*. doi:10.1016/j.sbi.2015.12.007.
318. Russo CJ, Passmore LA (2014) Ultrastable gold substrates for electron cryomicroscopy. *Science*. doi:10.1126/science.1259530.

XV List of figures

XVI Appendix

1 Publication I: Atomic structure of PI3-kinase SH3 amyloid fibrils by cryo-electron microscopy

Röder, C., Vettore, N., Mangels, L.N. *et al.* Atomic structure of PI3-kinase SH3 amyloid fibrils by cryo-electron microscopy. *Nat Commun* **10,** 3754 (2019). https://doi.org/10.1038/s41467-019-11320-8

nature COMMUNICATIONS

ARTICLE

https://doi.org/10.1038/s41467-019-11320-8 OPEN

Atomic structure of PI3-kinase SH3 amyloid fibrils by cryo-electron microscopy

Christine Röder[1,2], Nicola Vettore[2,6], Lena N. Mangels[2,6], Lothar Gremer[1,2], Raimond B.G. Ravelli[3], Dieter Willbold[1,2], Wolfgang Hoyer[1,2], Alexander K. Buell[2,4] & Gunnar F. Schröder[1,5]

High resolution structural information on amyloid fibrils is crucial for the understanding of their formation mechanisms and for the rational design of amyloid inhibitors in the context of protein misfolding diseases. The Src-homology 3 domain of phosphatidyl-inositol-3-kinase (PI3K-SH3) is a model amyloid system that plays a pivotal role in our basic understanding of protein misfolding and aggregation. Here, we present the atomic model of the PI3K-SH3 amyloid fibril with a resolution determined to 3.4 Å by cryo-electron microscopy (cryo-EM). The fibril is composed of two intertwined protofilaments that create an interface spanning 13 residues from each monomer. The model comprises residues 1–77 out of 86 amino acids in total, with the missing residues located in the highly flexible C-terminus. The fibril structure allows us to rationalise the effects of chemically conservative point mutations as well as of the previously reported sequence perturbations on PI3K-SH3 fibril formation and growth.

[1] Institute of Complex Systems, Structural Biochemistry (ICS-6) and JuStruct, Jülich Center for Structural Biology, Forschungszentrum Jülich, 52425 Jülich, Germany. [2] Institut für Physikalische Biologie, Heinrich-Heine-Universität Düsseldorf, 40225 Düsseldorf, Germany. [3] The Maastricht Multimodal Molecular Imaging Institute, Maastricht University, Universiteitssingel 50, 6229 ER Maastricht, The Netherlands. [4] Department of Biotechnology and Biomedicine, Technical University of Denmark, Søltofts Plads, 2800 Kgs Lyngby, Denmark. [5] Physics Department, Heinrich-Heine-Universität Düsseldorf, 40225 Düsseldorf, Germany. [6] These authors contributed equally: Nicola Vettore, Lena N. Mangels. Correspondence and requests for materials should be addressed to A.K.B. (email: alebu@dtu.dk) or to G.F.S. (email: gu.schroeder@fz-juelich.de)

Alzheimer's and Parkinson's Disease as well as spongiform encephalopathies are prominent examples of protein misfolding diseases[1]. These disorders are characterised by the presence of amyloid fibrils[2]. Amyloid fibrils are straight and unbranched thread-like homopolymeric protein assemblies, which are stabilised by backbone hydrogen bonding between individual peptide molecules. These interactions lead to a highly ordered, repetitive cross-β architecture, in which the β-strands run perpendicularly to the fibril axis.

It has been shown that in the case of neurodegenerative protein misfolding diseases, the final amyloid fibrils are often not the most cytotoxic species, but that small, oligomeric precursors are more hydrophobic and more mobile and hence more prone to deleterious interactions with cellular components[3]. However, recent progress in the mechanistic understanding of amyloid fibril formation shows that the mature fibrils can be the main source of toxic oligomers, due to their role as catalytic sites in secondary nucleation processes[4]. Furthermore, in the case of systemic amyloidosis diseases, where amyloid fibrils form in organs other than the brain, the amyloid fibrils themselves are the deleterious species, as their presence in large quantities can disrupt organ functions[5].

Until recently, structural information on amyloid fibrils could only be obtained from relatively low-resolution methods, such as X-ray fibre diffraction[6], limited proteolysis[7] and H/D exchange[8]. High-resolution structural information on amyloid fibrils has only become available in recent years through progress in solid state NMR spectroscopy (ssNMR)[9–11] and cryo-electron microscopy (cryo-EM). In particular cryo-EM enables atomic resolution structures of amyloid fibrils to be determined, and this has indeed been achieved in a few cases so far[12–23]. Such detailed structural information is crucial for the understanding of amyloid formation mechanisms, as well as for the rational design of inhibitors of the individual mechanistic steps, such as fibril nucleation and growth[24].

Here we present the high-resolution cryo-EM structure of amyloid fibrils of the Src-homology 3 domain of phosphatidylinositol-3-kinase (PI3K-SH3). SH3 domains are kinase subdomains of usually <100 amino acids length and have been found to be part of more than 350 proteins, ranging from kinases and GTPases to adaptor and structural proteins, within various organisms[25]. SH3 domains are known to play a significant role in several signalling pathways where they mediate protein-protein interactions by recognising PxxP sequence motifs[26,27]. The structure of natively folded PI3K-SH3, a domain consisting of 86 amino acids from bovine PI3K, has been well-characterised by X-ray crystallography and NMR spectroscopy[26,28].

Used initially as a model system for protein folding studies[29], PI3K-SH3 was among the first proteins discovered to form amyloid fibrils in the test tube, while not being associated to any known human disease[30]. Fibril formation was observed at acidic pH, where in contrast to the native fold at neutral pH[27,28], monomeric PI3K-SH3 lacks a well-defined secondary structure[30–32]. Since this discovery, PI3K-SH3 has played a pivotal role in advancing our fundamental understanding of the relationships between protein folding, misfolding and aggregation. Indeed, the hypothesis of the amyloid fibril as the most generic 'fold'[1] that a polypeptide can adopt was significantly shaped by the finding that PI3K-SH3 forms amyloid fibrils. Many pioneering studies on the basic biochemical, structural and mechanistic features of amyloid fibrils have been performed with PI3K-SH3. Early cryo-EM measurements highlighted the need for conformational rearrangement of the sequence within the fibril[33]. The important role of the destabilisation of native secondary structure elements and the need for non-native contacts and extensive structural rearrangements during the formation of fibrillar aggregates was also observed for a related SH3 domain[34]. Despite not being related to any human disease, PI3K-SH3 aggregates were shown to be cytotoxic, suggesting sequence-independent toxic properties of amyloid fibrils and their precursors[35]. PI3K-SH3 also provided insight into the kinetics of molecular recycling of the monomeric building blocks of the fibril[36], as well as into the dynamics of the formation of oligomeric precursors of amyloid fibrils[37].

The structure of PI3K-SH3 fibrils we present here is in agreement with previous ssNMR data[38], but we find that its interface is orthogonal to that suggested previously based on a low resolution reconstruction[33]. Indeed, the inter-filament interface in PI3K-SH3 fibrils is large compared to that of other amyloid fibrils determined to-date, and is formed from residues distant in primary sequence. With the atomic model we can rationalise the effect of newly designed, as well as previously reported sequence variants of PI3K-SH3 on the kinetics of fibril growth. Our study therefore not only adds important insight into the structural variety of amyloid fibrils, but also demonstrates how such structures can be used to rationalise the dynamics of protein assembly processes.

Results

Structure determination by cryo-EM. Fibril formation by the full-length PI3K-SH3 domain under acidic solution conditions[30] led to long, straight fibrils of which the main population could be structurally determined by cryo-EM (Fig. 1). High overall homogeneity of the preparation has been shown by atomic force microscopy (AFM) and negative staining EM imaging (Fig. 2, Supplementary Figs. 1 and 2). Nevertheless, two different morphologies could be distinguished in both AFM and EM images (Fig. 2, Supplementary Fig. 1). The predominant, thick morphology has a diameter of 7–8 nm while the other, thinner morphology exhibits about half the diameter of the thick fibril (Supplementary Fig. 2).

For cryo-EM imaging, samples of PI3K-SH3 amyloid fibrils were flash-frozen on Quantifoil cryo-EM grids and imaged with a Tecnai Arctica microscope (200 kV) equipped with a Falcon 3 direct electron detector (Supplementary Fig. 3). Image processing and helical reconstruction were performed with RELION-2[39–41]. A three-dimensional density map for the thick PI3K-SH3 fibril could be reconstructed to an overall resolution of 3.4 Å. The clear density of the fibril allowed us to build an atomic model for residues 1–77 out of a total of 86 amino acids (Fig. 1). The missing nine residues are located at the C-terminus, which shows blurred density likely due to substantial flexibility. Previously reported low-resolution cryo-EM[33] data are in good agreement with our structure (Supplementary Fig. 4).

Architecture of the PI3K-SH3 amyloid fibril. The thick PI3K-SH3 fibril is a left-handed helical structure consisting of two intertwined protofilaments, and is thus called DF (double filament) fibril. The handedness of the density reconstruction was determined by comparison with AFM images (see Methods and Supplementary Fig. 5). From an analysis of the fibril height profiles in AFM images, we determined the helical pitch to be 170 ± 10 nm in reasonable agreement with a pitch of 140 nm obtained from the cryo-EM structure.

Protofilament subunits (PI3K-SH3 monomers) are stacked in a parallel, in-register cross-β structure. The spacing between the layers of the cross-β structure is around 4.7 Å and well visible in the density (Supplementary Fig. 6). The subunits in the two opposing protofilaments are not on the same z-position along the fibril axis but are arranged in a staggered fashion (Fig. 1c). The helical symmetry is therefore described by a twist of 179.4 ° and

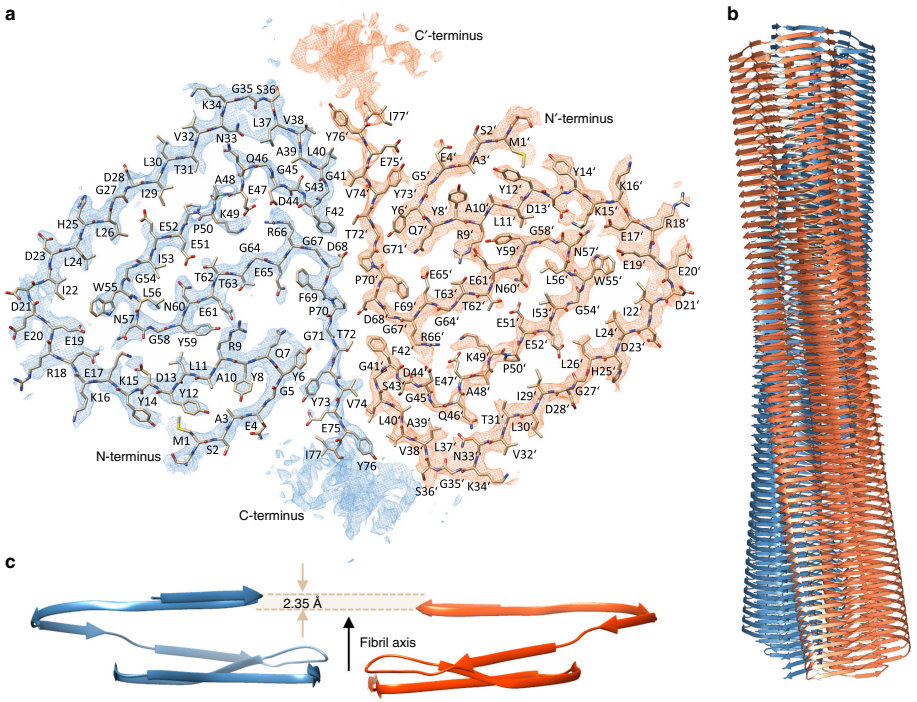

Fig. 1 Double Filament SH3 fibril structure. **a** Cross-section of the double filament (DF) PI3K-SH3 fibril (two monomers). The different protofilaments are colored blue and orange. Density maps are shown at a contour level of 1.4 σ. The density map was sufficiently clear to model residues 1–77. **b** Side view of filaments twisting around each other displaying a total of 125 layers. **c** Relative arrangement of two adjacent PI3K-SH3 monomers within the fibril, showing a 2.35 Å shift between the protofilaments

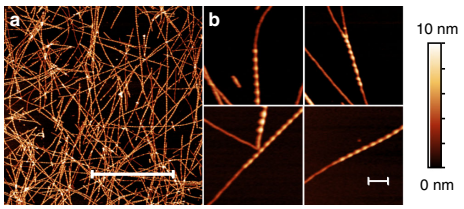

Fig. 2 AFM images of PI3K-SH3 amyloid fibrils. **a** AFM image of PI3K-SH3 fibrils (scale bar, 3 µm). **b** Four different close-up views of fibrils showing both the thick, double filament (DF) fibril and thin, single filament (SF) fibril morphology (scale bar, 300 nm)

rise of 2.35 Å, which corresponds to an approximate 2_1-screw symmetry. The same staggering arrangement has been observed previously for other fibril structures, such as amyloid-β(1–42)[13] and paired-helical filaments of tau[23].

Each protofilament subunit, or PI3K-SH3 monomer, consists of seven parallel in-register β-strands (β1, aa1-5; β2, aa7-19; β3, aa22-26; β4, aa28-34; β5, aa46-56; β6, aa59-68; β7, aa72-77) that are interrupted by either sharp kinks, glycine or proline residues —or a combination of those (Figs. 1a and 3, Supplementary Fig. 6). In particular glycine residues at kink positions have also been observed in other amyloid structures[17]. The total of seven kinks and turns (Fig. 3a) results in an amyloid key topology[20], which includes a structural motif similar to the bent β-arch described by Li et al.[17] for the α-synuclein fibril.

By encompassing 13 residues of each monomer, 26 in total (Supplementary Fig. 7), the inter-filament interface of the PI3K-SH3 DF fibril is very large. The protofilaments mainly interact through two identical symmetry-related hydrophobic patches (Fig. 4) at the periphery of their interface, between the bottom part of the bent β-arch motif and the respective C-terminal part of the opposing protofilament. The stability is provided by the hydrophobic clusters of Val^{38}, Leu^{40}, Gly^{41}, Phe^{42}, Val^{74}, Tyr^{67} and $Val^{38'}$, $Leu^{40'}$, $Gly^{41'}$, $Phe^{42'}$, Val^{74}, Tyr^{67} (Figs. 1a and 4).

The amyloid-characteristic cross-β motif composed of parallel in-register β-sheets connects the different DF fibril layers and therefore contributes the largest share of intermolecular contacts (Fig. 5, Supplementary Fig. 6). This cross-β stacking is complemented by multiple inter- and intramolecular contacts including side chain interactions in homosteric and heterosteric zippers[42]. A further noteworthy feature of the structure is the fact that the PI3K-SH3 subunits are not planar but extent along

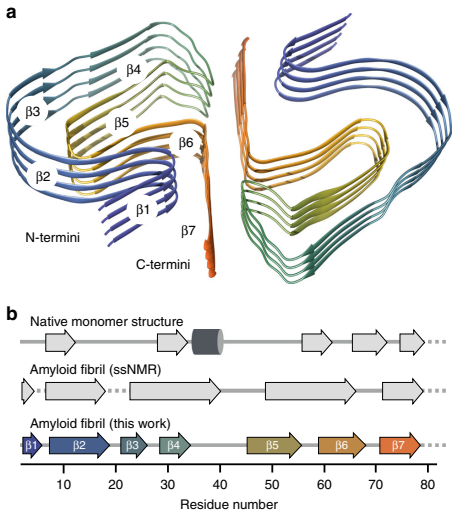

Fig. 3 Secondary structure comparison of the PI3K-SH3 DF fibril. Secondary structure of the presented cryo-EM structure compared to data obtained previously by solid-state NMR (fibrils) or liquid-state NMR (monomeric, native state). **a** Tilted cross-section of four SH3 DF fibril layers. Secondary structure is predominantly formed by seven cross-β sheets. **b** Secondary structure comparison to the native solution structure (PDB: 1PKS[28]) and ssNMR results (fibrils) modified according to Bayro et al.[38]. Flexible regions are shown as dashed lines, β-sheets as arrows, and the helix as a cylinder

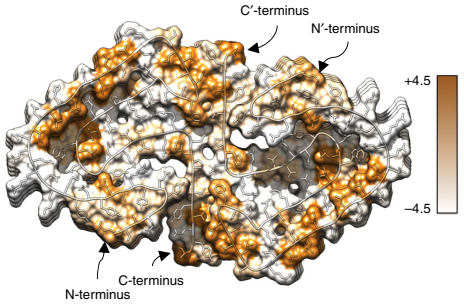

Fig. 4 Hydrophobicity of the fibril cross-section. Hydrophobicity levels of the SH3 DF fibril cross-section are coloured according to Kyte-Doolittle[61]. Hydrophobic residues are mainly packed within the fibril core, while hydrophilic residues point towards the solvent. Hydrophobic patches in both monomers are clearly visible and are spanning several β-sheets

the fibril axis (Fig. 5). The subunits within a protofilament therefore interact not only with the layer directly above $(i+2)$ and below $(i-2)$, but also with layers up to $(i+6)$ and $(i-6)$; the subunits are interlocked.

A single PI3K-SH3 monomer in the DF fibril exhibits an amyloid key topology (Fig. 1a), which is stabilised mainly by hydrophobic patches stretching between the strands β3–β5 (Ile^{22} (i), Trp^{55} $(i-4)$, Leu^{24}(i), Leu^{26}(i)) (Fig. 4), and hydrogen bonds

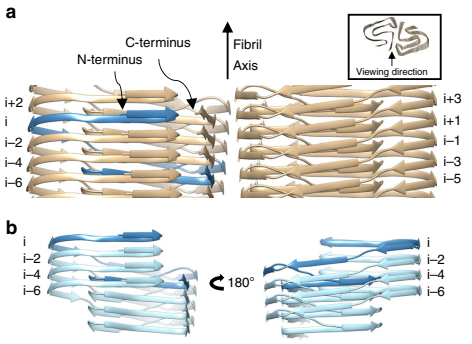

Fig. 5 Side view of the secondary structure of the atomic model. **a** Single subunit *i* highlighted in blue with adjacent subunits in beige, described by even numbers, while the subunits of the opposite protofilament are described by odd numbers. **b** View of the minimal fibril unit (*i*) to (*i*-6) in one filament. The minimal fibril unit is displayed from two views by a turn of 180° highlighting the course of one monomer spanning several fibril layers

or salt bridges between strands β5 and β6 (Asp^{44}(i), Arg^{66}$(i-2)$, Glu^{47}(i)) and β2–β6 (Arg^{9}(i), Glu^{61}$(i-6)$) (Figs. 1a and 3a). In the turn between strands β5 and β6, Asp^{13}$(i+4)$ might bind to Lys^{15}$(i+4)$ while Glu^{17}$(i+4)$ might interact with Asn^{57}(i) (Figs. 1a and 3a). The bent β-arch motif between strands β4 and β5 is potentially strengthened by a contact between Asn^{33}(i) and Gln^{46}(i) that would tie the motif together (Figs. 1a and 3a). Further possible electrostatic interactions can be observed between strands β2 and β6 where the amino-group of Arg^{9} $(i+4)$ might exhibit a salt bridge to Glu^{61}$(i-2)$ (Figs. 1a and 3a). In addition, aromatic side chains are located in close proximity to glycine residues Tyr^{6}(i)-Gly^{71}$(i+6)$, Phe^{42}(i)-Gly^{67}$(i+2)$, Tyr^{73} (i)-Gly^{5}$(i-6)$, indicating a potential involvement of glycine-aromatic Cα-H···π-interactions[43,44]. Further aliphatic-aliphatic and aromatic-aliphatic interactions comprise Ile^{29}(i)-Pro^{50}$(i-2$, $i-4)$-Ala^{48}$(i-2$, $i-4)$, Met^{1}(i)-Tyr^{12}(i), and Leu^{11}(i)-Tyr^{59} $(i$-4). We could also observe possible interactions in-between monomer layers, so-called hydrogen bond ladders, e.g. with Gln^{7}, Gln^{46}, Asn^{57} and Asn^{60}. Additionally, these ladders could potentially be formed as well by side chains pointing outside of the fibril such as Glu^{4}, Glu^{20}, Asp^{21}, Asp^{23} and Asp^{28}. Remarkably, nearly all side chains in the outer Cα-chain that are oriented towards the solvent are non-hydrophobic (Fig. 1a) (Ser^{0}-Glu^{4}, Tyr^{14}-Ser^{36}). Hence, the polar outside of the fibril shields the hydrophobic interface (Fig. 4). Only the hydrophobic residues Leu^{30} and Val^{32}, which are located on the fibril surface next to the bent β-arch motif, disrupt this pattern (Figs. 1a and 4).

Further hints towards the role of electrostatic interactions in maintaining the structure, comes from a pH-shift experiment. By changing the pH from 2 to 7.4, we observed that fibrils depolymerise almost completely after 1 h (Supplementary Fig. 8), in agreement with the highly dynamic nature of PI3K-SH3 fibrils reported previously[36]. We propose three clusters that may be highly influenced by this pH shift: (a) the space between strands β5 and β6 (Asp^{44}(i), Arg^{66}$(i-2)$, Glu^{47}(i)); (b) the interactions between Asp^{13}(i) and Lys^{15}(i), and between Glu^{17}$(i+4)$ and Asn^{57}(i); (c) the solvent-exposed and protonatable patch involving Asp^{21}(i), Asp^{23}(i) and His^{25}(i) (also highlighted as having a fundamental role in amyloid formation[45]).

The secondary structure of PI3K-SH3 fibrils and monomers has been analysed by comparing available solution NMR

(monomeric native fold, PDB: 1PKS)[28] and ssNMR data (amyloid fold)[38] with our model (Fig. 3b). The only feature that is shared by all models is the flexible C-terminus starting around residue 80. Analysis of protein contact maps via the Contact Map WebViewer[46] of the DF fibril compared to the monomeric native structure[28] showed no consistent residue contacts in both structures, illustrating the substantially different conformation that the monomer unit has to adopt in order to incorporate into the fibril. The secondary structure of the native and amyloid fold differs substantially apart from a β-sheet between residues 70–80. While the monomeric native structure is characterised by one helix between residues 34 and 39, β-sheets and multiple flexible loop-regions, the DF fibril consists of seven β-sheets exclusively, that are almost uninterrupted (Fig. 3b). The longest break in the β-sheet pattern of the fibril is the bent β-arch motif leading to a rigid loop between Gly^{35} and Gly^{45} (Figs. 1a and 3a). Our findings are consistent with former results by Bayro et al.[38] who proposed a PI3K-SH3 amyloid model based on solid-state NMR data. Both structures show β-sheets as the only secondary structure motif with most of the β-sheet regions corresponding (Fig. 3b). The main differences between the ssNMR and cryo-EM structures are found in the region between residues 25 and 60. Here, ssNMR data suggest two wide-spanning β-sheets while according to cryo-EM data this region consists of not two but four β-sheets, that are disrupted by a glycine residue, Gly^{27} (β3–β4) (Supplementary Fig. 6) and a sharp kink, Gly^{54}-Tyr^{59} (β5–β6) (Fig. 3a).

Impact of mutations on the SH3 aggregation. We probed the sensitivity of the fibril growth kinetics towards chemically conservative single point mutations by substituting isoleucine residues for alanine across the protein sequence. We expressed and purified the sequence variants and experimentally quantified the rates at which five different variants (I22A, I29A, I53A, I77A, I82A) elongated wildtype (WT) fibrils by quartz crystal microbalance (QCM) measurements (Supplementary Fig. 9)[47,48]. This technology is ideally suited for such cross-seeding experiments. The fibril growth rates of WT and variant proteins can be directly compared, given that the same, constant ensemble of fibrils is monitored. An additional big advantage is that the use of WT seeds as templates ensures that the sequence variants adopt the same fibril structure as the WT, and therefore the change in fibril growth kinetics with respect to the wild type can be interpreted in terms of the perturbation induced by the sequence modification.

We measured the rates of WT fibril elongation by the different variants and expressed the rates relative to that of the elongation by WT monomer (Fig. 6, Supplementary Fig. 9). We found that the relative elongation rates differ by more than two orders of magnitude, with the mutations in the first third of the sequence, as well as around the middle of the sequence, displaying slow elongation rates (I22A = 0.02 ± 10.9%, I29A = 0.02 ± 7.5%, I53A = 0.003 ± 72.7%), whereas the mutations close to or within the disordered C-terminus display approximately the same rates as the wild type (I77A = 1.13 ± 9.3%, I82A = 1.59 ± 10.3%). We also took AFM images of the different single point mutants at a concentration of 100 μM that were all seeded with WT-derived fibrils and incubated for 2 days at room temperature under quiescent conditions (Supplementary Fig. 10). From these images, it can be seen that all fibrils at the end of the experiment have a very similar morphology and length, except for those in the sample with I53A, where shorter fibrils are observed. The fibril growth of all the mutants seems to have come to completion within this time scale leading to very similar fibril lengths. Only in the case of I53A, the fibril growth rate is so slow that the available monomer was only partly incorporated into the seed fibrils during the course of the experiment. However, the very high mass sensitivity of the QCM permits to resolve even the growth rate of this slow growing mutant, and hence we base our analysis of the relative growth rates exclusively on the QCM experiments (Supplementary Fig. 9).

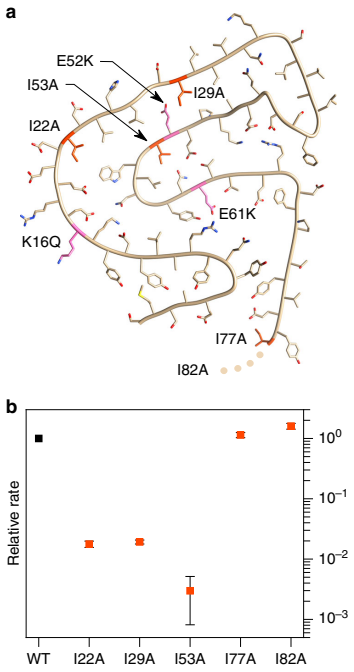

Fig. 6 Point mutations and their effect on fibril elongation rates. **a** Top view of a PI3K-SH3 monomer derived from DF fibrils. Highlighted residues: Isoleucine residues mutated to alanine (I22A, I29A, I53A, I77A, I82A), from this work (red) and charged residues mutated by Buell et al.[47] (K16Q, E52K, E61K, pink). Mutation I82A is missing in the model due to the flexible C-terminus. **b** Elongation rate of Ile-to-Ala mutants. The elongation rates are normalised to a WT rate of one. Source data are provided as a Source Data file

Discussion

Concerning fibril architecture and polymorphism, we observed that, in addition to the thick 7–8 nm SH3 DF fibril consisting of two filaments, also thin fibrils of about half the diameter are present in both AFM (Fig. 2, Supplementary Fig. 2) and negative stain EM images (Supplementary Fig. 1). We therefore hypothesise that the thin fibrils correspond to single filament fibrils (SF fibrils) of the same type that make up the DF fibrils. Our hypothesis is further supported by AFM images that suggest that long SF fibrils can contain stretches that appear to be identical to DF fibrils (Supplementary Fig. 2). It therefore seems likely that fragments of an additional protofilament can attach to or grow on a given SF fibril, to form DF fibrils. The incomplete cooperativity between the elongation of the individual filaments in a DF fibril suggests relatively weak interactions between the filaments. This, in turn, implies that one filament could well be stable without

contact to another filament. We conclude that, at least in the case of PI3K-SH3, inter-filament interface contacts are not necessary for fibril formation.

A similar observation has been made for β2-microglobulin fibrils[15], which can comprise a single protofilament as well as two or more filaments resulting in at least six different polymorphs without major differences in the filament structure. Accordingly, a mixture of all polymorphs yielded only a single set of NMR resonances[15]. The stability of individual PI3K-SH3 filaments is particularly noteworthy, inasmuch as the inter-filament interface in the DF fibrils is comparatively large (Supplementary Fig. 7). A large inter-filament interface does therefore not indicate stable inter-filament interactions. We note here also that the identical conformation of every subunit along the fibril axis is in line with fibril growth by PI3K-SH3 monomer addition[49,50].

A single subunit in the PI3K-SH3 DF fibril is not planar but winds itself along the protofilament axis (Fig. 5), which leads to interlocking within a protofilament. In contrast, in a planar subunit, the inter-subunit interactions within one protofilament would consist exclusively of the cross-β pattern, while all transverse interactions would be intramolecular. Here, however, one subunit within one protofilament is not only in contact with its direct neighbours (above and below) but with four other monomers in total, i.e. in addition to the longitudinal hydrogen bonds in the cross-β structure, there are other transverse interactions between the subunits. This staggered arrangement leads to an interlocking mechanism connecting several monomers within a protofilament, which very likely further stabilises the structure (Fig. 5). Interestingly, this interlocking mechanism is commonly seen in other amyloid fibril structures determined by cryo-EM[13,17,18,20,21]. It should be noted that NMR data can only distinguish between intra- and intermolecular contacts but cannot directly reveal a potential staggering of subunits along the fibril axis.

Given that the interlocking is observed in other fibril structures as well, it might in general contribute to the formation of stable fibrils by optimisation of the side chain packing[10]. In addition, the staggered architecture might in part be responsible for the templating effect during fibril elongation, as it establishes a rugged binding interface that may guide the incoming monomer into the fibril conformation, engaging it in more intermolecular contacts than a flat interface could.

As a measure for the interlocking of subunits we have previously defined the concept of a minimal fibril unit[13], which is the smallest fibril structure fragment in which the capping subunits at both ends would have established the same full contact interface with other constituting monomers as the capping subunits of an extended fibril. Since we hypothesise that one protofilament of the DF fibril could exist on its own and is identical to the SF fibril, here we describe the minimal fibril unit also for a single protofilament. For the PI3K-SH3 fibril, the minimal fibril unit has a size of four subunits when considering an individual protofilament, and a size of eight subunits in the case of the DF fibril (Fig. 5b).

In order to rationalise kinetic data of fibril formation and growth, we substituted five different isoleucine residues with alanines, probing how these chemically conservative single point mutations at different positions affect the addition of new monomers to the fibrillar structure formed by the wild type sequence. Three mutations (I22A, I29A, I53A) showed a strong decrease of the elongation rate of two to three orders of magnitude compared to the wild type sequence (Fig. 6). In these positions, the side chains of the three isoleucines are all pointing towards the fibrillar core (Fig. 6). While the chemical nature of the amino acid substitution we chose is conservative (aliphatic to aliphatic), the bulkiness of the side chain decreases. The ability of these variants to elongate the WT structure, albeit significantly slower than the WT sequence itself, suggests that the formation of a cavity due to the reduced bulkiness is energetically tolerated. However, the free energy difference between the monomeric state and the transition state (structural ensemble) of the elongation reaction appears to be increased. Such an increase in energy difference could come either from a stabilisation of the monomeric state, or from a destabilisation of the transition state. The former seems less likely, due to the mostly disordered nature of PI3K-SH3 at pH 2, while the latter possibility could be caused by the reduction in hydrophobic contacts between the monomer and the fibril end. This conclusion, which assumes some degree of contact between the monomer and the fibril end in the transition state for fibril growth, is in excellent agreement with previous results that underline the importance of the sequence hydrophobicity for the magnitude of the elongation free energy barrier[51]. The remaining two mutations (I77A, I82A) (Fig. 6) are instead located close to or within the flexible C-terminus and show indeed a much weaker or no effect on the elongation rate. In both cases a chemical modification to alanine does not perturb any interactions crucial for the energetics of the transition state.

The availability of the high-resolution structure also allows us to rationalise the influence of previously reported single point mutations of PI3K-SH3 on the kinetics of fibril elongation. In a previous study[47], the effect of changes in charge at three different positions (Fig. 6; K16Q, E52K, E61K; residues depicted in pink) led to very different effects on the elongation rate. While these mutations, similar to the ones we have designed and studied in the present work, could lead to different fibrillar structures if induced to form fibrils de novo, the use of WT seed fibrils in both studies allows us to discuss here the effect of these mutations in the light of the present fibril structure. This is because the well-known templating effect in amyloid fibril growth imprints the structure of the fibril template onto the monomeric protein that adds onto the fibril end. The mutation E52K probably leads to the creation of a positive charge inside the hydrophobic fibril core, a highly unstable arrangement. In the WT fibril, Glu^{61} can form a salt bridge with Arg^{9}, which leads to an additional driving force for the deprotonation of Glu^{61}. If Glu^{61} is substituted by a lysine (E61K), two positive charges come into close proximity, again leading to a highly unstable situation. On the other hand, the mutation K16Q does not lead to any major change in the kinetics of fibril elongation, which is most likely due to the side chain pointing towards the outside of the fibril[52].

Our structural model can also help to understand the effects of further sets of previously investigated sequence changes[45]. With the aim of understanding which part of the sequence plays a major role in the amyloidogenicity of the protein, different portions of the sequence were replaced or mutated. In the vast majority of cases, the amyloidogenic behaviour was completely abolished, which we can now explain with our structural model: the introduction of bulky or charged residues facing the inner core of the structure destabilises the present amyloid fold, as evidenced by the mutants E17R/D23R and Q7E/R9K/E17R/D23R[45]. The only mutation that does not show a significant decrease in amyloidogenicity does not involve changing the charge of a buried residue: the mutant referred to as PI3-QMR (E17Q/D23M/H25R) modifies a single charge of outward pointing residue 25 (assuming Glu^{17} and Asp^{23} to be protonated at pH 2[45]).

It should also be noted that the circularisation of the PI3K-SH3 sequence through the use of disulphide bridges causes a decrease of the elongation rate but does not prevent the circularised mutant to acquire the amyloid conformation[53]. The close proximity of the N- and C-termini (Fig. 1a), in combination with the flexibility of the C-terminal nine residues, likely allows the

cyclised (disulfide bridge between Cys^3 and Cys^{82}) sequence to form an amyloid structure very similar, if not identical to the one presented here.

A noteworthy example of substantial sequence modification is the grafting of the N-Src loop of SPC-SH3 onto PI3K-SH3, while simultaneously removing the stretch from residue 31 to 53 from PI3K-SH3[54]. This operation did not remove the amyloidogenic properties from the modified PI3K-SH3 domain. The removed sequence stretch is part of the bent β-arch motif in the amyloid conformation. The removal of this prominent motif could have been expected to lead to a more significant impairment of amyloid fibril formation. However, the altered sequence is likely to be able to respond to this strong perturbation by forming an alternative structure.

In summary, we have determined the structure of a PI3K-SH3 amyloid fibril. The PI3K-SH3 fibril has been extensively studied in the past and the effect of many mutations on the kinetics of amyloid formation has been described. The atomic structure of the PI3K-SH3 fibril enables us now to rationalise the effect of these mutations, which is the basis for understanding the sequence-dependence of amyloidogenicity and ultimately the determinants of amyloid formation in general.

Methods

Protein production. WT and mutants of the bovine PI3K-SH3 domain were purified according to the protocol of Zurdo et al.[31]. All constructs contain a 6xHis-tag linked to the protein by a thrombin cleavage site. The sequence of the WT protein after cleavage is the following, with the peptide Gly-Ser remaining as overhang from the cleavage:

GSMSAEGYQYRALYDYKKEREEDIDLHLGDILTVNKGSL
VALGFSDGQEAKPEEIGWLNGYNETTGERGDFPGTYVEYIGRK
KISP

The protein was expressed in a BL21 *E. coli* strain with TB medium for auto-induction containing 0.012 % glucose and 0.048 % lactose. The cells were grown for over 24 h and then harvested by centrifugation. After resuspension in sodium phosphate buffer (50 mM sodium phosphate pH 8, 5 mM imidazole and 100 mM NaCl), the cells were disrupted by sonication, in presence of protease inhibitors and DNAse. The lysate was centrifuged, and the supernatant loaded on a Ni-NTA Superflow Cartridge (Qiagen, Venlo, Netherlands) equilibrated in 50 mM sodium phosphate pH 8, 5 mM imidazole and 100 mM NaCl. The protein was eluted with a linear gradient from 5 to 300 mM imidazole in 50 mM sodium phosphate pH 8, 100 mM NaCl in 25 ml elution volume. Fractions containing the protein were collected and cleaved overnight at 7 °C with 1 unit of thrombin (from bovine plasma, Sigma-Aldrich Saint Louis, Missouri, USA) per 1 mg of protein. The cleaved solution was then concentrated and loaded on a SEC HiLoad 26/60 Superdex 75 column (GE Healthcare, Chicago, Illinois, USA) equilibrated with 5 mM ammonium acetate pH 7. Fractions containing the PI3K-SH3 domain were collected and lyophilised for further use.

Fibril formation. The lyophilised protein was resuspended in 10 mM glycine-hydrochloride pH 2.5 buffer at a final concentration of ca. 200 µM. The solution was shaken in an Eppendorf tube at 1400 rpm at 42 °C for 24 h to form seeds. These seeds were then sonicated in an Eppendorf tube in a volume of ca. 500 µl for 15 s (1 s 'on', 2 s 'off', 10 % amplitude) with a Bandelin Sonopuls using a M72 probe. To prepare the twisted fibrils, a new solution with ca. 100 µM monomer in 10 mM glycine-hydrochloride pH 2.5 was then mixed with 5 µM of equivalent seeds mass and incubated without stirring at 50 °C overnight.

AFM imaging. The fibril samples were diluted in 10 mM glycine-hydrochloride, pH 2.5 to a concentration of 5 µM and 10 µl were pipetted on a mica substrate. After 10 min of incubation, the mica was washed extensively with milliQ water and dried under a nitrogen gas flush. The pictures were taken in tapping mode on a Bruker Multimode 8 (Billerica, Massachusetts, USA) using OMCL-AC160TS cantilevers (Shinjuku, Tokyo, Japan).

Fibril elongation measurements with QCM. The elongation rate of PI3K-SH3 fibrils was measured through immobilisation of fibrils on a QCM sensor and subsequent incubation with monomer solution[50]. To immobilise the fibrils on the sensor, chemical modification is necessary. To achieve that, the fibrils were mixed at a final concentration of 50 µM in buffer (10 mM glycine-hydrochloride, pH 2) with EDC (1-ethyl-3-(3-dimethylaminopropyl)carbodiimide hydrochloride) (1 M) and cystamine hydrochloride (0.5 mg ml^{-1}). After pelleting and washing the chemically modified fibrils, they were sonicated in an Eppendorf tube in a volume of ca. 500 microlitre with a Bandelin Sonopuls using a MS72 probe (10% amplitude, 15 s, 1 s 'on', 2 s 'off'). The gold sensors (Biolin Scientific, Gothenburg, Sweden) were then incubated with the above-mentioned solution overnight in a 100% humidity environment. The measurements were performed with a QSense Pro (Biolin Scientific, Gothenburg, Sweden) by measuring the elongation rate as change in resonant frequency over time. With the temperature set at 25 °C, the monomer solutions were injected for 30 s at a flow rate of 100 µl per second and the measurement lasted until a stable slope was reached. To obtain the relative rates, the protein solutions were injected in different sensor chambers after a WT injection, the latter being used as normalization reference. Two different triplicate measurements were performed for I53A. Two different duplicate measurements were performed for all the other mutants. The rate was measured as slope of the 3rd overtone and averaged among the multiple injections. The data are presented as average values with error bars indicating the standard deviation.

Fibril dissociation at pH 7.4. Fibril dissociation at pH 7.4 was probed by measuring ThT and intrinsic fluorescence change over time in two series of triplicates. The ThT measurements were performed by mixing 40 µl of 100 µM PI3K-SH3 fibrils and 50 µM ThT in 10 mM glycine-hydrochloride pH 2 with 60 µl of 100 mM sodium phosphate pH 7.4. The mixing was carried out using the injection system of a CLARIOstar plate reader (BMG LABTECH, Ortenberg, Germany) and measuring immediately afterwards by exciting at 440 nm and recording the signal intensity at 480 nm. The intrinsic tryptophan fluorescence measurements were carried out by mixing the same two solutions (without ThT) by pipetting, followed by the measurement of fluorescence spectra every 15 s by exciting at 290 nm and recording between 300 and 380 nm in 2 nm intervals.

The analysis of soluble peptide by concentration determination at the end of the dissolution experiment was performed after one night of equilibration after the mixing of the two solutions mentioned above (without ThT). The samples were spun down for 30 min at 16,100 g. The protein concentration in the supernatant was determined by measuring the asorbance at 280 nm together with the extinction coefficient of PI3K-SH3 of $\varepsilon_{280} = 15{,}930\ M^{-1}cm^{-1}$ using a V650 UV-Vis spectrophotometer (Jasco, Easton, MD, USA).

Negative stain and cryo-EM image acquisition. Negatively stained fibrils were prepared on 400 mesh carbon-coated copper grids (S160-4, Plano GmbH, Germany), stained with 1% uranyl acetate, and imaged using a Libra120 electron microscope (Zeiss) operated at 120 kV. Cryo-preparation was performed on glow-discharged holey carbon films (Quantifoil R 1.2/1.3, 300 mesh). The sample containing 50 µM PI3K-SH3 was 4×/10×/20x diluted with 10 mM glycine-hydrochloride (pH 2) to a final concentration of 12.5, 5 or 2.5 µM monomer equivalent. A total sample volume of 2.5 µl was applied onto the carbon grid and blotted for 3.5 s before being cryo-plunged using a Vitrobot (FEI). With 110,000-fold nominal magnification 622 micrographs have been recorded on a Tecnai Arctica electron microscope operating at 200 kV with a field emission gun using a Falcon III (FEI) direct electron detector in electron counting mode directed by EPU data collection software. Each micrograph was composed of 60 fractions. Each fraction contained 42 frames, i.e. in total 2520 frames were recorded per micrograph. The samples were exposed for 65 s to an integrated flux of 0.4 $e^{-}/Å^2/s$. Applied underfocus values ranged between 1.5 and 2.25 µm. The pixel size was 0.935 Å, as calibrated using gold diffraction rings within the powerspectra of a cross grating grid (EMS, Hatfield).

Cryo-EM image processing and helical reconstruction. MotionCor2[55] was used for movie correction. Fitting CTF parameters for all 622 micrographs was performed using CTFFIND4[56]. Further image processing and 3D reconstructions were done with RELION-2[39,40]. Selection of 256 micrographs was done with CCTFFIND by estimating the maximum resolution at which Thon rings could be detected to be better than 5 Å. From these micrographs, 4540 fibrils were manually picked. From these fibrils, 103,733 segments were extracted using an overlap of 90 % between neighbouring segments. The size of the segment images is 220 pixels. For data set characterisation we performed 2D classification (Supplementary Fig. 11). As an initial model for the refinement we used a noise-filled cylinder.

After several rounds of 3D refinements with helical symmetry search, we found a problem with the tilt priors: the tilt angle distribution became bimodal with maxima at 85° and 95°. However, we would expect the tilt angles to show a unimodal distribution around 90°. The ~4.7 Å cross-β pattern is a strong signal and substantially affects the alignment. If the helical rise parameter is slightly smaller than the correct value, the cross-β pattern can still be aligned by changing the tilt angles to higher or lower values (which accordingly reduces the spacing of the cross-β pattern). To overcome this problem, we fixed the tilt prior to 90° by usage of the RELION option *helical_keep_tilt_prior_fixed*, and then first optimized the helical parameters. In subsequent refinements, the helical symmetry parameters were fixed and the tilt angles (together with the other angles) were optimized.

Since the automated 3D refinement in RELION did not yield high-resolution reconstructions, we performed gold-standard refinements by splitting the data into an even and an odd set by selecting entire fibrils (not just segments, as they are overlapping). The FSC curve (Supplementary Fig. 12) was computed between the two half-maps and yields a resolution (with the 0.143 criterion) of 3.4 Å.

The handedness of the fibril structure was determined by comparing the reconstructed density with AFM images (Supplementary Fig. 5). For this comparison, the 3D density map of the fibril was converted to a height profile using Chimera[57] as follows: set surface color by height and set the color scale to gray. Then set camera projection mode to orthographic and save the image. The alignment of the AFM image with the calculated height profiles yields a cross-correlation coefficient of 0.943 for the left-handed and 0.914 for the right-handed helix.

Model building and refinement. A single chain atomic model of PI3K-SH3 was built with Coot[58,59]. Subsequently, seven copies of a single chain were placed into the EM density map. At residues Gln[46] and Glu[47], between strands β4 and β5, the density map is slightly ambiguous and could possibly be in agreement with an alternative interpretation for the trace of the Cα-chain (Supplementary Fig. 13).

The final model containing seven helical symmetry-related chains was used for further real space refinement in PHENIX[60]. Refinement was carried out using a resolution cut-off of 3.4 Å and NCS restraints between all seven subunits. At later stages of the refinement, hydrogen-bond restraints were defined for the cross-β sheets and Ramachandran restraints were used. The model-map FSC curve as obtained from *phenix.real_space_refine* is shown in Supplementary Fig. 12 (dashed line). The final statistics on the details of the refinement are shown in Supplementary Table 1. Molecular graphics and analyses were performed with Chimera[57].

Reporting summary. Further information on research design is available in the Nature Research Reporting Summary linked to this article.

Data availability

The structure of the PI3K-SH3 fibril has been deposited in the Protein Data Bank under accession code 6R4R [https://doi.org/10.2210/pdb6R4R/pdb]. The 3.4 Å cryo-EM density map has been deposited in the Electron Microscopy Data Bank under accession code EMD-4727. The source data underlying Fig. 6b and Supplementary Fig. 8 are provided as a Source Data file. Other data are available from the corresponding authors upon reasonable request.

Received: 26 March 2019 Accepted: 9 July 2019
Published online: 21 August 2019

References

1. Dobson, C. M. Protein folding and misfolding. *Nature* **426**, 884–890 (2003).
2. Knowles, T. P. J., Vendruscolo, M. & Dobson, C. M. The amyloid state and its association with protein misfolding diseases. *Nat. Rev. Mol. Cell Biol.* **15**, 384–396 (2014).
3. Kayed, R. et al. Common structure of soluble amyloid oligomers implies common mechanism of pathogenesis. *Science* **300**, 486–489 (2003).
4. Cohen, S. I. A. et al. Proliferation of amyloid-β42 aggregates occurs through a secondary nucleation mechanism. *PNAS* **110**, 9758–9763 (2013).
5. Pepys, M. B. et al. Human lysozyme gene mutations cause hereditary systemic amyloidosis. *Nature* **362**, 553 (1993).
6. Sunde, M. et al. Common core structure of amyloid fibrils by synchrotron X-ray diffraction. *J. Mol. Biol.* **273**, 729–739 (1997).
7. Kheterpal, I., Williams, A., Murphy, C., Bledsoe, B. & Wetzel, R. Structural features of the Abeta amyloid fibril elucidated by limited proteolysis. *Biochemistry* **40**, 11757–11767 (2001).
8. Hoshino, M. et al. Mapping the core of the β2-microglobulin amyloid fibril by H/D exchange. *Nat. Struct. Mol. Biol.* **9**, 332–336 (2002).
9. Fitzpatrick, A. W. P. et al. Atomic structure and hierarchical assembly of a cross-β amyloid fibril. *PNAS* **110**, 5468–5473 (2013).
10. Tycko, R. Molecular structure of aggregated amyloid-β: insights from solid state nuclear magnetic resonance. *Q. Rev. Biophys.* **39**, 1–55 (2016).
11. Wasmer, C. et al. Amyloid fibrils of the HET-s(218-289) prion form a β solenoid with a triangular hydrophobic core. *Science* **319**, 1523–1526 (2008).
12. Radamaker, L. et al. Cryo-EM structure of a light chain-derived amyloid fibril from a patient with systemic AL amyloidosis. *Nat. Commun.* **10**, 1103 (2019).
13. Gremer, L. et al. Fibril structure of amyloid-β(1–42) by cryo–electron microscopy. *Science* **358**, 116–119 (2017).
14. Zhang, W. et al. Heparin-induced tau filaments are polymorphic and differ from those in Alzheimer's and Pick's diseases. *eLife* **8**, e43584 (2019).
15. Iadanza, M. G. et al. The structure of a β2-microglobulin fibril suggests a molecular basis for its amyloid polymorphism. *Nat. Commun.* **9**, 4517 (2018).
16. Falcon, B. et al. Structures of filaments from Pick's disease reveal a novel tau protein fold. *Nature* **561**, 137–146 (2018).
17. Li, B. et al. Cryo-EM of full-length α-synuclein reveals fibril polymorphs with a common structural kernel. *Nat. Commun.* **9**, 3609 (2018).
18. Guerrero-Ferreira, R. et al. Cryo-EM structure of alpha-synuclein fibrils. *eLife* **7**, e360402 (2018).
19. Li, Y. et al. Amyloid fibril structure of α-synuclein determined by cryo-electron microscopy. *Cell Res.* **28**, 897–903 (2018).
20. Liberta, F. et al. Cryo-EM fibril structures from systemic AA amyloidosis reveal the species complementarity of pathological amyloids. *Nat. Commun.* **10**, 1104 (2019).
21. Swuec, P. et al. Cryo-EM structure of cardiac amyloid fibrils from an immunoglobulin light chain (AL) amyloidosis patient. *Nat. Commun.* **10**, 1269 (2019).
22. Falcon, B. et al. Tau filaments from multiple cases of sporadic and inherited Alzheimer's disease adopt a common fold. *Acta Neuropathol.* **136**, 699–708 (2018).
23. Fitzpatrick, A. W. P. et al. Cryo-EM structures of tau filaments from Alzheimer's disease. *Nature* **547**, 185–190 (2017).
24. Arosio, P. et al. Kinetic analysis reveals the diversity of microscopic mechanisms through which molecular chaperones suppress amyloid formation. *Nat. Commun.* **7**, 10948 (2016).
25. Koch, C. A., Anderson, D., Moran, M. F., Ellis, C. & Pawson, T. SH2 and SH3 domains: elements that control interactions of cytoplasmic signaling proteins. *Science* **252**, 668–674 (1991).
26. Yu, H. et al. Structural basis for the binding of proline-rich peptides to SH3 domains. *Cell* **76**, 933–945 (1994).
27. Batra-Safferling, R., Granzin, J., Mödder, S., Hoffmann, S. & Willbold, D. Structural studies of the phosphatidylinositol 3-kinase (PI3K) SH3 domain in complex with a peptide ligand: Role of the anchor residue in ligand binding. *Biol. Chem.* **391**, 33–42 (2010).
28. Koyama, S. et al. Structure of the Pl3K SH3 domain and analysis of the SH3 family. *Cell* **72**, 945–952 (1993).
29. Guijarro, J. I., Morton, C. J., Plaxco, K. W., Campbell, I. D. & Dobson, C. M. Folding kinetics of the SH3 domain of PI3 kinase by real-time NMR combined with optical spectroscopy. *J. Mol. Biol.* **276**, 657–667 (1998).
30. Guijarro, J. I., Sunde, M., Jones, J. A., Campbell, I. D. & Dobson, C. M. Amyloid fibril formation by an SH3 domain. *PNAS* **95**, 4224–4228 (1998).
31. Zurdo, J., Guijarro, J. I., Jiménez, J. L., Saibil, H. R. & Dobson, C. M. Dependence on solution conditions of aggregation and amyloid formation by an SH3 domain. *J. Mol. Biol.* **311**, 325–340 (2001).
32. Polverino de Laureto, P. et al. Protein aggregation and amyloid fibril formation by an SH3 domain probed by limited proteolysis. *J. Mol. Biol.* **334**, 129–141 (2003).
33. Jiménez, J. L. et al. Cryo-electron microscopy structure of an SH3 amyloid fibril and model of the molecular packing. *EMBO J.* **18**, 815–821 (1999).
34. Neudecker, P. et al. Structure of an intermediate state in protein folding and aggregation. *Science* **336**, 362–366 (2012).
35. Bucciantini, M. et al. Inherent toxicity of aggregates implies a common mechanism for protein misfolding diseases. *Nature* **416**, 507–511 (2002).
36. Carulla, N. et al. Molecular recycling within amyloid fibrils. *Nature* **436**, 554–558 (2005).
37. Orte, A. et al. Direct characterization of amyloidogenic oligomers by single-molecule fluorescence. *PNAS* **105**, 14424–14429 (2008).
38. Bayro, M. J. et al. High-resolution MAS NMR analysis of PI3-SH3 amyloid fibrils: backbone conformation and implications for protofilament assembly and structure. *Biochemistry* **49**, 7474–7484 (2010).
39. Scheres, S. H. W. RELION: implementation of a Bayesian approach to cryo-EM structure determination. *J. Struct. Biol.* **180**, 519–530 (2012).
40. He, S. & Scheres, S. H. W. Helical reconstruction in RELION. *J. Struct. Biol.* **198**, 163–176 (2017).
41. Kimanius, D., Forsberg, B. O., Scheres, S. H. W. & Lindahl, E. Accelerated cryo-EM structure determination with parallelisation using GPUs in RELION-2. *eLife* **5**, e18722 (2016).
42. Riek, R. & Eisenberg, D. S. The activities of amyloids from a structural perspective. *Nature* **539**, 227–235 (2016).
43. Zondlo, N. J. Aromatic-proline interactions: electronically tunable CH/π interactions. *Acc. Chem. Res.* **36**, 1039–1049 (2013).
44. Unterreitmeier, S. et al. Phenylalanine promotes interaction of transmembrane domains via GxxxG motifs. *J. Mol. Biol.* **374**, 705–718 (2007).
45. Ventura, S. et al. Short amino acid stretches can mediate amyloid formation in globular proteins: the Src homology 3 (SH3) case. *PNAS* **101**, 7258–7263 (2004).
46. Kozma, D., Simon, I. & Tusnády, G. E. CMWeb: an interactive on-line tool for analysing residue-residue contacts and contact prediction methods. *Nucleic Acids Res.* **40**, 329–333 (2012).
47. Buell, A. K. et al. Position-dependent electrostatic protection against protein aggregation. *ChemBioChem* **10**, 1309–1312 (2009).
48. Knowles, T. P. J. et al. Kinetics and thermodynamics of amyloid formation from direct measurements of fluctuations in fibril mass. *PNAS* **104**, 10016–10021 (2007).
49. Collins, S. R., Douglass, A., Vale, R. D. & Weissman, J. S. Mechanism of prion propagation: amyloid growth occurs by monomer addition. *PLoS Biol.* **2**, e321 (2004).

50. Buell, A. K. et al. Frequency factors in a landscape model of filamentous protein aggregation. *Phys. Rev. Lett.* **104**, 228101 (2010).
51. Buell, A. K. et al. Detailed analysis of the energy barriers for amyloid fibril growth. *Angew. Chem. Int. Ed.* **51**, 5247–5251 (2012).
52. Buell, A. K. et al. Electrostatic effects in filamentous protein aggregation. *Biophys. J.* **104**, 1116–1126 (2013).
53. Graña-Montes, R. et al. Contribution of disulfide bonds to stability, folding, and amyloid fibril formation: the PI3-SH3 domain case. *Antioxid. Redox Signal.* **16**, 1–15 (2011).
54. Ventura, S., Lacroix, E. & Serrano, L. Insights into the origin of the tendency of the PI3-SH3 domain to form amyloid fibrils. *J. Mol. Biol.* **322**, 1147–1158 (2002).
55. Zheng, S. Q., Palovcak, E., Armache, J.-P., Cheng, Y. & Agard, D. A. MotionCor2: anisotropic correction of beam-induced motion for improved single-particle electron cryo-microscopy. *Nat. Methods* **14**, 331–332 (2017).
56. Rohou, A. & Grigorieff, N. CTFFIND4: fast and accurate defocus estimation from electron micrographs. *J. Struct. Biol.* **192**, 216–221 (2015).
57. Pettersen, E. F. et al. UCSF chimera—a visualization system for exploratory research and analysis. *J. Comput. Chem.* **25**, 1605–1612 (2004).
58. Emsley, P., Lohkamp, B., Scott, W. G. & Cowtan, K. Features and development of Coot. *Acta Crystallogr. Sect. D. Biol. Crystallogr.* **66**, 486–501 (2010).
59. Emsley, P. & Cowtan, K. Coot: model-building tools for molecular graphics. *Acta Crystallogr. Sect. D. Biol. Crystallogr.* **60**, 2126–2132 (2004).
60. Adams, P. D. et al. PHENIX: a comprehensive Python-based system for macromolecular structure solution. *Acta Crystallogr. Sect. D. Biol. Crystallogr.* **66**, 213–221 (2010).
61. Kyte, J. & Doolittle, R. F. A simple method for displaying the hydropathic character of a protein. *J. Mol. Biol.* **157**, 105–132 (1982).

Acknowledgements

We thank P.J. Peters and C. López-Iglesias for their advice and helpful discussions, H. Duimel for help with sample preparation, and the M4I Division of Nanoscopy of Maastricht University for microscope access and support. We thank P. Neudecker for helpful comments on the paper. We gratefully acknowledge the computing time granted by the Jülich Aachen Research Alliance High-Peformance Computing (JARA-HPC) Vergabegremium and VSR commission on the supercomputer JURECA at Forschungszentrum Jülich. Computational support and infrastructure was provided by the Center for Information and Media Technology (ZIM) at the University of Düsseldorf (Germany). A.K.B. and N.V. thank the Deutsche Forschungsgemeinschaft (DFG) for funding. D.W. was supported by grants from the Portfolio Technology and Medicine, the Portfolio Drug Design, and the Helmholtz-Validierungsfonds of the Impuls und Vernetzungs-Fonds der Helmholtzgemeinschaft. This study was funded in part by the DFG SFB 974 and SFB 1208 (to D.W.). Support from a European Research Council (ERC) Consolidator Grant (grant agreement no. 726368) to W.H. is acknowledged. A.K.B. thanks the Novo Nordisk Foundation for support through a Novo Nordisk Foundation Professorship.

Author contributions

A.K.B. and G.F.S. conceived the study. N.V. and L.N.M. performed the biochemical experiments. A.K.B., N.V., L.N.M. analysed the biochemical and kinetics data. R.G.B.R. performed cryo-EM experiments and initial data analysis. C.R. and G.F.S. performed image processing, reconstruction and model building. C.R., A.K.B., N.V., G.F.S., W.H. and L.G. wrote the paper. D.W. and all other authors discussed results and commented on the paper.

Additional information

Supplementary Information accompanies this paper at https://doi.org/10.1038/s41467-019-11320-8.

Competing interests: The authors declare no competing interests.

Reprints and permission information is available online at http://npg.nature.com/reprintsandpermissions/

Peer review information: *Nature Communications* thanks Henning Stahlberg, Stefano Ricagno and other anonymous reviewer(s) for their contribution to the peer review of this work. Peer reviewer reports are available.

Publisher's note: Springer Nature remains neutral with regard to jurisdictional claims in published maps and institutional affiliations.

1.1 Publication I: Supplementary material

Supplementary Table

Supplementary Table 1: Statistics of cryo-EM data collection, reconstruction and model building

Data Collection	
Microscope	Tecnai Arctica
Camera	Falcon 3
Acceleration voltage (kV)	200
Nominal Magnification	110,000
Defocus range (μm)	1.5 to 2.25
Dose rate (e^-/ Å^2/s)	0.4
Number of movie frames	2520
Exposure time (s)	65
Total electron dose (e^-/Å^2)	26.2
Pixel size (Å)	0.935
Reconstruction	
Box size (pixel)	200
Interbox distance (Å)	18.8
Number of extracted segments	103,733
Number of segments after 3D classification	27,681
Resolution based on the 0.143 FSC criterion (Å)	3.4
Map sharpening B-Factor (Å^2)	150
Helical rise (Å)	2.3548
Helical twist (°)	179.436
Symmetry	C1 (pseudo-2_1 helical)
Model Composition	
Non-hydrogen atoms	4494
Number of chains	7
Model Refinement	
Resolution (Å)	3.4
Map CC (around atoms)	0.6457
RMSD bonds (Å)	0.008
RMSD angles (°)	1.426
All-atom clash score	6.73
Ramachandran outliers/favored (%)	0/88 %
Rotamer outliers	0/1.59 %
C-beta deviations	0/0
EMRinger score	4.98
Molprobility score	1.97

Supplementary Figures

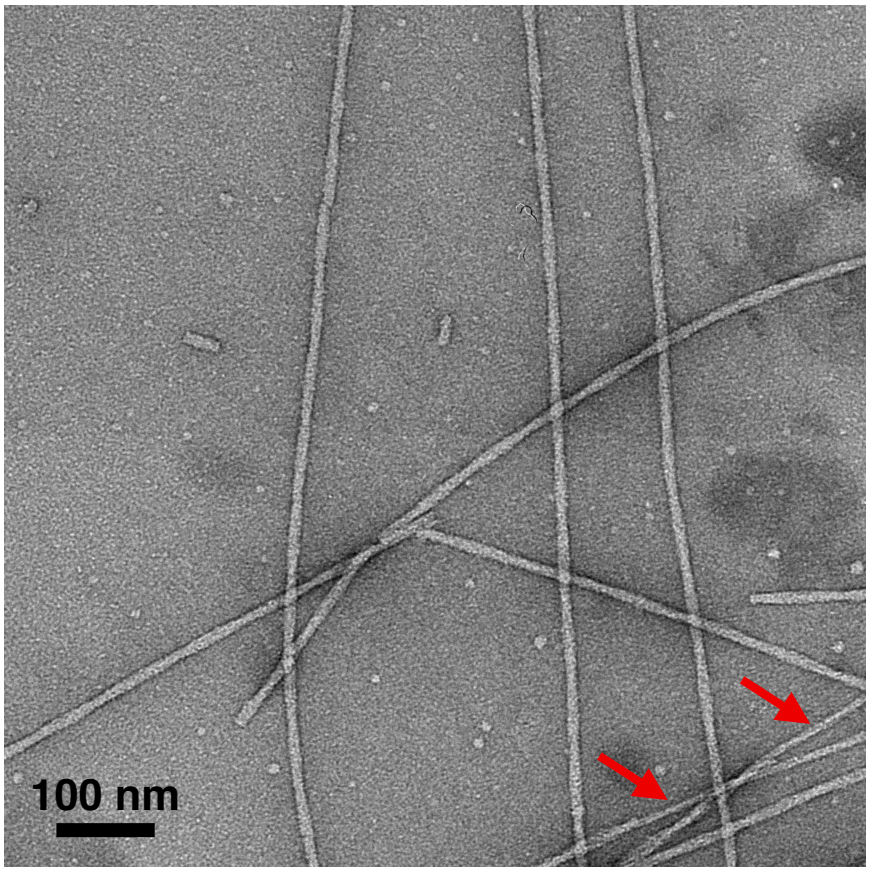

Supplementary Fig. 1 Exemplary negative stain micrograph showing the predominant thick double filament (DF) PI3K-SH3 fibrils and less dominant thin single filament (SF) fibrils (red arrows).

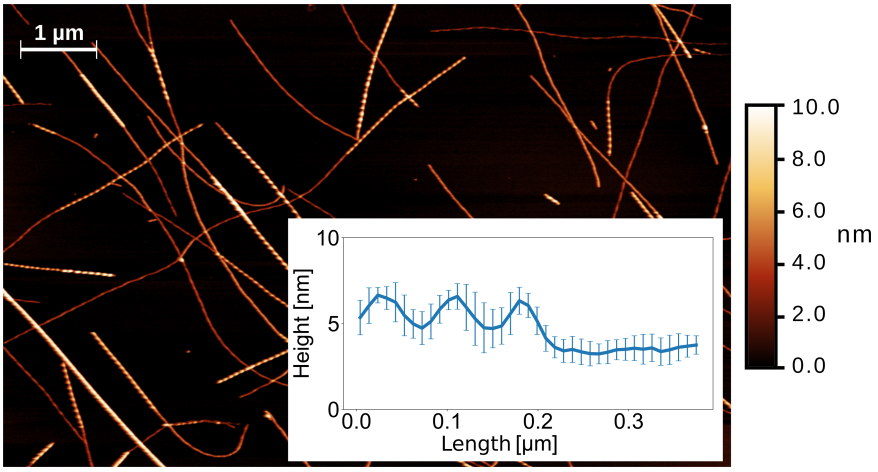

Supplementary Fig. 2 Averaged height pattern of different fibril profiles along their length. The different profiles were aligned on the peak position, the shortest profile was chosen as a minimum length, and their height averaged (error bars correspond to the standard deviation). The first three peaks are indicative of the double filament (DF) portion of the fibrils, while the flat part is indicative of the single filament (SF) portion.

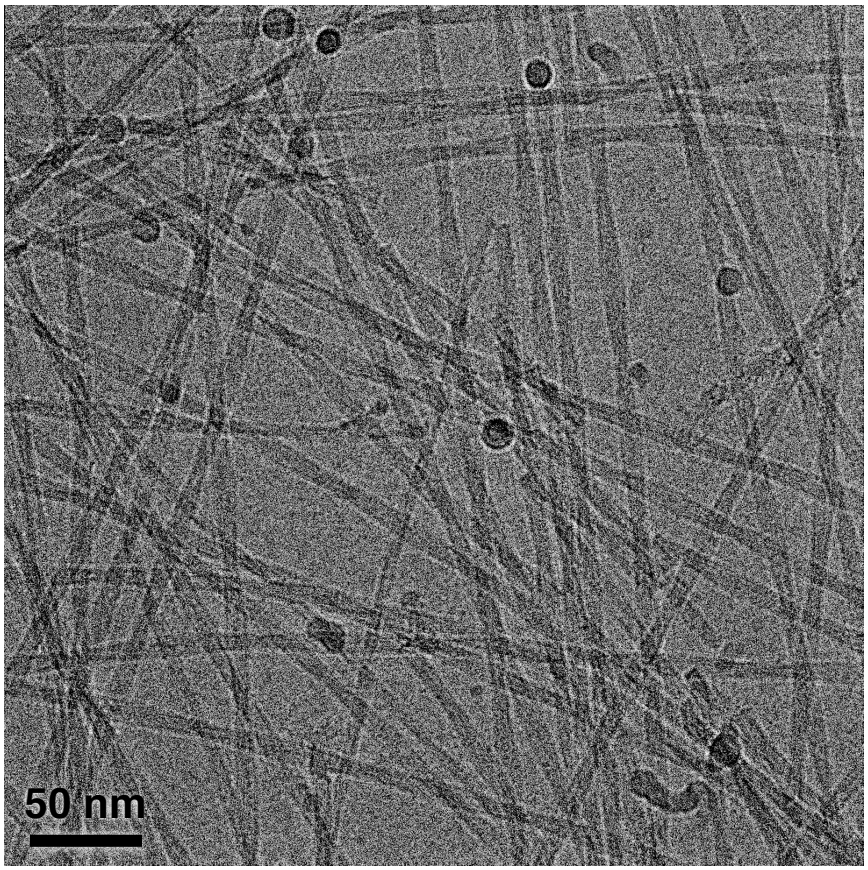

Supplementary Fig. 3 Representative cryo-EM micrograph of DF PI3K-SH3 fibrils. The fibril twist of the thick DF fibril is already well visible in this low-contrast image.

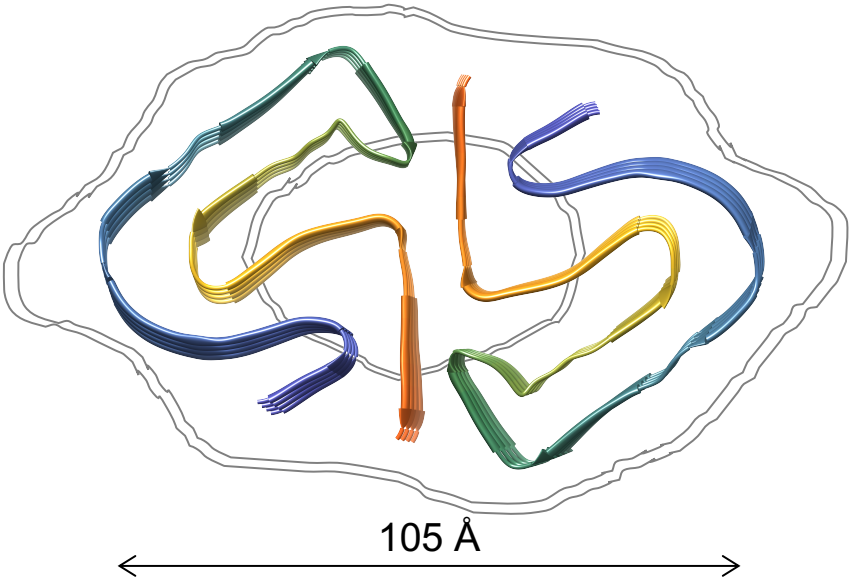

Supplementary Fig. 4 Overlay of the presented DF PI3K-SH3 fibril model with the low-resolution cryo-EM density (contour graphically extracted) from Jimenez *et al.* (1999)[5]. The model and the density are in good agreement, which suggests that both preparations likely yield the same structure.

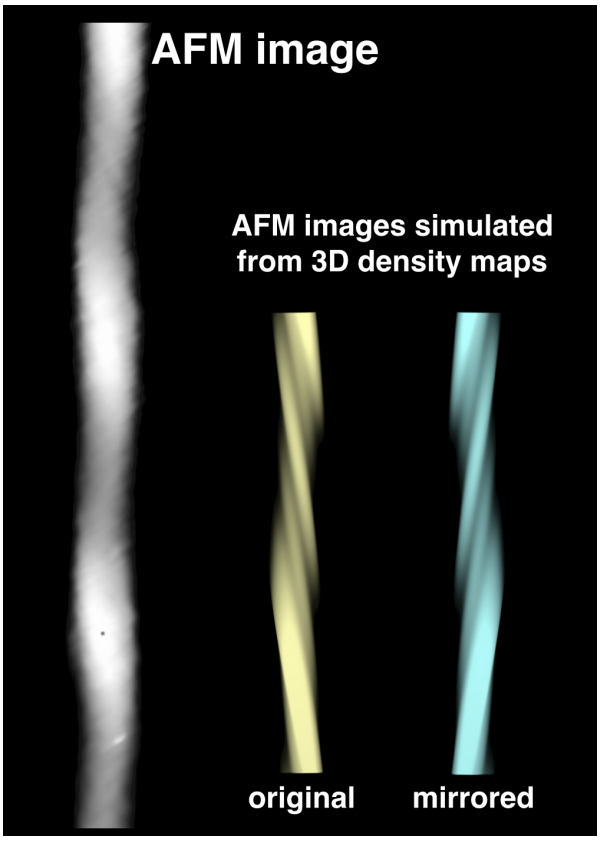

Supplementary Fig. 5 Comparison of an AFM image of a DF PI3K-SH3 fibril with height profiles computed from the 3D EM reconstructions. The original left-handed reconstruction (yellow) yields a higher cross-correlation coefficient (0.943) with the AFM images (grey) than the mirrored reconstruction (0.914, cyan), indicating that the DF PI3K-SH3 fibril is left-handed.

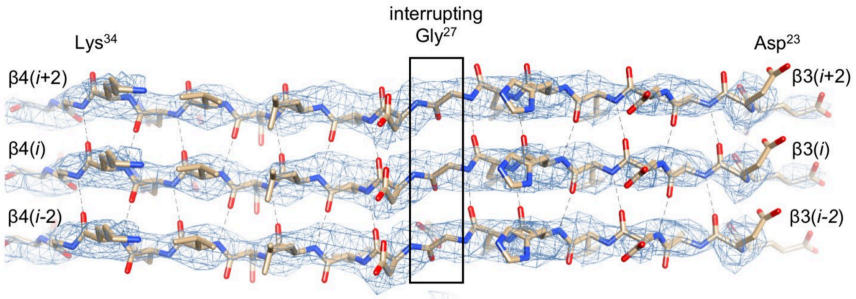

Supplementary Fig. 6 Side view of DF PI3K-SH3 amyloid fibril showing residues 22–35. Displayed are three layers of DF PI3K-SH3 encompassing parts of in-register sheets β3 and β4 with hydrogen bonds highlighted as dashed lines. The cross-β pattern between sheets β3 and β4 is only interrupted by residue Gly^{27}.

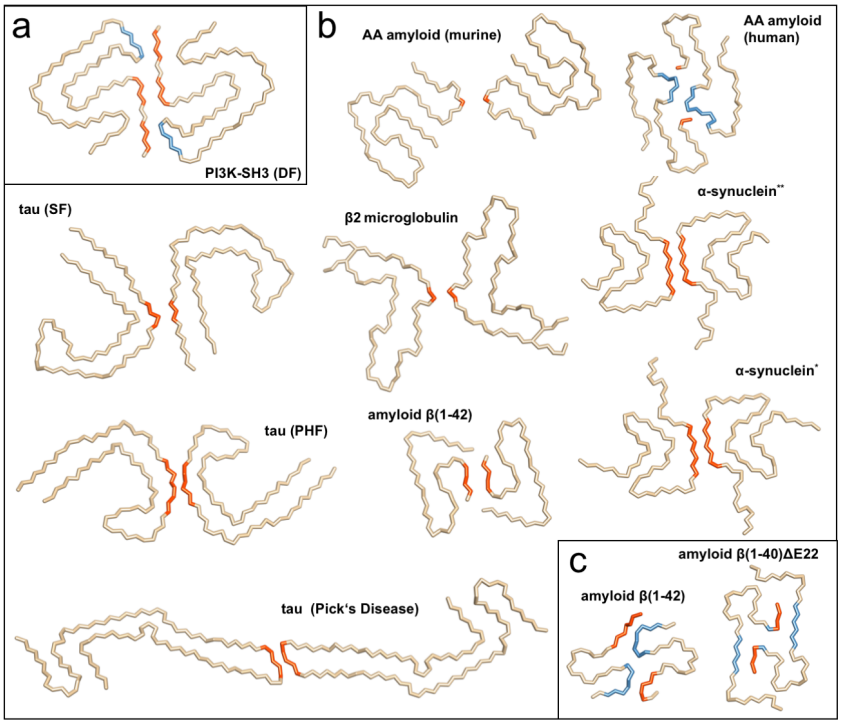

Supplementary Fig. 7 Interface gallery. **a** The protofilament interface of DF PI3K-SH3 fibrils is composed of two sequence regions (orange and blue) and is large compared to those of amyloid fibrils previously determined by cryo-EM (**b**) (Aβ(1–42), PDB: 5OQ5[6]; β2 microglobulin, PDB: 6GK3[7]; AA amyloidosis (human), PDB: 6MST[8]; AA amyloidosis (murine), PDB: 6DSO[8]; α-synuclein*, PDB: 6A6B[9]; α-synuclein**, PDB: 6H6B[10]; tau (PHF)[11], PDB: 5O3L; tau (SF), PDB: 5O3T[11]; tau Pick's Disease, PDB: 6GX5[12]) [6,7,10–13] . **c** Protofilament interfaces of different Aβ variants determined by solid-state NMR (Aβ(1-40)ΔE22, PDB: 2MVX[14]; Aβ(1-42), PDB: 5KK3[15]) exhibit similar sizes and complexities as observed for DF PI3K-SH3 fibrils. Interfaces are shown as Cα-chain. Interface contacts have been defined as Cα-contacts with a cut-off of <10 Å. Beige, no interface contacts; orange, interface contact formed by first involved β-sheet; blue, interface contact formed by second β-sheet.

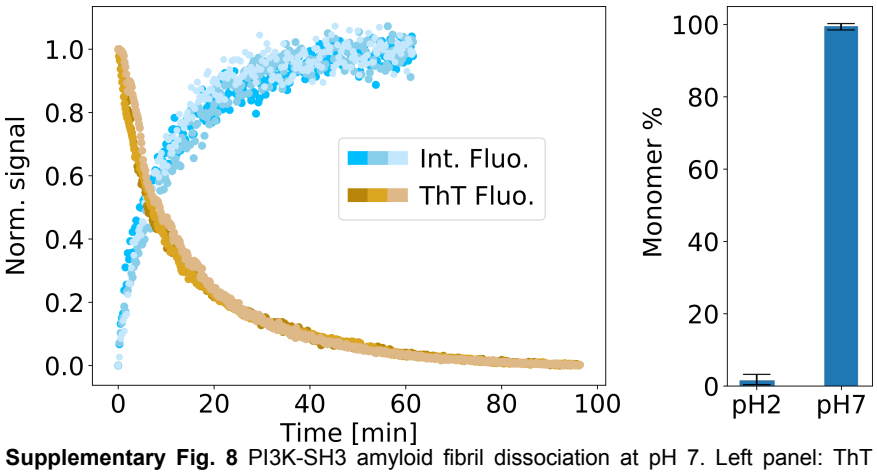

Supplementary Fig. 8 PI3K-SH3 amyloid fibril dissociation at pH 7. Left panel: ThT (brown data points) and intrinsic tryptophan fluorescence intensity ratio 340 nm/310 nm (blue data points) traces of fibril dissociation after dilution into pH 7.4 buffer (measurements are done in triplicate). Right panel: Concentration of protein in the supernatant as percentage of the total protein concentration after incubation for 24 h and centrifugation for 30 min at 16,100 g. Error bars represent the standard deviation on a triplicate measurement. Source data are provided as a Source Data file.

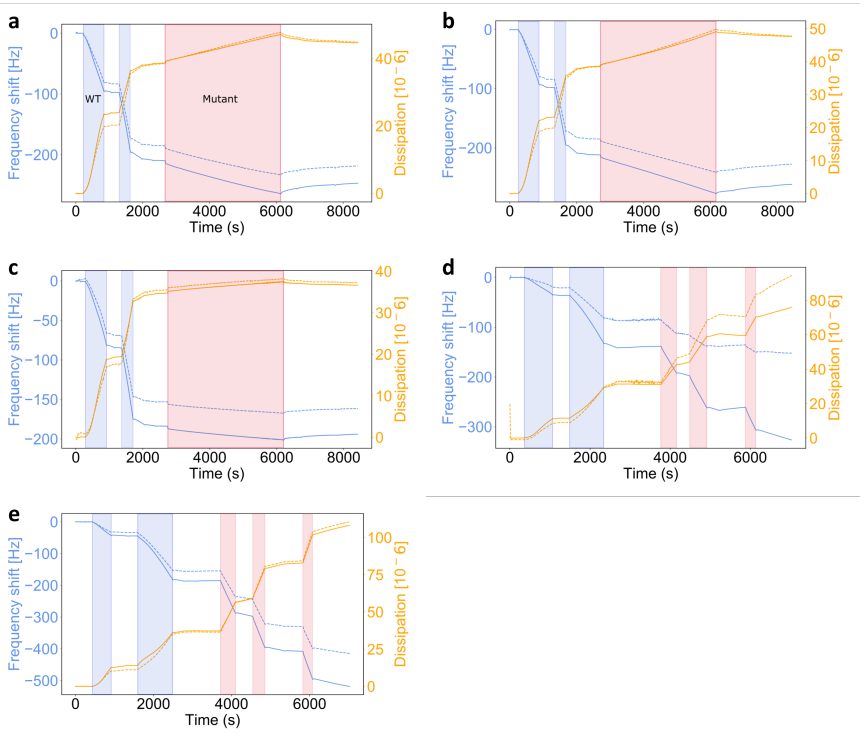

Supplementary Fig. 9 Example of QCM-D traces. Injections of monomeric wild-type (WT) PI3K-SH3 are highlighted with blue bands, and injections of monomeric Ile-to-Ala mutants of PI3K-SH3 are highlighted with red bands (**a** I22A; **b** I29A; **c** I53A; **d** I77A; **e** I82A). The white regions correspond to contact of the QCM sensor surface with buffer. Shown are both the changes in resonant frequency (blue), as well as dissipation (orange). In both cases, the signal for the two overtones N = 3 (dashed line) and N = 5 (solid line) are shown.

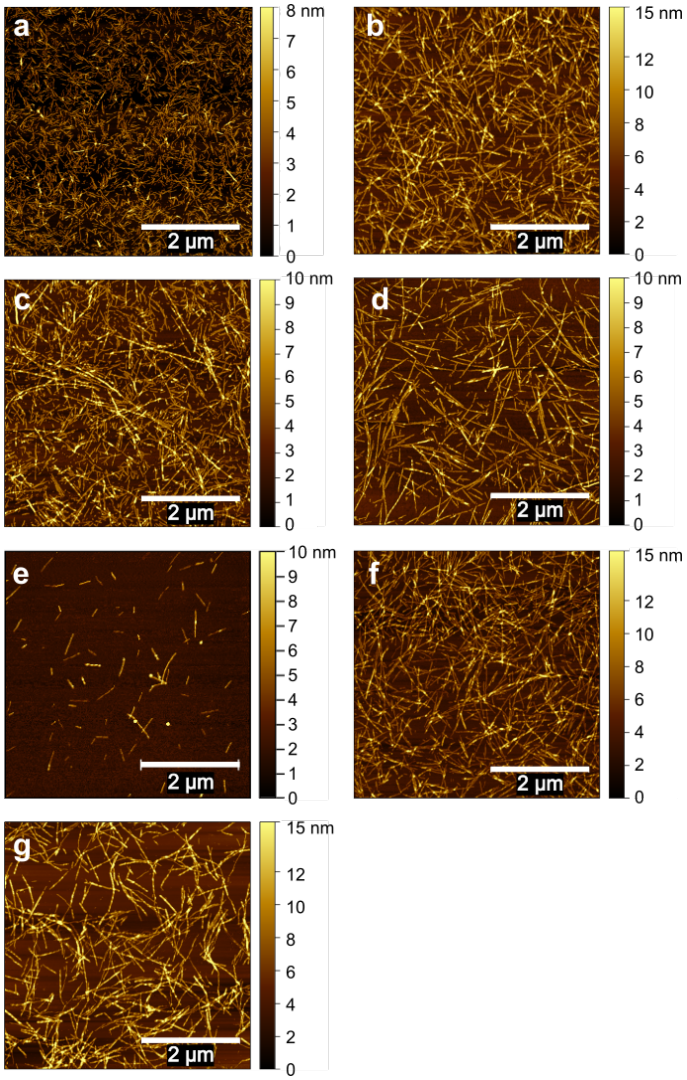

Supplementary Fig. 10 AFM images of **a** WT seeds before elongation experiments. **b** WT seeds incubated with WT monomer. **c**-**g** WT seeds incubated with monomer of I22A (**c**), I29A (**d**), I53A (**e**), I77A (**f**), I82A (**g**).

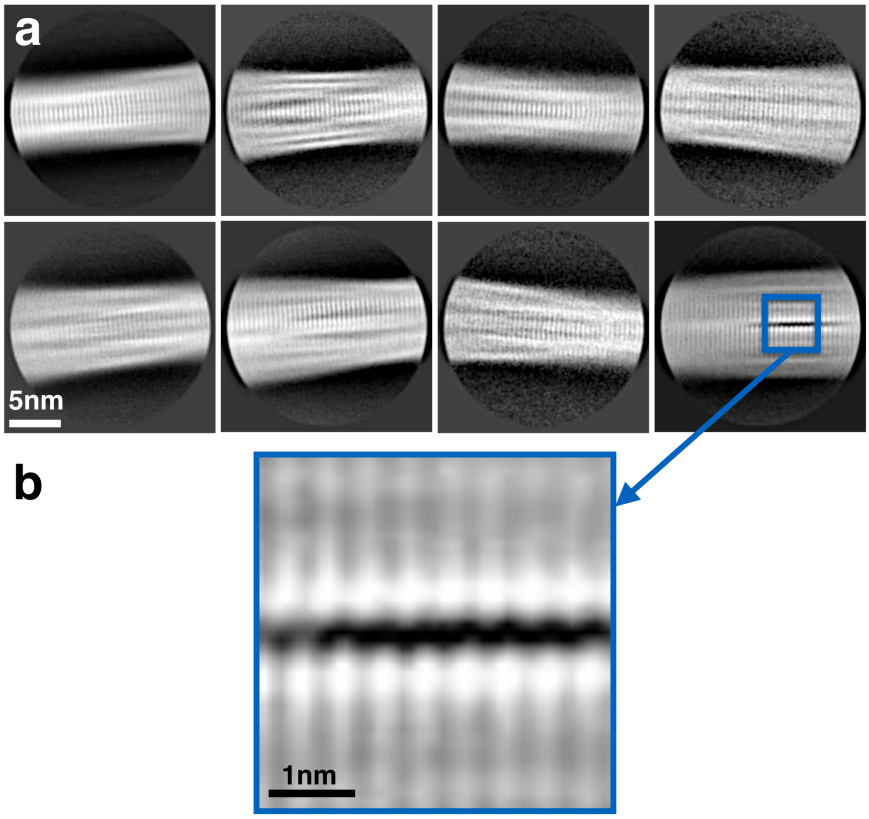

Supplementary Fig. 11 Exemplary 2D classes of DF PI3K-SH3 fibrils. **a** Overview of eight 2D classes comprising 146,215 particles. **b** Magnification of one of the classes displaying the characteristic β-sheet stacking.

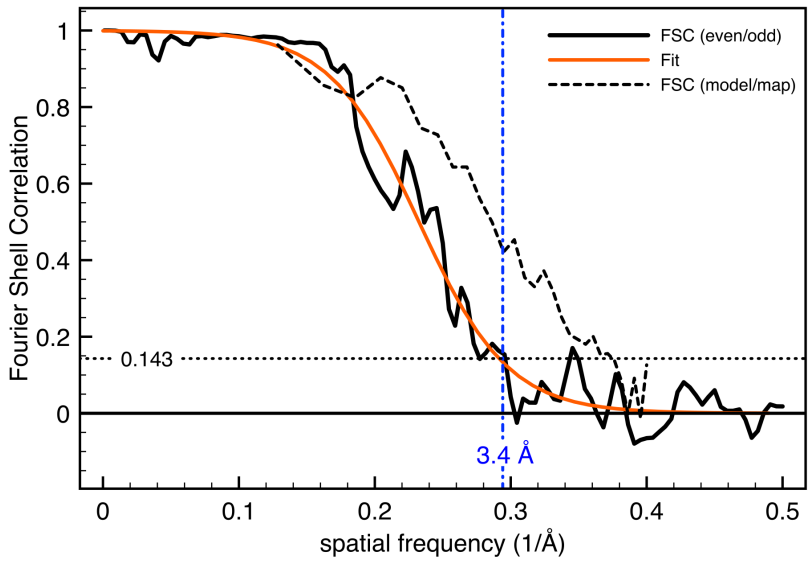

Supplementary Fig. 12 FSC Analysis. FSC curves from the even/odd test (solid black) from the gold-standard refinement yields a resolution of 3.4 Å (using the 0.143 criterion). The even/odd FSC curve is fitted (orange) with the model function 1/(1+e(x-A)/B)) (with A=0.2325 and B=0.03286) to obtain a more robust resolution estimate. The FSC curve comparing the density map computed from the atomic model with the full density reconstruction yields a cross-resolution of 3.4 Å (dashed black).

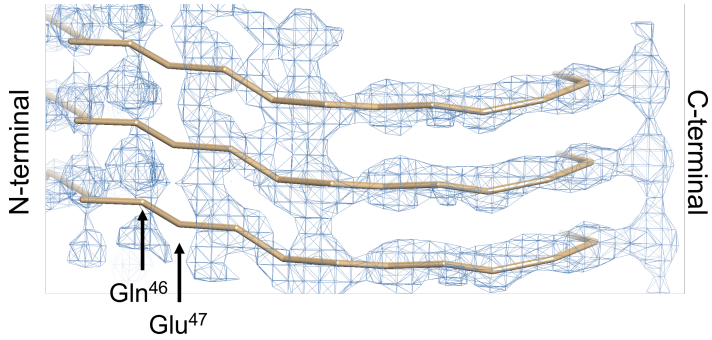

Supplementary Fig. 13 Details of map density between residues 45 and 55. The density around residues Gln^{46} and Glu^{47} does not allow for unambiguous chain tracing, which is mostly due to the weak density of the Glu^{47}. Weak densities of negatively charged residues are typically observed in cryo-EM density maps. The unclear density might also indicate the presence of a less populated second conformer. Detailed magnification of the density map shows the critical area. The Cα-chain trace is shown (brown).

Supplementary References

1. Koyama, S. *et al.* Structure of the PI3K SH3 domain and analysis of the SH3 family. *Cell* **72,** 945–952 (1993).
2. Bayro, M. J. *et al.* High-resolution MAS NMR analysis of PI3-SH3 amyloid fibrils: Backbone conformation and implications for protofilament assembly and structure. *Biochemistry* **49,** 7474–7484 (2010).
3. Kyte, J. & Doolittle, R. F. A simple method for displaying the hydropathic character of a protein. *J. Mol. Biol.* **157,** 105–132 (1982).
4. Buell, A. K. *et al.* Position-dependent electrostatic protection against protein aggregation. *ChemBioChem* **10,** 1309–1312 (2009).
5. Jiménez, J. L. *et al.* Cryo-electron microscopy structure of an SH3 amyloid fibril and model of the molecular packing. *EMBO J.* **18,** 815–821 (1999).
6. Gremer, L. *et al.* Fibril structure of amyloid-β(1–42) by cryo–electron microscopy. *Science* **358,** 116–119 (2017).
7. Iadanza, M. G. *et al.* The structure of a β2-microglobulin fibril suggests a molecular basis for its amyloid polymorphism. *Nat. Commun.* **9,** 4517 (2018).
8. Liberta, F. *et al.* Cryo-EM structure of an amyloid fibril from systemic amyloidosis. *Nat. Commun.* **10,** 1104 (2019).
9. Li, B. *et al.* Cryo-EM of full-length α-synuclein reveals fibril polymorphs with a common structural kernel. *Nat. Commun.* **9,** 3609 (2018).
10. Guerrero-Ferreira, R. *et al.* Cryo-EM structure of alpha-synuclein fibrils. *eLife* **7,** e360402 (2018).
11. Fitzpatrick, A. W. P. *et al.* Cryo-EM structures of tau filaments from Alzheimer's disease. *Nature* **547,** 185–190 (2017).
12. Falcon, B. *et al.* Structures of filaments from Pick's disease reveal a novel tau protein fold. *Nature* **561,** 137–140 (2018).
13. Li, Y. *et al.* Amyloid fibril structure of α-synuclein determined by cryo-electron microscopy. *Cell Res.* **28,** 897–903 (2018).
14. Schütz, A. K. *et al.* Atomic-resolution three-dimensional structure of amyloid β fibrils bearing the osaka mutation. *Angew. Chemie Int. Ed.* **54,** 331–335 (2015).
15. Colvin, M. T. *et al.* Atomic resolution structure of monomorphic Aβ(42) amyloid fibrils. *J. Am. Chem. Soc.* **138,** 9663–9674 (2016).

Primer Sequences

I22A:

GTTTAACTTTAAGAAGGAGATATACCATGGGCAGCAGCCATCACCATCATCATCAT
AGCAGCGGTCTGGTTCCGCGTGGTAGCATGAGTGCCGAAGGTTATCAGTATCGTG
CACTGTATGATTACAAAAAAGAACGCGAAGAAGATGCCGATCTGCACCTGGGTGAT
ATTCTGACCGTTAATAAAGGTAGCCTGGTTGCACTGGGTTTTAGTGATGGTCAAGA
AGCAAAACCGGAAGAAATTGGTTGGCTGAATGGTTATAATGAAACCACCGGTGAAC
GTGGTGATTTTCCGGGTACATATGTTGAATATATCGGTCGCAAAAAAATCAGCCCG
TAGGATCCGGCTGCTAACAAAGCCCGAA

I29A:

GTTTAACTTTAAGAAGGAGATATACCATGGGCAGCAGCCATCACCATCATCATCAT
AGCAGCGGTCTGGTTCCGCGTGGTAGCATGAGTGCCGAAGGTTATCAGTATCGTG
CACTGTATGATTACAAAAAAGAACGCGAAGAGGATATCGATCTGCATCTGGGTGAT
GCACTGACCGTTAATAAAGGTAGCCTGGTTGCACTGGGTTTTAGTGATGGTCAAGA
AGCAAAACCGGAAGAAATTGGTTGGCTGAATGGTTATAATGAAACCACCGGTGAAC
GTGGTGATTTTCCGGGTACATATGTTGAATATATCGGTCGCAAAAAAATCAGCCCG
TAGGATCCGGCTGCTAACAAAGCCCGAA

I53A:

GTTTAACTTTAAGAAGGAGATATACCATGGGCAGCAGCCATCACCATCATCATCAT
AGCAGCGGTCTGGTTCCGCGTGGTAGCATGAGTGCCGAAGGTTATCAGTATCGTG
CACTGTATGATTACAAAAAAGAACGCGAAGAGGATATCGATCTGCATCTGGGTGAT
ATTCTGACCGTTAATAAAGGTAGCCTGGTTGCACTGGGTTTTAGTGATGGTCAAGA
AGCAAAACCGGAAGAGGCAGGTTGGCTGAATGGTTATAATGAAACCACCGGTGAA
CGTGGTGATTTTCCGGGTACATATGTTGAATATATCGGTCGCAAAAAAATCAGCCC
GTAGGATCCGGCTGCTAACAAAGCCCGAA

I77A:

GTTTAACTTTAAGAAGGAGATATACCATGGGCAGCAGCCATCACCATCATCATCAT
AGCAGCGGTCTGGTTCCGCGTGGTAGCATGAGTGCCGAAGGTTATCAGTATCGTG
CACTGTATGATTACAAAAAAGAACGCGAAGAGGATATCGATCTGCATCTGGGTGAT
ATTCTGACCGTTAATAAAGGTAGCCTGGTTGCACTGGGTTTTAGTGATGGTCAAGA
AGCAAAACCGGAAGAAATTGGTTGGCTGAATGGTTATAATGAAACCACCGGTGAAC
GTGGTGATTTTCCGGGTACATATGTTGAATATGCAGGTCGCAAAAAAATCAGCCCG
TAGGATCCGGCTGCTAACAAAGCCCGAA

I82A:

GTTTAACTTTAAGAAGGAGATATACCATGGGCAGCAGCCATCACCATCATCATCAT
AGCAGCGGTCTGGTTCCGCGTGGTAGCATGAGTGCCGAAGGTTATCAGTATCGTG
CACTGTATGATTACAAAAAAGAACGCGAAGAGGATATCGATCTGCATCTGGGTGAT
ATTCTGACCGTTAATAAAGGTAGCCTGGTTGCACTGGGTTTTAGTGATGGTCAAGA
AGCAAAACCGGAAGAAATTGGTTGGCTGAATGGTTATAATGAAACCACCGGTGAAC
GTGGTGATTTTCCGGGTACATATGTTGAATATATCGGTCGTAAAAAAGCGAGCCCG
TAGGATCCGGCTGCTAACAAAGCCCGAA

2 Publication II: Cryo-EM structure of islet amyloid polypeptide fibrils reveals similarities with amyloid-β fibrils

Röder, C.*, Kupreichyk, T.*, Gremer, L. *et al.* Cryo-EM structure of islet amyloid polypeptide fibrils reveals similarities with amyloid-β fibrils. *Nat Struct Mol Biol* **27,** 660–667 (2020). https://doi.org/10.1038/s41594-020-0442-4

ARTICLES
https://doi.org/10.1038/s41594-020-0442-4

nature structural & molecular biology

Cryo-EM structure of islet amyloid polypeptide fibrils reveals similarities with amyloid-β fibrils

Christine Röder[1,2,3,6], Tatsiana Kupreichyk[1,2,3,6], Lothar Gremer[1,2,3], Luisa U. Schäfer[1,2], Karunakar R. Pothula[1,2], Raimond B. G. Ravelli[4], Dieter Willbold[1,2,3], Wolfgang Hoyer[1,2,3] ✉ and Gunnar F. Schröder[1,2,5] ✉

Amyloid deposits consisting of fibrillar islet amyloid polypeptide (IAPP) in pancreatic islets are associated with beta-cell loss and have been implicated in type 2 diabetes (T2D). Here, we applied cryo-EM to reconstruct densities of three dominant IAPP fibril polymorphs, formed in vitro from synthetic human IAPP. An atomic model of the main polymorph, built from a density map of 4.2-Å resolution, reveals two S-shaped, intertwined protofilaments. The segment 21-NNFGAIL-27, essential for IAPP amyloidogenicity, forms the protofilament interface together with Tyr37 and the amidated C terminus. The S-fold resembles polymorphs of Alzheimer's disease (AD)-associated amyloid-β (Aβ) fibrils, which might account for the epidemiological link between T2D and AD and reports on IAPP–Aβ cross-seeding in vivo. The results structurally link the early-onset T2D IAPP genetic polymorphism (encoding Ser20Gly) with the AD Arctic mutation (Glu22Gly) of Aβ and support the design of inhibitors and imaging probes for IAPP fibrils.

Pancreatic islet amyloid deposits are a hallmark of T2D. Islet amyloid, first reported almost 120 years ago as islet hyaline[1], is found in >90% of individuals with T2D[2,3]. The main constituents of islet amyloid are fibrillar aggregates of the 37-residue polypeptide hormone IAPP, also called amylin. IAPP is detected in many organs, including the brain, but is mainly localized in the beta-cells of pancreatic islets, where it is co-synthesized and co-secreted with insulin[3,4]. IAPP is involved in glucose homeostasis and metabolism, with putative functions as a regulator of insulin and glucagon secretion, satiety and gastric emptying[3,5]. Formation of toxic IAPP amyloid aggregates has been associated with dysfunction and death of beta-cells, placing T2D in the group of protein misfolding disorders[2,3,5–8]. However, the nature of the toxic IAPP species and the mechanisms of beta-cell death are not well determined[9]. Potential toxic effects of IAPP amyloid include induction of apoptosis[10], chronic inflammation[11], defects in autophagy[12,13], endoplasmic reticulum stress[14,15] and membrane disruption[16]. Apart from its association with T2D, IAPP amyloid might also play a role in type 1 diabetes[10,17].

IAPP interacts with amyloidogenic proteins that trigger other protein misfolding disorders[18–20]. Of particular interest is its relation to the Aβ peptide, the main component of senile plaques found in the brain tissue of patients with AD. IAPP and Aβ are infamous not only for their strong aggregation propensity and the insolubility of their aggregates[3], but also for their primary sequence similarity[21]. IAPP and Aβ colocalize in Aβ deposits in the brain tissue of patients with AD[19]. Mutual cross-seeding of IAPP and Aβ aggregation observed in transgenic mice further supports a role of the IAPP–Aβ interaction in pathogenesis[19,20].

Structural information on IAPP amyloid is fundamental for improving understanding of the mechanism of amyloid formation, for defining toxic IAPP species and for elucidating IAPP–Aβ cross-seeding[5,7]. Furthermore, high-resolution IAPP fibril structures can inform the design of fibril growth inhibitors and support the development of soluble, nontoxic IAPP analogs for co-formulation with insulin and leptin for treatment of type 1 diabetes and obesity, respectively[5]. Current structural models of IAPP fibrils at physiological pH based on, for example, solid-state NMR (ssNMR) of full-length IAPP and X-ray crystallography of IAPP fragments consistently place the majority of the 37 amino acid residues into the fibril core, while the N terminus is located at the periphery[22–27]. Conversely, the available models also exhibit substantial differences, which could be either a consequence of the limited, distinct restraints obtained by the different techniques applied or a reflection of IAPP fibril polymorphism[5,28]. Here, we have applied cryo-EM to determine the structure of IAPP amyloid fibrils grown at physiologically relevant pH. We provide a structural analysis of three dominant polymorphs, including an atomic model of the main polymorph comprising residues 13–37 in a density map of 4.2-Å resolution.

Results

Polymorphism of IAPP fibrils. For this work, amyloid fibrils were prepared from synthetic human IAPP including the amidated C terminus. Islet amyloid in T2D is typically extracellular, but IAPP aggregation is supposedly initiated intracellularly, possibly in the secretory granules at a pH of 5.0–6.0 (refs. [3,29]); therefore, IAPP fibrils were prepared at a pH of 6.0. Long, well-ordered fibrils were obtained, as shown by atomic force microscopy (AFM) imaging (Extended Data Figs. 1 and 2). We could differentiate at least five different polymorphs in the AFM images and in subsequently performed cryo-EM experiments. Of these five polymorphs, three were

[1]Institute of Biological Information Processing (IBI-7: Structural Biochemistry), Forschungszentrum Jülich, Jülich, Germany. [2]Jülich Centre for Structural Biology (JuStruct), Forschungszentrum Jülich, Jülich, Germany. [3]Institut für Physikalische Biologie, Heinrich Heine University Düsseldorf, Düsseldorf, Germany. [4]The Multimodal Molecular Imaging Institute, Maastricht University, Maastricht, the Netherlands. [5]Physics Department, Heinrich Heine University Düsseldorf, Düsseldorf, Germany. [6]These authors contributed equally: Christine Röder, Tatsiana Kupreichyk. ✉e-mail: wolfgang.hoyer@uni-duesseldorf.de; gu.schroeder@fz-juelich.de

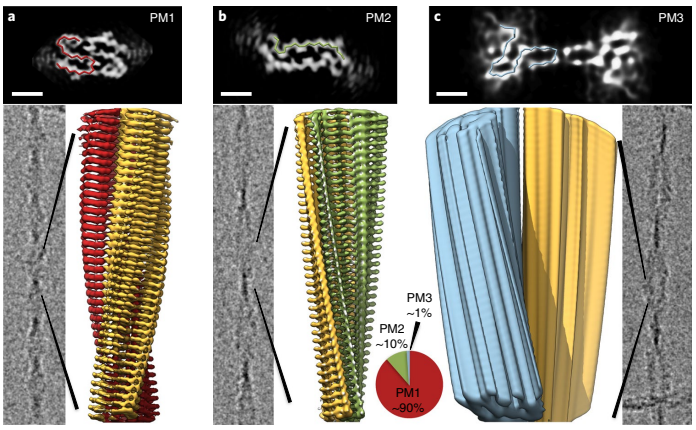

Fig. 1 | Comparison of reconstructed IAPP polymorphs. a–c, PM1 (**a**), PM2 (**b**) and PM3 (**c**). For each polymorph, three panels are shown: a slice of a 3D reconstruction superimposed on the respective Cα chain for one monomer (black; scale bars, 2 nm); a micrograph displaying the respective polymorph (gray); and 3D density (red/yellow, PM1 (**a**); green/yellow, PM2 (**b**); blue/yellow, PM3 (**c**)). The pie chart visualizes the fraction of each polymorph in the dataset.

present in sufficient amounts for further analysis (Fig. 1, Table 1, and Extended Data Figs. 1 and 2). The main polymorph, polymorph 1 (PM1), makes up ~90% of all fibrils, while polymorph 2 (PM2) and polymorph 3 (PM3) represent up to ~10% and ~1%, respectively, of the total number of fibrils in the dataset.

PM1 has a right-handed helical symmetry with a pitch of 48 nm and a width of 2.5–4.5 nm (Figs. 1a and 2a). Three-dimensional (3D) reconstruction of 1,161 individual fibril images using a helical pseudo-2_1 symmetry led to 4.2-Å resolution, which was sufficient to unambiguously build an atomic model with helical parameters of 2.35 Å (helical rise) and 178.23° (helical twist). The fibril consists of two stacks of S-shaped IAPP monomers winding around each other. Further details of the structure and molecular characteristics of PM1 are described later.

PM2 also consists of two protofilaments and exhibits pseudo-2_1 symmetry (Fig. 1b). With a maximum and minimum width of 52 Å and 17 Å, respectively, PM2 shows a more pronounced twist in the projection images (Fig. 1b) and is remarkably flatter than PM1 (Fig. 1a). The helical pitch is 94 nm, and AFM experiments suggest a left-handed twist. In contrast to the S-shaped PM1, the density map indicates an extended conformation of two IAPP monomers in PM2. The protofilament interface consists of a continuous sequence region of at least 18 amino acids. The density map with approximately 4.2-Å resolution would in principle allow for model building of 21 amino acid residues, but the sequence assignment is ambiguous. Therefore, we modeled all 17 possible sequence assignments in both forward and backward backbone trace directions, leading to $17 \times 2 = 34$ different models. All 34 models were refined in DireX[30] using cross-validation in the resolution range of 3.0–4.0 Å for calculation of the C_{free} value[31]. Results were ranked by C_{free} value (Extended Data Fig. 3). According to this criterion, the most probable model for PM2, which also exhibits the highest C_{work} value, shares important features with the PM1 model, as discussed below.

Compared to the other polymorphs, PM3 was not well represented in the micrographs. The overall features of PM3, namely the broad width (110 Å) and pronounced twist (159-nm pitch), lead to a dumbbell shape (Fig. 1c). From the 4,591 particles extracted, we could reconstruct a density with 8.1-Å resolution. Because the resolution was rather low, we were not able to build an atomic model but only hypothesize a possible Cα backbone trace (Fig. 1c). Nonetheless, the density also clearly indicates two symmetric protofilaments and reveals that the 10-Å-wide protofilament interface of PM3, presumably consisting of three residues, is very small compared to those of PM1 and PM2 (Fig. 1).

Fibril architectures of PM1 and PM2. In PM1, each monomer exhibits an overall S-fold that comprises residues Ala13–Tyr37 (Fig. 2). Up to residue 12, the N-terminal part including the disulfide bond between Cys2 and Cys7 is largely disordered and, therefore, does not reveal clear density (Fig. 1a). The side view of PM1 shows the typical cross-β pattern of amyloid fibril structures with a spacing of 4.7 Å between the layers (Fig. 2c). The cross-β layers are well resolved in the density, as shown in Fig. 2d. On the secondary structure level, we observed three β-sheets: residues 14–20, 26–32 and 35–37. Figure 3b shows the comparison of our model with former secondary structure predictions based on sequence analysis[22], NMR[23,26,27], electron paramagnetic resonance (EPR)[25] and X-ray crystallography experiments[24].

The cross-section of the PM1 fibril displays two monomeric S-folds related by approximate 2_1 symmetry (Fig. 2b). The double-S shape is stabilized by both hydrophobic and polar interactions. The central part of the protofilament interface contains a hydrophobic cluster comprising residues Phe23, Gly24, Ala25 and Leu27 as well as Phe23′, Gly24′, Ala25′ and Leu27′ (Fig. 2b and Extended Data Fig. 4). Additionally, the backbone of Phe23 and Ala25 forms hydrogen bonds at the center of the fibril, thereby connecting one subunit with two neighboring subunits above and below in the opposing protofilament (Fig. 3c). More precisely, there is a hydrogen bond between the carbonyl group of Phe23 of chain i and the amide group of Ala25 of chain $i+1$ and another hydrogen bond between the amide group of Ala25 of chain i and the carbonyl group of Phe23 of chain $i-1$. The backbone around Gly24 does not maintain the cross-β hydrogen-bonding pattern along the fibril. The aforementioned interactions are formed by residues located in the sequence motif (N)NFGAIL, shown earlier to be important for fibrillization of IAPP[5,32–34]. This motif is located in the central part

Table 1 | Cryo-EM data collection, refinement and validation statistics

	PM1 (EMD-10669, PDB 6Y1A)	PM2 (EMD-10670)	PM3 (EMD-10671)
Data collection and processing			
Magnification	110,000	110,000	110,000
Voltage (kV)	200	200	200
Dose rate (e^{-} Å^{-2} s^{-1})	0.9	0.9	0.9
Exposure time (s)	46	46	46
Movie frames (no.)	1,800	1,800	1,800
Defocus range (μm)	−1.0 to −2.2	−1.0 to −2.2	−1.0 to −2.2
Pixel size (Å)	0.935	0.935	0.935
Symmetry imposed	helical, pseudo 2_1	helical, pseudo 2_1	helical, pseudo 2_1
Helical rise (Å)	2.351	2.352	2.323
Helical twist (°)	178.23	179.10	179.47
Helical pitch (Å)	479.5	940	1590
Final fibril images (no.)	1,161	1,480	99
Final particle images (no.)	37,120	24,011	4,591
Map resolution (Å)	4.2	4.2	8.1
FSC threshold	0.143	0.143	0.143
Refinement			
Initial density model used	Noise-filled cylinder	Noise-filled cylinder	Noise-filled cylinder
Model composition			
Non-hydrogen atoms	2,975		
Protein residues	416		
R.m.s. deviations			
Bond lengths (Å)	0.0039		
Bond angles (°)	0.60		
Validation			
MolProbity score	1.99		
Clashscore	15.2		
Poor rotamers (%)	0		
Ramachandran plot			
Favored (%)	95.7		
Allowed (%)	4.3		
Disallowed (%)	0		

of the structure, in the turn between the first two β-sheets (Figs. 2b and 3a,b). Within this turn, the kink around Phe23 and Asn21 is stabilized by hydrogen bonds between Asn22 and Ser19, as well as between Asn22 and Gly24 (Figs. 2b and 3c). Additionally, Ile26 might support this turn by hydrophobic interactions with Val17. In the second turn, between β-sheets 2 and 3, Asn31 together with Ser29, Asn35 and Tyr37 creates a hydrophilic cluster at the C terminus of IAPP with possible interactions between Asn31 and Ser29, as well as Asn31 and Asn35. In addition, Tyr37 might interact with both Asn35 and Ser29 (Fig. 2b). Moreover, the amidated C terminus itself forms a polar ladder (Fig. 3d). This ladder is further connected to Asn21′ of the opposite protofilament with slightly longer and, therefore, weaker hydrogen bonds. The overall cross-β arrangement is further stabilized by Asn14, Asn21 and Asn31, which form polar ladders alongside the fibril axis. Asn22 does not form a polar ladder, but instead its Nδ2 atom forms a hydrogen bond with the carbonyl group of Gly24 within the same monomer (Fig. 3c). It should be noted that the detailed analysis of the hydrogen-bonding network is derived from the atomic model, which is an interpretation of the experimental density map.

IAPP contains an unusually large number of the polar residues asparagine, serine and threonine[5]. We found that these residues form polar streaks within the fibril core of PM1 (Extended Data Fig. 4). The polar streaks are characterized by extensive networks of hydrogen bonds, as discussed earlier. The segregation of polar and apolar residues into distinct clusters within the fibril core likely contributes to the high stability of IAPP amyloid. In IAPP, this segregation is facilitated by the preorganization of amino acid residues in polar and apolar clusters within the primary structure, in the fashion of a block copolymer with polar blocks 19-SSNN-22 and 28-SSTN-31 and apolar block 23-FGAIL-27.

All-atom molecular dynamic (MD) simulations were performed to evaluate the overall stability of the model. In two independent 250-ns simulations, the model remained stable (Extended Data Fig. 5) with an all-atom r.m.s. deviation (r.m.s.d.) of a single subunit from the deposited model of ~2 Å and an r.m.s. fluctuation (r.m.s.f.) of residues 16–37 of 0.8 Å. The N-terminal part including Phe15 was already substantially more mobile (Extended Data Fig. 5a,b,e). Notably, we observed ladder formation for Asn22 in the MD simulation, which was not supported by the density map.

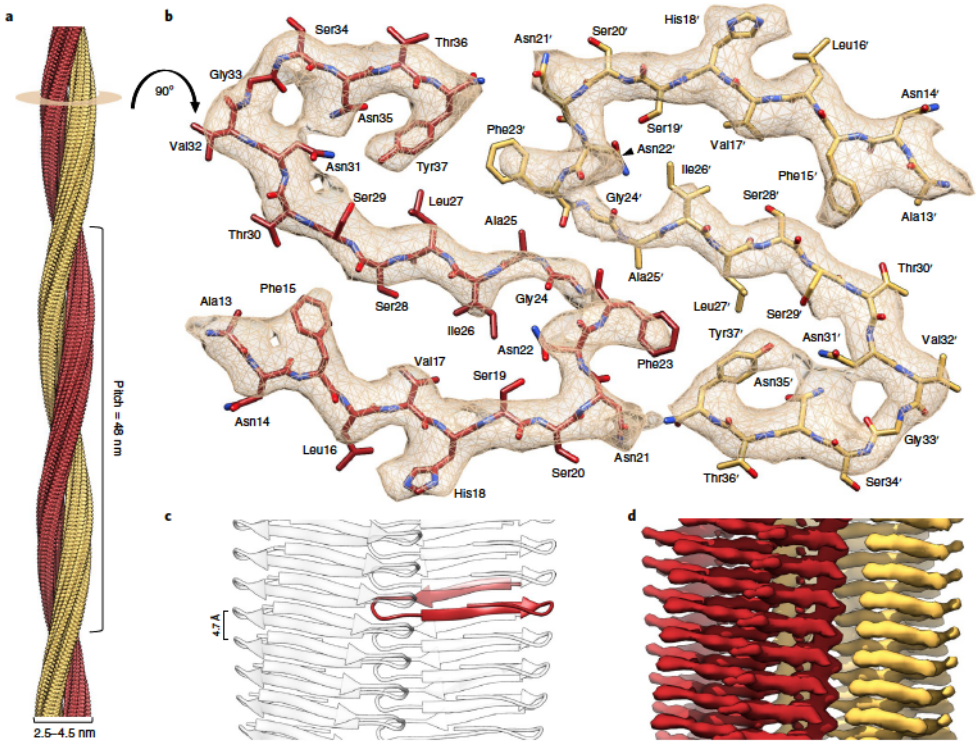

Fig. 2 | Architecture of the main polymorph, PM1. a, PM1 exhibits a helical pitch of 48 nm and a minimum and maximum width of 2.5 and 4.5 nm, respectively. The fibril consists of two protofilaments (red and yellow). **b**, Cross-sectional view: two symmetry-related monomers, with an atomic model of residues 13–37 built into the 4.2-Å-resolution density (contour level of 1.5σ). **c**, Side view: one monomer is highlighted (red) to show its integration in the fibrillar structure. Cross-β layers are separated by 4.7 Å. **d**, Side view: reconstructed density corresponding to **c**.

For earlier structures of amyloid fibrils, we discussed the need for a minimal fibril unit, which is the smallest fibril structure fragment in which the capping subunits at both ends would have established the same full contact interface with other constituting monomers as the capping subunits of an extended fibril[35,36]. Here, the minimal fibril unit consists of only three monomers, which is the smallest possible unit. One subunit is in contact exclusively with its neighboring monomers above and below and with its opposing monomers through protofilament interface contacts (Fig. 2c). Indeed, we did not observe any interlocking of different cross-β layers, which was postulated to have a stabilizing effect on other amyloid fibrils[35,36].

The IAPP folds in PM1 and PM2 are clearly distinct, yet the most probable model for PM2 shares important features with the PM1 model (Extended Data Fig. 3). First, the NFGAIL motif forms the center of the fibril interface. Second, the N terminus is rather flexible and thus not resolved in the density map. The first visible residue in the density of the PM2 model is Phe15. In contrast to PM1, not only the N terminus but also the two C-terminal residues Thr36 and Tyr37 are not clearly resolved and are potentially mobile. In between the two protofilaments is a relatively large cavity lined by hydrophobic residues Phe23, Ala25 and Ile26. It is not clear whether this gap is water filled.

Similar S-folds in IAPP and Aβ fibrils. Colocalization of IAPP and Aβ has been observed in patients with T2D and AD[19]. The epidemiological link between diabetes and dementia might be explained by cross-seeding of IAPP and Aβ aggregation[19,20,37,38]. Different sites on amyloid fibrils are relevant for cross-seeding: cross-elongation (that is, the elongation of a fibril with a heterologous protein) occurs at the fibril end, while cross-nucleation (that is, the fibril-catalyzed formation of a heterologous fibril nucleus) may occur both at the fibril end and along the fibril surface. Like IAPP, Aβ forms different fibril polymorphs, according to ssNMR and cryo-EM studies[35,39–43]. Comparing IAPP PM1 to multiple $A\beta_{1-42}$ polymorphs containing S-shaped folds[35,40,44], we found that the backbones superimpose (Fig. 4b,c). The structural similarity of the backbones is highest when superimposing the models in an antiparallel arrangement (Fig. 4c). The similarity between IAPP and $A\beta_{1-42}$ fibril folds regarding topology and size might promote cross-seeding at the fibril end, which could further be supported by the sequence similarity of IAPP and Aβ[21]. The sequence similarity is highest around the Gly-Ala-Ile segment at positions 24–26 of IAPP and positions 29–31 of Aβ. In both IAPP and Aβ, this segment is located in the solvent-excluded center of the S-fold (Fig. 4d). A further segment that can be superimposed in parallel arrangement is the N-terminal strand of the

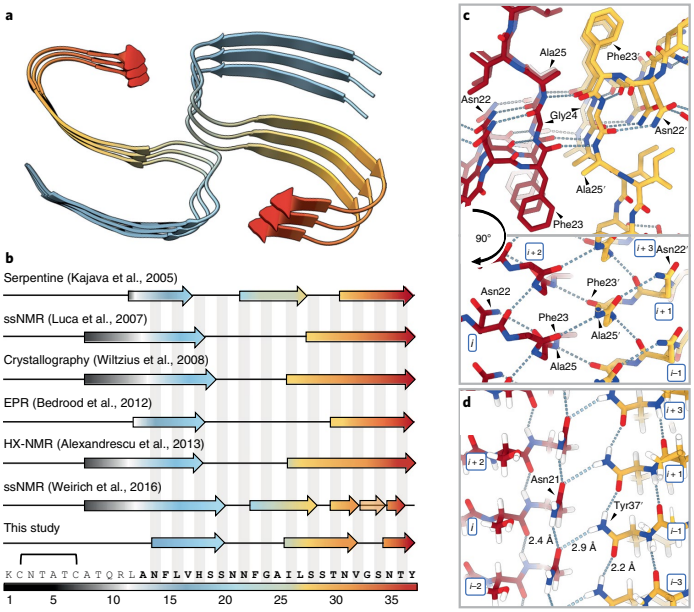

Fig. 3 | Secondary structure and hydrogen bonding in PM1. a, Secondary structure of the IAPP model. Tilted cross-section of three fibril layers with representation of the three β-sheets. **b**, Comparison of our PM1 structure to former models derived from sequence-based prediction[22], EPR[25], ssNMR[27], X-ray crystallography[24] and hydrogen-exchange NMR (HX-NMR) studies[26]. Arrows indicate β-sheets (one potential β-sheet is shown as transparent). The disulfide bridge between residues Cys2 and Cys7 is indicated. Fibril formation was performed at pH 7.4 (refs. [23,25–27]) or 6.5 (ref. [24]), while our IAPP fibrils were formed at pH 6.0. **c**, Top view of the fibril core showing the two NFGAIL motifs in the opposing protofilaments (red and yellow), as well as the hydrogen-bonding network (dashed lines). Bottom, side view of the fibril core illustrating the interlocking of the protofilaments by hydrogen bonds. **d**, Side view of the fibril showing the hydrogen-bonding interaction of Asn21 with the amidated C terminus of the opposing protofilament (yellow), as well as polar ladders of Asn21 and Tyr37′ along the fibril axis.

S-fold in IAPP PM1 and in the LS-shaped $A\beta_{1-42}$ polymorph, corresponding to 14-NFLVHSSNN-22 of IAPP and 16-KLVFFAEDV-24 of Aβ (Fig. 4d).

A serine-to-glycine substitution at position 20 (Ser20Gly), the only known IAPP genetic polymorphism in humans, is associated with early onset of T2D[45,46]. The Ser20Gly substitution enhances aggregation and toxicity of IAPP and leads to increased beta-cell apoptosis[47–50]. Substitution of serine with glycine has been suggested to promote turn formation at residue 20, favoring the amyloid fibril conformation[51,52]. In line with this notion, Ser20 is located at the edge of the turn comprising residues 20–25 in PM1. Interestingly, when comparing the S-fold of IAPP with the LS-fold of Aβ[35] (Fig. 4c,d), the Ser20Gly substitution in IAPP and the Arctic mutation (encoding a Glu22Gly substitution) of Aβ[53], which causes early-onset AD, are located at corresponding positions (Fig. 4d). This suggests that these two replacements with glycine might have analogous conformational consequences.

Discussion

The IAPP fibril samples investigated here displayed fibril polymorphism. While all three main polymorphs consist of two (pseudo) symmetric, helically intertwined protofilaments, they exhibit substantial differences in the protein fold (Fig. 1). PM1 consists of a compact S-shaped fold, PM2 features an extended IAPP conformation and the PM3 cross-section shows two compact motifs connected by an extended bridge. Marked differences are also observed between the protofilament interfaces: in PM1, the interface consists of one of the turns and the C-terminal end of the S-fold; in PM2, the entire extended IAPP segment that constitutes the fibril core is involved in the protofilament interface; and in PM3, a very narrow interface of probably only three residues is observed. Despite these differences, certain IAPP sequence segments might contribute similarly to distinct fibril polymorphs—in both PM1 and the most probable PM2 model, residues 22-NFGAIL-27 form the central fibril core.

In an early report[28] of IAPP fibril polymorphism, the most common polymorph consisted of two protofilaments coiled around each other with a helical pitch of 50 nm, while another polymorph showed a helical pitch of 100 nm. These values are in good agreement with PM1 (48 nm) and PM2 (94 nm). Despite these similarities, when comparing the cryo-EM results with previous structural data, it must be considered that variations may arise from differences between both the applied techniques and the polymorphs present in the samples. In line with previous studies[22–27], we found that the IAPP N terminus including the disulfide bond between Cys2 and Cys7 is not part of the fibril core, neither in PM1 (Fig. 3b) nor in the most probable model of PM2 (Extended Data Fig. 3). While well-defined density starts from residue 13 in the cryo-EM data, some studies reported the fibril core to begin around residue 8 (Fig. 3b). However, HX-NMR data indicated that residues 8–14

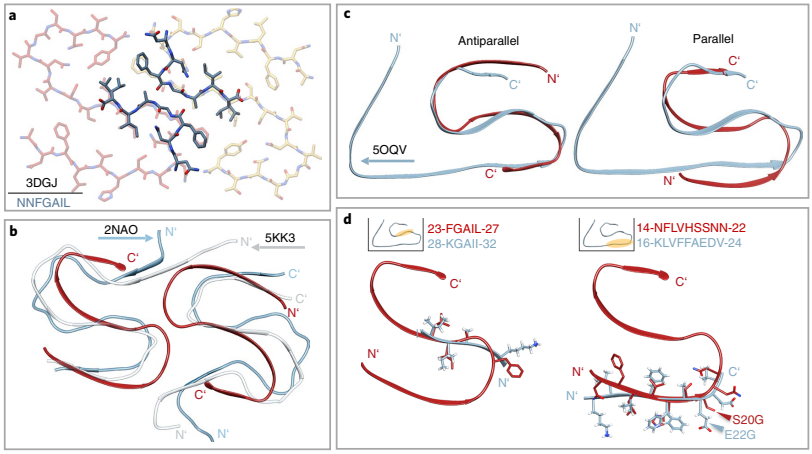

Fig. 4 | Structural comparison of PM1 with fibrillar IAPP peptide and Aβ fibril models. a, Overlay of our model with a crystal structure (dark; 3DGJ) of the NNFGAIL peptide from Wiltzius et al.[24]. **b**, Overlay of IAPP (red) with NMR structures by Wälti et al.[40] (light blue; 2NAO) and Colvin et al.[44] (gray; 5KK3). **c**, Antiparallel (left) and parallel (right) overlay of one IAPP PM1 monomer (red) with the atomic model of $A\beta_{1-42}$ (light blue; 5OQV) from Gremer et al.[35]. **d**, Detailed parallel overlay of sequence segments in IAPP (red) and $A\beta_{1-42}$ (light blue; 5OQV) from Gremer et al.[35]. Small boxes indicate where the respective sequence motif is located in the $A\beta_{1-42}$ model. Left, the FGAIL motif of IAPP shows high sequence identity to KGAII in $A\beta_{1-42}$. Right, the NFLVHSSNN motif of IAPP corresponds to the KLVFFAEDV motif of $A\beta_{(1-42)}$ with high structural similarity. Disease-related substitutions in IAPP (Ser20Gly) and $A\beta_{1-42}$ (Glu22Gly) are located at corresponding positions.

were less protected than those in the central fibril core[26]. In agreement with previous data, residues 13–37 are largely in β-sheet conformation in PM1, although variation exists with respect to the precise location of β-strands (Fig. 3b). A common feature of the PM1 cryo-EM structure and previous models is a turn in segment 20-SNNFG-24 (refs. [23–27]). A second turn is formed in PM1 in segment 32-VGS-34 and was also supported by ssNMR and HX-NMR studies[26,27]. Both turns establish an S-shaped fold of IAPP in PM1. Consequently, the tyrosyl ring of the C-terminal Tyr37 packs against Phe23′ in the adjacent protofilament, which is in line with distance restraints for IAPP fibrils obtained by fluorescence resonance energy transfer[54]. In addition, these energy-transfer experiments proposed a maximum distance of 11 Å between Tyr37 and a second phenylalanine, coinciding with the Tyr37–Phe15 distance in the PM1 model[54]. The C-terminal amide stabilizes the S-shaped fibril structure by forming a polar ladder and a hydrogen bond with Asn21 in the adjacent protofilament (Fig. 3d), in line with enhanced amyloid formation upon C-terminal amidation of IAPP[55,56].

The sequence region at positions 20–29 is particularly important for the amyloidogenicity of IAPP[5,32,33]. This can be rationalized with the PM1 fibril structure. First, residues 22-NFGAILSS-29 constitute the solvent-excluded central core of PM1 fibrils (Fig. 2b). Second, residues 21-NNFGAIL-27 form, together with Tyr37 and the amidated C terminus, the protofilament interface. In previous structural models of IAPP fibrils, the region encompassing residues 20–29 was associated with formation of a partially ordered loop rather than a β-structure, which was surprising considering the sensitivity of IAPP amyloid formation to mutations mapping to this region[7]. The PM1 fibril structure shows that residues 20–25 indeed form a turn, albeit one that is an integral part of the fibril core, featuring an extensive hydrogen-bonding network (Fig. 3c,d). Residues 26–29, on the other hand, are part of the central β-sheet of IAPP PM1 fibrils. Remarkably, the structure of the 21-NNFGAIL-27 segment in PM1 is highly similar in atomic detail to a crystal structure of the NNFGAIL peptide[24] (Fig. 4a). This applies both to the fold of the individual polypeptide molecules and to the peptide–protofilament interface, which displays extensive main chain–main chain interactions between the 23-FGA-25 segments. The similarity of the NNFGAIL structure between the peptide crystal and the PM1 fibril indicates that the 21-NNFGAIL-27 segment drives IAPP amyloid formation.

In contrast to the human protein, IAPP proteins from several other species were found to be non-amyloidogenic[5]. The non-amyloidogenic rat and mouse IAPP contain six amino acids that are different from the human sequence[33]. Five of these are located in the sequence region encompassing residues 23–29, which is part of the central core of PM1 fibrils, as discussed above. The differing amino acids include three prolines in rat and mouse IAPP at positions 25, 28 and 29. As proline disrupts secondary structures, these proline residues are incompatible with the PM1 structure, consistent with the low amyloidogenicity of rat and mouse IAPP. The insights gained from the rat and mouse IAPP sequences were exploited in the design of pramlintide, a non-amyloidogenic IAPP analog carrying proline substitutions at positions 25, 28 and 29 (ref. [57]). Pramlintide is co-administered with insulin in type 1 diabetes to improve glucose level regulation. Similarly, the combination of a non-amyloidogenic IAPP analog and leptin could be a promising treatment option for obesity[58]. However, these drugs would benefit from increased solubility[59]. The structural data on IAPP fibrils presented here may aid in the design of non-amyloidogenic, soluble IAPP analogs by suggesting potential sites for chemical modifications of IAPP that counteract fibril formation.

This study presents the 4.2-Å-resolution structure of an IAPP fibril polymorph consisting of two S-shaped protofilaments but also highlights the polymorphism of IAPP fibrils. The dominant S-shaped PM1 can rationalize many of the characteristics of IAPP fibrils described by various groups, suggesting that PM1 is a common polymorph or that it at least represents general features of

prevalent IAPP polymorphs. The study provides detailed insight into the link between the IAPP amino acid sequence and fibril structure; furthermore, it reveals similarities between IAPP and Aβ fibril structures, which are particularly striking in consideration of the link between diabetes and AD. The structural information gained may serve as a basis to define the mechanisms of amyloid formation and toxicity of IAPP. Moreover, the PM1 fibril may be used as a target structure to design imaging probes for IAPP fibrils and inhibitors of IAPP fibril growth.

Online content

Any methods, additional references, Nature Research reporting summaries, source data, extended data, supplementary information, acknowledgements, peer review information; details of author contributions and competing interests; and statements of data and code availability are available at https://doi.org/10.1038/s41594-020-0442-4.

Received: 12 February 2020; Accepted: 30 April 2020;
Published online: 15 June 2020

References

1. Opie, E. L. On the relation of chronic interstitial pancreatitis to the islands of Langerhans and to diabetes mellitus. *J. Exp. Med.* **5**, 397–428 (1901).
2. Jurgens, C. A. et al. β-cell loss and β-cell apoptosis in human type 2 diabetes are related to islet amyloid deposition. *Am. J. Pathol.* **178**, 2632–2640 (2011).
3. Westermark, P., Andersson, A. & Westermark, G. T. Islet amyloid polypeptide, islet amyloid, and diabetes mellitus. *Physiol. Rev.* **91**, 795–826 (2011).
4. Wimalawansa, S. J. Amylin, calcitonin gene-related peptide, calcitonin, and adrenomedullin: a peptide superfamily. *Crit. Rev. Neurobiol.* **11**, 167–239 (1997).
5. Akter, R. et al. Islet amyloid polypeptide: structure, function, and pathophysiology. *J. Diabetes Res.* **2016**, 2798269 (2016).
6. Mukherjee, A., Morales-Scheihing, D., Butler, P. C. & Soto, C. Type 2 diabetes as a protein misfolding disease. *Trends Mol. Med.* **21**, 439–449 (2015).
7. Cao, P., Abedini, A. & Raleigh, D. P. Aggregation of islet amyloid polypeptide: from physical chemistry to cell biology. *Curr. Opin. Struct. Biol.* **23**, 82–89 (2013).
8. Halban, P. A. et al. β-cell failure in type 2 diabetes: postulated mechanisms and prospects for prevention and treatment. *J. Clin. Endocrinol. Metab.* **99**, 1983–1992 (2014).
9. Zraika, S. et al. Toxic oligomers and islet beta cell death: guilty by association or convicted by circumstantial evidence? *Diabetologia* **53**, 1046–1056 (2010).
10. Zhang, S. et al. The pathogenic mechanism of diabetes varies with the degree of overexpression and oligomerization of human amylin in the pancreatic islet β cells. *FASEB J.* **28**, 5083–5096 (2014).
11. Masters, S. L. et al. Activation of the NLRP3 inflammasome by islet amyloid polypeptide provides a mechanism for enhanced IL-1β in type 2 diabetes. *Nat. Immunol.* **11**, 897–904 (2010).
12. Rivera, J. F. et al. Human IAPP disrupts the autophagy/lysosomal pathway in pancreatic β-cells: protective role of p62-positive cytoplasmic inclusions. *Cell Death Differ.* **18**, 415–426 (2011).
13. Gupta, D. & Leahy, J. L. Islet amyloid and type 2 diabetes: overproduction or inadequate clearance and detoxification? *J. Clin. Invest.* **124**, 3292–3294 (2014).
14. Casas, S. et al. Impairment of the ubiquitin–proteasome pathway is a downstream endoplasmic reticulum stress response induced by extracellular human islet amyloid polypeptide and contributes to pancreatic β-cell apoptosis. *Diabetes* **56**, 2284–2294 (2007).
15. Hull, R. L. et al. Amyloid formation in human IAPP transgenic mouse islets and pancreas, and human pancreas, is not associated with endoplasmic reticulum stress. *Diabetologia* **52**, 1102–1111 (2009).
16. Janson, J., Ashley, R. H., Harrison, D., McIntyre, S. & Butler, P. C. The mechanism of islet amyloid polypeptide toxicity is membrane disruption by intermediate-sized toxic amyloid particles. *Diabetes* **48**, 491–498 (1999).
17. Paulsson, J. F. et al. High plasma levels of islet amyloid polypeptide in young with new-onset of type 1 diabetes mellitus. *PLoS ONE* **9**, e93053 (2014).
18. Martinez-Valbuena, I. et al. Interaction of amyloidogenic proteins in pancreatic β cells from subjects with synucleinopathies. *Acta Neuropathol.* **135**, 877–886 (2018).
19. Oskarsson, M. E. et al. In vivo seeding and cross-seeding of localized amyloidosis: a molecular link between type 2 diabetes and Alzheimer's disease. *Am. J. Pathol.* **185**, 834–846 (2015).
20. Moreno-Gonzalez, I. et al. Molecular interaction between type 2 diabetes and Alzheimer's disease through cross-seeding of protein misfolding. *Mol. Psychiatry* **9**, 1327–1334 (2017).
21. O'Nuallain, B., Williams, A. D., Westermark, P. & Wetzel, R. Seeding specificity in amyloid growth induced by heterologous fibrils. *J. Biol. Chem.* **279**, 17490–17499 (2004).
22. Kajava, A. V., Aebi, U. & Steven, A. C. The parallel superpleated β-structure as a model for amyloid fibrils of human amylin. *J. Mol. Biol.* **348**, 247–252 (2005).
23. Luca, S., Yau, W. M., Leapman, R. & Tycko, R. Peptide conformation and supramolecular organization in amylin fibrils: constraints from solid-state NMR. *Biochemistry* **46**, 13505–13522 (2007).
24. Wiltzius, J. J. W. et al. Atomic structure of the cross-β spine of islet amyloid polypeptide (amylin). *Protein Sci.* **17**, 1467–1474 (2008).
25. Bedrood, S. et al. Fibril structure of human islet amyloid polypeptide. *J. Biol. Chem.* **287**, 5235–5241 (2012).
26. Alexandrescu, A. T. Amide proton solvent protection in amylin fibrils probed by quenched hydrogen-exchange NMR. *PLoS ONE* **8**, e56467 (2013).
27. Weirich, F. et al. Structural characterization of fibrils from recombinant human islet amyloid polypeptide by solid-state NMR: the central FGAILS segment is part of the β-sheet core. *PLoS ONE* **11**, e0161243 (2016).
28. Goldsbury, C. S. et al. Polymorphic fibrillar assembly of human amylin. *J. Struct. Biol.* **119**, 17–27 (1997).
29. Hutton, J. C. The internal pH and membrane potential of the insulin-secretory granule. *Biochem. J.* **204**, 171–178 (1982).
30. Wang, Z. & Schröder, G. F. Real-space refinement with DireX: from global fitting to side-chain improvements. *Biopolymers* **97**, 687–697 (2012).
31. Falkner, B. & Schröder, G. F. Cross-validation in cryo-EM-based structural modeling. *Proc. Natl Acad. Sci. USA* **110**, 8930–8935 (2013).
32. Westermark, P., Engstrom, U., Johnson, K. H., Westermark, G. T. & Betsholtz, C. Islet amyloid polypeptide: pinpointing amino acid residues linked to amyloid fibril formation. *Proc. Natl Acad. Sci. USA* **87**, 5036–5040 (1990).
33. Betsholtz, C. et al. Sequence divergence in a specific region of islet amyloid polypeptide (IAPP) explains differences in islet amyloid formation between species. *FEBS Lett.* **251**, 261–264 (1989).
34. Tenidis, K. et al. Identification of a penta- and hexapeptide of islet amyloid polypeptide (IAPP) with amyloidogenic and cytotoxic properties. *J. Mol. Biol.* **295**, 1055–1071 (2000).
35. Gremer, L. et al. Fibril structure of amyloid-β(1–42) by cryo–electron microscopy. *Science* **358**, 116–119 (2017).
36. Röder, C. et al. Atomic structure of PI3-kinase SH3 amyloid fibrils by cryo-electron microscopy. *Nat. Commun.* **10**, 3754 (2019).
37. Janson, J. et al. Increased risk of type 2 diabetes in Alzheimer's disease. *Diabetes* **53**, 474–481 (2004).
38. Yang, Y. & Song, W. Molecular links between Alzheimer's disease and diabetes mellitus. *Neuroscience* **250**, 140–150 (2013).
39. Colvin, M. T. et al. Atomic resolution structure of monomorphic $A\beta_{42}$ amyloid fibrils. *J. Am. Chem. Soc.* **138**, 9663–9674 (2016).
40. Wälti, M. A. et al. Atomic-resolution structure of a disease-relevant $A\beta_{1-42}$ amyloid fibril. *Proc. Natl Acad. Sci. USA* **113**, 4976–4984 (2016).
41. Tycko, R. Molecular structure of aggregated amyloid-β: insights from solid state nuclear magnetic resonance. *Cold Spring Harb. Perspect. Med.* **6**, a024083 (2016).
42. Xiao, Y. et al. $A\beta_{1-42}$ fibril structure illuminates self-recognition and replication of amyloid in Alzheimer's disease. *Nat. Struct. Mol. Biol.* **22**, 499–505 (2015).
43. Kollmer, M. et al. Cryo-EM structure and polymorphism of Aβ amyloid fibrils purified from Alzheimer's brain tissue. *Nat. Commun.* **10**, 4760 (2019).
44. Colvin, M. T. et al. Atomic resolution structure of monomorphic $A\beta_{42}$ amyloid fibrils. *J. Am. Chem. Soc.* **138**, 9663–9674 (2016).
45. Sakagashira, S. et al. Missense mutation of amylin gene (S20G) in Japanese NIDDM patients. *Diabetes* **45**, 1279–1281 (1996).
46. Seino, S. S20G mutation of the amylin gene is associated with type II diabetes in Japanese. Study Group of Comprehensive Analysis of Genetic Factors in Diabetes Mellitus. *Diabetologia* **44**, 906–909 (2001).
47. Meier, D. T. et al. The S20G substitution in hIAPP is more amyloidogenic and cytotoxic than wild-type hIAPP in mouse islets. *Diabetologia* **59**, 2166–2171 (2016).
48. Cao, P. et al. Sensitivity of amyloid formation by human islet amyloid polypeptide to mutations at residue 20. *J. Mol. Biol.* **421**, 282–295 (2012).
49. Sakagashira, S. et al. S20G mutant amylin exhibits increased in vitro amyloidogenicity and increased intracellular cytotoxicity compared to wild-type amylin. *Am. J. Pathol.* **157**, 2101–2109 (2000).
50. Ma, Z. et al. Enhanced in vitro production of amyloid-like fibrils from mutant (S20G) islet amyloid polypeptide. *Amyloid* **8**, 242–249 (2001).
51. Xu, W., Jiang, P. & Mu, Y. Conformation preorganization: effects of S20G mutation on the structure of human islet amyloid polypeptide segment. *J. Phys. Chem. B* **113**, 7308–7314 (2009).
52. Mirecka, E. A. et al. β-hairpin of islet amyloid polypeptide bound to an aggregation inhibitor. *Sci. Rep.* **6**, 33474 (2016).
53. Nilsberth, C. et al. The 'Arctic' APP mutation (E693G) causes Alzheimer's disease by enhanced Aβ protofibril formation. *Nat. Neurosci.* **4**, 887–893 (2001).

54. Padrick, S. B. & Miranker, A. D. Islet amyloid polypeptide: identification of long-range contacts and local order on the fibrillogenesis pathway. *J. Mol. Biol.* **308**, 783–794 (2001).
55. Chen, M. S. et al. Characterizing the assembly behaviors of human amylin: a perspective derived from C-terminal variants. *Chem. Commun.* **49**, 1799–1801 (2013).
56. Yonemoto, I. T., Kroon, G. J. A., Dyson, H. J., Balch, W. E. & Kelly, J. W. Amylin proprotein processing generates progressively more amyloidogenic peptides that initially sample the helical state. *Biochemistry* **47**, 9900–9910 (2008).
57. Kruger, D. F. & Gloster, M. A. Pramlintide for the treatment of insulin-requiring diabetes mellitus: rationale and review of clinical data. *Drugs* **64**, 1419–1432 (2004).
58. Roth, J. D. et al. Leptin responsiveness restored by amylin agonism in diet-induced obesity: evidence from nonclinical and clinical studies. *Proc. Natl Acad. Sci. USA* **105**, 7257–7262 (2008).
59. Wang, H., Abedini, A., Ruzsicska, B. & Raleigh, D. P. Rationally designed, nontoxic, nonamyloidogenic analogues of human islet amyloid polypeptide with improved solubility. *Biochemistry* **53**, 5876–5884 (2014).

Methods

Sample preparation. Human IAPP (H-KCNTATCATQRLANFLVHSSNNFGA ILSSTNVGSNTY-NH_2; molecular mass 3903.4 Da) with an amidated C terminus and a disulfide bond between Cys2 and Cys7 was custom synthesized (Pepscan, Lelystad). Identity and purity (93.1%) were confirmed by reverse-phase HPLC (RP-HPLC) and mass spectroscopy. RP-HPLC of a reduced sample confirmed that the disulfide bond between Cys2 and Cys7 was fully established in the non-reduced sample. To ensure monomeric starting material, the peptide was dissolved at 2 mg ml^{-1} in 1,1,1,3,3,3-hexafluoro-2-propanol at room temperature for 1 h and lyophilized. Afterward, 1 mg peptide powder was dissolved in 0.5 ml aqueous 6 M guanidine hydrochloride solution, and size-exclusion chromatography was performed on a Superdex 75 Increase 10/300 column (GE Healthcare) equilibrated with 10 mM 2-(*N*-morpholino)ethanesulfonic acid (MES)/NaOH buffer at a pH of 6.0 using an ÄKTA Purifier system (GE Healthcare). The monomeric peak fraction was collected, aliquotted, flash frozen in liquid nitrogen and stored at −80 °C for further use. The purity of the IAPP monomer fraction was 93.8% according to RP-HPLC. IAPP fibrils were prepared from the stock solution by diluting to a final concentration of 100 µM peptide with 10 mM MES/NaOH buffer (pH 6.0, 6 mM NaN_3). Fibrillation occurred by incubation within 7 d at room temperature under quiescent conditions in 1.5-ml Protein LoBind tubes (Eppendorf). As a control, we also prepared fibrils from an IAPP monomer sample of increased purity (96.9% after size-exclusion chromatography) due to an additional preparative RP-HPLC purification step preceding monomerization. All three dominant polymorphs were recovered in this sample, indicating that increasing peptide purity does not affect aggregation kinetics or thermodynamics in a way that would result in monomorphic fibrillation.

Atomic force microscopy. IAPP fibrils in 10 mM MES/NaOH buffer (pH 6.0, 6 mM NaN_3) were diluted to a peptide concentration of 10 µM monomer equivalent. Afterward, 5 µl of the fibril solution was applied to freshly cleaved muscovite mica and incubated under a humid atmosphere for 10 min. After three washing steps with 100 µl ddH_2O, the samples were dried with a stream of N_2 gas. Imaging was performed in intermittent contact mode (AC mode) in a Nano Wizard 3 atomic force microscope (JPK, Berlin) using a silicon cantilever and tip (OMCL-AC160TS-R3, Olympus) with a typical tip radius of 9 ± 2 nm, a force constant of 26 N m^{-1} and a resonance frequency of approximately 300 kHz. The images were processed using JPK data processing software (version spm-5.0.84). For the height profiles presented, a polynomial fit was subtracted from each scan line, first independently and then using limited data range.

Cryo-electron microscopy image acquisition. Cryo-EM sample preparation was performed on glow-discharged holey carbon films (Quantifoil R 1.2/1.3, 300 mesh). A 2.5-µl sample containing 100 µM IAPP in 10 mM MES/NaOH buffer (pH 6.0, 6 mM NaN_3) was applied to the carbon grid and incubated for 1 min. Subsequently, the sample was blotted for 5 s (blotting force 5) before cryo-plunging using a Vitrobot (FEI). With 110,000-fold nominal magnification, 1,330 micrographs were recorded on a Tecnai Arctica electron microscope operating at 200 kV with a field emission gun using a Falcon III (FEI) direct electron detector in electron counting mode directed by EPU data collection software (version 1.5). Each movie was composed of 50 fractions, and each fraction contained 36 frames, resulting in a total of 1,800 frames recorded per micrograph. The sample was exposed to an integrated flux of 0.9 e^- Aring;$^{-2}$ s^{-1} for 46.33 s. Applied defocus values ranged from −1 to −2.2 µm. The pixel size was calibrated to 0.935 Å as described previously[36]. Details of data acquisition are summarized in Table 1.

Cryo-electron microscopy image processing and helical reconstruction. For all polymorphs, MotionCor2 (ref. [60]) was used for movie correction, and contrast transfer function parameters were fitted with CTFFIND4 (ref. [61]). Fibrils were manually picked, and segments were extracted with an inter-box distance of 10% of the box sizes. Box sizes were chosen as 220 Å, 200 Å and 220 Å for PM1, PM2 and PM3, respectively. Further image processing, including 3D reconstructions, was performed with RELION 3.0.5 (refs. [62,63]).

For all polymorphs (PM1, PM2 and PM3), we used a noise-filled cylinder as an initial density model. Initial rounds of density refinement used the relion_refine command without the auto_refine option ($K = 1$) and a T value of 20. Final refinements were conducted with a T value of 200. Gold-standard refinements were performed as described previously[35] by selecting entire fibrils and splitting the dataset accordingly into an even and an odd set. Fourier shell correlation curves were computed between two half maps. According to the 0.143 criterion, the obtained resolutions were 4.2 Å (PM1), 4.2 Å (PM2) and 8.1 Å (PM3) (Extended Data Figs. 6–8). Image processing and reconstruction details for all polymorphs are presented in Table 1.

Model building and refinement of PM1. For PM1, a single-chain atomic model was built with Coot[64,65] by placing a polyalanine model de novo into the density. The density was clearly resolved and unambiguously defined the backbone trace. After manual optimization of the protein backbone, side chains were added and rotamers were manually refined with respect to Ramachandran outliers and potential clashes. Five copies of the final single-chain model were placed into the EM density map. The final model, containing six symmetry-related monomers of IAPP PM1, was used for real-space refinement in PHENIX[66] with manually assigned β-sheets. Subsequently, the model was refined by multiple rounds of optimization in Coot, PHENIX and MDFF[67,68]. MDFF was performed using an explicit solvent. The structure was embedded in a box of water, and ions were added to the system (concentration, 1.5 M). Secondary structure, *cis*-peptide and chirality restraints were applied. The scaling factor of the map potential was set to $g = 0.3$, and a time period of 10 ns was simulated. The final model of PM1 was obtained by averaging the coordinates of the MDFF trajectory and a final energy minimization with the non-crystallographic symmetry restraints and position restraints using CNS[69,70], including hydrogen atoms. *B* factors were assigned based on r.m.s.f. values calculated from the MDFF trajectory. After model evaluation using MolProbity[71], molecular graphics and further analyses were performed using Chimera[72] and ChimeraX[73]. The final statistics of the refinement are shown in Table 1.

Model building and refinement of PM2. Because of the difficulties in assigning residues to the density of PM2, two polyalanine backbones, each containing 21 residues, were built in both forward and backward trace directions in Coot[64,65]. A total of 17 possible assignments of segments from the IAPP sequence to the 21 residues were visible in the density. Accordingly, we performed 17 side chain assignments for each backbone using Scwrl4 (ref. [74]). The resulting 34 models were energy minimized with CNS[69] and refined into the density map using DireX[30]. The C_{free} value[31] is the real-space map correlation coefficient computed from the density map filtered with a bandpass of 3.0- to 4.0-Å resolution and served as a criterion to rank the models (Extended Data Fig. 3). The model that scored best according to this ranking was further refined using MDFF[67,68] with the same settings as those for PM1. Refinement was finalized by averaging the coordinates of the MDFF trajectory.

Molecular dynamics simulation. MD simulations were performed to test the stability of the PM1 model. The starting structure for the simulation was built using CHARMM-GUI solution builder[75,76] by inserting the cryo-EM structure of PM1 into a cubic water box containing 38,907 water molecules and further adding 10 chloride ions to neutralize the system. We carried out two independent all-atom simulations using GROMACS[77] (version 2019.3) and CHARMM36 force fields for protein[78], water[79] and ions[80]. The systems were first minimized using the steepest descent algorithm in 5,000 steps to remove bad contacts, followed by 500 ps (time step, 1 fs) of equilibration in an ensemble with constant volume and temperature. Later, two production runs of 250 ns were conducted under conditions of constant pressure and temperature, with a time step of 2 fs, by applying LINCS constraints to the bonds containing hydrogen atoms[81]. The temperature of the systems was maintained at 300 K using a Nosé-Hoover thermostat[82,83], and the pressure was maintained at 1 bar with a Parrinello–Rahman barostat[84]. Short-range electrostatic and van der Waals interactions were computed up to a cutoff of 12 Å using potential-shift and force-switch methods, respectively. Long-range electrostatic interactions beyond the 12 Å cutoff were computed using the particle-mesh Ewald algorithm[85].

Reporting Summary. Further information on research design is available in the Nature Research Reporting Summary linked to this article.

Data availability

The structure of IAPP PM1 has been deposited in the Protein Data Bank under accession code PDB 6Y1A. The cryo-EM density maps have been deposited in the Electron Microscopy Data Bank under accession codes EMD-10669 (PM1), EMD-10670 (PM2) and EMD-10671 (PM3).

References

60. Zheng, S. Q., Palovcak, E., Armache, J.-P., Cheng, Y. & Agard, D. A. MotionCor2: anisotropic correction of beam-induced motion for improved cryo-electron microscopy. *Nat. Methods* **14**, 331–332 (2017).
61. Rohou, A. & Grigorieff, N. CTFFIND4: fast and accurate defocus estimation from electron micrographs. *J. Struct. Biol.* **192**, 216–221 (2015).
62. He, S. & Scheres, S. H. W. Helical reconstruction in RELION. *J. Struct. Biol.* **198**, 163–176 (2017).
63. Scheres, S. H. W. RELION: implementation of a Bayesian approach to cryo-EM structure determination. *J. Struct. Biol.* **180**, 519–530 (2012).
64. Emsley, P. & Cowtan, K. Coot: model-building tools for molecular graphics. *Acta Crystallogr. D Biol. Crystallogr.* **60**, 2126–2132 (2004).
65. Emsley, P., Lohkamp, B., Scott, W. G. & Cowtan, K. Features and development of Coot. *Acta Crystallogr. D Biol. Crystallogr.* **66**, 486–501 (2010).
66. Adams, P. D. et al. PHENIX: a comprehensive Python-based system for macromolecular structure solution. *Acta Crystallogr. D Biol. Crystallogr.* **66**, 213–221 (2010).
67. Trabuco, L. G., Villa, E., Schreiner, E., Harrison, C. B. & Schulten, K. Molecular dynamics flexible fitting: a practical guide to combine cryo-electron microscopy and X-ray crystallography. *Methods* **49**, 174–180 (2009).

68. Trabuco, L. G., Villa, E., Mitra, K., Frank, J. & Schulten, K. Flexible fitting of atomic structures into electron microscopy maps using molecular dynamics. *Structure* **16**, 673–683 (2008).
69. Brunger, A. T. et al. Crystallography & NMR system: a new software suite for macromolecular structure determination. *Acta Crystallogr. D Biol. Crystallogr.* **54**, 905–921 (1998).
70. Brunger, A. T. Version 1.2 of the Crystallography and NMR system. *Nat. Protoc.* **2**, 2728–2733 (2007).
71. Chen, V. B. et al. MolProbity: all-atom structure validation for macromolecular crystallography. *Acta Crystallogr. D Biol. Crystallogr.* **66**, 12–21 (2010).
72. Pettersen, E. F. et al. UCSF Chimera—a visualization system for exploratory research and analysis. *J. Comput. Chem.* **25**, 1605–1612 (2004).
73. Goddard, T. D. et al. UCSF ChimeraX: meeting modern challenges in visualization and analysis. *Protein Sci.* **27**, 14–25 (2018).
74. Krivov, G. G., Shapovalov, M. V. & Dunbrack, R. L. Improved prediction of protein side-chain conformations with SCWRL4. *Proteins* **77**, 778–795 (2009).
75. Jo, S., Kim, T., Iyer, V. G. & Im, W. CHARMM-GUI: a web-based graphical user interface for CHARMM. *J. Comput. Chem.* **29**, 1859–1865 (2008).
76. Lee, J. et al. CHARMM-GUI input generator for NAMD, GROMACS, AMBER, OpenMM, and CHARMM/OpenMM simulations using the CHARMM36 Additive Force Field. *J. Chem. Theory Comput.* **12**, 405–413 (2016).
77. Abraham, M. J. et al. GROMACS: high performance molecular simulations through multi-level parallelism from laptops to supercomputers. *SoftwareX* **1–2**, 19–25 (2015).
78. Best, R. B. et al. Optimization of the additive CHARMM all-atom protein force field targeting improved sampling of the backbone φ, ψ and side-chain χ_1 and χ_2 dihedral angles. *J. Chem. Theory Comput.* **8**, 3237–3256 (2012).
79. MacKerell, A. D. et al. All-atom empirical potential for molecular modeling and dynamics studies of proteins. *J. Phys. Chem. B* **102**, 3586–3616 (1998).
80. Beglov, D. & Roux, B. Finite representation of an infinite bulk system: solvent boundary potential for computer simulations. *J. Chem. Phys.* **100**, 9050–9063 (1994).
81. Hess, B., Bekker, H., Berendsen, H. J. C. & Fraaije, J. G. E. M. LINCS: a linear constraint solver for molecular simulations. *J. Comput. Chem.* **18**, 1463–1472 (1997).
82. Nosé, S. A unified formulation of the constant temperature molecular dynamics methods. *J. Chem. Phys.* **81**, 511–519 (1984).
83. Hoover, W. G. Canonical dynamics: equilibrium phase-space distributions. *Phys. Rev. A Gen. Phys.* **31**, 1695–1697 (1985).
84. Parrinello, M. & Rahman, A. Polymorphic transitions in single crystals: a new molecular dynamics method. *J. Appl. Phys.* **52**, 7182–7190 (1981).
85. Darden, T., York, D. & Pedersen, L. Particle mesh Ewald: an *N*·log(*N*) method for Ewald sums in large systems. *J. Chem. Phys.* **98**, 10089–10092 (1993).

Acknowledgements

We thank P.J. Peters and C. López-Iglesias for advice and helpful discussions, H. Duimel for help with sample preparation and the M4I Division of Nanoscopy of Maastricht University for microscope access and support. The authors gratefully acknowledge the computing time granted by the Jülich Aachen Research Alliance High-Performance Computing (JARA-HPC) Vergabegremium and VSR commission on the supercomputer JURECA at Forschungszentrum Jülich. We acknowledge support from a European Research Council (ERC) Consolidator grant (no. 726368; W.H.), the Alzheimer Forschung Initiative e.V. and Alzheimer Nederland (project no. 19082CB; R.B.G.R. and G.F.S.), the Russian Science Foundation (RSF; project no. 20-64-46027; L.G. and D.W.) and the Helmholtz Association Initiative and Networking Fund (project no. ZT-I-0003; K.R.P. and G.F.S.).

Author contributions

L.G., W.H., T.K. and G.F.S. conceived the study. T.K. and L.G. performed and analyzed fibril preparation and AFM experiments. R.G.B.R. performed cryo-EM experiments and the initial data analysis. C.R., T.K. and G.F.S. performed image processing and initial reconstruction. C.R. and G.F.S. performed reconstruction, model building and refinement. L.U.S., K.R.P. and G.F.S. performed molecular dynamics simulations and structure fitting. C.R., T.K., G.F.S., W.H., L.G., K.R.P. and L.U.S. wrote the manuscript. D.W. and all other authors discussed the results and commented on the manuscript.

Competing interests

The authors declare no competing interests.

Additional information

Extended data is available for this paper at https://doi.org/10.1038/s41594-020-0442-4.

Supplementary information is available for this paper at https://doi.org/10.1038/s41594-020-0442-4.

Correspondence and requests for materials should be addressed to W.H. or G.F.S.

Peer review information Peer reviewer reports are available. Inês Chen was the primary editor on this article and managed its editorial process and peer review in collaboration with the rest of the editorial team.

Reprints and permissions information is available at www.nature.com/reprints.

2.1 Publication II: Supplementary material

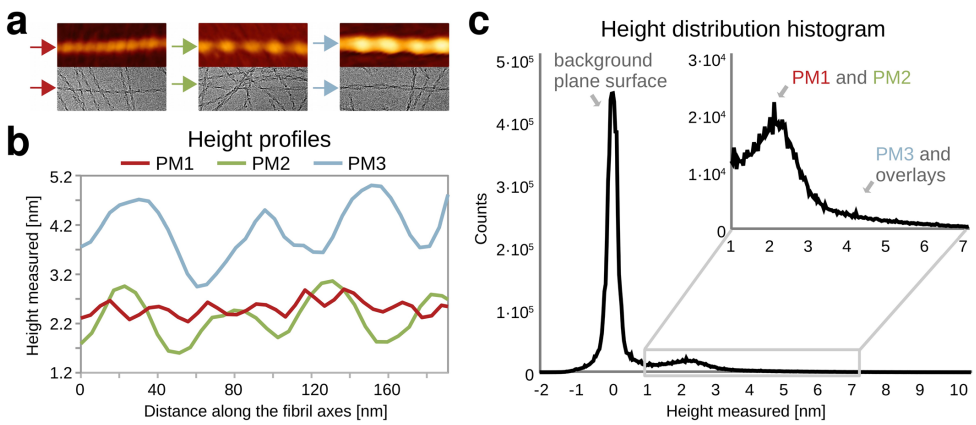

Extended Data Fig. 1 | Comparison of described IAPP polymorphs. a, Single fibril cut-outs of polymorphs PM1, PM2 and PM3 from AFM images (top row) and cryo-EM micrographs (bottom row); single box size is 100 × 250 nm. **b**, Height profiles of individual fibrils extracted from AFM images. **c,** Height distribution histogram, showing the highest number of counts for the plane background surface around 0 nm and a distinct peak around 2.2 nm. The peak around 2.2 nm includes both PM1 and PM2 which are non-distinguishable in sense of height distribution. Moreover, a pronounced shoulder on the right corresponds to the presence of lower amounts of PM3 as well as the overlaps of single PM1/PM2 fibrils. For the height distribution analysis, histograms from six height images of 5 × 5 µm size and a resolution of 1024 × 1024 pixels were obtained, binned and presented in one graph. An example of the image used can be seen in Supplementary Figure 2.

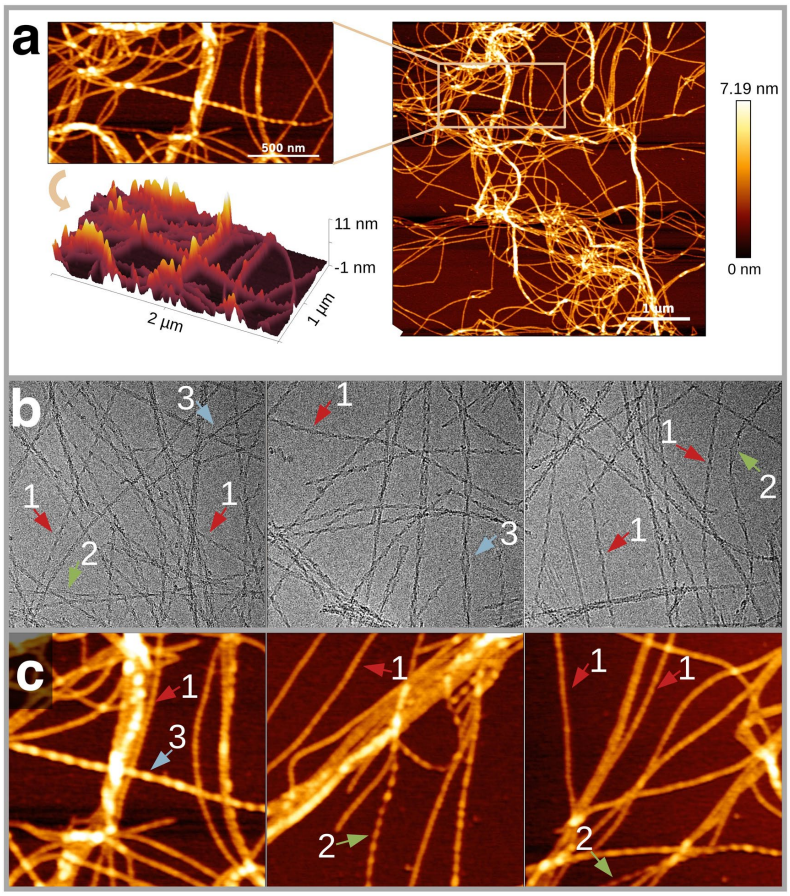

Extended Data Fig. 2 | Overview of IAPP polymorphs. a, Typical height profile AFM image used for polymorph distribution analysis. **b**, Cryo-EM micrographs showing 370 × 370 nm areas. **c**, AFM overview images showing 1 × 1 µm areas. Arrows indicate the presence of PM1 (red), PM2 (green) and PM3 (blue).

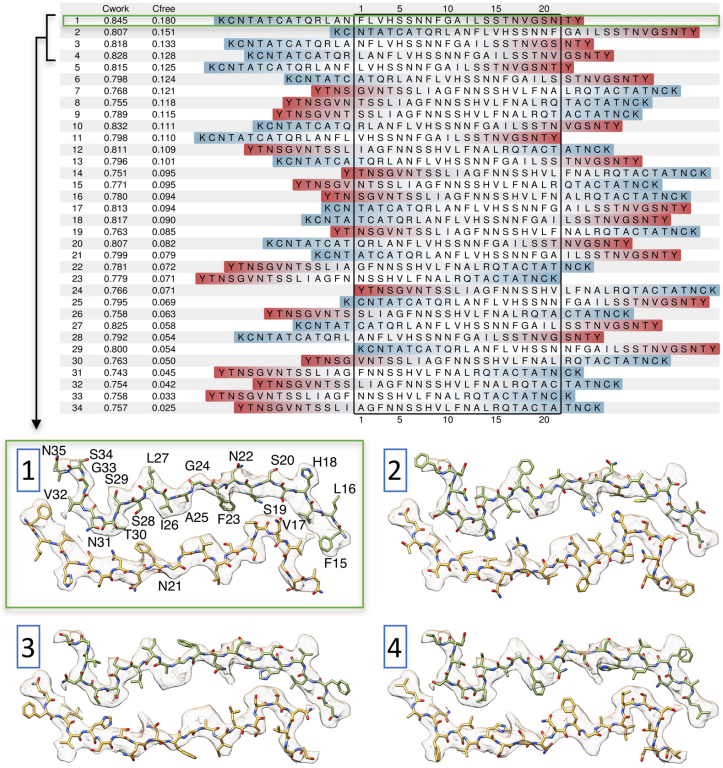

Extended Data Fig. 3 | DireX analysis of polymorph 2 (PM2). The table contains the C_{work} and C_{free} values from DireX fitting of 21-residue-long sequence snippets (black box) of IAPP in both possible Cα-chain directions into a density layer of PM2 together with the respective amino acid sequence. The results are ranked according to their C_{free} values. Highlighted (green box) is the most favorable sequence fit. Atomic models of the four most favorable sequence snippets are shown at the bottom. Note that some models, for example model 2, can be excluded since they are incompatible with the disulfide bond between residues Cys2 and Cys7.

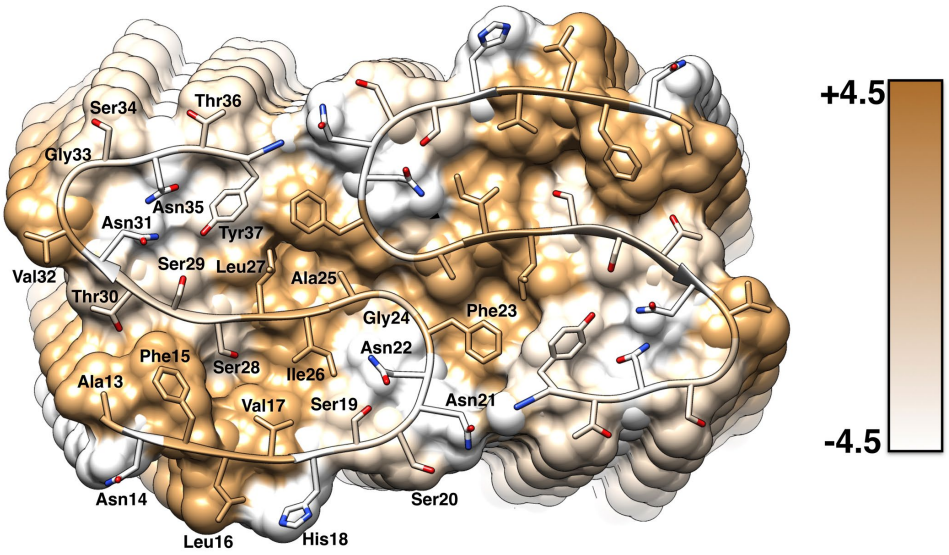

Extended Data Fig. 4 | Hydrophobicity plot of the fibril displayed as top view. Hydrophobicity levels of the IAPP polymorph 1 (PM1) fibril are colored according to Kyte-Doolittle in the hydrophobicity score range −4.5 (white) to 4.5 (gold). One hydrophobic cluster spans the entire diagonal of the fibril cross-section. This hydrophobic streak is surrounded by highly ordered polar clusters.

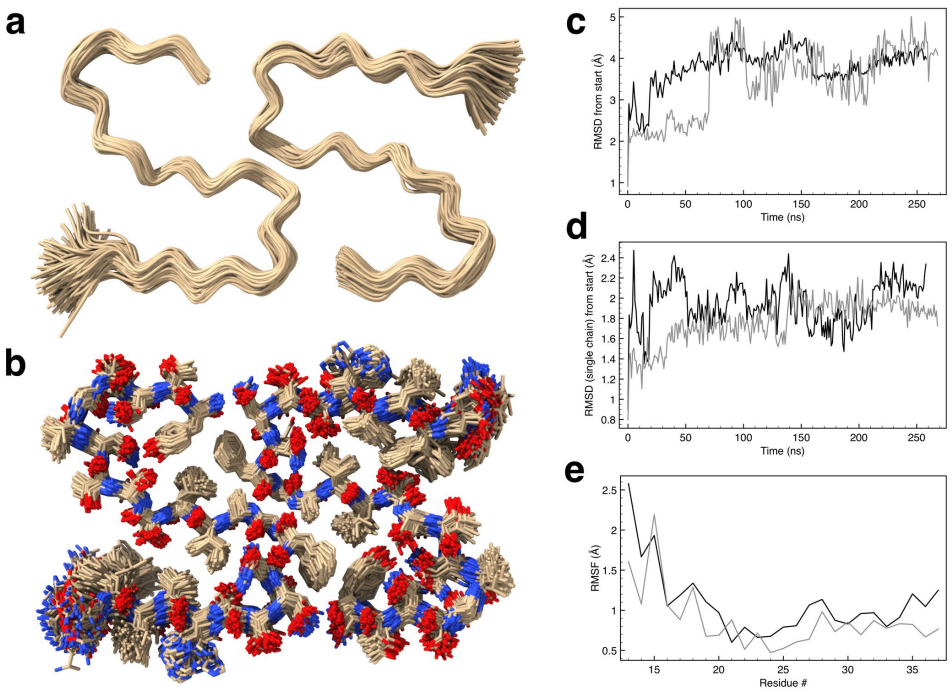

Extended Data Fig. 5 | Results of molecular dynamics simulations of IAPP polymorph 1 (PM1). Superimposed snapshots from a 250 ns simulation displaying only the backbone (**a**) or all atoms (except for solvent and hydrogen) (**b**). **c,** Showing the RMSD from the deposited structure of PM1 (PDB ID 6Y1A) for two 250 ns simulations (black and grey lines, respectively). **d,** Showing the RMSD of a single chain from the deposited structure during the two 250 ns simulations. **e,** Showing the atomic root mean square fluctuations (RMSF) for each residue calculated over each 250 ns simulation.

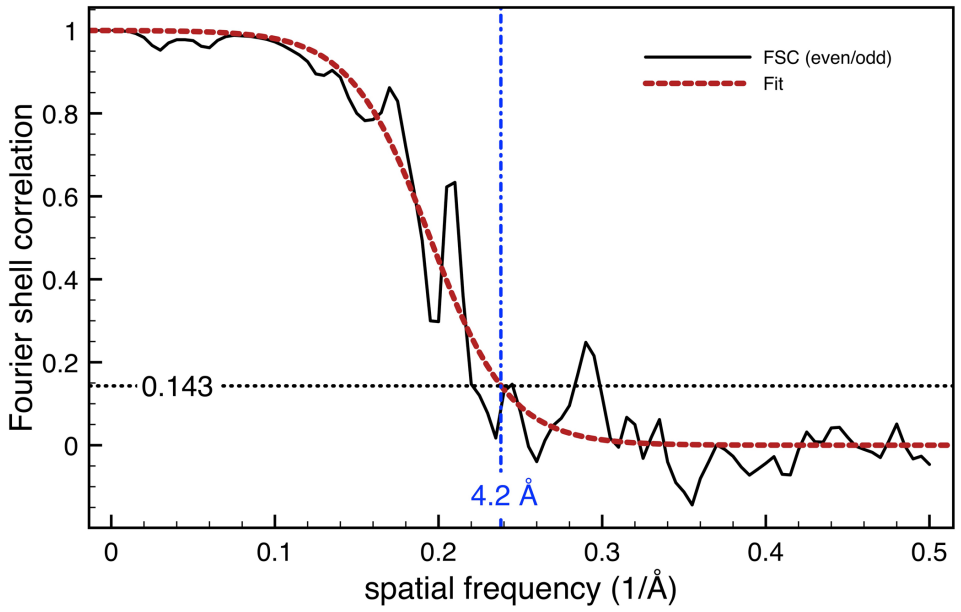

Extended Data Fig. 6 | FSC Analysis of polymorph 1 (PM1). FSC curves from the even/odd test (solid black) from the gold-standard refinement yields a resolution of 4.2 Å (using the 0.143 criterion). The even/odd FSC curve is fitted (red) with the model function 1/(1+exp((x-A)/B)) (with A = 0.1947 and B = 0.026) to obtain a more robust resolution estimate.

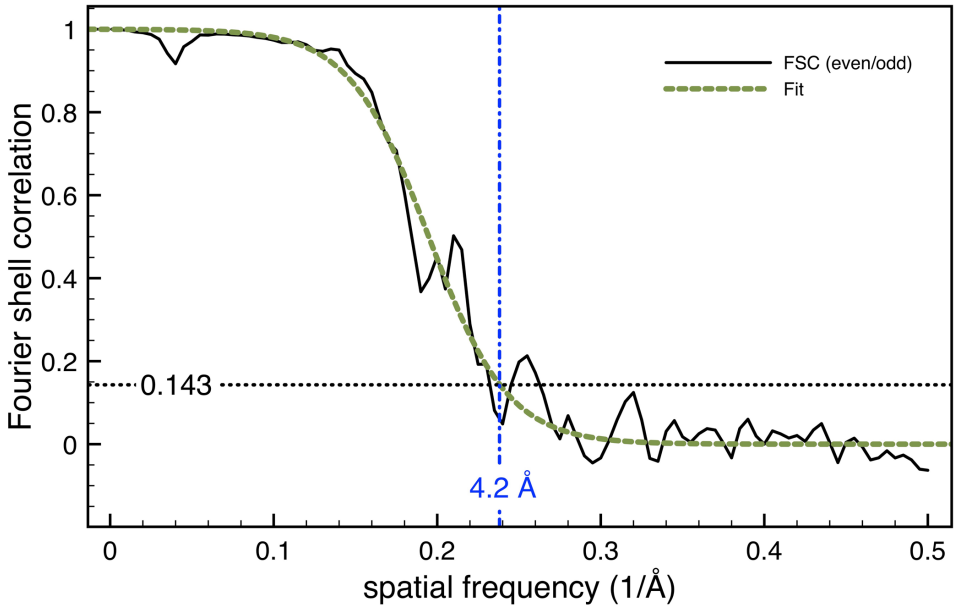

Extended Data Fig. 7 | FSC analysis of polymorph 2 (PM2). FSC curves from the even/odd test (solid black) from the gold-standard refinement yields a resolution of 4.2 Å (using the 0.143 criterion). The even/odd FSC curve is fitted (green) with the model function 1/(1+exp((x-A)/B))) (with A = 0.194789 and B = 0.02427) to obtain a more robust resolution estimate.

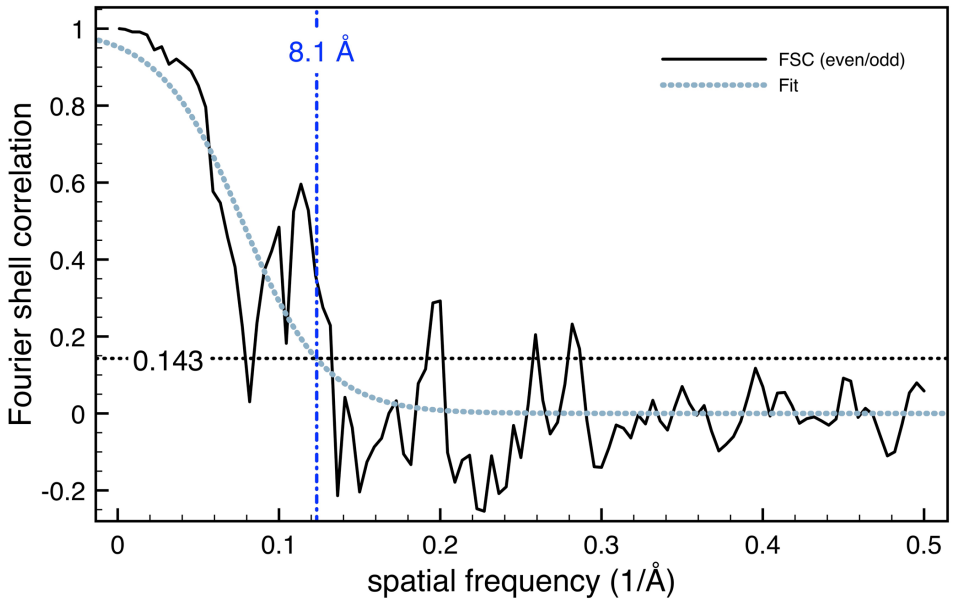

Extended Data Fig. 8 | FSC analysis of Polymorph 3 (PM3). FSC curves from the even/odd test (solid black) from the gold-standard refinement yields a resolution of 8.1 Å (using the 0.143 criterion). The even/odd FSC curve is fitted (light blue) with the model function 1/(1+exp((x-A)/B)) (with A = 0.0772 and B = 0.0256) to obtain a more robust resolution estimate.

3 Results

3.1 Reconstruction of pGlu-Aβ(3-42) PM1

Table 33: Information on microscope settings and data acquisition for the September 2020 data set of pGlu-Aβ(3-42)

Parameter	Information
Microscope settings	
Nominal magnification	SA105,000x
C1 aperture	2000
Spot size	7
C2 aperture	50
Illumination area	1
Objective aperture	100
Voltage [kV]	300
Spherical aberration [mm|	2.7
Data acquisition	
Data collection software	EPU 2.8.1
Detector	Gatan K3
Mode	Counting super-res
Pixel size [Å]	0.418
Dose rate [e/Å^2/frame]	1
Total dose [e/Å^2]	40
Exposure time [s]	2
Number of fractions	40
Exposure per hole	3
Defocus [µm]	-1.5, -1.8, -2.1, -2.4, -2.7, -3.0
Repeated focus distance [µm]	5
Number of raw movies	1,861
Processing	
Pixel size [Å] after binning	0.836
Particles used for final density map	31,408
Symmetry	C_2
Twist [°]	2.21
Rise [Å]	4.70095
Resolution [Å]	3.8 – 4.4

3.1.1 RELION-3.1.0 commands

The following commands were used to calculate 2D classes, initial models or 3D reconstructions in RELION-3.1.0.

3.1.1.1 First 3D reconstruction with the initial model based on 2D classes

srun `which relion_refine` --o Class3D/job186/run --i Select/job171/particles.star --ref InitialModel/bigclasses/bigclass_sym1/inimodel_bigclass_sym1_box300.mrc --ini_high 10 --dont_combine_weights_via_disc --pool 3 --pad 2 --ctf --ctf_corrected_ref --iter 25 --tau2_fudge 2 --particle_diameter 220 --fast_subsets --K 1 --flatten_solvent --zero_mask --strict_highres_exp 5 --oversampling 1 --healpix_order 3 --offset_range 8 --offset_step 2 --sym C1 --norm --scale --helix --helical_outer_diameter 150 --helical_nr_asu 5 --helical_twist_initial 2.0 --helical_rise_initial 4.75 --helical_z_percentage 0.3 --helical_symmetry_search --helical_twist_min 1.8 --helical_twist_max 2.2 --helical_twist_inistep 0.1 --helical_rise_min 4.6 --helical_rise_max 4.9 --helical_rise_inistep 0.1 --helical_keep_tilt_prior_fixed --sigma_tilt 5 --sigma_psi 3.33333 --sigma_rot 0 --j 64 --pipeline_control Class3D/job186/

3.1.2 Initial backbone trace for PM1 built in coot

An initial backbone trace was built with coot, for both the hairpin and S-fold. Both traces are displayed in Figure 67 with (A,B) and without (C,D) surrounding density (green) and coot-built alanine-chain (purple).

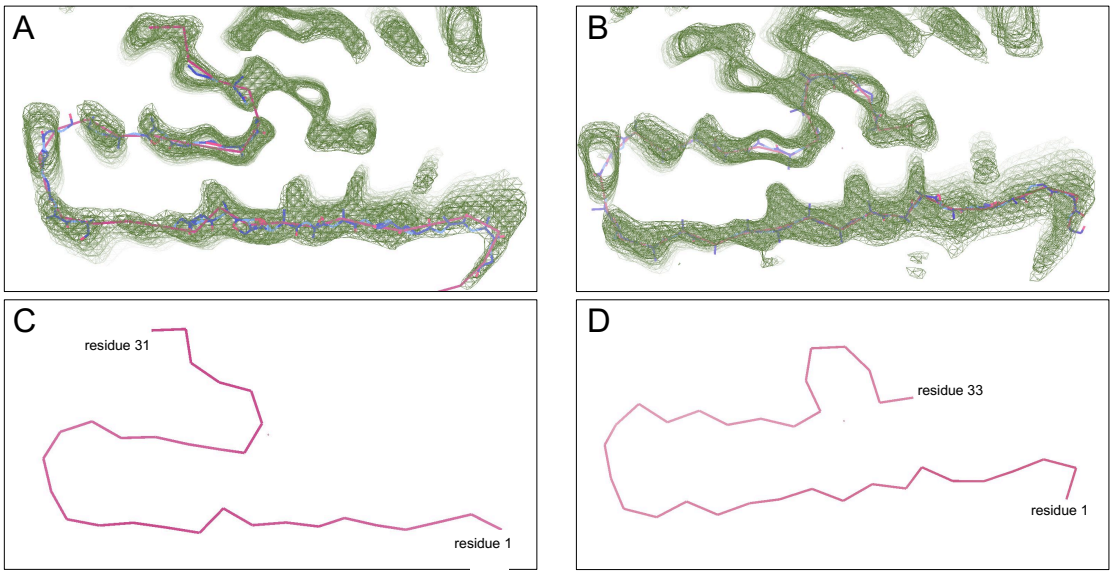

Figure 67: Initial backbone trace for pGlu-Aβ(3-42) PM1. (A) Initial backbone trace for the S-fold built with coot (pink) into the density map based on job385 (green) and with the coot-built resulting alanine-chain (purple). (B) Initial backbone trace for the hairpin fold built with coot (pink) into the density map based on job385 (green) and with the coot-built resulting alanine-chain (purple). (C) Initial backbone trace for the S-fold without surroundings displaying 31 C_α -atoms. (D) Initial backbone trace for the hairpin fold without surroundings displaying 33 C_α -atoms.

3.1.3 Overview of the pGlu-Aβ(3-42) PM1 reconstruction

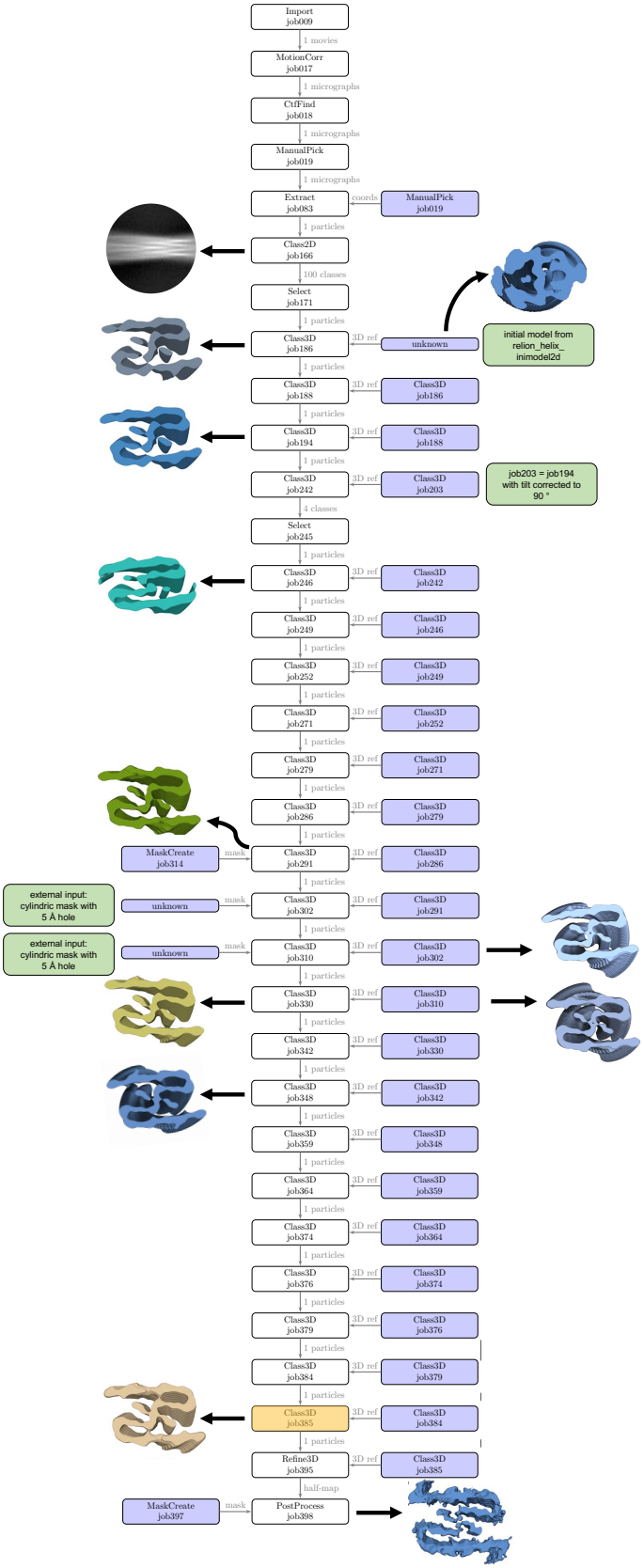

Figure 68: Overview of the pGlu-Aβ(3-42) PM1 reconstruction. The branched flowchart of PostProcess/job398 is an automated output from RELION-3.1.0 and was modified with respective density maps and information. Class3D/job385 was used for estimation of a protein backbone etc. and is highlighted in yellow.

3.2 Mass spectrometry data on pGlu-Aβ(3-42)

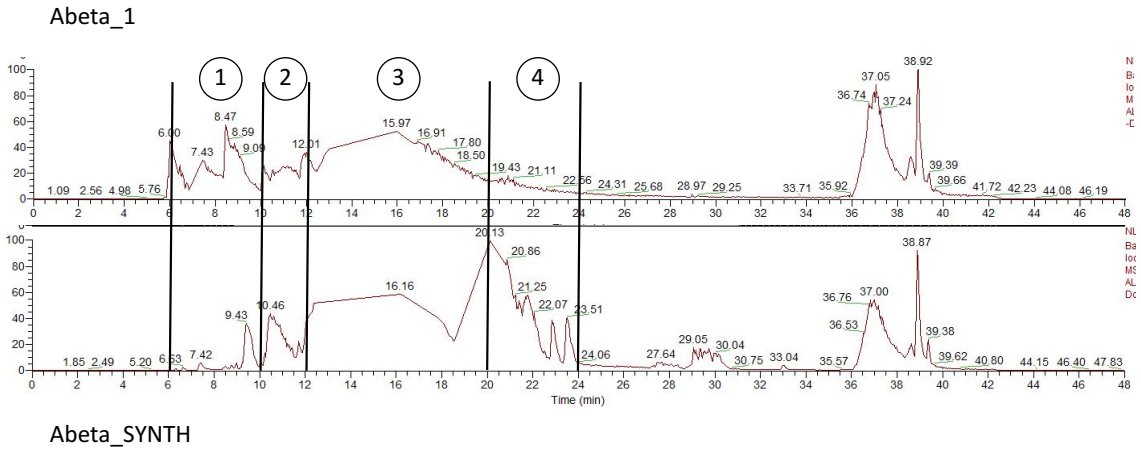

Figure 69: RP-HPLC chromatogram of pGlu-Aβ(3-42) before mass spectrometry. According to the chromatogram, the sample (top) and control (bottom) were collected in four fractions (indicated by numbers 1-4) and analyzed via MS.

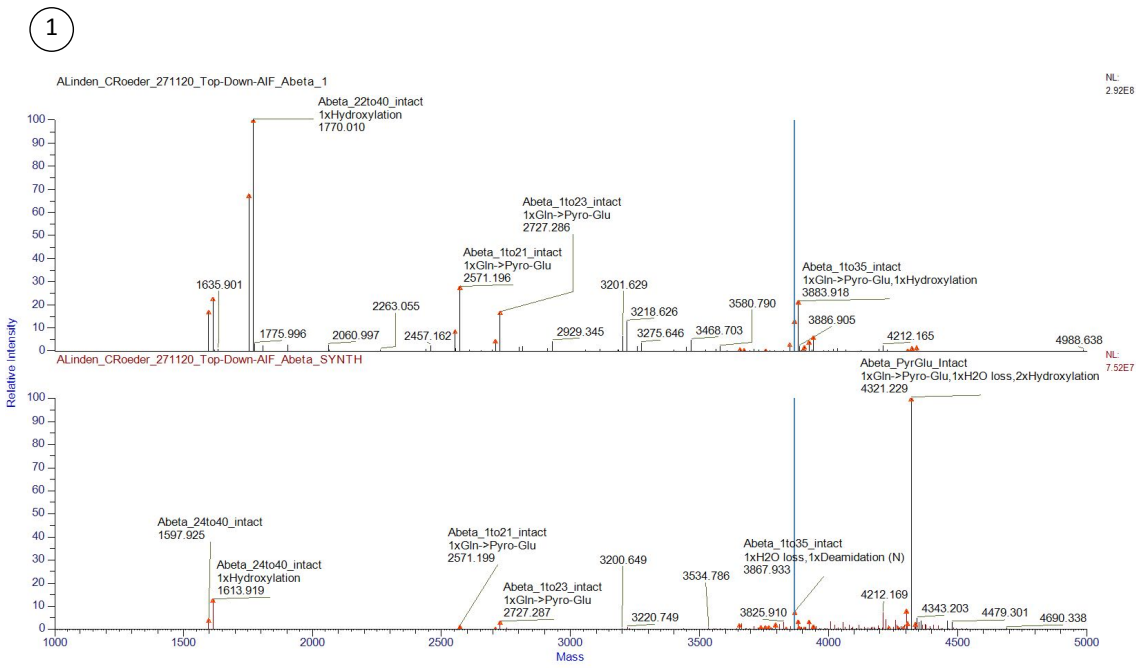

Figure 70: Mass spectrometry profile of pGlu-Aβ(3-42) sample and control in fraction 1. Top: Data for pGlu-Aβ(3-42) sample. Bottom: Data for pGlu-Aβ(3-42) control. Experiments and evaluation were performed by Andreas Linden.

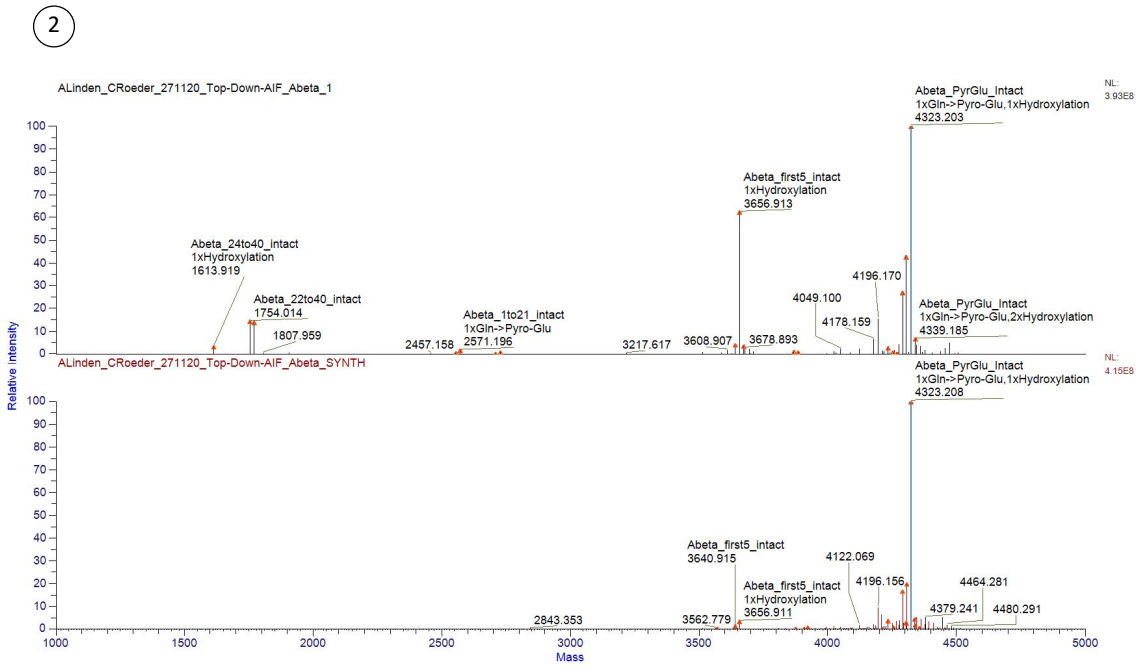

Figure 71: Mass spectrometry profile of pGlu-Aβ(3-42) sample and control in fraction 2. Top: Data for pGlu-Aβ(3-42) sample. Bottom: Data for pGlu-Aβ(3-42) control. Experiments and evaluation were performed by Andreas Linden.

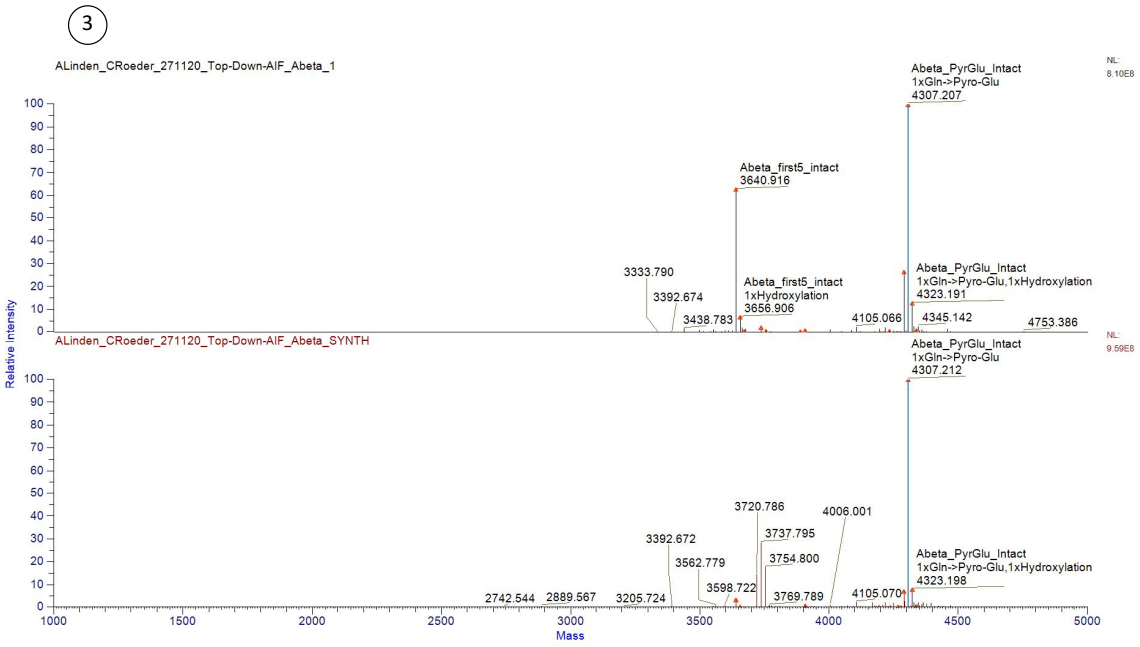

Figure 72: Mass spectrometry profile of pGlu-Aβ(3-42) sample and control in fraction 3. Top: Data for pGlu-Aβ(3-42) sample. Bottom: Data for pGlu-Aβ(3-42) control. Experiments and evaluation were performed by Andreas Linden.

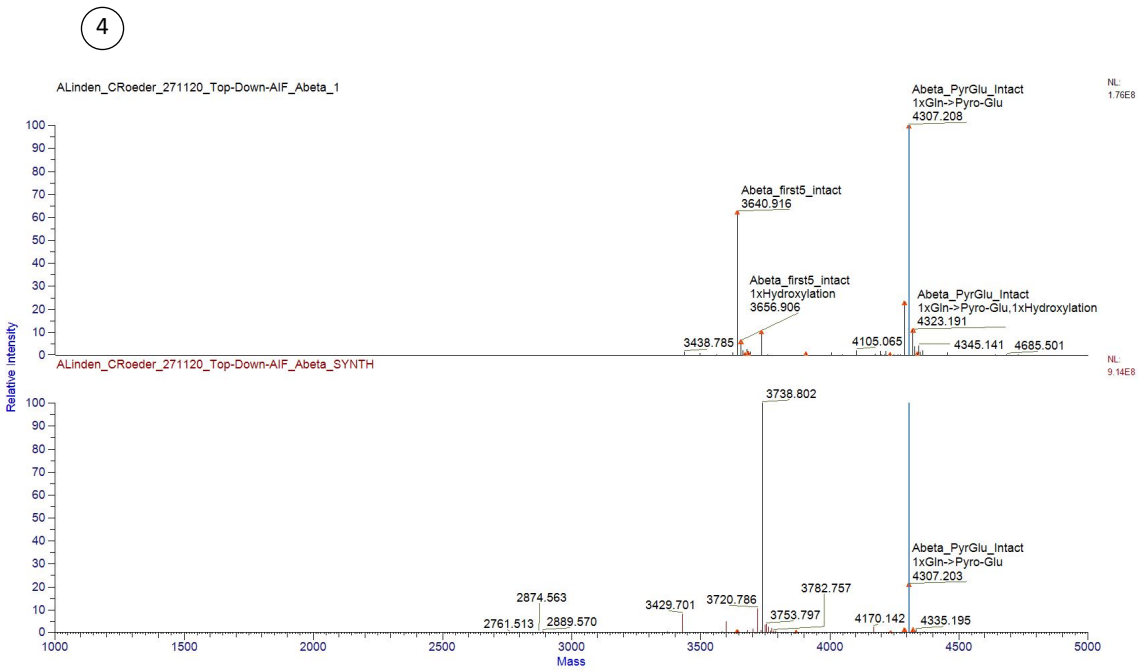

Figure 73: Mass spectrometry profile of pGlu-Aβ(3-42) sample and control in fraction 4. Top: Data for pGlu-Aβ(3-42) sample. Bottom: Data for pGlu-Aβ(3-42) control. Experiments and evaluation were performed by Andreas Linden.

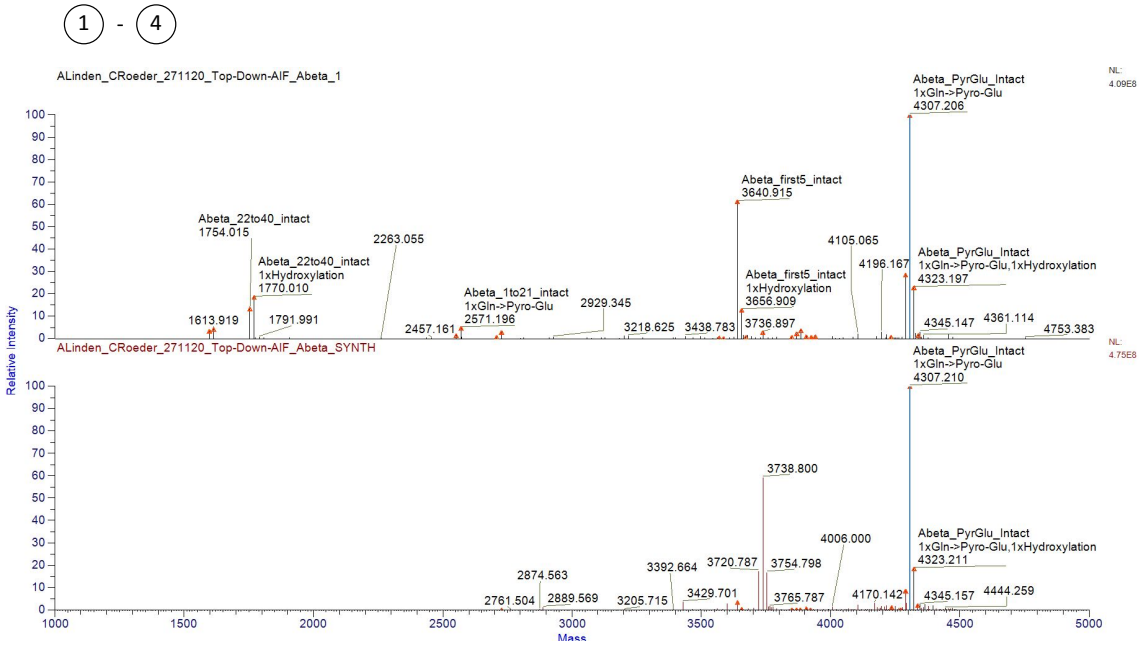

Figure 74: Mass spectrometry profile of pGlu-Aβ(3-42) sample and control in all fractions 1-4. Top: Data for pGlu-Aβ(3-42) sample. Bottom: Data for pGlu-Aβ(3-42) control. Experiments and evaluation were performed by Andreas Linden.

Table 34: Detailed mass spectrometry results on pGlu-Aβ(3-42)

fraction	mass [Da]	fragment	modification	sample	relative abundance [%]
1	4321,229	FL	1xH2O loss, 2xHydroxylation	ctrl	100
1	1613,919	AA 26-42	1xHydroxylation	pGlu	23
				ctrl	13
1	1597,925	AA 26-42		pGlu	17
				ctrl	4
1	2571,197	AA 3-23		pGlu	27
				ctrl	1
1	2727,287	AA 3-25		pGlu	16
				ctrl	3
1	3867,920	AA 3-37		pGlu	13
				ctrl	7
1	1770,010	AA 24-42	1xHydroxylation	pGlu	100
1	1754,015	AA 24-42		pGlu	67
1	2553,185	AA 3-23	1xH2O loss	pGlu	8
1	3883,918	AA 3-37	1xHydroxylation	pGlu	21
2	4307,199	FL		ctrl	20
2	4323,206	FL	1xHydroxylation	pGlu	100
				ctrl	100
2	4289,200	FL	1xH2O loss	pGlu	27
				ctrl	17
2	3656,912	AA 8-42	1xHydroxylation	pGlu	62
				ctrl	3
2	1754,014	AA 24-42		pGlu	14
2	1770,010	AA 24-42	1xHydroxylation	pGlu	14
2	4305,192	FL	1xH2O loss, 1xHydroxylation	pGlu	43
3	4307,210	FL		pGlu	100
				ctrl	100
3	4289,196	FL	1xH2O loss	pGlu	26
				ctrl	7
3	4323,195	FL	1xHydroxylation	pGlu	13
				ctrl	8
3	3640,915	AA 8-42		pGlu	63
				ctrl	3

fraction	mass [Da]	fragment	modification	sample	relative abundance [%]
3	3656,913	AA 8-42	1xHydroxylation	pGlu	6
				ctrl	0.2
4	4307,206	FL		pGlu	100
				ctrl	21
4	3640,912	AA 8-42		pGlu	62
				ctrl	1

3.3 AFM images of Aβ36

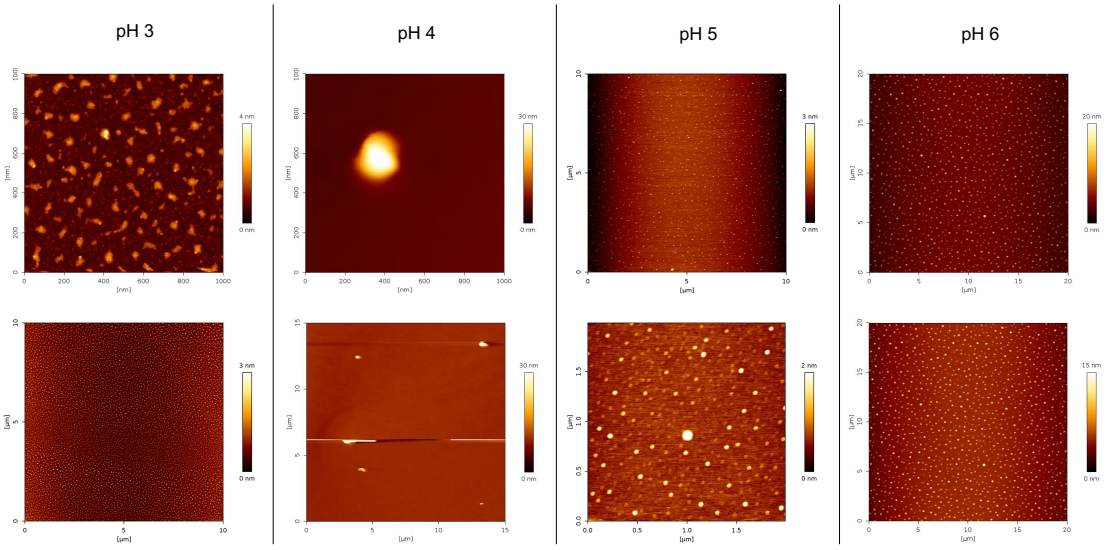

Figure 75: AFM images of Aβ36 in citrate buffer of pH values 3 – 6. Most images are empty (height up to 3 nm) with a few (pH 4, pH 6) showing globular shapes with heights up to 30 nm. Images at pH 3 display a background that does not seem to resemble aggregates but could also not be reproduced with pure buffer. No fibrils have been observed in any sample.

3.4 Negative stain EM of centrifuged Aβ(1-42)-pS8

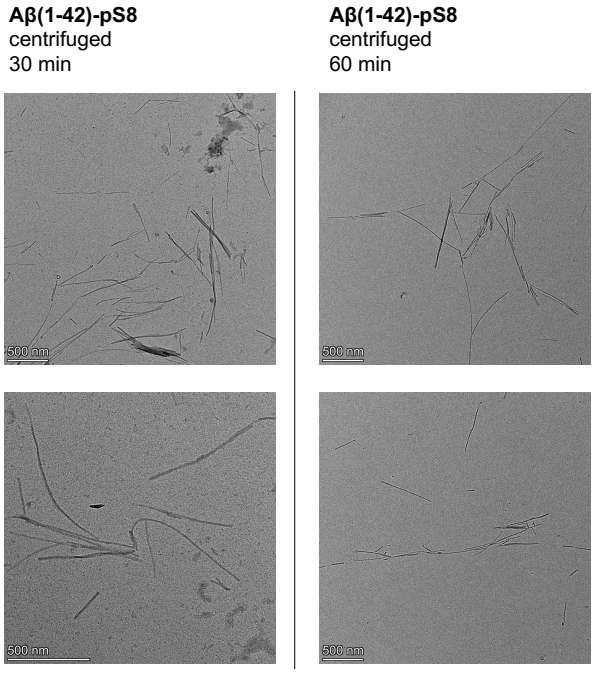

Figure 76: Negative stain EM of Aβ(1-42)-pS8 after 30 and 60 min centrifugation. Representative negative stain micrographs acquired on a Talos 120. Samples were either centrifuged for 30 or 60 min at 16,000 *g*. Magnification: 17,300x or 35,500x (bottom left)

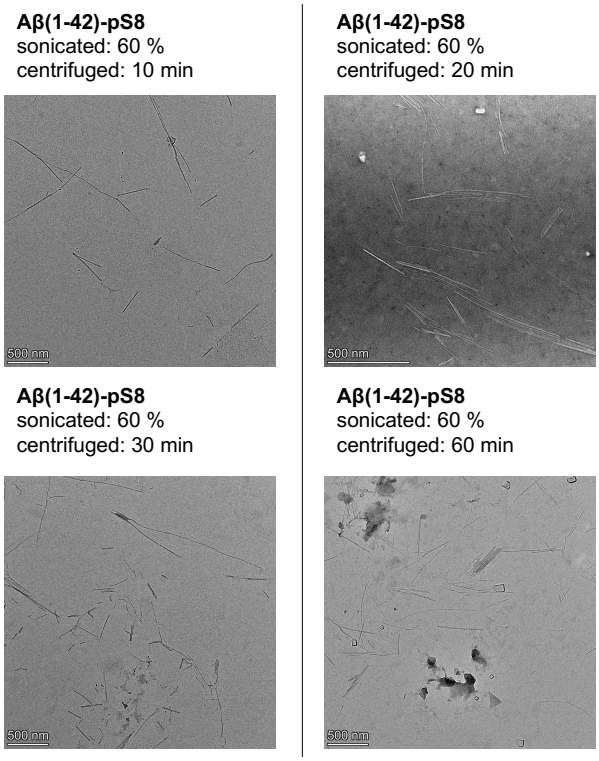

Figure 77: Negative stain EM of Aβ(1-42)-pS8 after sonication at 60 % amplitude and multiple centrifugation time points. Representative negative stain micrographs acquired on a Talos 120. The sample had been sonicated at 60 % amplitude with a VialTweeter and then centrifuged for 10, 20, 30 or 60 min at 16,000 *g*. Magnification: 17,300x or 35,500x (top right)

4 Material and Methods

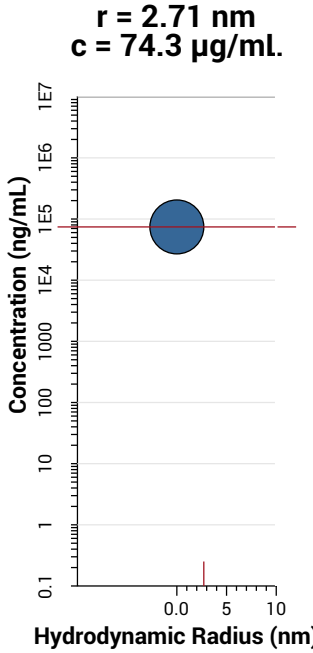

Figure 78: Output from microfluidics device Mk1. The Mk1 gives information about the hydrodynamic radius (r) of a sample and its concentration (c).

Eidesstattliche Versicherung

Ich versichere an Eides Statt, dass die Dissertation von mir selbständig und ohne unzulässige fremde Hilfe unter Beachtung der „Grundsätze zur Sicherung guter wissenschaftlicher Praxis an der Heinrich-Heine-Universität Düsseldorf“ erstellt worden ist.

_____

Datum, Unterschrift